# A New Approach to the Synthesis of Selenium Based Nanoparticles

A Thesis Presented by

**Oluwafemi Samuel Oluwatobi**

In fulfilment of the requirement for the award of the degree of

**Doctor of Philosophy**

**in the Department of Chemistry**

**University of Zululand**

**Promoter** : Prof. N. Revaprasadu

Department of Chemistry

University of Zululand

Private bag X1001

Kwadlangezwa

3886

November 2008

# CERTIFICATION

I hereby certify that this thesis is a record of original research carried out under my supervision by Mr. Oluwafemi, Samuel Oluwatobi (056766) of the Chemistry Department, University of Zululand, South Africa.

.....

**SUPERVISOR**
**PROF. N. Revaprasadu**

## DEDICATION

To God Almighty, my Jehovah Jareh who provided the strength and material needed; to Jehovah Rohi, my Shepherd who has been my guardian since birth; to Jehovah Shammah, whose presence always abide with me; to Jehovah Shalom for His ever-abiding peace throughout the course of this programme and, to Jehovah El- Shaddai my all sufficient God.

## ACKNOWLEDGEMENT

*"But ye have unction from the holy one, and you know all things.... Therefore thanks be to God which always causeth us to triumph in Christ...." (1Jh:2$^{20}$, II Cor: 2$^{14}$).*

My sincere and immense appreciation to my parents, PASTOR & MRS OLUWAFEMI, for their indefatigable love, care, prayers and magnanimous support in all ramifications right through my childhood, to this stage. You have deprived yourself of pleasure to bring me this far and make this dream a reality. Oh I love you.

I acknowledge with respect and gratitude my supervisor, Prof. Neerish Revaprasadu for inviting me in the first instance, to further my studies at the University of Zululand and for giving me the opportunity to work in this field. Thanks Prof. for all your support, care and guidance throughout the duration of the entire programme. My sincere gratitude also goes to your wife, Shaneera and your lovely triplet.

My unalloyed gratitude goes to the Oyedeji family; Daddy, Aunty, Engr. Tomi and Dr. Toluwanimi for their support in all areas since my arrival at UNIZULU and, for supporting my sister throughout her studies at UNIZULU. Daddy Oyedeji, I thank you very much for all the fatherly advice. Though due to circumstances beyond our control, I only see you once in a while however, you have never allowed this to take away the fatherly connection we have. Aunty, thank you very much for being there at all times, especially during the synthesis of my water-soluble materials. Your advice has really been of great help. Word-of-mouth can not really be enough to appreciate you. May the Lord Almighty bless you and cause His favour to abide in your family forever, for you have made this place a pleasant home for me.

My profound gratitude goes to Olabisi Onabanjo University (OOU), Ago- Iwoye, Ogun State, Nigeria, for granting me study leave to undertake this research outside the country; also the entire staff and the students of the Faculty of Science, especially the Department of Chemical Sciences, OOU. Special thanks to Prof. Afolabi Shoyode (Former V.C); Dr O.O Adeyemi, for leading me in the right direction; Dr Felix and Mrs Olubomehin, for taking care of my interest at OOU. Also a big thank you to my academic mentors for their contribution from my undergraduate days, Prof. Adamson, Prof. T. Arowolo, Prof. O. Bamgbose, Dr (Mrs) J.T Bamgbose, and my former supervisor, Prof. T. I. Odiaka for being there at all times, right till today.

My sincere appreciation to Mrs H. L Bisschoff, my God sent mother at the right time. Thank you for all your advice (spiritually & socially) and for all the pain you underwent in proof-reading this thesis. Finally, I must never forget to say thank you for your thirst-quenching and soul-refreshing coffee all the time. Mum, may the favour of God, long life and sound health abide with you and your children in Jesus name.

My warm regards to Prof. H. Swart for his keen interest in my progress, career and, for hosting me in his group. There is no doubt that knowing you lifted my career to an outstanding level. I really enjoyed every day I spent in your department during my one month visit. I also thank all the staff members of your department, your research group. especially Dr Martins and Simon for their supports during my visit. I hope that the collaboration that has begun between us will continue for a life-time.

I also want to say a chemo-thunderous thank you to Dr. Ajibade Peter and family. You are truly a brother. Thanks for your interest and advices all the time. May the Lord bless you. My special gratitude also goes to Prof. Banjo & his family, Dr. Ifedayo and architect Ifedapo, God bless you for being a source of blessing.

I also want to thank staff members, colleagues and students of the Department of Chemistry, UNIZULU, for efforts rendered in various ways and the moments we shared and, to all my friends at the University especially, Mr Peckham, Tokozani, Nelly, Ntshangase, Milicent, Ben, Ziningi, Mpumelelo, Philile, Chili, Sosibu, Phumlane, Nosipo, Mbuso, Stranger, Thandeka, Vezi, Khethiwe, Khoza, Norman, Fisiwe, Alu and Patience; the students I supervised: Maseko and Mtungwa and, my friend Sbu for being there at the start of my research and for taking me around. To Prof. Kolawole I say may the Lord reward you according to the desire of your heart towards me. A big thank-you to the National Research Foundation (NRF), South Africa and the Research Committee, UNIZULU for financial support and also, a special word of thanks to Daniela, Norman and Prof. Hoopers for their support and assistance. My appreciation also goes to the Protective Service Department (PSD) UNIZULU.

My appreciation to all my friends and students from Nigeria, for keeping in touch even though we are far apart, especially pastor Richard and family, Bro. Kola, Sis Yetty, Arotiba and family, Bro. Pius, Busayo, Adeoluwabomi, Abiola, Egbon Niyi, Yemi, Funmi Ajayi, Yinka, Dotun, Leke, Sola, Anu, Bolatito and Salewa. Thank you to Mr Lekan Jimoh and Prof. Adegoke for the time we shared during their stay here in South Africa. Seye, I really appreciate your assistance in getting journals for me.

Also, a word of appreciation to a sincere brother and esteem friend, Mr Olugbara and his wife, and to the following people, Pastor Bruce and his family; Pastor Wesley; all the members of Empangeni Baptist Church; all the members of Empangeni Baptist Church Student Society UNIZULU especially the choir members, for the opportunity granted me to serve you. I also thank the International Student Society, UNIZULU and members of the executive 2005/2006 session, all member of the Post graduate Students Association UNIZULU of which I'm the elected pioneer president, for the opportunity to serve you. Not forgetting the Dean of students (Dr. Hlongwane), Dr Lubusi and Mr Mashaba. God bless you all.

A warm appreciation to my uncle and his family, Mr & Mrs Durokijesu and my nieces : Anuoluwapo, Oluwatobiloba, Oluwatomisin and Oluwatimileyin.

I am also very grateful to all the members of C.A.C Olorunkosehunti Ayekale Agugu, Ibadan and Apata branch, all my family friends and well wishers.

Finally I specially appreciate my one and only sister OLUWATOYIN for all her support.

**I pray that, *"He which hath begun a good work in you all, will perform it until the day of JESUS CHRIST".* Thank you all and God bless.**

## ABSTRACT

We report the synthesis of high quality aqueous and organically soluble selenide nanoparticles by a novel greener, quick, facile, environmentally-benign and effective non-organometallic solution-based method. Briefly, the method involves the reduction of selenium powder to produce selenide ions which act as the selenide source, followed by the addition of $MCl_2$ (M = Cd or Zn) or $Zn(CH_3COO)_2$. The nanoparticles were passivated with organic surfactants such as hexadecylamine (HDA) and tri-octylphosphine oxide (TOPO), for their solubility and stability in organic solvents, while passivation with biomolecules such as L-cysteine ethyl ester hydrochloride, methionine, ascorbic acid, starch, polyvinyl alcohol (PVA) and poly (vinylpyrrolidone) (PVP), rendered them water-soluble and also acted as an agent of stabilisation and facilitate conjugation with biomolecules. CdSe/ZnSe nano-composite and core-shell nanoparticles were also synthesised, using this new synthetic approach.

The high quality of the as-synthesised nanoparticles was confirmed using absorption and photoluminescence spectroscopy (PL), Fourier transform infrared spectroscopy (FT-IR), powder x-ray diffraction (XRD), transmission electron microscopy (TEM), high resolution transmission electron microscopy (HRTEM), selected area diffractometry (SAD) and energy dispersive spectroscopy (EDS). All measurements were performed without any post-preparative size separation of the nanoparticles.

The thesis is divided into six chapters. Chapter one deals with the introduction and comprehensive review on previous works done on the synthesis of nanoparticles,

highlighting their advantages and disadvantages. The aim and objective of the study is also stated in this chapter.

In chapter two, the systematic study of the effects of the capping group, growth time, temperature, reduction time and monomer concentration on the size, optical properties and morphology of the as-synthesized TOPO and HDA-capped CdSe nanoparticles was investigated. All the as-synthesised particles are blue-shifted in relation to the bulk band-gap of CdSe. The absorption and emission maxima are shifted to higher band-gap (lower wavelengths) as the reduction time increases from 2 to 6 hrs, indicating a decrease in particle size for the HDA-capped CdSe. The particle size ranges between, 2.3-3.2 (5-30 mins) 2.4-3.0 nm (5 -30 mins) and 2.5- 2.7 nm (15-30 mins) for the reduction time of 2, 4 and 6 hrs respectively. At higher temperature (200 $^{o}$C), particles with different shapes, i.e dot, rod and multi armed rods are produced. The presence of the elongated particles was attributed to the phenomenon of oriented attachment (self-assembly), due to dipole-dipole interactions between the highly charged surfaces of II-VI semiconductor nanocrystals.

The synthesis of TOPO and HDA-capped ZnSe nanoparticles were investigated in chapter three. Increasing the monomer concentration and temperature, led to a faster growth rate, increase in particle sizes and narrowing of the size distribution. XRD analysis show phase transitions from sphalerite cubic to wurtzite hexagonal phase, on increasing the monomer concentration. The mean average particle diameters are, 3.71 $\pm$ 0.40 nm 3.26 $\pm$ 0.37 nm and 2.95 $\pm$ 0.32 nm for the reduction time of 2, 4 and 6 hrs respectively.

Chapter four describes the synthesis of water-soluble CdSe and ZnSe nanoparticles. The synthesis was carried-out at elevated and room temperatures, using biomolecules and polymers as passivating agents. A systematic study of the effects of parameters such as pH, reaction time, concentration, refluxing time, reactant ratio, passivating ligand and temperature on dispersibility, size, optical properties and morphology of the nanoparticles, was also investigated. At elevated temperature, the particle size decreases while the luminescence properties improve with increasing pH. Increasing the cadmium to cysteine ratio systematically from 1:10 to 1:60 at different pH, did not have any significant effect on the luminescence intensity of the nanoparticles. In contrast to the synthesis at higher temperature, particles with very sharp excitonic shoulders, absorption edges and high luminescence with narrower size distributions, are produced at room temperature. Particles with the first absorption peak at a wavelength as low as 415 nm, with a clearly resolved higher energy electronic transition, high luminescence without trap emission and particles size as small as 1.68 nm are obtained at pH 11.

The synthesis and characterisation of highly monodispersed HDA-capped CdSe-ZnSe nanocomposites and CdSe/ZnSe core/shell nanoparticles were reported in chapter five. The study of the core/shell growth at different reaction times and the effect of temperature on the optical and structural properties, was also investigated. The absorption and emission maxima of the CdSe/ZnSe core/shell nanoparticles are red-shifted in relation to the core CdSe, with a visible second absorption band at higher temperature (250 °C). The emission spectra confirmed that separate ZnSe nanoparticles are not formed in the solution. XRD analysis indicates that the diffraction is predominantly due to the CdSe core. The average particle diameter of

the CdSe/ZnSe are 3.99 ± 0.16 nm (230 °C) and 4.51 ± 0.27 nm at 30 mins reaction time. The absorption and emission maxima of the CdSe-ZnSe nanocomposite are blue-shifted in relation to pure CdSe, with a small particle size (2.91 ± 0.20 nm) as compared to the core CdSe (3.00 ± 0.24 nm). The XRD analysis shows a phase transition from the hexagonal phase of the pure CdSe to the cubic phase.

Chapter six gives a short description of the experimental details. Without any further post preparation, the qualities of the particles formed by this new method, are comparable to that of the best CdSe and ZnSe nanocrystals reported in literature, synthesised by the high temperature conventional organometallic methods. This new synthetic route is safe, inexpensive, involve the use of non-toxic chemicals, reproducible and can be readily used for large scale synthesis.

We believe the knowledge gained from this work, will enable the direct green synthesis of functionalised organic and water-soluble selenide nanoparticles for large-scale production and commercial purposes, due to the economical and environmentally-benign nature of the synthetic method.

## CONTENTS

## LIST OF FIGURES

## LIST OF TABLES

# LIST OF ABBREVIATIONS AND SYMBOLS

*CHEMICALS*

| | |
|---|---|
| $CdCl_2$ | cadmium chloride |
| HDA | hexadecylamine |
| MeOH | methanol |
| $NaBH_4$ | sodium borohydride |
| $NH_3$ | Ammonia. |
| TOPO | tri-n-octylphosphine oxide. |
| TOP | tri-n-octylphosphine |
| PVP | poly(vinylpyrrolidone) |
| PVA | polyvinyl alcohol. |
| Se | selenium |
| $ZnCl_2$ | zinc chloride |
| $Zn(CH_3COO)_2$ | zinc acetate. |

*TECHNIQUES AND METHODS*

| | |
|---|---|
| EDS | energy dispersive spectroscopy. |
| EMA | effective mass approximation model |
| FTIR | fourier transforms infrared |
| HRTEM | high resolution transmission electron microscopy |
| UV/ Vis | ultra violet visible |
| PL | photoluminescence |
| TEM | transmission electron microscopy |
| SAD | selected area diffraction |
| XRD | x-ray powder diffraction |

| | |
|---|---|
| a | lattice spacing |
| $a_B$ | Bohr radius |
| a.u | arbitrary units |
| $\alpha$ | absorption coefficient |
| d | diameter |
| e | elementary charge |
| $E_x$ | exciton energy |
| $E_g$ | band gap |
| f | oscillator strength |
| $\varepsilon$ | dielectric coefficient |
| h | planck's constant |
| $k$ | wave vector |
| $\lambda_{exc}$ | excitation wavelength (luminescence) |
| m* | effective mass (e : electron, h = hole) |
| $\mu$ | mobility |
| v | frequency |
| R | radius |
| T | temperature |
| t | time |

# *CHAPTER ONE*

## GENERAL INTRODUCTION

## 1.1 Background

Nanotechnology is the creation and utilization of materials and devices at the level of atoms, molecules, clusters and supramolecular structures and the exploitation of their unique properties at the nanoscale level. Nanotechnology can be seen as a recent offshoot of the semiconductor microelectronic revolution which earlier spawned the development of micro-electrochemical systems. The commercial needs of electronic manufacturers and biological applications have generated the necessity to create, understand and control objects on ever-smaller scales, thus giving an impetus to researchers to come up with novel ideas. To fully benefit from the advantages offered by nanotechnology, it is important to understand how to build, analyse and predict the properties of these nanoscopic entities. Hence, nanotechnology is a multidisciplinary field, bringing together chemists, physicists, biologists and engineers to investigate this unique field.

Currently we are witnessing an explosion of research in nanoscience, engineering and biotechnology. As the nanorevolution proceeds, basic research is leading to the development of true nanotechnologies which have potential to impact fields from healthcare, data storage, sensing and optoelectronic to energy and environment. The ultimate scientific and technological impact of these materials mainly depends on their novel electronic, optical, catalytic, physical and chemical properties. Hence, studies concerning quantum and electronic confinement observed in these materials are of exceptional importance.

Semiconductor nanoparticles are materials which fall in an intermediate position between molecular and bulk materials. These materials most often referred to in

literature as nanoparticles, nanocrystals, Quantum dots (QDs), Q-particles, nanoclusters or artificial atoms, typically have dimensions in the range of 1-20 nm.[1,2] They exhibit both physical and chemical properties within an intermediate state of matter, between molecular and bulk. Their unique properties are attributed to two main factors: the large surface-to-volume ratio of atoms and their reduced dimensions in relation to the excitonic radius of the bulk material known as quantum confinement.[3] This quantum-sized effect causes structural and electronic changes that, in turn, induce other novel properties that largely dominate the behaviour of these materials and make them different from that of the bulk. Unique photophysical, photochemical, photoelectronic and photocatalytic properties can occur in a semiconductor nanoparticle system.[4] The differences can be found in both the equilibrium and non-equilibrium state, including thermodynamics and kinetics.[5,6] The decrease in particle size leads to extremely high surface area to volume ratio which leads to an increase in surface specific active sites for chemical reactions and photon absorption and hence enhance the reaction and absorption efficiency. For example, a 1.2 nm nanocrystal will have 88 % of its atoms on the surface and absorb light at 450 nm while, an 8.5 nm nanocrystals consists of 20 % surface atoms and absorb light at 650 nm. The enhanced surface area also increases surface states, which changes the activity of electrons and holes and affects the chemical reaction dynamics. These unique properties make semiconductor nanoparticles potentially useful in many areas of applications, which include catalysis, optical recording materials, solar cells, biotechnology, sensor and lasing materials. They are also an important class of material for the photonic, electronic, biological and other technologies of the 21st century.

## 1.2 Electronic Properties

One of the defining features of a semiconductor is the energy gap separating the conduction and valence energy bands. The colour of light emitted by the semiconductor material is determined by the width of the band gap. In semiconductors of microscopic sizes, i.e bulk semiconductors, the gap width is a fixed parameter determined by the material's identity.

In a bulk semiconductor, the large numbers of atoms lead to the generation of sets of molecular orbitals with very similar energies. At 0 K the lower energy levels or valence bands, are filled with electrons while the conduction bands, consisting of higher energy levels are unoccupied. These two bands are separated by an energy gap ($E_g$), the magnitude of which is a characteristic property of the bulk microcrystalline material (at a specific temperature). Materials normally considered semiconductors, typically exhibit band gaps in the range 0.3 – 3.8 eV. At temperature above 0 K, electrons in the valence band may receive enough thermal energy to be excited across the band gap into the conduction band. When an electron, $e^-$ is excited from the valence band to the conduction band, it leaves behind a "hole" which can be regarded as a particle with its own charge (+1) and effective mass, thus creating an electron-hole pair. The electron and hole are considered "bound" to each other via a coulombic attraction and this quasiparticle is then known as an "exciton". Thus, it is impossible to ignore the coulombic interaction between the electron and hole and they consequently assume a higher state of kinetic energy than in the bulk material. In this novel state of the matter, the valence band and conduction band split, giving rise to discrete, quantized, energy levels rather than a continuous band, as observed in the bulk material (Figure 1.1) and the 'band gap' increases.

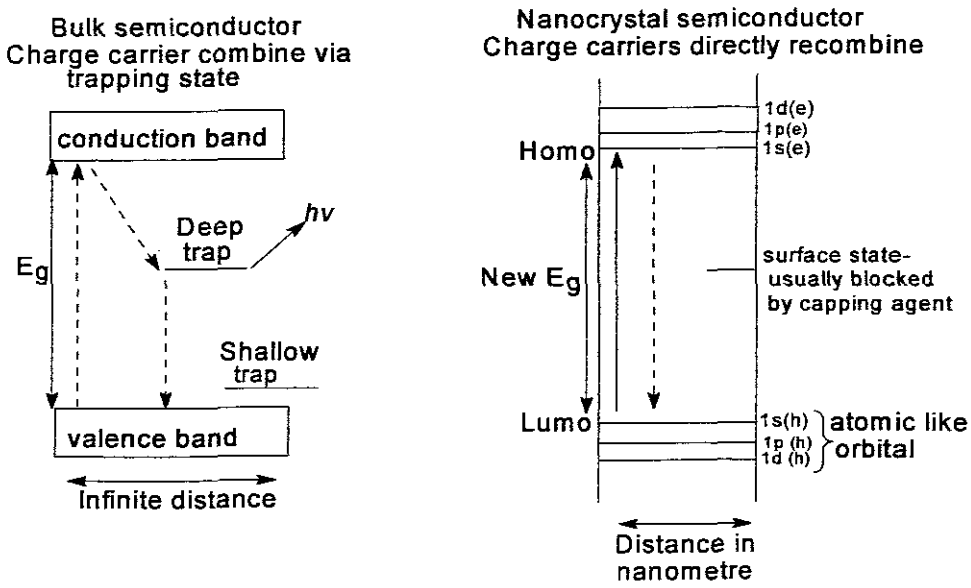


***Figure 1.1*** *Spatial electronic state diagrams for bulk and nanocrystalline semiconductors.*[7]

The electron and hole each relax to the respective band edge states by non-radiative processes. During the band edge transition a photon is emitted as the excited electron spontaneously recombines with the hole. The band edge is explained as the direct recombination of charge carriers from atomic-like orbitals. Charge carriers in bulk semiconductor recombine from deep and shallow traps, giving emission at different wavelengths from the band edges.[8] In the case of nanoscale semiconductor particles with smaller sizes (< 10 nm), the situation changes. As the diameter of the crystalline material approaches the exciton Bohr diameter, its electronic properties start to change. This reduction of particle size, with corresponding increase in the band gap of the nanocrystalline material is known as the quantum confinement effect. The charge carrier is confined in all three dimensions in a quantum dot and thus, the

exciton has zero degree of freedom for its motion, with the result that the electron exhibits a discrete atomic-like spectrum.

The discrete structure of the energy state leads to a discrete absorption spectrum of quantum dots, which is in contrast to the absorption spectrum of a bulk semiconductor. This quantum dot absorption spectrum can be used to determine the energy gap of a semiconductor material. For crystalline materials the electronic transition occurring on the absorption of light, are subjected to certain selection rules. Besides $h\nu \geq$ energy gap, there is the additional requirement that the vector must be conserved

$$K_e + K_{photon} = K'_e \quad \ldots\ldots\ldots\ldots\ldots\ldots \qquad (1.1)$$

where $K_e$ and $K'_e$ are the electron wave vectors, before and after excitation respectively. Due to high velocity of light, the photon wave is very small compared to the electron wave vectors, so equation 1.1 reduces to the conservation rule:

$$K_e = K'_e \quad \ldots\ldots\ldots\ldots\ldots\ldots \qquad (1.2)$$

Therefore, for excitation across the narrowest part of the energy to occur, the minimum of the conduction band must have the same vector as the maximum of the valence band (Figure 1.2), i.e. the wave vector for optical transitions is conserved. Materials with this type of electronic transitions are known as direct band gap semiconductors and they have large absorption coefficients. For other semiconductors, the lowest energy electronic transition between the valence band and

conductor band is formally forbidden, but can occur via a photon assisted process as seen in Figure 1.2.[9]

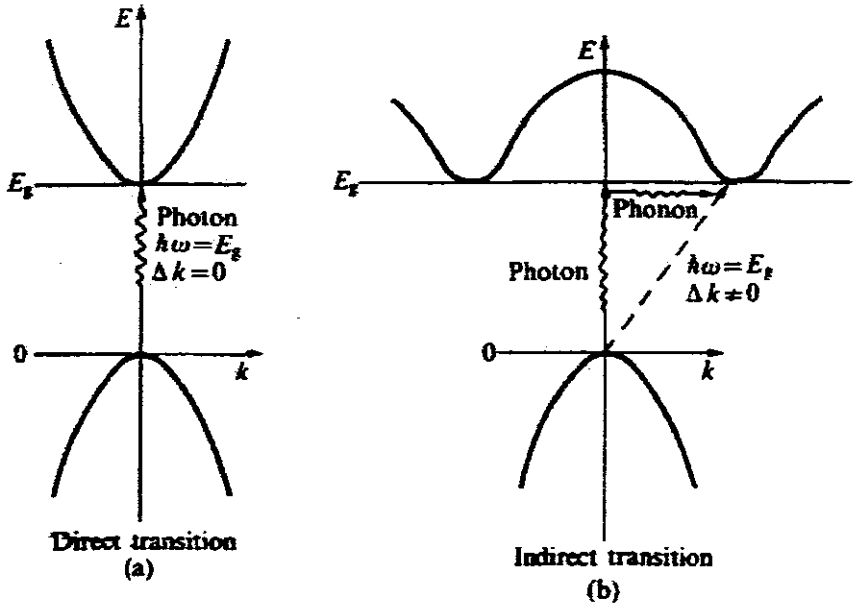


*Figure 1.2 Direct and indirect optical transitions in semiconductors.*[9]

Because the physical dimension of the quantum dot can be smaller than the exciton diameter, the quantum dot is a good example of a 'particle-in-a-box' in which the energy of the particle in the box, depends upon the size of the box. In a quantum dot, the band gap becomes energy dependent that is, as the size decreases the absorption edge is blue-shifted (higher energy/lower wavelength) indicating an increase in the band gap. For a spherical quantum dot with radius R, this model predicts that a size-dependent contribution to the energy gap is simply proportional to $1/R^2$, which implies that as the band gap increases the quantum dot size decreases. Experimentally, this increase in energy is observed in the optical spectra, for a range of nanocrystalline semiconductors, where there is blue-shift in the band gap as the particle size decreases. The shifts in the absorption edge of II-VI semiconductors

such as CdSe and CdS can be a large fraction of the bulk band gap and for CdSe can result in turning across a large portion of the visible spectrum. For example, the band gap of CdSe can be tuned from 1.7 eV (deep red) to 2.4 eV (green) by reducing the particle diameter from 200 Å to 20 Å. (Figure 1.3)

***Figure 1.3*** *Size selected solutions of CdSe nanoparticles from yellow to wine red as the particle size increases.*[1]

In addition to a blue-shift in the absorption edge, the presence of a peak often described as excitonic, is taken as evidence of quantum confinement that is, the spectrum starts to resemble a molecule with discrete absorptions rather than a solid with continuous bonds.

## 1.3 Optical Properties

Quantum confinement affects the optical properties of nanoparticles. The electrical and optical energies of the band gap are equivalent through the following conversion:[10]

$$E = h\nu = \frac{hc}{\lambda} \quad \text{.....} \quad (1.3)$$

E = band gap energy difference, h = Planck's constant, c = the speed of light, $\nu$ = the frequency of the incident light, and $\lambda$ = the wavelength of incident light.

Thus, the energy difference of the band gap is inversely proportional to the wave length of incident light. Nanoparticles will only absorb light of wavelengths shorter than that determined by the band gap value. For example, CdSe (bulk) has a band gap of 1.73 eV, which corresponds to a wavelength of 716 nm. CdSe begins to adsorb light at 716nm and absorbs continuously into the UV (e.g. shorter wavelengths). As the particle size declines, the band gap increases and the absorbance onset shifts to shorter wavelengths. Thus, onset of absorbance is directly related to particle size. The band gap is inversely related to absorbance onset ($\lambda$) through the relationship

$$E = \frac{hc}{\lambda} \quad \text{.....} \quad (1.4)$$

E = band gap energy difference, h = Planck's constant, c = the speed of light, and $\lambda$ = the wavelength of incident light. Therefore, smaller particles begin to absorb at shorter wavelengths.[11]

The influence of particle size on optical properties is not limited to absorbance. Particle fluorescence is also a function of the band gap. Photon absorption creates an excited electron. This electron loses some of its energy to atomic vibrations, thereby satisfying the second law of thermodynamics. Typically, this energy is converted to heat. The electron then decays to ground, emitting a photon. The emitted photon has

a longer wavelength than the absorbed photon because of the energy lost to heat. As the band gap decreases, the particle will absorb at longer wavelengths. This will produce a concomitant red-shift in particle fluorescent emission. Because band gap is inversely proportional to the nanocrystal size, larger nanocrystals display red-shifted emission. Additionally, the energy lost to heat decreases in a size-dependant manner.

In a system with a defect state, electrons that enter into this state will become trapped. The electron first decays into the trap and then recombines with the hole, producing a photon at a longer wavelength than the band gap state. Because of this delay, the lifetime of an excited electron in a trapped state is significantly longer than that of an electron in an exciton or band gap state, as much as 3 orders of magnitude.[12] Additionally, the shift between the absorbance wavelength and the emitted wavelength will be larger as a result of the energy lost in decaying to the trapped state.

### 1.4 Particle Size

Many model calculations of size quantization effects have been published in the last few years.[13-16] The majority of these calculations starts from the macroscopic solid state and determine the increase of the band gap with decreasing particle size on the basis of a particle-in-a-box assumption. The differences in the models lie in the complexity of the calculation and the boundary conditions. Efros *et al.*,[13] described the first calculation where they used spherical, infinite potential wells which ignored the coulombic interactions. Brus *et al.*, developed the energy levels of the first excited state by considering the coulombic interactions and polarization terms.[14,15] On the basis of the effective mass approximation, they have developed an equation

(1.5) connecting the energy of the first electronic transition of the exciton and the band gap shift with respect to typical bulk value.

$$E_x = E_g(\text{bulk}) + \frac{2h^2\pi^2}{R^2}\left[\frac{1}{m_e^*} + \frac{1}{m_h^*}\right] - \frac{3.6e^2}{\varepsilon R} \quad \ldots\ldots\ldots (1.5)$$

Here $E_x$ is the exciton energy, $E_g$ (bulk) the energy band gap of the bulk crystal of 1.74 eV at 300 K, $m_e$ and $m_h$ the respective effective mass of an electron of 0.13 $m_e$ and 0.44 $m_e$, $\theta$ is the bulk optical dielectric constant of 9.40, *e* represents the elementary charge and, R is the radius of the spherical crystallite. The middle term on the right-hand side of the equation is a particle-in-a-box-like term for the exciton and the third term represents the electron-hole pair coulombic interaction. Hu *et al.*, reported that the coulomb interaction significantly influences electron and hole interaction.[17] Implicit in this equation is the assumption that the quantum dots are spherical and the effective masses of charge carriers and the dielectric constant of the solid, are constant as a function of size. From the above equation to a first approximation, the energy spacing between quantized level is inversely proportional to the effective mass and the square of the particle radius therefore, the first electronic transition increases in energy with decreasing particle size. The model is not quantitative, as it does not account for the coupling of electronic states to vibrations and the surface defects of the crystallites. The appropriate values for the effective masses, as well as high frequency dielectric constants, are taken from macro crystalline solids and could vary for smaller particles which results in the uncertainty of this calculation. Although the model deviates for smaller particles, it is useful in determining the energy shift for nanocrystalline semiconductors. The above calculation is usually used for materials in the 'strong confinement' limit, that is, the

physical dimensions of the semiconductor nanoparticles are substantially smaller than the excitonic Bohr radius.

Other calculations have been performed that better match experimentally determined bandgap energies and quantum dot sizes for smaller particle sizes.[18] Most of these models determine the increase of the band gap with decreasing particle size of a particle-in-a-box assumption, with the crystallite size making up the dimensions of the box. The models differ on the complexity of the calculation and the boundary conditions. Weller *et al.*,[11,19] made quantum mechanical calculations for higher excited states as a function of particle size. However, the values for the effective masses and high frequency dielectric constants are taken from macrocrystalline solids, which results in uncertainty in the accuracy in the calculation. The most universal particle-in-a-box calculation has been represented by Nosaka,[16] whose calculations assume the validity of the effective mass approximation.

Other models have also been proposed for particle sizes apart from those based on the particle-in-a-box assumption, by relating the particle size determined by transmission emission microscopy (TEM) and X-ray diffraction (XRD) measurements with the electronic transition occurring in nanoparticles. Bawendi *et al.*, showed the relationship between the particle size determined by TEM for sizes ranging from ~ 12 to 115 Å and the wavelength of the first electronic transition [$1S_{3/2}$(h) -1S (e)] occurring in CdSe nanoparticles (Figure 1.4).[20] They compared the experimentally observed HOMO-LUMO gap as a function of particle size, with the prediction of the simple effective mass approximation with the coulombic interaction treated in first-order perturbation.[21] All the particle sizes were determined by TEM and confirmed

by X-ray line-shape analysis. Although experiment and theory agree reasonably well at large sizes, the simple theory diverges from the experimental values for small sizes (Figure 1.4). Lippens and Lannoo[22] have shown that tight binding calculations can yield better agreement for these smaller sizes.

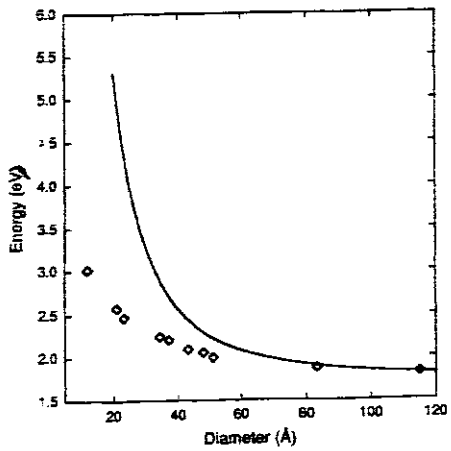


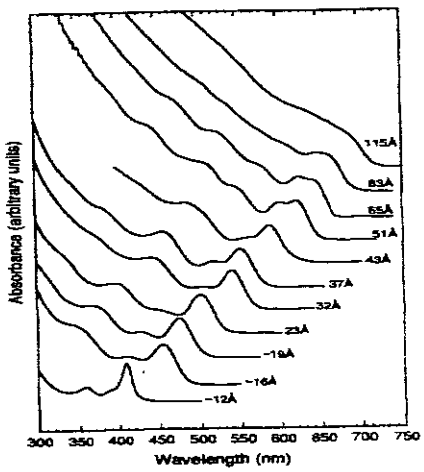


**Fig. 1.4a** **Fig.1.4b**

***Figure 1.4(a)*** *HOMO-LUMO transition energy of CdSe crystallites as a function of size (diamonds) compared with the prediction of the effective mass approximation.*
***(b)*** *Room temperature optical absorption spectra of the CdSe nanocrystallite dispersed in hexane and ranging in size from ~ 12 to 115Å.*

Recently Yu *et al.*,[23] developed an equation connecting the wavelength of the first excitonic absorption peak and the diameter for CdS, CdSe and CdTe nanoparticles.

## 1.5 Luminescence Properties

The emission properties of a semiconductor nanocrystal can be characterised by four fundamental parameters which are : emission colour, colour purity, brightness, quantum yield (QY) and stability of the emission.[24] In the assignment of photoluminescence (PL), the behaviour of semiconductor nanocrystals is considered,

where two types of emission bands can be detected : the "band gap" emission and the "deep trap" emission.[25] The band gap is narrow (width determined by the size distribution) and is only slightly red-shifted from the absorption onset (up to 0.1eV for a CdSe nanocrystal, 2 nm in diameter). It is characterized by a continuous surface, with most surface atoms exhibiting the coordination and oxidation state of the bulk. The deep trap PL is broad and is substantially red-shifted from the absorption onset (typically by 0.5 eV). It has been associated with radiative recombination of localized surface trapped charge carriers and, because of its long lifetime, its intensity relative to the band gap PL is enhanced at low temperatures.[26,27]

Because of high surface-to-volume ratio, surface atoms play a more important role in the emission properties of the nanoparticles as the particle size decreases. For example, as the size of CdSe particles decreases from 10 nm to 1 nm, the percentage of the surface atom increases from 20 to 100%. For bulk materials, the bulk atoms dominate the properties of the materials, while for nanomaterials the surface atoms may dominate. These surface atoms usually have unsaturated bonds or dangling bonds, extra free energy and are more active than those in the bulk. The phenomenon that nanoparticles can easily transform from one phase to another and have a low transformation temperature, can be attributed to this. Furthermore, in a semiconductor surface atoms usually induce extra electronic states in the band gap, which mix with the intrinsic state to a substantial extent. These influences the spacing of the energy levels and lead to debase the optical properties of quantum dots. In a large crystal this effect is a small perturbation and can be ignored. However, as the size of the crystal decreases and the percentage of the surface atoms increases, more electronic states are induced in the band gap and this effect cannot be ignored

anymore. These states may act as electron and hole trapping centres. When an electron is promoted from the valence band to the conduction band, the resultant electron-hole pair (or an exciton) may recombine immediately, to produce heat or light with an energy equal to $E_g$. It is more likely that the trap states within the material caused by defects (such as vacancies, local mismatches, dangling bonds or absorbates at the surface) trap either the excited electron or the hole and thus become less available for the radiative recombination of luminescence. Hence the PL can be quenched, which is undesirable for some applications such as optical diodes, lasers and biological markers. On the other hand, these states can also act as effective intermediate states during photochemical reactions, which require effective localization of electrons or holes on the surface.[28]

For bulk semiconductors, "surface passivation" is a well-known phenomenon that decreases the possibility of charge carriers residing in traps. Silicon, for example, is passivated with a layer of silicon dioxide. For quantum dots, proper surface modification can remove the local trap sites from the surface and thus, significantly increase the quantum yield of the near band gap emission. Coating the surface of the nanocrystals with suitable organic molecules does not only provide electronic passivation (by terminating the dangling bonds on the semiconductor's surface that lead to a loss mechanism wherein electrons are trapped at the surface before they have a chance to emit a photon) but also prevents agglomeration, controls the growth rate of the nanocrystals, its size, shape and solubility.[29] Passivation by means of organic molecule sometimes has the draw-back of incomplete or irreversible passivation. This passivation can expose some of the regions of the surface to degradation effects, such as photo oxidation over time. In some cases, it can also

cause fluorescence quenching when maximum passivation has been attained.[30] Alternatively, the surface of the nanocrystals can be passivated with a second inorganic material of wider band gap. When wrapped in wider band gap materials, the electron-hole pair is further confined and surface states are eliminated. For example, CdSe nanocrystals can be passivated with CdS, ZnS or ZnSe to create a core-shell nanocrystal. If the interface between the two inorganic materials is perfect, a near unity quantum yield (QY) material may result.[31]

In general, a low PL QY is considered as a result of the surface states located in the band gap of the nanocrystals. These surface states are originated from the dangling bonds of some of the surface atoms. The ligands on the surface of nanocrystals may remove some or the entire surface trapping states and increase the PL QY of the nanocrystals. Theoretical treatments indicate that the efficiency of the electronic passivation provided by the surface ligands, depends strongly on the surface structure and the nature of the surface states of the nanocrystals themselves. High PL QY means that the surface ligands provide good passivation for the surface defects located in the band gap of the nanocrystals, which act as trapping states for the photo-generated charges i.e., behaving as a non-radiative relaxation centre for the electron-hole recombination. This also indicates that there is optimal surface structure/ reconstruction of the nanocrystals which minimizes the effect of the atomic configuration on the surface of nanocrystals which would significantly affect the efficiency of the electronic passivation provided by the surface ligand.[24]

It has been acknowledged that slower growth in size results in less surface roughness and less surface defects, thus leading to higher PL efficiency. Higher growth

temperatures lead to faster growth rates and therefore, surface roughening and degradation compete with surface ordering. This induces faster surface degradation, which reduces the luminescence efficiency shortly after maximum efficiency has been reached. The use of lower temperatures, during the surface reorganisation process has proven to give lowest degree of surface disorder namely, the smoothest and defect-free surface due to the slower growth rate.[32-34]

## 1.6 Methods for Preparing Semiconductor Nanoparticles

Synthesis of high quality semiconductor nanocrystals has been an important topic in the field of material chemistry in recent years because of the technical and fundamental importance of these novel materials. There are three distinct approaches for the synthesis and functionalisation of nanoparticles. These are the bottom–up, top-down and template-directed approaches.

*Bottom-up approach* : This synthesis involves conversion of a precursor through a specific reaction such as reduction, decomposition or hydrolysis into nuclei that subsequently grow into monodispersed nanoparticles.

*Top-down approach* : Under this approach the bulk material is added to a hot solvent, melted and sheared to produce colloidal spheres.

*Template-directed approach* : Here colloidal spheres serve as physical or chemical templates to coat their surfaces with other materials or, to convert them into a different material with a rich variety of composition, structure, and functionality.

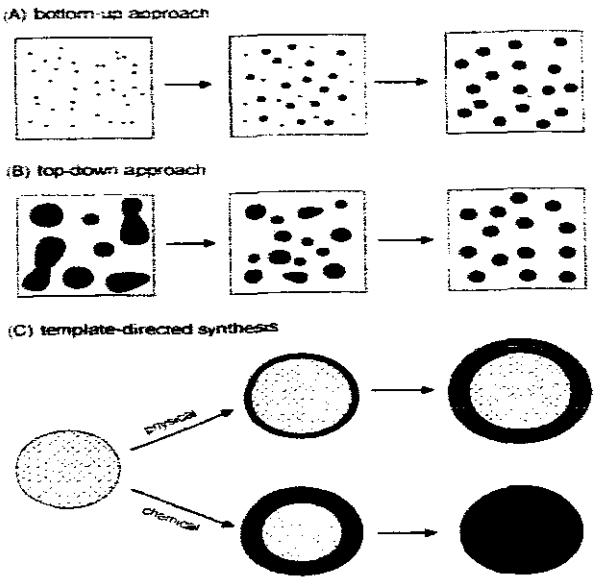


***Figure 1.5*** *Three different approaches for the synthesis and functionalisation of colloidal sphere.*[35]

The key to all semiconductor nanoparticle research is the ability to synthesis high quality nanoparticles with well-defined properties. Generally, the chemical methods for producing semiconductors nanoparticles can be divided into four categories : the colloidal route, growth in confirmed matrices, gas phase synthesis and the organometallic/metal organic route[1]. The two principal methods in use are colloidal and organometallic routes [2] and these will be reviewed in this report. In addition to semiconductor nanoparticles, metallic systems have been investigated and nanocrystalline metal oxides, carbides, borides and nitrides have been produced.[36] An ideal synthetic route should produce pure, high quality nanoparticles with well-defined properties.

### 1.6.1 *Colloidal Routes*

The colloidal route is the pioneering method for the preparation of various nanoparticles. The colloidal access to quantum dots is achieved by carrying out a controlled precipitation in homogenous solution in the presence of a so-called 'stabilizer' and the cessation of growth soon after nucleation.[3,37] The role of the stabilizer is to prevent agglomeration and further growth of the colloid, thereby keeping them in solution. The synthesis of highly monodispersed colloids was explained in the 1940's by La Mer *et al.*,[38-40] who suggested that if seeds (nuclei) could be made to grow in concert into large particles, monodispersed sols could be formed. In this early work, the particles were typically micrometric. However, if nucleation and growth is properly controlled, particles with dimensions of the order of nanometres can be reproducibly synthesized. Small crystals which are less stable dissolve and then re-crystallize to form larger, more stable crystals, by a process known as Ostwald ripening. For such methods to be effective, the quantum dot in question must have low solubility, which can be achieved by the correct choice of solvent, pH, temperature and passivating agent. Highly monodispersed samples are obtained if the processes of nucleation and growth are distinctly separated i.e., fast nucleation and slow growth. Lower temperatures are used or favoured for such reactions, because the ratio of the rates of the nucleation to growth is large. The stability of the colloidal crystals can be improved by using solvent with low dielectric constants, e.g. acetonitrile or, by the addition of a stabiliser such as styrene/maleic acid co-polymer. The co-polymers prevent coagulation and flocculation.

Brus,[41] Weller,[42] and Henglein[43] have used this method to synthesize semiconductor nanoparticles of CdS and ZnS. Their work has contributed significantly towards the

understanding of some of the fundamental properties of nanoparticles. Brus reported the synthesis of Q-CdS by mixing aqueous solutions of $CdSO_4$ and $(NH_4)S$.[41] By altering the nucleation kinetics using pH, the subsequent size of the nanocrystalline Q-CdS could be controlled. ZnS and CdS nanoparticles were synthesised in methanolic media without organic surfactants.[44] The repulsion of the electrostatic double layer prevented agglomeration and/or sedimentation. The optical spectra showed a blue-shift in band edge in relation to the bulk material. Structural characterisation by high resolution electron microscopy (HRTEM) and electron diffraction, revealed a zinc blende structure.

Henglein, Weller and co-workers studied the photophysical properties of nanocrystalline CdS.[42,43] The analysis of the size distribution revealed that, a certain size with the greatest oscillator strength was favoured, which corresponded to the optical transition in the absorption spectrum. This was attributed to the existence of 'magic agglomeration' numbers in the size distribution of the sample[1]. 'Magic agglomeration' numbers, integral multiples N of a large number $m_o$ arise due to the stability of a certain size or because of the kinetics of particle growth. The fast precipitation of the colloids renders a primary size distribution of small particles, peaking at an initial size $m_o$.

$$m_oCd^{2+} + m_oS^{2-} \longrightarrow (CdS)m_o \quad \ldots\ldots\ldots\ldots\ldots\ldots \quad (1.6)$$

Growth via Ostwald ripening occurs and, the initial size ($m_o$) is preserved in the form of integer multiples:

$$(CdS)m_o \longrightarrow (CdS)m_{o-1} + Cd^{2+} + S^{2-} \quad \ldots\ldots\ldots\ldots\ldots \quad (1.7)$$

$$(CdS)m_o + Cd^{2+} + S^{2-} \longrightarrow (CdS)m_{o-1} \quad \ldots\ldots\ldots\ldots\ldots \quad (1.8)$$

Post preparative techniques such as size exclusion chromatography[41] and gel electrophoresis[42] were used to narrow the particle size distribution. The latter technique is favoured because it is fast and efficient, producing highly monodispersed colloidal nanoparticles.

Nanocrystalline $Zn_3P_2$ and $Cd_3P_2$ have been synthesized by the aqueous methods, by the injection of phosphine gas ($PH_3$) into a solution of the relevant metal salt.[43,44,47] The nanoparticles show dramatic changes in appearance and electronic properties, as the size of the particles is varied. Bulk $Cd_3P_2$ is black in colour, whereas nanocrystalline $Cd_3P_2$ displays a wide range of colours, from white for the smallest, to brown for the largest particles. The smallest particles have a band gap of 4.0 eV (310 nm) with an excitonic peak at 3.93 eV (315 nm). Murphy and co-workers have produced manganese (Mn) activated (Mn occupying surface sites) and manganese doped (Mn occupying lattice sites) ZnS dots by aqueous routes, displaying increased quantum yields and orange emissions respectively.[48]

Wang *et al.* reported a milder synthetic route to MSe ( M = Zn, Cd, Sn and Cu) using ethylenediamine as the solvent both in an autoclave [49] and at room temperature (80 - 100 °C) with $KBH_4$ serving as the reducing agent.[50] The reaction at room temperature produced spherical particles of large grain size, while the reaction inside an autoclave yielded nanorods. By varying reaction conditions such as precursor concentration, reaction temperature and reducing agent, Yoon *et al.*,[51] produced ultra-small CdSe

QDs in ethylenediamine solution containing $Cd(NO_3)_2$ and elemental selenium at an even lower temperature than 100 $^0$C . This prolonged synthesis showed two strong absorption peaks at 310 and 315 nm respectively, along with two weak absorption shoulders at 385 and 410 nm. As the precursor concentration and temperature increases the two weak absorption shoulders (at 385 and 410 nm) gradually increase, while the two strong absorption peaks (at 310 and 315 nm) decrease.[51]

A wet chemical route was used for the synthesis of CdS,[53] CdSe,[54] CdTe,[54-56] HgSe,[57] HgTe[58] and CdHgTe[59] nanoparticles in a reaction involving the dissolution of the metal salt in water, in the presence of the stabilising thiol. The chalcogen sources were produced under nitrogen atmosphere by titration between NaOH and $H_2M$ (M = S, Se and Te generated by the reaction of $Al_2M_3$ with 10% $H_2SO_4$). The stabilising thiols used were 1-thioglcerol, 2-mercaptoethanol, 1-mercapto-2-propanol, 1,2-dimercapto-3-propanol, thioglycolic acids and thiolactic acid.

The colloidal route is an efficient one for the preparation of nanosized semiconductor particles. However, certain types of semiconductors, such as CdSe, GaAs, InP and InAs, cannot be synthesized easily via this route. Annealing of the colloidal particle is also a problem as these tend to be a low temperature process. Such aqueous prepared nanoparticles are not sufficiently stable at higher temperature and thus makes annealing of the particle difficult, thereby making the material poorly crystalline. As a result of these difficulties, there have been several modifications to the synthesis via colloidal route.

Using the same chalcogen source reported by Weller *et al.*,[53] Li *et al.*[60] synthesised high-quality CdTe nanocrystals rapidly in aqueous phase by microwave irradiation with controllable temperature, while 3-mercaptopropionic acid (MPA) was used as the stabilising agent. Gautam *et al.* reported *in situ* generation of $H_2Se$ through the aromatisation of tetralin by Se for the preparation of large quantities of cubic phase CdSe nanocrystals.[61] The reaction was carried out in toluene, using stainless bombs with dodecanethiol as capping agent. The cubic phases of the resultant nanoparticles were attributed to the autogenous pressure that developed during the preparative procedure.

Yang *et al.*,[62] used the redox reaction of selenite and tellurite salts with cadmium nitrate to produce CdSe and CdTe nanowires in an autoclave, through a poly vinyl alcohol (PVA) assisted ethylenediamine solvothermal method at 160 °C -180 °C. They attributed that the PVA used in the process, was favourable for the formation of nanowires by promoting the oriented attachment growth in solvothermal conditions. By varying the current density and temperature of the solution, Sarangi and Sahu used cathodic electrodeposition techniques to produced nanocrystalline CdSe semiconductor thin films of different crystalline sizes.[63]

Chen *et al.*,[64] reported simple solution-phase synthesis, of crystalline and water-soluble CdS and CdSe nanorods via the arrested precipitation from their respective inorganic ions in a micellar solution. They attributed the various aspect ratios of the nanorods obtained, to different concentrations of cyclohexane added into the micellar solution. Spontaneous reorganization of single CdTe nanoparticles into luminescent nanowires upon controlled removal of the protective shell of organic stabiliser, was

described by Tang *et al.*[65] The intermediate step in the nanowire formation was found to be pearl-necklace aggregate. They believed that strong dipole-dipole interaction was the driving force of nanoparticle self-organisation.

In a recent development, selenosulphate and selenourea were identified as the main sources to provide $Se^{2-}$ ions for the preparation of selenides through reactive solution growth. The reaction between selenosulphate and Cd ions, is the basis of most commonly used techniques for chemical bath deposition (CBD) of CdSe films.[66] The Cd is normally complexed in the CBD process to prevent gross $Cd(OH)_2$ precipitation at relatively high pH values normally used, as well as to control the rate of the overall reaction.[67] This chemical reaction of complexed cadmium salts with sodium selenosulphate ($Na_2Se_2SO_3$), has been used to produce cubic CdSe semiconductor thin film in aqueous alkaline medium.[68,69] In the absence of a complexant for Cd, a precipitate is normally formed and little or no film formation occurs. This complex-free reaction has been used to produce PbSe precipitates[70] and CdSe colloidal quantum dots.[71]

Yochelis and Hodes[67] investigated the reaction between selenosulfate and non-complexed Cd ions in aqueous solution to form CdSe. Their results show that the initial precipitate that is formed ($CdSO_3$) gradually react with selelnosulfate to give largely amorphous CdSe. These CdSe were formed as a disordered phase surrounding the $CdSO_3$ and breaks off from the $CdSO_3$ crystals to form nanocrystals of CdSe. Han *et al.*,[72] modified Yang *et al.*[73] and Zhu *et al.*[74] synthesis by using $Na_2SeSO_3$ as the selenium source together with mercaptoacetic acid (MAA) as the

stabilizing agent to produce water soluble and small sized CdSe QDs via a sonochemical method.

As a result of the simplicity involved in the synthesis of $Na_2SeSO_3$, even though it requires long reaction time, it has been used as selenium source together with various cationic precursors to synthesise CdSe nanoparticles via microwave irradiation,[75,76] ultrasonic irradiation,[77] and photochemical methods.[74,78,79] In the presence of additives such as poly(vinylpyrolidone) (PVP),[80] polyvinylalcohol (PVA),[81,82] tartaric acid[77] and starch,[83] it has also been used to produce water soluble CdSe nanoparticles.

Using several less-toxic metal salts of stearate, acetate, chloride and sulphate, Zhong *et al.*, synthesised CdS, ZnS, and $Zn_xCd_{1-x}S$ nanocrystals in a one-pot method, with elemental sulphur as the sulphide source.[84] The resultant nanoparticles spectra were dominated by band-edge emission and, cubic zinc-blende phase was obtained at high temperature. However, the PL QYs for the obtained CdS nanocrystals from non $Cd(stearate)_2$ salt are nearly zero. Also in this approach, a less than stoichiometric amount of sulphur was used. If an equimolar or excess amount of sulphur was used, the QYs of the obtained CdS would be dramatically reduced. In a very time consuming reaction, Badr and Mahmoud [85] produced selenide analogue by reduction of elemental selenium in polyvinyl alcohol (PVA) photopolymer films in the presence of additional stabiliser, cetyl trimethyl ammonium bromide (CTAB), but the obtained nanoparticles possessed poor optical properties with very broad trapped state emission.

### 1.6.2 *Organometallic/Metal-Organic Routes*

The early problems associated with the synthesis of nanoparticles via the colloidal route was overcome by a method that makes use of organometallic and/or metal organic compounds under anaerobic conditions. Bawendi *et al.*,[20] in 1993, pioneered this method whereby good quality, monodispersed, highly crystalline nanoparticles were synthesized. This method (also called the East Coast Method), involves rapid injection of a volatile metal alkyl (dimethyl cadmium or dimethyl zinc) and a chalcogen source TOP-E (E=Se, Te) mixed in tri-*n*-octylphosphine (TOP) and injected into hot tri-n-octylphosphine oxide (TOPO), a polar coordinating Lewis base solvent. This afforded precise control of the nanocrystal size and subsequent assignment of the electronic structure both, experimentally and theoretically.[86-91] Nucleation of the CdSe nanoparticles was achieved by the sudden introduction of the concentrated reagents resulting in the abrupt supersaturation and formation of nuclei, followed by slower growth and annealing, consistent with an Ostwald ripening process. The nanoparticles were passivated by a monolayer of the solvent ligand and hence could be isolated/purified by solvent/non-solvent interactions. Purified nanocrystals undergo size selective precipitation to provide powders of nearly monodispersed nanocrystals which can be dispersed in a variety of solvents. The particle size can be controlled by varying the temperature and the time of the reaction.

Other precursors used are tri-n-octylphosphine sulphide (TOPS) for sulphur containing particles and tri-n-butylphosphine instead of TOP for phosphorus containing particles.[92] The choice of TOPO as the coordinating solvent allows the reaction to take place above the nucleation temperature and allows the nanocrystals to be soluble in organic solvents or dispersed in a polymer film. However, it was

discovered early on that there were peculiarities in the TOPO. For example 90 % TOPO (technical grade) produced nanocrystals with sharp absorption features whereas, 99 % TOPO yielded nanocrystals with a broad absorption onset and no sharp features. It became apparent that there was an impurity in the TOPO that was affecting the synthesis in a positive way. This important impurity was postulated by Peng *et al.*, to be phosphonic acid.[29] The organic surface cap of the nanocrystals can be replaced by other organic groups such as pyridine, 4-picoline, tris(2-ethyl hexyl) phosphate and 4-(trifluoromethyl) thiophenol.[1] This can also be used for surface modification, which is critical for nanocrystal applications in biological systems which are always in aqueous buffer solutions.

Improvement to this synthesis was made on the West Coast by the Alivisatos group, which led to an improvement in the size distribution of the crystals and eliminated the need for size-selected separation, which is a time consuming, wasteful and a tedious process.[91] The principal difference is the temperature of injection (which affects the growth time, crystallinity and shape of the nanocrystal) and the use of tributylphosphine (TBP) to coordinate to Se instead of TOP. In 1998, Peng *et al.*[93] used this method to study the kinetics of the nanocrystal growth and, demonstrated how the nanocrystal size can be 'focused' through the addition of a monomer reagent (initial reagent solution) during the course of reaction. The strategy was designed to overcome Ostwald ripening or 'defocusing' of the size distribution. Ostwald ripening occurs when smaller nanocrystals in the distribution dissolve and become smaller and, the monomers released allow the larger nanocrystals in the solution to grow further, subsequently broadening the size distribution.

Hines and Guyot-Sionnest reported the synthesis of ZnSe nanoparticles,[94] using the same methodology reported by Bawendi *et al.*[20] i.e., dimethylzinc and tri-n-octylphosphine selenide as precursors. However the use of TOP/TOPO as coordination solvent failed. The resultant nanocrystals are either so small that they cannot be isolated by standard solvent/nonsolvent precipitation techniques or they precipitated out of the growth solution probably as large aggregates. The difficulties arise from TOPO binding too strongly to Zn and to TOP too weakly. Therefore, another solvent, hexadecylamine (HDA) with a much higher boiling point, larger capping density which probably increases the surface passivation and a weaker base than phosphine oxide, was used.

Talapin *et al.*,[95] introduced the use of HDA into the widely used TOPO-TOP synthesis to give a three-component HDA-TOPO-TOP mixture. This modification of the conventional organometallic synthesis of CdSe nanocrystals in the TOPO-TOP mixture provides much better control over growth dynamics, resulting in the absence of defocusing of the size distribution during the entire growth process and hence eliminates the need of post preparative size selective fractionation. It also improves the PL quantum efficiency.

The Bawendi [20] method in general, has advantages over other synthetic methods, it produces high quality particles and possess a low number of defects per particle but the reaction requires harsh/difficult conditions such as injection of hazardous metal-alkyls, which are toxic, volatile, low boiling point materials, explosive at elevated temperature (up to 350 $^{0}$C), pyrophoric and therefore requires standard airless techniques (Schlenk lines and glove boxes). This is fine for a research setting but is

undesirable for commercial exploitation due to the need of critical experimental conditions.[3] Nevertheless, this synthetic route has been used extensively to synthesise and study the optical and structural properties of nanocrystals. Katari *et al.*,[91] used X-ray photoelectron spectroscopy (XPS) to study the surface of TOPO-capped CdSe nanocrystals covalently bound to Au and Si surfaces and concluded that the formation of a compound oxide is unlikely and that the oxide formed is $SeO_2$, which causes the nanocrystals to degrade on time. On dispersing the crystals in pyridine neither the Cd nor Se surface site was completely passivated and upon exposure to air both Cd and Se oxidised. Peng *et al.*,[96] synthesised epitaxially grown, wurtzite CdSe/CdS core/shell nanocrystals using this technique and used XPS to demonstrate that the structure was indeed a core/shell and not an alloy.

Hines *et al.*[4] verified shelling when making CdSe/ZnS core/shell nanocrystals. Their results indicate three-times as much as Zn than Cd. The degree of passivation of the CdSe surface with ZnS was studied by Daboussi *et al.*,[97] by exposing the nanocrystal surface to air and studying the evolution of the Se peak. Their results show that ~ 1.3 monolayers of ZnS is sufficient to create a continuous shell of ZnS around the CdSe core, even at long exposure time in air.

Danek *et al.*,[98] extended the methodology to synthesise luminescent thin-film CdSe/ ZnSe quantum dot composites, using CdSe quantum dot composites passivated with an overlayer of ZnSe prior to their incorporation into the host matrix by an electrospray organometallic chemical vapour deposition (ES-OMCVD) technique. Their results show that the photoluminescence spectra of the composites with bare CdSe dots, were dominated by broad deep-level emission and the photoluminescence

yield deteriorated with increasing deposition temperature. In contrast, the over-coated dots showed sharp band-edge emission with a dramatic enhancement of the photoluminescence yield which was insensitive to the deposition temperature over the range study. This was an improvement over Liu *et al.*,[99] whose work on silicon based quantum dot composites gave low photoluminescence yield. Becerra *et al.*,[100] used nuclear magnetic resonance (NMR) to investigate the surface morphology of 37 Å diameter CdSe nanocrystals prepared in TOP/TOPO. Their results show that the two capping species, TOPO and TOP:Se, form a close packed shell which physically stabilizes the nanocrystals and electronically passivates the surface.

Manna *et al.*,[101] extended the methodology of doping pure TOPO and hexylphosphonic acid (HPA) to create a variety of nanocrystal shapes. By controlling the ratio of the surfactants, injection volumes and time-dependent monomer concentration, they produced arrow, tetradrop, tetrapod and extremely high aspect ratio CdSe nanorods (30:1).

Peng and Peng [102] studied the mechanism of the shape evolution using CdSe quantum confined nanorods in a non-aqueous solution and revealed three distinguished stages of shape evolution. At high monomer concentration, nanocrystals grow exclusively along the *c*-axis of the wurtzite structure, making this axis the long axis of the rods. At an intermediate concentration, the nanocrystals grow in three dimensions while at the lower monomer concentration the growth of the particle is controlled by intraparticle diffusion on the surface of the nanocrystals, resulting in decreased aspect ratios. Leatherdale *et al.*,[103] determined the QD absorption cross section on the basis

of measured reaction yields and showed that it is largely independent of solvent refractive index.

By controlling the relative amount of precursors to be injected into the coordinating solvent e.g. TOPO, Hashizume *et al.*,[104] modified the size and quality of the synthesised CdSe nanocrystals. Overcoating of the core CdSe with ZnS led to a large enhancement of the quantum efficiency. In order to synthesise, larger nanoparticles and still maintain its quality a two-step injection of CdSe precursors was used. Addition of TOPO separately prior to the secondary injection of precursors and overcoating of ZnS, was found to be useful in obtaining nanocrystals of high quantum efficiency and high reproducibility.

The distribution of properties within ensembles of colloidally grown II-VI and III-V semiconductor nanocrystals was investigated by Talapin *et al.*,[105] by analysing size-selected fractions. A drastic difference was observed in the PL efficiencies of the size-selected fractions between the organometallically prepared CdSe and InAs colloids and aqueous synthesised CdTe. This was attributed to differences in surface disorder of the nanocrystal as a consequence of the Ostwald ripening growth mechanism. The particles with the lowest growth rate within the ensemble, were assumed to have the lowest degree of surface disorder and therefore the highest PL quantum yield at any given condition.

Donega *et al.*,[32] investigated the mechanism underlying the correlation between the surface quality and the growth conditions. They modified Talapin *et al.*,[105] route by using a large reaction volume, variable growth temperatures, different Cd:Se

precursors ratios and the addition of anhydrous triethylorthoformate (TEOF), a dehydrating agent to remove any moisture in the coordinating solvent and to achieve high degree of reproducibility for the growth kinetics and QYs. The modification was carried out in order to determine the role of growth temperature and cadmium to selenium ratio on PL QY, size dispersion and exciton life time of the colloidal CdSe nanocrystals. They attributed low quantum yields to poor passivation, surface disorder and surface degradation which arise at different stages of growth and demonstrated that high QYs can be achieved and maintained only under an ideal combination of growth temperature, solvent composition and Cd:Se ratio, which leads to an optimum surface. Under their synthetic condition Cd:Se ratio of 1:5 and the growth temperature of 240 °C, are the best conditions to obtain reproducibly highly luminescent nearly monodisperse CdSe nanocrystals, without any post preparative treatment.

He and Gu [34] synthesised CdSe nanocrystals at very low temperatures compared to the high temperatures reported by Donega *et al.*[32] Phenyl ether was used as the only non-coordinating solvent with $Cd(Ac)_2$ and TOPSe as the Cd and Se sources respectively. They investigated the effects of growth temperatures (110-170 °C) on the properties of the obtained QDs. Their results also indicated that higher temperatures facilitate formation of larger particles sizes and increase QYs.

In the search for a greener method to avoid the use of fire hazard pyrophoric precursors and reduce hazards to health and environment, Peng and Peng[106] reported the synthesis of high quality CdTe, CdSe and CdS nanocrystals using CdO as a cadmium precursor, instead of Cd $(CH_3)_2$. In this one pot approach, CdO, TOPO and

either (HPA) or tetradecylphosphonic acid (TDPA) were loaded into a three-necked flask. At temperatures above 270 °C, the phosphonic acid complexes with the CdO to form a clear and colourless solution. After the formation of the colourless cadmium phosphonate complex, TBP: E (E = S, Se or Te) was then injected which initiated the formation of the nanocrystals. This synthetic scheme produced both quantum-confined dots and rods. Without any size-sorting, the quality of the quantum dots and rods of all cadmium chalcogenides formed by the new method, is comparable to that of the best CdSe nanocrystals reported in the literature.[20,95,105] They postulated that CdO works well as a precursor due to its low stability, relative to phosphonic acid and other precursor candidates, such as $CdCl_2$. This 'green route' proved to be reproducible, involving mild and simple reaction conditions and had potential to be scaled up for industrial applications. Using this synthetic scheme, Peng *et al.*[107] used, apart from CdO, other cadmium sources such as $Cd(CH_3COO)_2$, ($Cd(Ac)_2$), $CaCO_3$, $CaSO_4$ and $CdCl_2$, as an alternative to $Cd(CH_3)_2$ in the presence of different solvents, like fatty acids and amines. Their results proved fatty acid to be an excellent solvent for synthesising relatively large-sized CdSe nanoparticles but not for smaller sized nanoparticles because of the fast growth rate of the nanocrystals. The use of $CdCl_2$ and $CdSO_4$ generated only bulk-sized CdSe. They attributed this to relatively high stability under acidic conditions of the salt formed by cadmium and a strong acid in comparison to that of CdSe.

Peng and Peng utilized this synthetic route to elucidate the shape evolution, nucleation and growth kinetics of colloidal CdSe nanocrystals with a variety of elongated shapes.[108] They observed that the growth mechanisms of colloidal CdSe anisotropic structures (dot, rice, tadpoles and branched), are complicated by the

required high monomer concentration, which dramatically impacts the initial nucleation stage and found a unique magic sized nanocluster with the first absorption peak at 394 nm as the common nuclei for the growth of CdSe anisotropic structures. This means that the classic nucleation model, the Gibb's-Thompson equation, is invalid for predicting the size of the critical nuclei. Their findings indicated that a large excess of the cadmium precursor, which is less reactive than the Se precursor, is beneficial for the system to reach the desired balance between nucleation and growth. Qu and Peng[24] extended this methodology to study the photoluminescence (PL) properties of semiconductor nanocrystals. The experimental results suggested the existence of the PL 'bright point' (maximum PL QY) as a signature of an optimal surface/reconstruction of the nanocrystals grown under a given set of initial conditions. The position of the bright point, the highest PL QY, the type of the bright point (sharp or flat) and the sharpness of the PL peak, were all reported to be strongly dependent on the initial Cd:Se ratio of the precursor solution.

Using this synthetic scheme, Qu *et al.*,[109] demonstrated a general strategy to study *in situ*, the crystallization systems using the size-dependent optical properties of crystals in the transition regime, from molecular precursors to regular nanocrystals. They suggested that the entire crystallization process can be divided into four stages: nucleation, focusing, stable and defocusing. Myung *et al.*,[110] observed electrogenerated chemiluminescence (ECL) of TOPO-capped CdSe nanocrystals dissolved in $CH_2Cl_2$ containing 0.1 M tetra butyl ammonium perchlorate (TBAP). The ECL spectrum was substantially red-shifted by ~ 200 nm from the PL spectrum, suggesting that surface states play an important role in the emission process.

A comprehensive examination of the effect of reaction media on the growth and photoluminescence of Colloidal CdSe nanocrystals was carried out by Yu *et al.*,[111] simply by varying the TOP/TOPO weight ratio while keeping all other reaction parameters constant. CdO was used as the cadmium precursor and TOPSe as the Se source without the use of any additional acid. A reaction medium of 100 % TOP or 80 % TOP, was found to produce high 'quality' nanocrystals in terms of sharp features and, rich substructures exhibited in the absorption spectra as well as sharp features in the emission spectra with narrow full width at half maximum (FWHM). Two distinguishable stages of growth were observed: an early and a later stage. The growth rate of the nanocrystals from the high TOP reaction media (80 and 100 %) was slow in the early stage (0.5 – 5 mins) but becomes faster in the later stages (after 5 mins). However, the reverse is the case for the low TOP reaction media (20 and 50 %). Additionally, the optical properties are optimised with the high TOP reaction media. These slow growths were further exploited by using different Cd sources such as $Cd(OAc)_2$, CdO/tetradecylphosphonic acid (4 %), CdO and CdO/oleylamine (4 %). The results showed that there is no significant difference in the nanoparticle size.[112]

Boatman *et al.*, also synthesised CdSe of varying particle sizes, using oleic acid and octadecene as a replacement for TOPO with CdO as the cadmium source.[113] The free cyanide in aqueous solution was determined by Jin *et al.*, using photoactivated water-soluble luminescent CdSe quantum dots as sensitive cyanide probes. The CdSe QDs were synthesised following the procedure described by Peng's group. The TOP/TOPO capping group was subsequently exchanged with 2-mercapoethane sulphonic acid to make the QDs water soluble. [114]

Using octadecene as the non-coordinating solvent instead of TOPO, Bullen and Mulvaney [115] investigated the effect of temperature and oleic acid concentration on the growth kinetics of CdSe nanocrystals nucleated from TBPSe and cadmium oleate. It was found that increasing the oleic acid concentration led to smaller numbers of nuclei, smaller initial nuclei size and large final particle sizes. The rate constant for steady-state CdSe deposition, was found to be far slower than the diffusion limit. The same result was obtained by Pan *et al.*,[116] when CdO and octadecene was replaced by $Cd(OAc)_2$ and dodecylamine as cadmium precursors and non-coordinating solvents respectively. Micro-reactors have been used for the large batch synthesis of CdS, $TiO_2$ and CdSe nanoparticles.[117-119] These preparations facilitate accurate control of temperature and homogenous mixing problems, usually associated with such large synthesis. By substituting octadecene for TOPO, Omata *et al.*,[120] reported the synthesis of CdSe quantum dots at high temperatures in a micro flow reactor. In comparison with the QDs synthesised using a small batch reactor,[29,107,121,122] the particle size distribution obtained using the micro-flow reactor, was narrow. This was attributed to the short representative length of the micro flow reactor which enabled accurate controllability of reaction temperatures.

The reaction of metal-oleylamine complexes (which were obtained from the reaction of metal chloride and oleylamine) with elemental sulphur, was used by Joo *et al.*[123] to produce high crystalline metal sulphide nanocrystals of PbS, ZnS, CdS and MnS. Uniform cube-shaped PbS of varying particle sizes (6, 8, 9 and 13 nm) were produced, by changing the relative amount of $PbCl_2$ and sulphur. Large uniform size (11 nm) spherical ZnS nanocrystals were produced after one cycle of size-selective precipitation. Various shapes of CdS nanocrystals that consist of spherical, rods,

bipods and tripods, were produced by changing the cadmium to selenium ratio. While MnS nanocrystals, of various sizes and shapes (rods, novel-bullets, short-bullets and hexagonal) were also synthesized by varying the growth temperature, molar ratio and aging time.

Wang *et al.*,[124] developed a new solvothermal route for synthesizing size and shape controlled CdSe and CdTe nanocrystals, using cadmium-myristic acid complex and Se or Te solution (prepared by dissolving Se or Te powder in TOP under sonication) in a stainless steel autoclave. The seeding-growth technique was used to obtain large nanocrystals. It was found that initial precursor concentrations were the key factors in controlling the different shapes of the resultant nanocrystals, i.e. dots, rods and branched shapes. Moreover the obtained nanocrystals were all of zinc blende structure, regardless of their sizes and shapes. A possible mechanism was put forward for the formation and growth of the nanocrystals. It was inferred that the elongated nanocrystals was formed through adhesion and subsequent recrystallisation of nanocrystals, with the assistance of the remaining monomers.

In looking at the effect of additives on the photostability of semiconductor nanoparticles, Gaunt *et al.*[30] has shown an antioxidant to be effective in reducing the photooxidative degradation of nanoparticles when used to synthesise CdSe, CdSe/ZnSe and CdSe/ZnS nanoparticles in chloroform, compared to phosphine oxides and amine. In a non-TOP synthetic route, Deng *et al.*[125] synthesised cubic CdSe QDs using paraffin as the reaction medium for the first time and oleic acid as the capping agent. Very recently Yang *et al.*,[126] modified this synthetic route to

produce core shell CdSe/CdS QDs emitting in a wide wavelength range (from 510-615 nm).

As part of the investigation into replacing $Cd(CH_3)_2$ as a common precursor for the synthesis of cadmium containing nanoparticles, Hambrock *et al.*,[127] showed that dineopentyl cadmium, bis(3-diethylaminopropyl) cadmium and (2,2'-bipyridine) dimethyl cadmium could be used as potential substitutes for $Cd(CH_3)_2$. 7-membered alkeno-1,2,3-selenodiazole was also reported as a good selenium precursors when reacted with cadmium salt(s) in ethylene glycol.[128] The reaction produced nanocrystalline CdSe nanoparticles without unreacted selenium that is released from selenadiazole during thermolysis.

Another efficient and highly explored technique that has been used as an alternative to the conventional organometallic method in the synthesis of semiconductor nanoparticles, is the thermolysis of a single-molecular precursors in a high boiling coordinating solvent. These compounds, in which the metal-chalcogen bond is already in place, are considered to be versatile as a source for nanoparticle growth. An ideal precursor must be non-air sensitive, stable for a period of months, easy to synthesise and most of all, pyrolyse cleanly to give the highest yield.[1] These methods involve the dispersion of the single source precursor in TOP, followed by injection into hot TOPO (250 °C). The general scheme for nanoparticles synthesis, using single molecular precursors, is shown in Figure 1.6. The formation of the nanoparticles is consistent with the LaMer mechanism for colloids.[38] The decomposition of the precursor drives the formation of the nanoparticles with termination of growth, occurring when the precursor supply is depleted.

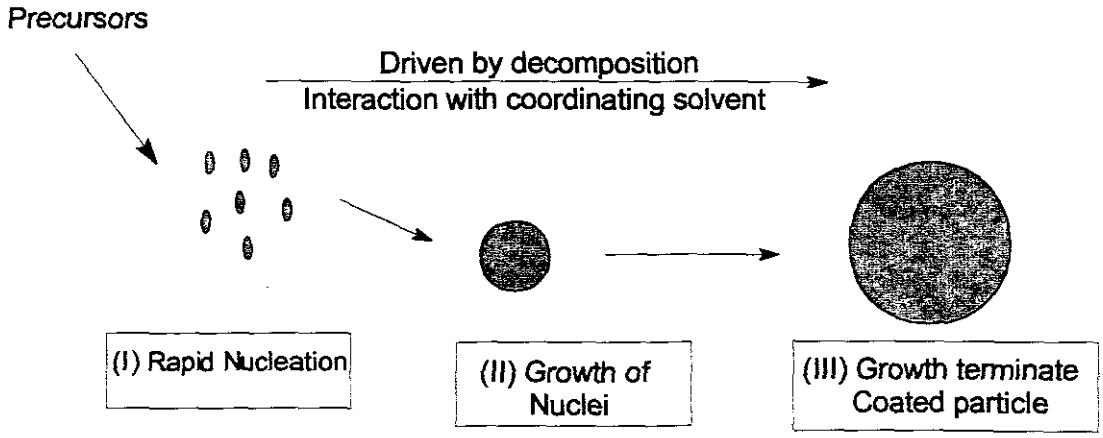


***Figure 1.6*** *Scheme for nanoparticle growth using single source precursor technique.*[1]

Trindade and O'Brien first reported the use of cadmium dithio- and diseleno-carbamate complexes as precursors for the preparation of TOPO-capped II-VI materials.[129,130] Thermolysis of the air-stable complex Cd $(S_2CNEt_2)_2$ in TOPO, resulted in high quality nanoparticles of CdS. The thermolysis of the analogous diselenocarbamate complex in TOPO resulted in micrometric particles of selenium. Compounds of the formula $RCd(E_2CNEt_2)$, (R = neopentyl, Me; E = S,Se) were also used as efficient precursors to CdE nanoparticles upon thermolysis in TOPO, but are however air-sensitive. Air-stable precursors would be preferred. Simple diselenocarbamate complexes of cadmium with unsymmetrical R groups such as hexyl and methyl $[Cd(Se_2CNMeHex)_2]$, are air-stable and are found to be excellent precursors for CdSe.[131] GC-MS studies have suggested the decomposition mechanisms of symmetrical diselenocarbamates, which produce selenium clusters.[132] However, unsymmetrical diselenocarbamate (with alkyl groups longer than hexyl) produce only the metal selenide and organic by-products.

Revaprasadu *et al.*,[133] reported the preparation of TOPO-capped ZnSe using the single source complex, $EtZn(Se_2CNEt_2)_2$ in contrast to the previous report by Hines and Guyot-Sionnest, where the use of TOP/TOPO as capping agent failed. Comparison of Hines' metal alkyl route and the single source route suggests there may be surface differences in the prepared materials. Comparison of IR spectroscopy results of CdSe nanoparticles prepared by single source precursors and the metal alkyl, again suggest different surface environments.[3] The use of dithio-/diseleno-carbamato complexes of cadmium/zinc containing asymmetrical alkyl groups, has proven to be the precursors that give nanoparticles of the highest quality.

By using HDA as the coordinating solvent instead of TOPO, Jun *et al.*[134] thermolysed air-stable $Cd(S_2CNEt_2)_2$ to synthesise CdS nanorods of various size and shapes. The shapes of the resulted nanocrystals were between monorods, bipods, tripods and tetrapods as well as pencil-type rods, by simply changing either the growth temperature or the precursor concentration. Sosibo and Revaprasadu recently used the rhodium analogue $Rh(S_2CNEt_2)_2$ for the synthesis of rod-shaped HDA capped $Rh_2S_3$ nanoparticles.[135] They also used the complex to produce $Rh_2S_3$ thin films by using the aerosol-assisted chemical vapour deposition (AACVD) techniques. $[Pt(S_2CNMe(Hex))_2]$ and $[Pd(S_2CNMe(Hex))_2]$ have been used respectively, for the synthesis of TOPO-capped PtS and PdS nanoparticles.[136]

Nair *et al.*,[137] used cadmium(II) complex of N,N'-bis(thiocarbamoyl)-hydrazine, $Cd(SCNHNH_2)_2Cl_2$,ethylxanthates,$Cd(C_2H_5OSC_2)_2$, dithiobiurea $Cd(NH_2CSNH_2)_2Cl_2$ and thiosemicarbazide $Cd(NH_2CSNHNH_2)_2Cl$ respectively, for the synthesis of CdS nanoparticles and carried-out a comparative study of their optical properties.

Similarly, thiourea and N-alkylthiourea cadmium (II) complex (using methyl or ethyl as the alkyl group) have been used by Moloto *et al.,*[138] for the synthesis of CdS nanoparticles. Its zinc and lead analogue was also used to produce MS nanoparticles (M= Zn and Pb).[139]

The effect of precursor solvent on shape and phase of nanocrystals was investigated by Li *et al.,*[140] by thermolysing the single source precursor, zinc ethylxanthate ($Zn(exan)_2$) using a different precursor solvent system. They observed that in the HDA + octylamine (OA) system, diameter- and aspect-ratio-tunable hexagonal wurtzite ZnS nanorods were formed by kinetic adjustment. Some of the rods self-assembled into two-dimensional (2-D) aligned arrays. While in the HDA +TOP system, a change from rod to dot shape and a phase transition from wurtzite to sphalerite, simultaneously occurred with increasing content of TOP in the mixed solution. Sphalerite nanodots were prepared in high TOP content or in TOP (or trioctylamine (TOA)) solution without HDA.

In finding the correlation between the pattern of thermal decomposition and morphology of nanocrystals, Nair and Scholes[141] analysed thermal decomposition of various cadmium containing single source precursors : N,N'-dioctylthiourea, N,N'-dicyclohexylthiourea, N,N'-disopropylthiourea, N,N'-tetramethylthiourea, dithiobiurea, ethylxanthic acid, thiosemicarbazide and selelosemicarbazide without the aid of any shape-directing agent. Their results show that only the cadmium complexes of thiosemicarbazide and selelosemicarbazide uniquely yield rod-shaped CdS and CdSe nanocrystals respectively, while all other precursors yield spherical CdS nanoparticles. They suggested that the formation of nanorods is unlikely to be

due to the presence of phosphonic acid impurities in commercial TOPO as previously reported,[29] because the same batch of TOPO was used for all the synthesis. They attributed the formation of nanorods to the low activation energy for the semicarbazide precursor decomposition and, the fact that they release structure directing agents during decomposition when compared with those that produced dot-shaped nanocrystals.

Recently Kedarnath reported the use of 2-(N, N-dimethylamino) ethylselenolates of cadmium (II): [Cd ($SeCH_2CH_2NMe_2)_2$] as a single source precursor for the synthesis of CdSe nanoparticles by pyrolysis in either a mixture of hot HDA and TOPO or in a furnace.[142] The result gave both cubic and hexagonal phase CdSe nanoparticles of varying sizes. Also, Bruce *et al.*[143] have showed that cadmium (II) complexes of N,N-diethyl-N'-bensoylthiourea and N,N-diethyl-N'-bensoylthio selenourea could be used as precursors for the synthesis of HDA capped CdS and CdSe nanoparticles respectively. The results showed that only spherical CdS and CdSe nanoparticles are formed with a predominantly cubic phase, independent of the reaction temperatures and the precursor concentrations.

As part of improvement and eliminating the use of toxic materials in the synthesis of nanoparticles, Sapra *et al.*[144] synthesised CdSe nanoparticles using an inexpensive, harmless olive oil as the coordinating solvent and cadmium oxide as the cadmium source. In a more recent development, Wang *et al.*[145] used N,N-dimethyl-oleyl amide (DMOA), a cheaper and environmentally friendly solvent, to dissolve CdO powder in oleic acid and form a homogenous cadmium oleate solution, which also acts as the capping ligand for the formation of the CdSe QDs.

## 1.7 Applications of Nanoparticles

Advances in the preparation of highly luminescent monodispersed nanoparticles and their unique properties, have led to materials which are now potentially useful in many areas of applications. These areas include catalysis, optical recording materials, solar cells, biotechnology, sensor and lasing materials. Thus, making TOPO then an important class of material for the photonic, electronic, biological and other technological industries in the 21st century.

### 1.7.1 *Electronic Devices*

Exceptional optical properties make quantum dots attractive components for integration into devices. One significant advantage of quantum dots over traditional optoelectronic materials is that they exist in the solid state. Solids tend to be more compact, easily cooled and allow for direct charge injection.[156] Additionally, quantum dots can interconvert light and electricity in a tunable manner, dependent on crystal size and allowing for facile wavelength selection. This is a significant improvement over silicon based materials, which require modification of their chemical composition (i.e., doping) to alter the optical properties. All these have led to the imperative applications of quantum dots in lasers, LEDs and photovoltaics. Though most of these applications are still in early development however, the benefits of quantum dot components are evident.

#### 1.7. 1.1 *Quantum Dot Lasers*

The main advantage of quantum dot lasers is that they possess fewer energy states than bulk materials which reduces the "spread" of electrons, thus making it easier to create lasing. Additionally, quantum dots can be tuned to a specific

emission wavelength by altering the size of the particle and can be operated within a narrow excitation wavelength range. All of these advantages have led to the development of numerous types of quantum dot lasers.

#### 1.7.1.2 *Quantum Dot LEDs*

Quantum dots provide a novel alternative to microfabricated semiconductor materials (that emit a fixed light wavelength) because emission wavelengths can be selected simply by changing the size of the particle. Additionally, because of their small size, quantum dots can be easily encapsulated into conducting organic polymers, allowing for the development of flexible displays. These two advantages make quantum dot LEDs useful in many devices, such as cell phones and laptop computers. One exciting prospect is the replacement of incandescent lights with paper thin materials that could produce illumination at a variety of wavelengths and could be moulded into any shape.[147]

#### 1.7.1.3 *Quantum Dot Photovoltaics*

Another use of quantum dots in electronics is for the creation of advanced photovoltaics or solar cells. The primary difficulty with photovoltaic devices is the efficient conversion of light to energy. Light with a wavelength below the value of the band gap will not be adsorbed and is not converted to energy. Furthermore, any electron excited with a photon greater than the band gap value, will dissipate the extra energy as heat. Only the portion of energy corresponding to the band gap will produce a current. In quantum dot photovoltaics, multiple particles can be incorporated into a single solar cell and each particle can have a different band gap.[148] Therefore, a solar cell can be constructed that is responsive to the entire spectrum of

emitted solar light. A specific example is, a device in which elongated CdSe nanocrystals (nanorods) are mixed with a conducting polymer and sandwiched between aluminium and indium tin oxide electrodes, to create a device with a power conversion efficiency of 1.7 % .[149]

### 1.7.2 Biological Applications

Quantum dots offer several enhancements over the organic fluorescent dyes that are typically used for biological labelling. Organic dyes can exhibit a low quantum yield or brightness, because of molecular interactions with themselves, each other and the solvent. Quantum dots are also susceptible to these limitations, but the particles may be passivated with protective insulating materials to produce quantum yields that are > 50 %.[4]

Another limitation of organic dyes is the loss of fluorescence that occurs when dye molecules react irreversibly with each other or the solvent, producing a non-fluorescent product. This process, known as photobleaching, can occur in aqueous solution on the order of minutes.[150] However, photobleaching in quantum dots is diminished as the same passivating layer, that enhances quantum yield, also protects particles from external interactions. Most notably, passivation reduces photo-oxidation of the particle core which can produce free ions (e.g., $Cd^{2+}$) and eventually, particle dissolution.[151] As a result of reduced photobleaching, quantum dots can exhibit continuous fluorescence for a time period, of an order of magnitude greater than organic fluorescent dyes.[150] Furthermore, organic fluorescent dyes typically exhibit fixed, narrow excitation spectra. Fluorescent excitation spectra reflect absorbance spectra thus, quantum dots may be excited in a range of wavelengths

selected by their size. Additionally, the emission bandwidth (e.g., wavelength range of emitted light) for organic dyes can be very large (> 40 nm, often with a tail into red wavelengths) when compared with nanoparticles which is very narrow (~20-30 nm), thus creating difficulty in distinguishing individual colours.[152] The narrow band widths result from the shrinking and splitting of potential energy bands as the particle size decreases. All of these properties have led to quantum dot applications in diverse biological fields, including biosensing, cellular labelling, and *in vivo* fluorescent detection and therapeutics.

### 1.7.2.1 *Quantum Dots Biosensors*

Biosensors detect molecules of biological significance through an optical or electrical signal produced upon analyte recognition. Although their initial use was primarily for disease detection and monitoring, there has been a recent resurgence in the detection of bio-warfare agents. Most biosensors operate on the principle of molecular recognition. Antibodies, peptides, proteins and DNA sequences, all bind tightly to their target biomolecules with high specificity.[153] Dyes can be coupled to these recognition molecules to produce a fluorescent event when binding occurs. Quantum dot biosensors offer many benefits compared to those based on dye molecules. The surface of quantum dots can be easily altered, providing a facile route for conjugation to recognition molecules.[154] Additionally, their small sizes allow for incorporation into existing electronic devices. The most common types of biosensors used to detect analytes, are fluorescence resonance energy transfer (FRET).

#### 1.7.2.2 *FRET-Based Biosensors*

The simplest method for detection, using fluorescent molecules, is a system that produces an on or off signal upon binding. This can be accomplished using FRET. First, an electron in a fluorescent molecule is excited. Then, instead of decaying through photon emission, the energy in that electron is dissipated by transfer to a second molecule. This quenches the fluorescence of the first molecule. FRET is a distance-dependant event. As the FRET donor and acceptor move away from each other, transfer no longer occurs and fluorescence in the donor is restored.[155] The major problem with FRET is, introduction of a continuous conformational change upon analyte binding that separates the two molecules, thus producing a continuous fluorescent on/off signal. This has been accomplished by using quantum dots. A combination of gold quantum dots (which do not fluoresce) and organic fluorophores, have been utilized to create DNA sensors.[156] Also, adhesion of cyclodextrin to maltose present on the surface of fluorescent CdSe/ZnS, quantum dots have been used to detect sugar binding.[157]

FRET-based quantum dot biosensors are elegant and in theory, can provide analyte detection of as few as 10 parts per trillion.[158] Additionally, the signal is easy to interpret, fluorescence indicates the presence of an analyte. FRET-based biosensors can also provide quantitative information, as fluorescent intensity can be correlated to the number of molecule binding events. Although FRET systems could be constructed entirely from fluorescent dye molecules, quantum dots provide an excellent alternative. They display high quantum yields and, their acceptor energy and emission wavelengths can be tailored by changing the size of the particle.

### 1.7.2.3 *Quantum Dot Fluorescent Labels For Cells*

The prevalent biological use of quantum dots has been fluorescent labeling of cells. In this function, quantum dots are not only superior to fluorescent dyes, but have also extended the potential applications of fluorescent labels in biological systems. For example, they have been used to investigate the motion of biomolecules, detect cell phenotype and study cell migration. In each of these uses, they present several enhancements over systems employing fluorescent dyes. Most importantly, their small size and high resistance to photobleaching, have allowed quantum dots to be used in a number of high throughput systems with real-time monitoring, a difficult feat with dye molecules.[159]

The most exciting possibility for quantum dot labels has been their use *in vivo*. Quantum dots have been utilized in a number of *in vivo* procedures that would not be possible with organic fluorescent dyes. Many of these take advantage of the longevity of their fluorescence, as a result of resistance to photobleaching,[160-163] while others exploit their electrical properties to deliver therapeutic treatment.[164-166] The majority of nanoparticles used in biological applications have been based on a Cd–X structure (X = tellurium, sulfur, or selenium). Cadmium is known to interfere with DNA mismatch repair,[167] can inhibit certain types of neuronal firing[168] and is a known carcinogen. [169] Therefore, the toxicity of the particles has been a major concern. Surface passivation can significantly reduce the risk of exposure to free cadmium,[170] and although the long-term effects of nanoparticle exposure have not yet been investigated, short-term *in vivo* studies do not demonstrate any acute effects.[160-166] One novel use of quantum dots *in vivo* has been to monitor embryogenesis in

frog.[160] The use of fluorescent dyes in this system would have been very demanding, because of high levels of photobleaching.

Quantum dots have been evident in limited therapeutic contexts. They can be used to image and, even penetrate cancer cells through receptor mediated endocytosis.[166] Particles can be coupled to therapeutic agents, which are activated in the presence of light excitation. Antibody-conjugated CdSe/ ZnS core shell nanocrystals have been used to detect respiratory syncytial virus.[171] The brightness of the quantum dots enables the virus to be detected in a matter of minutes, whereas the previous assay required four days. The ramification of this new technology is that, antiviral drugs can be given early in the infection when they are most effective, reducing hospitalization and death. Gold nanoshells conjugated to recognition molecules, can be used to image tumors.[164] When they are optically excited they produce heat, depending on the size of the nanoshell and heat production can be significant enough to kill the attached cells.

### 1.7.3 Other Areas of Nanoparticles Applications

#### 1.7.3.1 *Agriculture*

Many vitamins and their precursors, such as carotinoids, are insoluble in water. However, when capably produced and formulated as nanoparticles, these substances can be mixed easily with cold water and their bioavailability in the human body also increases. Nanoporous materials have been made for the slow release of water and nutrients in the soil. Nanomagnets are now available for the removal of soil contaminants. Zinc nanoparticles are also used as fungicides.

### 1.7.3.2 *Energy and Environment*

Nanocatalysts can reduce air pollution, especially from waste products of non-renewable energy sources. This includes nanocoatings for photocatalytic destruction of air pollutants and for reduction of emission from fossil fuel, gas separation devices and nanosensors for toxic materials and leaks. Cheap, easily transportable systems that purify, detoxify and desalinate water (such as nanomembranes) and small effective nanosensors for the detection of contaminants and pathogens, will contribute both to improve health and to maintain a safe supply of water, e.g. nanomagnets for removal of radioactive compounds.

Aluminium nanoparticles have been used to create rocket propellants that burn at double rate. Copper nanoparticles have also been produced that are incorporated into automotive lubricant to reduce engine wear. The addition of nanoparticulate ceria (cerium oxide) to diesel fuel improves fuel economy by reducing the degradation of fuel consumption over time. Incorporating nanoparticles in paints could improve their performance by making them lighter and giving them different properties.

### 1.7.3.3 *Sport*

Tennis balls made with nanocomposites bounce twice as long as conventional balls as a result of the coating. The used nanocomposite is a mixture of butyl rubber, intermingled with nanoclay particles, giving the ball substantially longer life. A tennis racket has been made, using carbon nanotubes. The yoke of the made racket bends less during ball impact, which contributes in improving the player's performance. A golf ball made with a nanomaterial can correct its own flight path, so it flies straighter than conventional balls. The ball will not shift 45 degrees in midair,

but the design of the ball and the materials it is made of, serve to better channel the energy received from the club head and thus correct a wobble or slight drift.

#### 1.7.3.4 *Fashion*

Nanoparticles of titanium and zinc oxide are currently used in some sunscreens because they absorb and reflect ultraviolet (UV) light. Socks made with nanomaterials do not smell terrible like normal socks do, this is due to the fact that nanotechnology materials such as nanosized silver particles have been included, that kill foot odour and bacteria.

## 1.8 Selenium Based Nanoparticles Synthetic Route Problem

Selenide semiconductors have raised considerable interest due to their important applications as thermoelectric cooling material, optical filters and sensors, optical recording materials, solar cells, superionic materials, laser materials and in biological applications. Therefore the synthesis of selenide nanomaterials has been the interest of many scientists. The key issue to all semiconductor nanoparticle research is the ability to synthesis high quality nanoparticles with well-defined properties. That is, high crystallinity, achievement of desirable particle sizes over the largest possible range, narrow size distribution, desired surface passivation and high luminescence. There are several methods for the preparation of selenides nanoparticles, these include solid-state reactions,[172] solid state metathesis[173] and self-propagation high temperature synthesis.[174] All of these reactions require high temperature (>500 $^0$C ) for initiating the reactions. When gaseous $H_2Se$ was used to prepare selenides, the process was deemed to be dangerous and highly toxic.[53,61,175] High-energy ball milling[176] of metal and selenium at room temperature has also been used to prepare

selenides. However, the product quality was difficult to control. Parkin *et al.*, reported a low temperature route to selenide in liquid ammonia.[177,178] During their experiment, several manipulations had to be carried out at -77 °C, in thick walled glass vessels and all operations had to be conducted with care and behind a safety screen.

In a landmark paper, Murray *et al.*[22] reported the synthesis of high quality CdSe nanoparticles using tri-*n*-octylphosphine selenide (TOPSe) and dimethyl cadmium [Cd $(CH_3)_2$], in the presence of a coordinating solvent at high temperatures.[4,29,32,86-105] The latter compound is toxic, unstable, explosive, expensive and unstable at high temperature. The synthesis of CdSe, using CdO and other non-toxic cadmium sources as a precursor instead of Cd $(CH_3)_2$,[24,106-116] first reported by Peng's group, proved to be reproducible involving mild and simple reaction conditions and could have potential for scaled-up industrial applications. However this process involves the presence of additional stabiliser such as hexylphosphonic acid (HPA) or tetradecylphosphonic acid (TDPA), which increases the cost of production and the initial temperature of the reaction is still very high. In addition the use of $CdCl_2$ and $CdSO_4$ as cadmium precursors generated only bulk-sized CdSe.

Another modification to Murray *et al.*[20] synthesis is, the single source precursor approach pioneered by O'Brien *et al.*[129-143] These precursors are excellent for the synthesis of air-stable, monodispersed, good quality selenide nanoparticles. A drawback to this route includes the use of toxic and noxious carbon diselenide as starting material, large amount of by-products and waste as majority of the starting materials used do not end up in product, i.e. poor yield if one takes into consideration various steps involved in the synthesis, poor size-dispersity for some of the as-

synthesised nanoparticles and unavailability of some of these precursors commercially. Further improvement to hot injection techniques is the introduction of additional reagents as the synthesis progressed, which helped to "focus the size distribution" and enabled larger, more monodispersed CdSe nanocrystals to be grown.[93] Although there have been significant improvements on the synthesis involved in the injection of organometallic precursors into hot coordination solvents, the reaction still needs to be performed with standard airless techniques (Schlenk lines and glove boxes), which is undesirable for commercial exploitation[3] and difficult for the standard undergraduate laboratory where fabrication and characterisation of CdSe nanocrystals provides a beautiful 'real world' application of the quantum mechanical concept of the particle-in-a-box.[179]

Other approaches that have also been used for the synthesis of selenide nanoparticles, include electrochemical methods,[180,181] micro-flow reactor,[117-119] micro-wave assisted preparation,[182,183] sonochemical methods,[72] microwave irradiation,[75,76] chemical bath vapour deposition[184,185] and photochemical methods.[74] Although most of these developed methods do not require difficult laboratory conditions, there are still some limitations to their utilities such as dissatisfying photoluminescence quantum yield in many cases, relatively broad particle size distribution, low solubility of the precursors in the dispersing solvent and long reaction time for processing the precursor material to be used. In addition, comparing the product yield to the total cost of production (taking into consideration the cost of the equipment and starting materials), these techniques seem not to be cost-effective and may not be desirable for large scale production.

Synthesis involving the use of cheaper and environmentally friendly solvents such as olive oil,[144] paraffin,[125,126] and DMOA[145], look very promising however, high temperatures are required for the dissolution of the precursors. This implies low energy efficiency, which is not desirable for green synthesis.[186,187] Milder synthetic temperatures would be preferred. There is also the problem of surface modification in other, to make the as-synthesised nanoparticles water-soluble.

In general, all synthesis involving organic solvent has major limitation of surface modification which sometimes is tedious, time-consuming and involves wastage of ancillary materials (solvents, processing aids) used for the reaction.

The synthesis of selenide nanomaterials via a solution route appears to be the most simple, cheapest and convenient approach to prepare the selenides in a controlled environment. Most of these methods involve arrested precipitation or titration in aqueous solution. The colloidal route has proven to be an efficient one for synthesizing semiconductor nanocrystals. However, certain types of nanosized semiconductor which are of immense application such as group $II^B$ selenides cannot be synthesized easily via this route.[1] Photobleaching, wider size distribution, air-sensitivity and instability of the colloids at high temperature which makes annealing of the particle difficult, thereby making the material poorly crystalline, are some of the limitations associated with this method. Improvements to this method has been reported in the literature, but most of these involve using highly toxic selenides source,[53, 61, 175] or oxyanions with a positive charge on selenium.[188] Though in the late 90's Wang *et al.*[49,50] reported a milder synthetic route to selenide nanoparticles using selenides ion, $Se^{2-}$ in an autoclave at 80 - 100 °C and also at room temperature.

An organic solvent, ethylenediamine (a bidentate ligand), was used and $KBH_4$ served as the reducing agent. The resultant nanoparticles were of large particle sizes. Time-consuming reduction of elemental selenium in the presence of additional stabilising agent CTAB, at 60 °C, reported by Badr[85] for the synthesis of PVA-CdSe nanoparticles, was characterised by poor optical properties with very broad emission.

A recent development is the use of selenosulphate and selenourea as the main sources to provide $Se^{2-}$ ions for the preparation of selenides through reactive solution growth.[66-83] However, these compounds are expensive and selenourea is not readily available.[80] Long reaction time and/or special instruments to synthesise the nanoparticles are some of the limitations involved, using selenosulphate in addition to broad particle size distribution, deep trap emission, tailing band edge and low quantum yield of some of the synthesised nanoparticles.

Conjugation of semiconductor nanoparticles with biomolecules through biosynthesis and biological surface modification of semiconductors,[189] has added a new dimension to research at the nanoscale. It is essential that the quantum dots be in a water-dispersible form for their use in any biological applications. The most common method for producing water-soluble selenide nanoparticles is through surface modification of organically soluble nanoparticles. Since the pioneering work of Chan *et al.*[150] and Alivisatos *et al.*,[152] where QDs were made biocompatible and water-soluble via surface coating, various methods have been developed in which a hydrophobic QD is first prepared and its surface is made hydrophilic by further modification with mercaptoacetic acid,[150] dihydrolipotic acid[190] or dithiothreitol.[191] The draw back to these techniques includes, the use of sophisticated equipment for

the synthesis, use of toxic and explosive starting materials, long reaction time (up to 3 days) and instability of the particles indicating possible loss of surface ligands.

A modification to this method is the synthesis of water-soluble nanoparticles in an aqueous solvent. Rogach *et al.*,[53] reported the direct synthesis of selenide nanoparticles in an aqueous solution, using $H_2Se$ produced by titration *as* the selenium source, while mercapto-alcohols and mercapto acids are used as stabilizers. The method is very efficient, flexible and several thiol ligands[51-57] and polymers[80-82] could be used as stabilizers. In addition, they have the unique ability of being manufactured using simple bench-top chemistry, requiring only a fume hood. However, reduced optical properties, large particle size distribution, low quantum yield and deep trapped emission are the main limitations of these procedures in addition to the toxic $H_2Se$ used as the selenium source. These have slowed down the production of stable QD-biomolecules complexes, hence limiting its biological applications.

## 1.9 Conclusions

In order to minimise or prevent chemical hazards to health and the environment, as there is a high increase in the considerable interest both from industry and academia in the use of selenide nanoparticles with the knowledge that these materials are toxic, there is a need for synthesis via a greener method. Such synthesis should be able to accommodate the production of either organic or aqueous soluble high quality selenide nanoparticles directly, without any surface modifications. In addition such synthesis as described by Murphy and Dahi must involve less toxic starting materials, least number of reagents, few synthetic steps, reduced amount of by-products and

wastes, low temperature reactions and if possible, the use of water as a solvent without the loss of their unique properties.

## 1.10 Aims and Objectives of the Project

### 1.10.1 *Aims*

1 To establish a novel, mild, non-noxious and convenient synthetic route to high quality, monodispersed, crystalline and stable, metal selenide nanoparticles without complicated equipment or organometallic precursor.

2 To synthesise organic-soluble group $II^A$ (Cd and Zn) selenide nanoparticles.

3 To synthesise water-soluble group $II^A$ (Cd and Zn) selenide nanoparticles capped with water-soluble surfactants such as cysteine, methionine and starch directly by a one-pot synthesis using water as the solvent.

4 To characterize and study the optical properties of the nanoparticles.

### 1.10.2 *Objectives*

The objective of this study is to use the new synthetic route for the following:

- To synthesise and characterize organically capped metal selenide nanoparticles with comparable or superior properties than those prepared with existing route.
- To determine the effect of organic surfactants, growth time, temperature, concentration and reduction time on the size, optical properties and morphology of the nanoparticles.
- To synthesise water-soluble selenide nanoparticles capped with cysteine, methionine and study the effect of pH and growth time on the size, optical properties and morphology of the nanoparticles.

➢ To synthesise starch-capped selenide nanoparticles and to study the effect of concentration on the size and morphology of the nanoparticles.

➢ To synthesise CdSe/ ZnSe core-shell and nanocomposites.

## 1.11 References


1) M. A. Malik and P. O'Brien, phosphorus, sulphur and silicon, 2005, **180**, 689.

2) M. A. Malik, P. O'Brien and N. Revaprasadu, *South African Journal of Science*, 2000, **96**, 55

3) M. Green and P. O'Brien, *Chem. Commun.*, 1999, 2235.

4) M. A. Hines and P. J. Guyot-Sionnest, *J. Phys. Chem.*, 1996, **100**, 468.

5) C. B. Murray, C. R. Kagan and M.G Bawendi, *Science,* 1995, **270**, 1335.

6) A. P. Alivisatos, *Science*, 1996, **271**, 933.

7) N. Chestoy, T. D. Harris, R. Hull and L. E. Brus, *J. Phys. Chem.*, 1986, **90**, 3393.

8) L. Z. Zhang, W. Sun and P. Cheng, *Molecules* 2003, **8**, 211, 220.

9) H. Richter, Z. P. Wang and L. Levy, *Solid. State. Commun.*, 1981, **39**, 625.

10) P. Atkins, Physical Chemistry, 5th Ed., W.H. Freeman and Co., New York: 1994, 540-541

11) H. Weller, H. M. Schmidt, U. Koch, A. Fojtik, S. Baral, A. Henglein, W. Kunath, K. Weiss and E. Dieman, Chem. Phys. Lett., 1986, **124**, 557.

12) Y. Wang and N. Herron, *J. Phys. Chem.*, 1991, **95**, 525.

13) A. L. Efros and A.L Efros, *Sov. Phys. Semicond.*, 1982, **16**, 772.

14) L. E. Brus, *J. Chem. Phys.*, 1983, **79**, 5566.

15) L. E. Brus, *J. Chem. Phys.*, 1984, **80**, 4403.

16) Y. Nosaka, *J. Phys. Chem.*, 1991, **95**, 5054.

17) Y. Z. Hu, M. Lindberg and S. W. Koch, *Phys. Rev.* B, 1990, **42**, 1713.

18) M. V. Rama Krishna and R. A. Freisner, *J. Chem. Phys.*, 1991, **95**, 8309.

19) H. M. Schmidt and H. Weller, Chem. Phys. Lett., 1986, **129**, 615.

20) C. B. Murray, D. J. Norris and M. G. Bawendi, *J. Am. Chem. Soc.*, 1993, **115**, 8706.

21) M. G. Bawendi, M. L. Steigerwald and L. E. Brus, *Annu. Rev. Phys. Chem.*, 1990, **41**, 477.

22) P. E. Lippens and M. Lannoo, *Phys. Rev.* B, 1989, **39**, 10935.

23) W. W. Yu, L. Qu, W. Guo and X. Peng, *Chem. Mater.*, 2003, **15**, 2854.

24) L. Qu and X. Peng, *J. Am .Chem. Soc.*, 2002, **124**, 2049.

25) W. Hoheisel, V. L. Colvin, C. S. Johnson and A. P. Alivisatos, *J. Chem. Phys.*, 1994, **101**, 8455.

26) C. F. Landes, S. Link, M. B. Mohammed, B. Nikoobakht and A. El-Sayed, Pure. Appl. Chem., 2002, **74**, 1675.

27) V. N. Soloviev, A. Eichhofer, D. Fenske and U. Banin, *J .Am. Chem. Soc.* 2000, **122**, 2673.

28) X. Chen, Y. Lou and C. Burda, *Int. J. of Nanotechnology*, 2004, **1**, 105.

29) X. G. Peng, L. Manna, W. D. Yang, J. Wickham, E. Scher, A. Kadavanich and A. P. Alivisatos, *Nature*, 2000, **404**, 59.

30) J. A. Gaunt, A. E. Knight, S. A. Windsor and V. Chechik, *J. Colloid and Interface Science*, 2005, **290**, 437.

31) J. McBride, J. Treadway, L. C. Feldman, S. J. Pennycook and S. J. Rosenthal, *Nano Lett.*, 2006, **6**, 1496.

32) C. D. Donega, S. G. Hickey, S. F. Wuister, D. Vanmaekelbergh and A. Meijerink, *J. Phys. Chem.* B, 2003, **107**, 489.

33) K. Yu, B. Zaman, R. Taal and J. A. Ripmeester, *J. Cryst. Growth, 2005*, **283**, 115.

34) R. He and H. Gu, *Colloids and Surfaces A: Physicochem. Eng. Aspects*, 2006, **272**, 111.

35) U. Jeong, Y. Wang, M. Ibisate and Y. Xia, *Adv. Funct. Mater.*, 2005, **15**, 1907.

36) R. A. Anderievskii, *Russ. Chem. Rev.*, 1994, **63**, 411.

37) A. Eychmuller, *J. Phys. Chem.* B, 2000, **104**, 6514.

38) V. K. La Mer and R. H. Dinegar, *J. Am. Chem. Soc.*, 1950, **72**, 4847.

39) T. Johnson and V. K. Lamer, *J. Am. Chem. Soc.*, 1947, **69**, 1184.

40) R. J. Hunter, Foundation of Colloid Science, Oxford University Press, 6th edition, Oxford, 1993, Vol.1, 13-17.

41) R. Rossetti, J. L. Ellison, J. M. Gibson and L. E. Brus, *J. Chem. Phys.*, 1984, **80**, 4464.

42) H. Weller, *Adv. Mater.*, 1993, **5**, 88.

43) H. Weller, A. Fojtik and A. Henglein, *Chem. Phys. Lett.*, 1985, **117**, 485.

44) R. Rosetti, J. L. Ellison, J. M. Gibson and L. E. Brus, *J. Chem. Phys.*, 1985 **82**, 552.

45) C. H. Fischer, J. Lilie, H. Weller, L. Katsikas and A. Henglein, *Langmuir*, 1989, **5**, 429.

46) A. Eychmuller, H. Weller and L. Katsikas, *Langmuir*, 1990, **6**, 1605.

47) H. Haase, H. Weller and A. Henglein, *Ber. Bunsenges. Phys. Chem.*, 1988, **92**, 1103.

48) K. Sookal, B. S. Cullum, S. M. Angel and C. J. Murphy, *J. Phys. Chem.* 1996, **100**, 4551.

49) W. Wang, Y. Geng, P. Yan, F. Liu, Y. Xie and Y. Qian, *Inorg. Chem. Commun.*, 1999, **2**, 83.

50) W. Wang, Y. Geng, P. Yan, F. Liu, Y. Xie and Y. Qian, *J. Am .Chem. Soc.*, 1999, **121**, 4062.

51) J. H. Yoon, W. S. Chae, S. J. Im and Y. R. Kim, Mater. lett., 2005, **59**, 1430.

52) T. Vossmeyer, L. Katsikas, M. Giersig, L. G. Popovic, K. Diesner, A. Chemseddine, A. Eychumuller and H. Weller, *J. Phys. Chem.*, 1994, **98**, 7665.

53) A. L. Rogach, A. Kornowski, M. Gao, A. Eychmuller and H. Weller, *J. Phys. Chem.*, 1999, **103**, 3065.

54) A. L. Rogach, L. Katsikas, A. Kornowski, D. S. Su, A. Eychmuller and H. Weller, *Ber. Bunsenges. Phys. Chem.*, 1996, **100**, 1772.

55) A. L. Rogach, L. Katsikas, A. Kornowski, D. S. Su, A. Eychmuller and H. Weller, *Ber. Bunsenges. Phys. Chem.*, 1997, **101**, 1668.

56) M. Gao, S. Kirstein, H. Mohwald, A. L. Rogach, A. Kornowski, A. Eychmuller and H. Weller, *J. Phys. Chem.* B, 1998, **102**, 8360.

57) A. L. Rogach, S. V. Kershaw, M. Burt, M. Harrison, A, Kornowski, A. Eychmuller and H. Weller, *Adv. Mater.*, 1999, **11**, 552.

58) S. V. Kershaw, M. Burt, M. Harrison, A. L. Rogach, H. Weller and A. Eychmuller, *Appl. Phys. Lett.*, 1999, **75**, 1694.

59) M. T. Harrison, unpublished.

60) L. Li, H. Qian and J. Ren, *Chem.Commun.*, 2005, 528.

61) U. K. Gautam, M. Rajamathai F. Meldrum, P. Morgan and R. Seshadri, Chem. Commun., 2001, 629.

62) Q. Yang, K. Tang, C. Wang, Y. Qian and S. Zhang, *J. Phys. Chem.* B, 2002, **106**, 9227.

63) S. N. Sarangi and S. N. Sahu, *Physica E*, 2004, **23**, 159.

64) C. C. Chen, C. Y. Chao and Z. H. Lang, *Chem. Mater.*, 2000, **12**, 1516.

65) Z. Tang, N. A. Kotov and M. Giersig, *Science*, 2002, **297**, 237.

66) G. Hodes, Chemical solution deposition of semiconductor films, Marcel Dekker: New York, 2002.

67) S. Yochelis and G. Hodes, *Chem. mater.*, 2004, **16**, 2740.

68) P. P. Hankare, V. M. Bhuse, K. M. Garadkar, S. D. Delekar and I. S Mulia, *Mater. Chem. Phys.*, 1989, **90**, 3463.

69) V. M. Bhuse, P. P. Hankare, K. M. Garadkar, and A. S. Khomane, *Mater. Chem. Phys.*, 2003, **80**, 82.

70) N. E. Glistenko, and A. A. Yeremina, *Zh. Neorg. Khim.*, 1960, **5**, 1003.

71) L. Xu, K. Chen, J. Zhu, H. Chen, H. Huang, J. Xu and X. Huang, *Superlattices Microstruct.*, 2001, **29**, 67.

72) H. Y. Han, Z. H. Sheng and J. G. Liang, *Mater. Lett.*, 2006, **60**, 3782.

73) J. Zhu, S. Xu, H. Wang, J. Zhu and H. Chen, *Adv. Mater.*, 2003, **15**, 156.

74) W. B. Zhao, J. J. Zhu and H. Y. Chen, *J. Cryst. Growth*, 2003, **252**, 587.

75) O. Palchik, R. Kerner, A. Gedanken, A. M. Weiss, M. A. Slifkinb and V. Palchikb, *J. Mater. Chem.*, 2001, **11**, 874.

76) J. J. Zhu, O. Palchik, S. G. Chen and A. Gedanken, *J. Phys. Chem.* B, 2000, **104**, 7334.

77) M. Behboudnia, and Y. Azizianekalandaragh, *Mater. Sci. and Eng.* B, 2007, **138**, 65.

78) J. J. Zhu, X. H. Liao, X. M. Zhao and J. Wang, *Mater. Lett.*, 2001, **47**, 339.

79) W. B. Zhao, J. J. Zhu and H. Y. Chen, *Scr. Mater.*, 2004, **50**, 1169.

80) Y. J. Yang and B. J. Xiang, *J. Cryst. Growth*, 2005, **284**, 453.

81) X. D. Ma, X. F. Qian, J. Yin and Z. K. Zhu, *J. Mater. Chem.*, 2002, **12**, 663.

82) X. D. Ma, X. F. Qian, J. Yin and Z. K. Zhu, *J. Colloid and Interface Science*, 2002, **252**, 77.

83) J. H. Li, C. L. Ren, X. Y. Liu, Z. D. Hu and D. S. Xue, *Mater. Sci. Eng.* B, 2007, **458**, 319.

84) X. Zhong, S. Liu, Z. Zhang, L. Li, Z. Wei and W. Knoll, *J. Mater. Chem.*, 2004, **14**, 2790.

85) Y. Badr and M. A. Mahmoud, *Physica* B, 2005, **369**, 278.

86) D. J. Norris and M. G Bawendi, *Phys. Rev. B*, 1996, **53**, 16338.

87) M. G. Bawendi, W. L. Wilson, L. Rotheberg, P. J. Carroll, T. M. Jedju, M. L. Steigerwald and L. E. Brus, *Phys. Rev. Lett.*, 1990, **65**, 1623.

88) M. Nirmal, D. J. Norris, M. kuno, M. G. Bawendi, A. L. Efros and M. Rosen, *Phys. Rev. Lett.*, 1995, **13**, (20), 3728.

89) A. Franceschetti and A. Zunger, *Phys. Rev. Lett.*, 1997, **78**, 915.

90) N. A. Hill and B. Whaley, *J. Chem. Phys.*, 1994, **100**, (4), 2831.

91) J. E. Bowen Katari, V. L. Colvin, and A. P. Alivisatos, *J. Phys. Chem.*, 1994, **98**, 4109.

92) N. L. Pickett and P. O'Brien, *The Chemical Record*, 2001, **1**, 467.

93) X. Peng, J. Wickham and P. A. Alivisatos, *J. Am. Chem. Soc.*, 1998, **120**, 5343.

94) M. A. Hines and P. J. Guyot-Sionnest, *J. Phys. Chem.* B, 1998, **102**, 3655.

95) D. V. Talapin, A. L. Rogach, A. Kornowski, M. Haase and H. Weller, *Nano. Lett.*, 2001, **1**, 207.

96) X. Peng, M. C. Schlamp, A. V. Kadavanich and A. P. Alivisatos, *J. Am. Chem. Soc.*, 1997, **119**, 7019.

97) B. O. Dabboussi, J. Rodriguez-Viejo, F. V. Mikulec, J. R. Heine, H. Mattoussi, R. Ober, K. F. Jensen and M. G. Bawendi, *J. Phys. Chem.* B, 1997, **101**, 9463.

98) M. Danek. K. F. Jensen, C. B. Murray, and M. G. Bawendi. *Chem. Mater.*, 1996, **8**, 173.

99) X. Liu, X. Wu, X. Bao and Y. He, *Apply. Phys. Lett.*, 1994, **64**, 220.

100) L. R. Becerra, C. B. Murray, R. G. Griffin and M. G. Bawendi, J. Chem. Phys., 1994, **100**, (4), 3297.

101) L. Manna, E. C. Scher and A. P Alivisatos, *J. Am. Chem. Soc.*, 2000, **122**, 12700.

102) Z. A. Peng and X. Peng, *J. Am. Chem. Soc.*, 2001, **123**, 1389.

103) C. A. Leatherdale, W. K. Woo, F. V. Mikulec and M. G. Bawendi, *J. Phys. Chem.* B, 2002, **106**, 7619.

104) K. Hashizume, M. Matsubayashi, M. Vacha and T. Tani, *J. Lumin.*, 2002, **98**, 49.

105) D. V. Talapin, A. L. Rogach, E. V. Shevchenko, A. Kornowski, M. Haase, and H. Weller, *J. Am .Chem. Soc.*, 2002, **124**, 5782.

106) Z. A. Peng and X. Peng, *J. Am. Chem. Soc.*, 2001, **123**, 183.

107) L. Qu, Z. A. Peng and X. Peng, *Nano. Lett.*, 2001, **1**, 333.

108) Z. A. Peng and X. Peng, *J. Am. Chem. Soc.*, 2002, **124**, 3343.

109) L. Qu, W. W. Yu and X. Peng, *Nano. Lett.*, 2004, **4**, 465.

110) N. Myung, Z. Ding, and A. J. Bard, *Nano. Lett.*, 2002, **2**, 1315.

111) K. Yu, S. Singh, N. Patrito and V. Chu, *Langmuir*, 2004, **20**, 11161.

112) K. Yu, B. Zaman, R. Taal and J. A. Ripmeester, *J. Cryst. Growth*, 2005, **283**, 115.

113) E. M. Boatman, G. C. Lisensky, K. J. Nordell, *J. Chem. Educ.*, 2005, **82,** 1697.

114) W. J. Jin, M. T. Fernandez-Arguelles, J. M. Costa-Fernandez, R. Pereiro and A. Sanz-Medel, *Chem. Commun.*, 2005, 883.

115) C. R. Bullen and P. Mulvaney, *Nano. Lett.*, 2004, **4**, 2303.

116) B. Pan, R. He, F. Gao, D. Cui and Y. Zhang, *J. Cryst. Growth*, 2006, **286**, 318.

117) J. B. Edel, R. Fortt, J. C. Demello and A. J. Demello, Chem. Commun., 2002, 1136.

118) H. Wang, H. Nakamura, M. Uehara, M. Miyazaki and H. Maeda, *Chem. Commun.*, 2002, 1462.

119) H. Nakamura, Y. Yamaguchi, M. Miyazaki, H. Maeda, M. Uehara and P. Mulvaney, *Chem. Commun.*, 2002, 2844.

120) T. Omata, K. Nose, S. O. Y. Matsuo, H. Nakamura and H. Maeda, *J. Apply. Phys.*, 2005, **44**, 452.

121) M. A. Malik, N. Revaprasadu and R. A. Fischer, *J. Mater. Chem.*, 2001, **11**, 3197.

122) N. Revaprasadu, M. A. Malik, P. O'Brien and G. Wakefield, *Chem. Commun.*, 1999, 1573.

123) J. Joo, H. B. Na, T. Yu, Y. W. Kim, F. Wu, J. Z. Zhang and T. Hyeon, *J. Am. Chem. Soc.*, 2003, **125**, 11100.

124) Q. Wang, D. Pan, S. Jiang, X. Ji, L. An and B. Jiang, *J. Cryst. Growth*, 2006, **286**, 83.

125) Z. T. Deng, C. Li, F. Q. Tang and B. S. Zou, *J. Phys. Chem. B*, 2005, **109**, 16671.

126) D. Yang, Q. Chen and S. Yu, *J. Lumin.*, 2007, **126**, 853.

127) J. Hambrock, A. Birkner and R. A. Fischer, *J. Mater. Chem.*, 2001, **11**, 3197.

128) P. K. Khanna, R. M. Gorte and R. Gokhale, *Mater. Lett.*, 2004, **58**, 966.

129) T. Trindade and P. O'Brien, *Adv. Mater.*, 1996, **8**, 161.

130) T. Trindade, P. O'Brien and X. Zhang, *Chem. Mater.*, 1997, **9**, 523.

131) B. Ludolph, M. A. Malik, P. O'Brien and N. Revaprasadu, *Chem. Commun.*, 1998, 1849.

132) M. Chunggaze, J. M. Aleese, P. O'Brien and D. J Ostway, *Chem. Commun.*, 1998, 833.

133) N. Revaprasadu, M. A. Malik, P. O'Brien, M. M. Zulu and G. Wakefield, *J. Mater. Chem.*, 1988, **8**, 1885.

134) Y. W. Jun, S. M. Lee, N. J. Kang and J. Cheon, *J. Am. Chem. Soc.*, 2001, **123**, 5150.

135) N. M. Sosibo and N. Revaprasadu, *Mat. Sci. Eng.* B, 2008, **150**, 111.

136) M. A. Malik, P. O'Brien and N. Revaprasadu, *J. Mater. Chem.*, 2002, **12**, 92.

137) P. S. Nair, T. Radhakrishnan, N. Revaprasadu and P.O' Brien, *Mat. Sci. Tech.*, 2005, **21**, 237.

138) M. J. Moloto and N. Revaprasadu, *J. Mater. Chem.*, 2004, **15**, 313.

139) N. Moloto, unpublished work.

140) Y. Li, X. Li, C. Yang and Y. Li, *J. Phys. Chem.* B, 2004, **108**, 16002.

141) P. S. Nair and G. D. Scholes. *J. Mater. Chem.*, 2006, **16**, 467.

142) G. Kedarnath, S. Dey, V. K. Jain, G. K. Dey and B. Varghese, *Polyhedron*, 2006, **25**, 2383.

143) J. C. Bruce, N. Revaprasadu and K. R. Koch, *New. J. Chem.*, 2007, **31**, 1647.

144) S. Sapra, A. L. Rogach and J. Feldmann, *J. Mater. Chem.*, 2006, **16**, 3391.

145) C. Wang, Y. Jiang, G. Li, Z. Zhang, J. Shi and N. Li, *J. Cryst. Growth*, 2008, **310**, 2890.

146) C. Weisbuch, H. Benisty and R. Houdre, *J. Lumin.*, 2000, **85**, 271.

147) S. C. Sullivan, W. K. Keung, J. S. Steckel, M. Bawendi and V. Bulovic, *Org. Elec. Phy. Mats. Appl.*, 2000, **4**, 123.

148) T. J. Bukowski and J. H. Simmons, *Crit. Rev. Solid State Mat. Sci.*, 2002. **27**, 119.

149) W. U. Huynh, J. J. Dittmer and A. P. Alivisatos, *Science*, 2002, **295**, 2425.

150) W. C. W. Chan and S. Nie, *Science,* 1998, **281**, 2016.

151) L. Spanhel, M. Haase, H. Weller and A. Henglein, *J. Am. Chem. Soc.*, 1987, **109**, 5649.

152) M. Bruchez, J. M. Moronne, P. Gin, S. Weiss and A.P. Alivisatos, *Science*, 1998, **281**, 2013.

153) J. A. McCammon, *Curr. Opin. Struct. Biol.*, 1998, **8**, 245.

154) A. P. Alivisatos, *J. Phys. Chem.*, 1996, **100**, 13226.

155) L. Stryer and R. P. Haugland, *Proc. Natl. Acad. Sci.*, 1967, **58**, 719.

156) D. J. Maxwell, J. R. Taylor and S. Nie. *J. Am. Chem. Soc.*, 2002, **124**, 9606.

157) I. L. Mendintz, A. R. Clapp, H. Mattoussi, E. R. Goldman, B. Fisher and J. M. Mauro, *Nature Mats.*, 2003, **2**, 630.

158) S. Wang, N. Mamedova, N. A. Kotov, W. Chen and J. Studer, *Nano Lett.*, 2002, **2**, 817.

159) L. C. Mattheakis, J. M. Dias, Y. J. Choi, J. Gong, M. P. Bruchez, J. Liu and E. Wang, *Anal. Chem.*, 2004, **327**, 200.

160) B. Dubertret, P. Skourides, D. J. Norris, V. Noireaux, A. H. Brivanlou and A. Libchaber, *Science*, 2002, **298**, 1759.

161) D. R. Larson, W. R. Zipfel, R. M. Williams, S.W. Clark, M. P. Bruchez, F.W. Wise and W.W. Webb, *Science*, 2003, **300**, 1434.

162) W. C. W. Chan, D. J. Maxwell, X. Gao, R. E. Bailey, M. Han and S. Nie, *Curr. Opin. Biotech.*, 2000, **13**, 40.

163) M. E. Åkerman, W. C. W. Chan, P. Laakkonen, S. N. Bhatia and E. Ruoslahti, *Proc. Nat. Acad. Sci.*, 2002, **99**, 12617.

164) C. Loo, A. Lin, L. Hirsch, M. H. Lee, J. Barton, N. Halas, J. West and R. Drezek, *Tech.Cancer Res. Treat.*, 2004, **3**, 33.

165) C. Seydel, *Science*, 2003, **300**, 80.

166) X. Wu, H. Liu, J. Liu, K. N. Haley, J. A. Treadway, J. P. Larson, N. Ge, F. Peale and M. P. Bruchez, *Nature Biotech.*, 2003, **21**, 41.

167) A. Hartwig and T. Schwedtle, *Toxic. Lett.*, 2002, **127**, 47.

168) J. B. Lansman, P. Hess and R. W. Tsien, *J. Gen. Physio.*,1986, **88**, 321.

169) M. P. Waalkes, *Mut. Res.*, 2003, **533**, 107.

170) A. M. Derfus, W. C. W. Chan and S. N. Bhatia, *Nano Lett.*, 2004, **4**, 11.

171) E. L. Bentzen, F. House, T. J. Utley, J. E. Crowe and D. W. Wright, *Nano. Lett.*, 2005, **5**, 591.

172) R. Coustal, *J. Chem. Phys.*, 1958, **38**, 277.

173) H. C. Yi and J. J. Moore, *J. Mater. Sci.*, 1990, **25**, 1159.

174) I. P. Parkin, *Chem. Soc. Rev.*, 1996, **25**, 199.

175) H. C Metcalf, J. E. Williams and J. F. Caskta, *Modern Chemistry*, Holt, Reinhart and Winston: New York, 1982, 454.

176) T. Ohtani and M. Motoki, *Mater. Res. Bull.*, 1995, **30**, 1495.

177) G. Henshaw, I. P. Parkin, G. Shaw, *J. Chem. Soc., Chem. Commun.*, 1996, 1095.

178) G. Henshaw, I. P. Parkin, G. Shaw, *J.Chem. Soc., Dalton Trans.*, 1997, 231.

179) T. C. Kippeny, L. A. Swafford and S. J. Rosenthal, *J. Chem, Ed.*, 2002, **79**, 1094.

180) D. S. Xu, X. S. Shi, G. L. Guo, L. Gui and Y. Q. Tang, *J. Phys. Chem.* B, 2000, **104**, 5061.

181) J. Z. hu, Y. Koltypin and A. Gedanken, *Chem. Mater.*, 2000, **12**, 73.

182) J. Zhu, O.Palchik, S. Chen and A. Gedanken, *J. Phys. Chem.* B, 2000, **104**, 7344.

183) Y. Wang, Z. Tang, M. A. Correa-Duarte, I. Pastorizanto, M. Giersig, N. A. Kotov, and L. M. Liz-Marzan, *J. Phys. Chem.* B, 2004, **108**, 15461.

184) S. Gorer, A. Albu-Yaron and G.Hodes, *Chem. Mater.*, 1995, **7**, 1243.

185) O. Yamamoto, T. Sasamoto, and M. Inagaki, *Mater. Res.*, 1998, **13**, 3394.

186) C. J. Murphy, *J. Mater. Chem.*, 2008, **18**, 2173.

187) J. A. Dahi, B. L. S. Maddux and J. E. Hutchison, *Chem. Rev.*, 2007, 2228.

188) U. K. Gautam, M. Nath, and C. N. R. Rao, *J. Mater. Chem.*, 2003, **13**, 2845.

189) S. Wang, N. Mamedova, N. A. Kotov, W. Chen, J. Studer, *Nano Lett.*, 2002, **2**, 817.

190) H. Mattoussi, J. *Am. Chem. Soc.*, 2000, **122**, 12142.

191) S. Pathak, *J. Am. Chem. Soc.*, 2001, **123**, 4103.

# *CHAPTER TWO*

## SYNTHESIS OF ORGANICALLY SOLUBLE CADMIUM SELENIDE NANOPARTICLES

## 2. 1 Introduction

Progress on the synthesis of high quality semiconductor nanocrystals has played and, is still playing a critical role in the advancement of quantum dot (QD) applications. Lithography-based technologies have been widely used for the QDs grown onto adequate substrates[1] but, have mainly been restricted to the preparation of optoelectronic devices. However, colloidal nanocrystals with single crystalline structures, well-controlled size and size distributions, can be prepared by relatively simple nanocrystal-growth processes. While there have been studies on II-VI, III-V and IV-VI nanocrystals, as well as metal oxide nanocrystals and others, chemically grown CdSe nanoparticles are probably the most extensively investigated colloidal II-VI semiconductor nanoparticles since the introduction of the "size quantization effect". Interest in CdSe is probably due to the availability of precursors, simplicity of crystallisation and its tunable band gap across the visible spectrum by variation of the particle size.[1,2] The key to the use of semiconductor nanoparticles in potential applications, is the ability to synthesise high quality particles with well-defined properties. Some of the essential properties include reasonable crystallinity, achievement of desirable particle sizes over the largest possible range, desired surface passivation, increased luminescence and a high degree of monodispersity in size and shape. There has been significant progress in the controlled synthesis and post-preparative separation of CdSe nanoparticles, whose narrow size distribution, high crystallinity, size-dependent absorption and photoluminescence features, allow them to be useful in applications such as thermoelectric cooling materials, optical filters, optical recording materials, solar cells, sensors, laser materials and more recently, in biological applications. Several methods have been reported for the synthesis of selenium nanoparticles and their limitations, as highlighted in chapter one. As a

result of these, an ever growing trend for the synthesis of highly luminescent and stable CdSe nanoparticles that can be incorporated into high performance products through a greener sustainable method, is still an ongoing challenge to material chemists. Such methods will involve less toxic starting materials, fewer reagents, smaller waste products and mild temperatures without any post-preparative methods or loss of their unique properties.[3] This will help to prevent or minimise the chemical hazards to health and the environment occurring through the synthesis of these resourceful materials.

This chapter describes the synthesis of high quality CdSe nanoparticles through a novel, greener, quick, facile and effective non-organometallic solution based method. The as-synthesised particles have similar or improved optical properties and morphology when compared to the existing methods. Studies have shown that the size and quality of the nanoparticles depends on several parameters such as monomer concentration, capping agents, injection temperature, growth temperature, growth time, pH, solvent and precursor ratio.[4-9] Hence, the systematic study of the effect of capping group, growth time, temperature, reduction time and monomer concentration on the size, absorption and emission properties and, morphology of the as-synthesized nanoparticles, will also be explored using this new approach.

## 2.2 Synthetic Method

The inspiration for the method employed in this study can be traced to a report by Rao *et al.*[10] on the synthesis of t-selenium nanorods and nanowires. This method involved the reduction of selenium powder in water. In our reaction, colloidal CdSe nanoparticles have been synthesized by the addition of an aqueous cadmium chloride

solution to a freshly prepared oxygen-free NaHSe. In a typical room temperature reaction, selenium powder was mixed with deionised water in a three-necked flask. $NaBH_4$ was carefully added to this mixture and the flask was immediately purged with nitrogen gas, in order to create an inert atmosphere. After a short period, the entire selenium dissolved in water to give a clear colourless solution. $CdCl_2$ solution was added to this selenium ion solution and stirring was continued. Methanol was then added and the resultant mixture was centrifuged. The CdSe produced was then dispersed in tri-octylphosphine (TOP) and after continuous stirring, the TOP-CdSe was injected into the hot coordinating solvent (tri-octylphosphine oxide (TOPO) or hexydecylamine (HDA)) under nitrogen flow. A decrease in temperature was observed by rapid introduction of the reagent mixture. The temperature was raised and maintained for a specific amount of time. After completion, the solution was allowed to cool and methanol was added to flocculate the nanoparticles. The flocculate was separated by centrifugation and dried. Dispersion of the flocculate in toluene resulted in an optically transparent solution of CdSe nanocrystals, which could be readily characterised.

The high quality of the synthesised nanoparticles was confirmed using absorption and photoluminescence spectroscopy, fourier transform infrared spectroscopy (FT-IR), powder x-ray diffraction (XRD), transmission electron microscopy (TEM), high resolution transmission electron microscopy (HRTEM), selected area diffractometry (SAD) and energy dispersive spectroscopy (EDS). All measurements were performed without any post-preparative size separation of the nanoparticles.

## 2.3 Results and Discussion

Colloidal CdSe nanoparticles were synthesized by the reduction of selenium powder using $NaBH_4$ as the reducing reagent to give an oxygen free selenide ion (NaHSe) followed by the addition of $CdCl_2$. The reduction is due to the presence of an active hydride in $NaBH_4$, which also activates the reaction between the selenide ion and $CdCl_2$ at room temperature.[11] Evidence of this reaction is the change in the reaction solution from colourless NaHSe solution to bright-yellow, orange or wine-red (depending on the reduction time) after the addition of $CdCl_2$. The reaction scheme is shown below:

$$4NaBH_4 + 2Se + 7H_2O \longrightarrow 2NaHSe + Na_2B_4O_7 + 14H_2 \quad (2:1)$$

$$NaHSe + CdCl_2 \longrightarrow CdSe + NaCl + HCl \quad (2:2)$$

***Figure 2.1*** *The reaction scheme for the synthesis of CdSe nanoparticles*

In this method, $CdCl_2$ was used as the cadmium precursor in contrast to previous reports from traditional methods which suggests that it is impossible to synthesise high quality CdSe nanocrystals with an anion of a strong acid in the form of cadmium precursor or, an added cadmium ligand such as $CdCl_2$ or $CdSO_4$ in non-aqueous solution, because the related cadmium salt complexes are too stable to properly initiate the nucleation process.[12]

### 2.3.1 Optical Properties

#### 2.3.1.1 *Effect of Capping Group*

The choice of an effective coordinating solvent is very important because the surface passivation of the nanocrystals, by organic molecules have been shown to

control the growth rate and particle size and also improve the luminescence efficiency, stability and solubility by removing the surface defects behaving as non-radiative relaxation centres for the electron hole recombination.[4,13-16] In this study, TOPO and HDA were used as the coordinating solvents (Figures 2.2 and 2.3) because they give higher surface passivation, due to greater coverage of the co-ordinately unsaturated Cd at the surface by the ligands.[4,14,17-19] The stability of the TOPO-capped particles is due to the high affinity of TOPO for $Cd^{2+}$ and, it's bulky nature also provides increased steric hindrance.[19,20] In contrast, HDA a primary amine, is a slightly weaker base than TOPO with less steric hindrance, high electron-donating ability and high capping density as a result of its small stererochemical interference.[4,16,18,21]

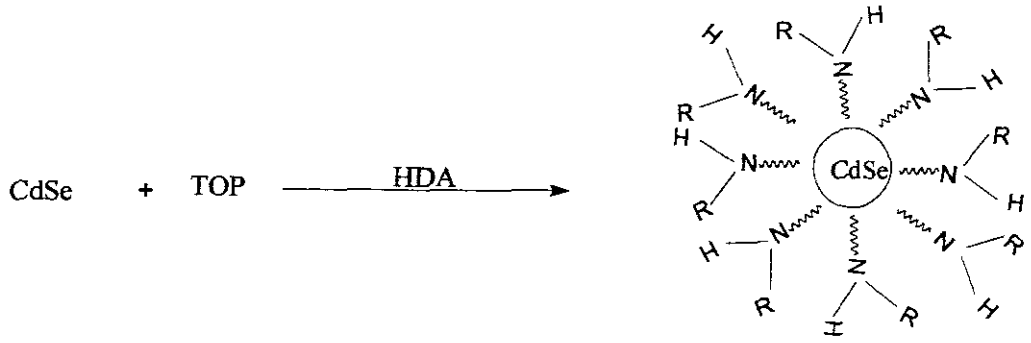


***Figure 2.2*** *Schematic diagram of hexadecylamine (HDA) – capped CdSe*

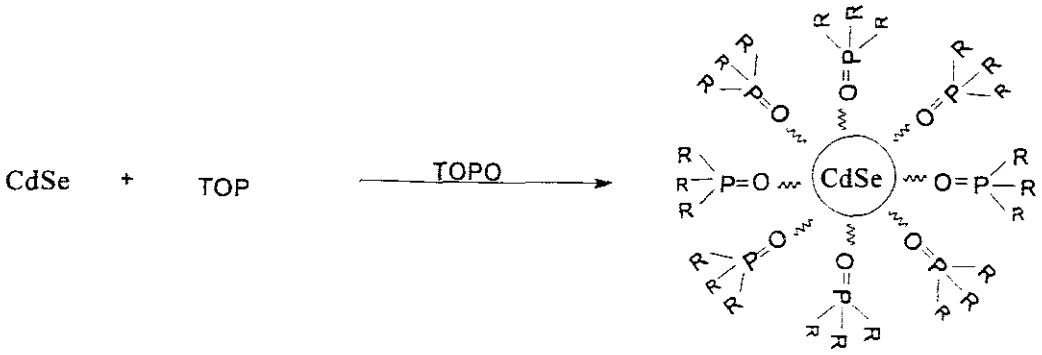


***Figure 2.3*** *Schematic diagram of tri - octylphosphine oxide (TOPO) – capped CdSe*

The UV-absorption spectra for the as-prepared HDA- and TOPO-capped CdSe nanoparticles after 30 mins, using 0.64 mmol monomer concentration are shown in Figure 2.4. The absorption band-edges as calculated using the direct band gap method[22] are 2.09 eV (593 nm, HDA) and 2.03 eV (618 nm, TOPO), both blue-shifted in relation to bulk CdSe, 1.73 eV (716nm). The HDA-capped CdSe is slightly more blue-shifted, indicating smaller particle sizes as compared to the TOPO-capped CdSe. The UV spectra also show distinct excitonic features at 2.20 eV (563nm, HDA) and 2.15 eV (576nm, TOPO) which can be attributed to the first electronic transition (1s-1s) occurring in CdSe nanoparticles.[19,23] The excitonic shoulder and sharp absorption edge are indicative of particles with a narrow size distribution. The sizes of the CdSe particles as calculated from the excitonic peak, using Yu's calibration data equation,[24] are 3.3 nm (HDA-capped) and 3.7 nm (TOPO-capped). Similar results were obtained using the effective mass approximation (EMA) model[25] and UV/Vis calibration curves published by Murray et al.[17] The slight increase in the size of the TOPO-capped CdSe particles as compared to the HDA-capped particles, has been reported previously for CdSe by Talapin *et al.*[21] The authors attributed the difference in sizes to the redistribution of electronic density in the semiconductor core under the influence of passivating groups.

The photoluminescence spectra for both, the HDA- and TOPO-capped particles, exhibit band-edge luminescence for excitation at 400 nm (Figure 2.5). The emission maxima show a red-shift in relation to the corresponding absorption maximum; 592 nm (2.09 eV) for the HDA-capped CdSe and 600 nm (2.07 eV) for the TOPO-capped CdSe. In correlation with the absorption spectra, the emission maximum for the HDA-capped CdSe is also slightly blue-shifted as compared to the TOPO-capped

CdSe. Emission line widths are narrow, indicating the growth of the crystallites with few electronic defect sites.[17] The sharp luminescence shows the efficiency of the capping group in electronically passivating the surface states or defects which are normally associated with semiconductor nanoparticles.[4,13,16] The enhancement of the band-edge PL in HDA in comparison with TOPO-capped CdSe nanocrystals can be attributed to the strong bonding of the amines to the nanocrystal surface, due to its high electron donating ability and capping density as compared to TOPO which enhances passivation.[14,16] Less sterically hindered amines may improve surface capping and hence, passivation of traps, by creating a larger capping density.[18,26] TOPO on the other hand has low capping density in order to avoid the stereochemical interference from its bulky alkyl chain. This leads to less surface structure/ reconstruction of the nanocrystals and as a result, the surface defects of the CdSe nanoparticles were insufficiently passivated by TOPO. This leads to the presence of surface states in the band gap of the nanocrystals which then affects the intensity of the PL spectra.[4]

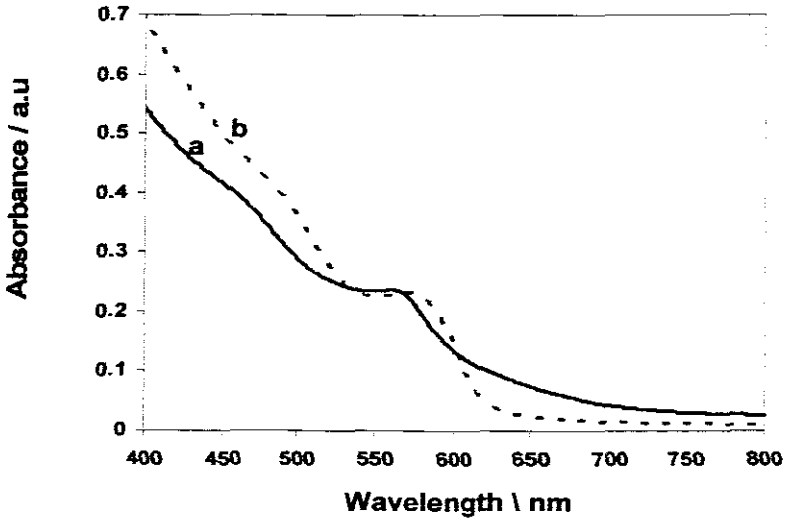


***Figure 2.4*** *Absorption spectra of (a) HDA and (b) TOPO-capped CdSe after 30 mins using 0.64 mmol monomer concentrations.*

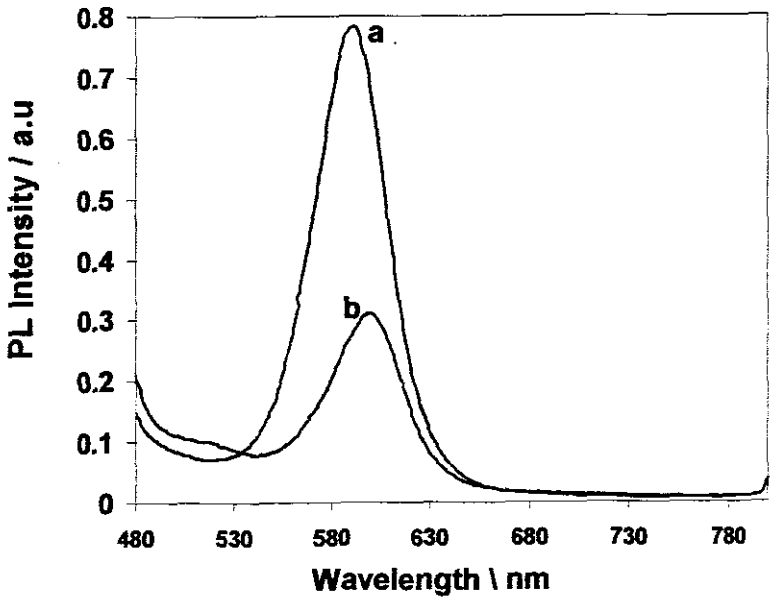


***Figure 2.5*** *Photoluminescence spectra ($\lambda_{400}$ nm) of (a) HDA and, (b) TOPO-capped CdSe after 30 mins, using 0.64 mmol monomer concentrations.*

### 2.3.1.2 *Effect of Reduction Time*

The quality of the nanoparticles synthesized via an aqueous route is controlled by subtle variation in synthetic parameters such as reactant ratio, pH of the solution and nature of the solvent. In addition, the type of reaction(s) (i.e. oxidation, reduction, precipitation, decomposition, displacement reaction, etc.) occurring between the reacting precursors also contribute to the nanoparticle size, quality and dispersity. This synthetic route is based on the reduction reaction hence, we look at the effect of time on the reducing power of the active hydride present in $NaBH_4$ on selenium powder before the addition of $CdCl_2$. The reduction was monitored between the periods of 2, 4 and 6 hrs, with initial monomer concentration of the precursors being 0.32 mmol. The entire selenium dissolves in water within 120 minutes, giving rise to a clear colourless solution. As the reduction time increases,

the resultant colourless solution becomes darker. The addition of $CdCl_2$ to the reaction flask after 2, 4 and 6 hrs reduction time, changes the colour of the solution to light yellow, orange and red, respectively. The effect of these reduction times on the size and optical properties of the CdSe nanoparticles was studied using HDA and TOPO as the coordinating solvent.

#### 2.3.1.2.1 *HDA-capped CdSe Nanoparticles*

Figures 2.6 - 2.11 show the temporal evolution of the absorption and photoluminescence spectra of HDA-capped CdSe nanoparticles, synthesized at reduction times of 2, 4 and 6 hrs. The emission and optical maxima of all the nanoparticles synthesized within these periods, are blue-shifted from the bulk band gap, clearly showing quantum confinement. The entire particle, synthesized for the period of 2 and 4 hrs reduction time, show sharp absorption edges and excitonic shoulders within the growth period of 0 to 30 mins (Figures 2.6 and 2.7) signifying particles with narrow size distributions, while a reduction time of 6 hrs (Figure 2.8) show sharp absorption edges and excitonic shoulders within the growth period of 10 to 30 mins. The featureless UV seen in the spectra for 6 hrs reduction time for the growth period of 2 and 5 mins, can be attributed to weak confinement.[27] It also indicates the presence of nanoparticles with different particle sizes and poor passivation within the growth time.[28]

The shift of absorption and emission maxima to higher band gap (lower wavelength) increases with increasing reduction time, indicating decrease in particle size as the reduction time increases. The particle sizes as calculated from the excitonic peak, shows that the smallest particle size resulted from 6 hrs reduction time. The particle

size within the growth period of 5 to 30 mins ranges between 2.4 - 3.0 and 2.3 - 3.2 nm for 2 and 4 hrs reduction time respectively, while the particle size for 6 hrs reduction time is between 2.5 - 2.7 nm within the growth period of 15 to 30 mins. This is contrary to the prediction from the colour of the solution, after addition of $CdCl_2$ which changes from transparent yellow to red, signifying an increase in the particle size as the reduction time increases.

The tailing band-edge observed in the absorption spectra for 2 and 5 mins growth period under 6 hrs reduction time which is absent in the spectra for 2 and 4 hrs reduction time, is characteristic of polydispersed semiconductor materials. This confirms that large CdSe nanoparticles are indeed produced after 6 hrs of reduction time. These large particles resulted in large nuclei during nucleation at the start of the reaction, immediately after the injection into hot HDA hence, tailing of the band-edge. As the reaction time increases these large nuclei produced, are further nucleated and serve as a stable precursor for the formation of smaller nuclei. This is favourable for the growth of monodispersed smaller size nanoparticles. These smaller nanoparticles are slightly larger than the critical size of the monomer concentration and grow faster than the larger ones in the solution, due to their higher energy and lower stability hence, focusing of the size distribution. This inference is confirmed by the emergence of excitonic shoulder and sharp absorption edge after 15 mins and for the rest of the reaction time. The full width at half-maximum (FWHM) remains stable (37 nm) throughout the reaction time after 15 mins.

The significant increase in the particle size under the reduction time of 4 hrs between the growth periods of 20 to 30 mins (2.7 - 3.2 nm) could be attributed to growth via

Ostwald ripening after the depletion of monomer concentration in which the larger particles grow on account of dissolution of smaller ones. Evidence of this is the presence of a broad excitonic shoulder and increase in the size distribution (of about 9 nm) at 30 mins reaction time. The FWHM (35 nm) remains constant between 5 and 20 mins growth period and increases to 44 nm after 30 mins.

The largest particle size obtained from the thermolysis of the species produced under 2 hrs of reduction time might be attributed to the instant formation of cadmium amine complexes in the source solution immediately after the injection. This is due to the smaller size of the precursor species. The diffusion of these complexes is slow because the mass of the complex is large. The slow diffusion suppresses the crystal growth of the CdSe compared to those from 4 and 6 hrs reduction times, leading to large particle sizes.

The contradiction between the particle size from the absorption maxima and prediction from the colour change after addition of $CdCl_2$ shows that temperature, growth time and passivating agent also have a substantial influence on the size of the synthesized nanoparticles.

The reduction time of 4 hrs gives the highest number of observed electronic transitions (Figure 2.7), starting with only one at 2 mins (416 nm) to three at 5 and 10 mins (416, 441 and 494 nm). As the reaction time increases the lowest energy peak, namely the first transition ($1S_{3/2} - 1S_e$) noticeably sharpens with increase in optical density as compared to the second transition, which also increases as compared to the third transition. The position of the second and third transition remain the same as the reaction time increases but, the optical density diminishes slightly in the order $3^{rd}$ <

2nd transition. Subsequently, the nanocrystals exhibit less sub-structures in their absorption spectra along with reaction time. At 15 mins, the second transition appears at a new wavelength (502 nm) with the disappearance of the third transition. This transition increases in optical density as the reaction time increases to 20 mins and disappears after 30 mins, appearing as a broad transition. These resolved electronic transitions could be attributed to the narrow size distribution for the reaction time of 5 to 20 mins (35 nm). The FWHM remains the same for these reaction times, signifying a uniform particle size distribution. Such stable FWHM for a longer period, is not observed for the nanocrystals synthesised under 2 and 6 hrs reduction times. The reduction time of 2 and 6 hrs shows only one pronounced transition.

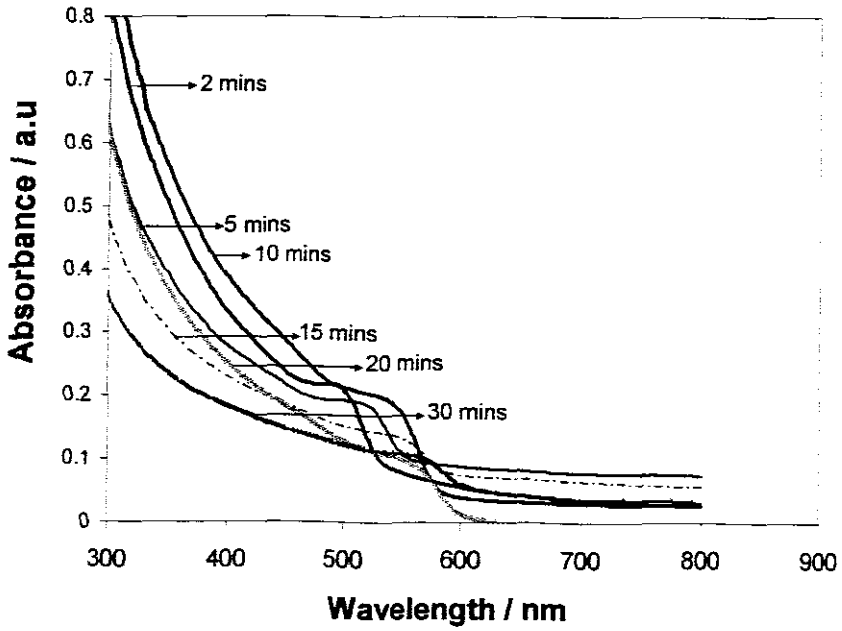


***Figure 2.6*** *Absorption spectra of HDA-capped CdSe under reduction time of 2 hrs for the growth time of 2, 5, 10, 15, 20 and 30 mins using 0.32 mmol concentrations*

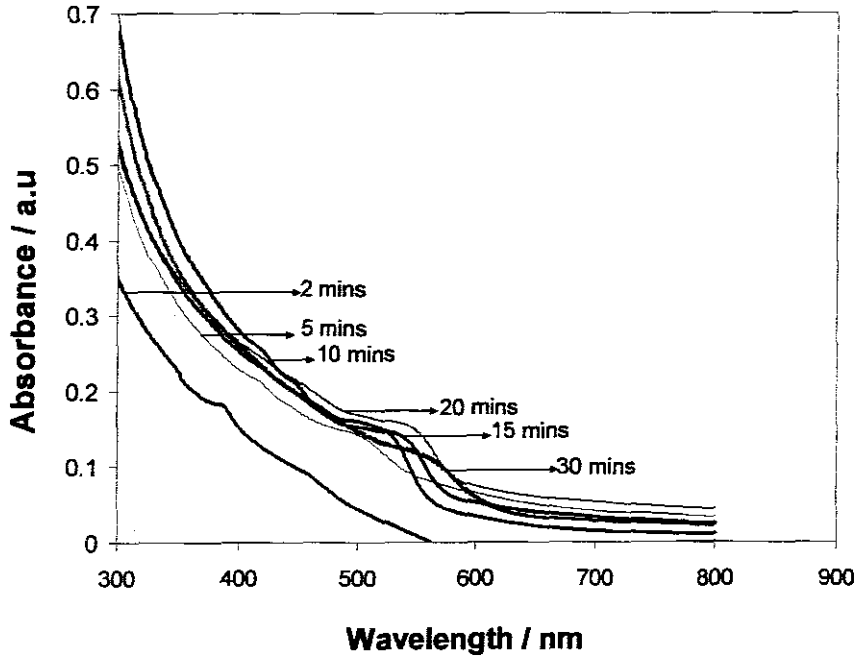


***Figure 2.7*** *Absorption spectra of HDA-capped CdSe under reduction time of 4 hrs for the growth time of 2, 5, 10, 15, 20 and 30 mins using 0.32 mmol concentrations*

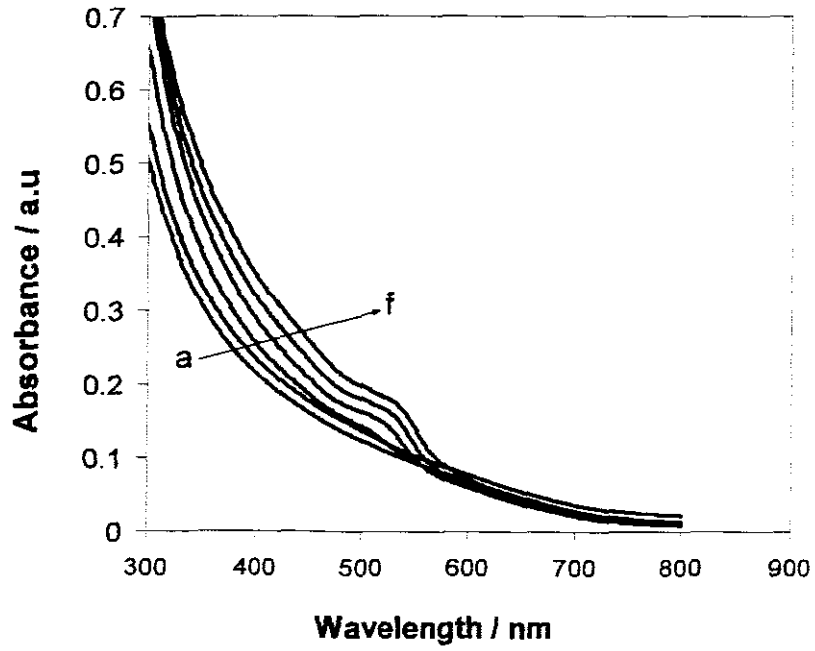


***Figure 2.8*** *Absorption spectra of HDA-capped CdSe under reduction time of 6 hrs for the growth time of (a) 2, (b) 5, (c) 10, (d) 15, (e) 20 and (f) 30 mins using 0.32 mmol concentrations.*

As the reduction time decreases, the synthesised nanoparticles exhibit sharper fine structures in their absorption spectra, indicative of a possible decrease in the size distribution. The reduction time of 2 hrs gives nanoparticles with the narrowest size distribution. These could be attributed to the fact that nucleation is very fast and well-separated from particle growth during thermolysis for particles synthesised under 2 hrs reduction time. The FWHM increases by 10 nm for a reaction period of 2 to 30 mins (28 - 38 nm).

All the emission spectra for 2 and 4 hrs reduction time, (2 to 30 mins) (Figures 2.9 and 2.10) and, between 5 and 30 mins growth period under 6 hrs reduction time (Figure 2.11), show narrow line widths and sharp luminescence, indicating the growth of the crystallites with few electronic defect sites, attributed to the efficiency of the capping group in electronically passivating the surface states or defects located in the band gap of the nanocrystals which act as trapping states for photogenerated charges.

The PL spectra exhibit only strong band-edge luminescence with the exception of the PL spectra of the smallest size samples (2 and 5 mins growth time for 2 and 4 hrs and, 5 and 10 mins for 6 hrs reduction times), which also shows a broad tail towards lower energy. This spectral anomaly is attributed to a trap state. This is also responsible for the asymmetric shape of the spectra during these reaction times. As the reaction time increases, this broad tail becomes reduced and finally disappears from the spectrum obtained after 10 mins and the shape of the spectra becomes symmetrical. This could be attributed to the fact that annealing and effective passivation of nanocrystal surface occurs as the reaction time increases.

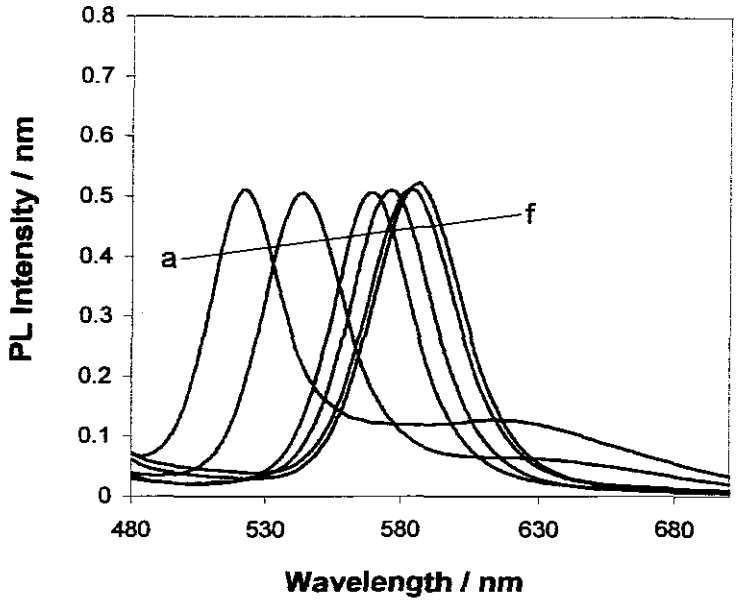


***Figure 2.9*** *Photoluminescence spectra ($\lambda_{400}$ nm) of HDA-capped CdSe under reduction time of 2 hrs for the growth time of (a) 2, (b) 5, (c) 10, (d) 15, (e) 20 and (f) 30 mins using 0.32 mmol concentrations.*

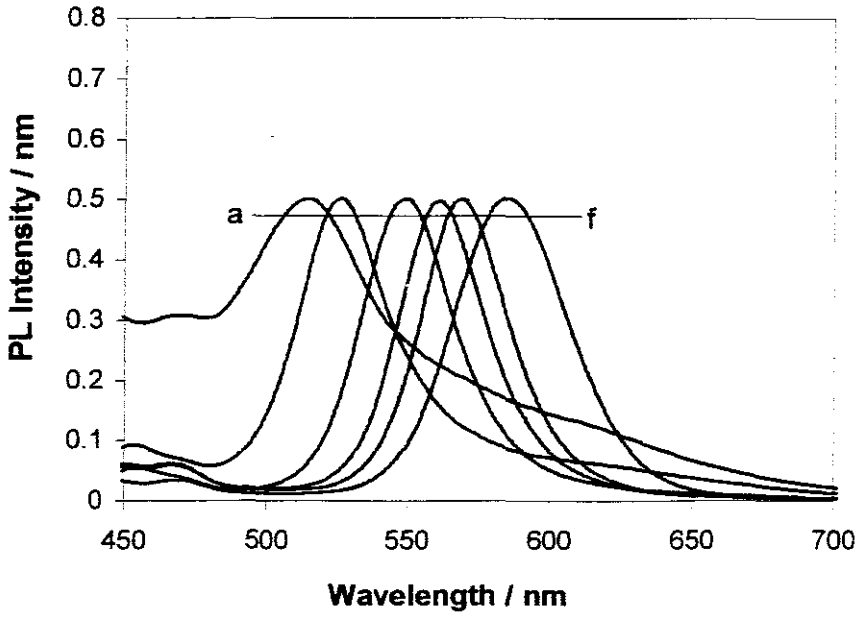


***Figure 2.10*** *Photoluminescence spectra ($\lambda_{400}$ nm) of HDA-capped CdSe under reduction time of 4 hrs For the growth time of (a) 2, (b) 5, (c) 10, (d) 15, (e) 20 and (f) 30 mins using 0.32 mmol concentrations.*

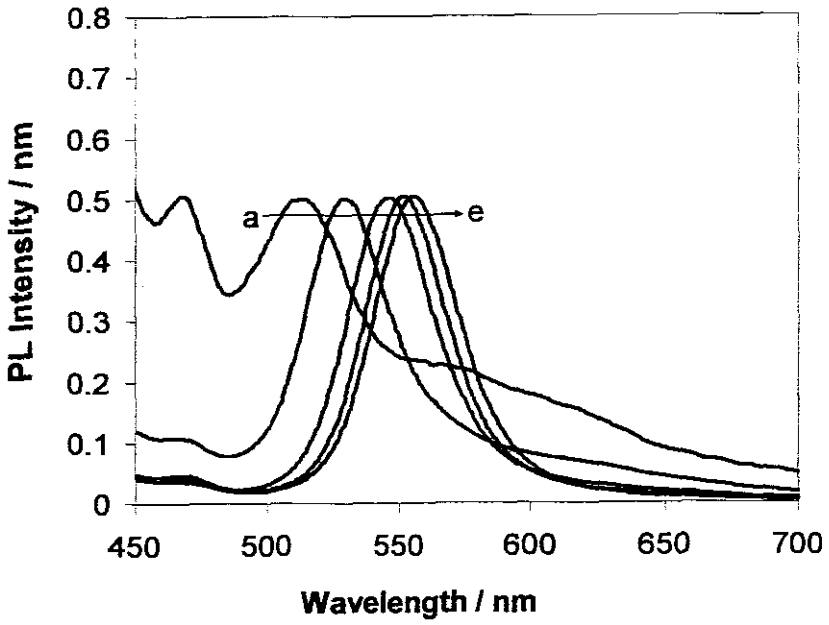


***Figure 2.11*** *Photoluminescence spectra ($\lambda_{400}$ nm) of HDA-capped CdSe under reduction time of 6 hrs For the growth time of (a) 5, (b) 10, (c) 15, (d) 20 and (e) 30 mins using 0.32 mmol concentrations.*

The obvious tail towards higher energy is attributed to the formation of small nanocrystals with poor surface quality.[5,28] These become less-pronounced as the reaction time increases.

#### 2.3.1.2.2 *TOPO-capped CdSe Nanoparticles*

The absorption and photoluminescence spectra, shown in Figures 2.12 and 2.13, indicates that the emission and absorption maxima of TOPO-capped CdSe at different hours of reduction is also blue-shifted from the bulk sample, signifying quantum confinement effects. The absorption band-edges as calculated using the direct band gap method[22] are 2.10 eV (591 nm), 2.06 eV (601 nm), and 2.11 eV (589 nm) for 2, 4 and 6 hrs reduction time respectively, all blue-shifted in relation to bulk CdSe, 1.73

eV (716nm). The shift of absorption and emission maxima to lower band gap energy (higher wavelength) increases as the reduction time increases from 2 to 4 hrs, indicating increase in particle size as the reduction time increases. This is in line with the prediction from the colour of the solution after the addition of $CdCl_2$. The absorption and emission maxima for the 6 hrs reduction time are shifted to lower wavelengths. This confirmed our inference that, larger nanoparticles synthesized after the addition of $CdCl_2$ solution was broken down into smaller nuclei (during the thermolysis), immediately after injection. This kind of shift to lower wavelength in contrast to the prediction from the colour of the solution after the addition of $CdCl_2$, further supports the significant influence of temperature, growth time and passivating agent on the particle size of the synthesized nanoparticles during thermolysis. The diameters of the samples estimated from the excitonic peaks are as follows : 2 hrs (3.08 nm), 4 hrs (3.28 nm) and 6 hrs (2.98 nm). All the PL spectra exhibit only strong band-edge luminescence for excitation at 400 nm, without any broad tailing towards lower energy. The spectra shows narrow emission line widths, indicating a monodispersed sample and growth of the crystallites with few electronic defects. This is in correlation with the absorption spectra which shows sharp absorption edges and narrow widths of the exciton absorption.

The PL intensities are about six-fold lower than those of HDA. This low intensity was discussed earlier and was attributed to low capping density of TOPO and incomplete removal of the entire surface trapping states.

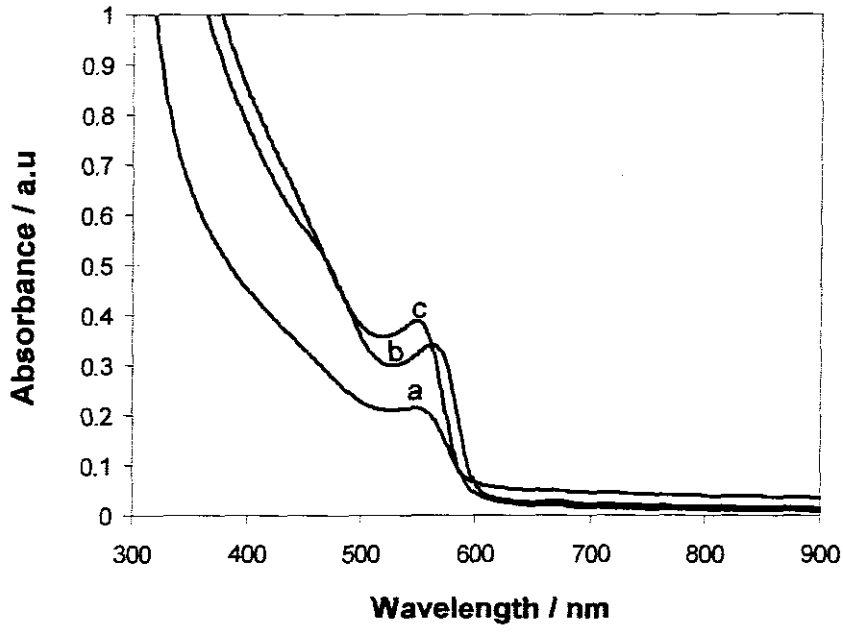


***Figure 2.12*** *Absorption spectra of TOPO-capped CdSe under reduction time of (a) 2, (b) 4, and (c) 6 hrs for the growth time of 30 mins using 0.32 mmol concentrations.*

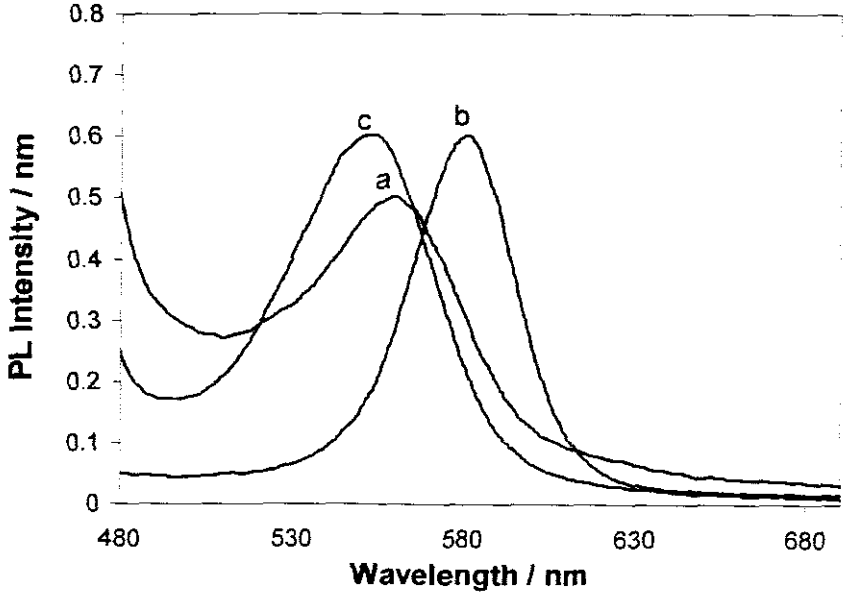


***Figure 2.13*** *Photoluminescence spectra ($\lambda_{400}$ nm) of TOPO-capped CdSe under reduction time of (a) 2, (b) 4 and (c) 6 hrs for the growth time of 30 mins using 0.32 mmol concentrations.*

### 2.3.1.3 *Effect of Monomer Concentration*

Control of the particle size corresponding to the tunable absorption onset and emission wavelength, can also be achieved by adjusting the monomer concentration. Increasing the initial monomer concentration may lead to a significant change in size, shape and emission properties of the nanoparticles as it changes from dot-shape to elongated nanocrystals. It has been demonstrated, both experimentally and theoretically, that high precursor concentration is important in achieving fast size focusing and slow defocusing.[29-33] According to Peng *et al.*,[31-33] at any monomer concentration, there exits a critical size which is at equilibrium. Nanocrystals smaller than the critical size, have negative growth rates and dissolve while the larger ones grow at a rate dependent strongly on size. At higher monomer concentrations, the average size of the nanocrystals increases relatively rapidly and becomes larger than the critical size. This increases their growth rate and hence focusing of the size distribution occurs. As the monomer concentration becomes depleted due to growth, the critical size becomes larger than the average size of the nanocrystals present and, the distribution broadens because some smaller nanocrystals are shrinking and eventually disappear while larger ones are still growing. This leads to defocusing of the size distribution as a result of decrease in the growth rate of the nanoparticles. The distribution can be refocused by injection of additional monomer at the growth temperature, which shifts the critical size back to a smaller value. For this reaction, the initial concentration was changed from 0.32 mmol to 0.64 mmol and the effect of this on the optical properties was monitored, using the reduction time of 2, 4 and 6 hrs.

The absorption and emission spectra for the nanoparticles synthesized using 0.64 mmol, are shown in Figures 2.14 - 2.21. In general, increasing the monomer concentration leads to a faster growth rate at the early stage of the reaction (0 to 10 mins) and, a slower growth rate at the later stage of the reaction (10 to 30 mins). The nanocrystals synthesized at this concentration exhibit large red-shifts (absorption and emission maxima) in the early stage of the reaction when the growth rate is rapid, due to an increase in monomer concentration but less in the later stage, because of slower growth rate. In addition, there is an increase in the particle size of the nanoparticle synthesized with 0.64, mmol when compared with those produced using 0.32 mmol. The increase in size is confirmed by the shift of absorption band-edge and maxima emission peak to lower energies (higher wavelength). This increase in particle size is also confirmed by the increase in the intensity/brightness of the colour of the solution. The colour changes from deep yellow to wine-red after the addition of $CdCl_2$ as the reduction time increases from 2 to 6 hrs. Also, it is noted that the emission line width becomes narrower with higher concentration, implying narrower size distribution. Peng[31] and Wang *et al.*[29] have observed a similar phenomenon and this has been attributed to the fact that increase in the monomer concentration, promotes the growth rate of the nanocrystals and focusing of the size distribution.

The HDA-capped CdSe nanoparticles synthesized with 0.32 mmol (Figures 2.6 - 2.11), as well as those with 0.64 mmol (Figures 2.14 - 2.19) monomer concentration under the same reduction time, exhibit similar properties. Such similarities include a blue-shift in absorption and emission spectra in relation to bulk band gap, due to quantum confinement, the presence of sharp absorption edges and excitonic shoulders as the reduction time reduces and growth time increases, tailing band-edges for larger

sized nanoparticles, narrow emission line widths, strong band-edge luminescence and richer and sharper fine structures in the absorption spectra as the reduction time decreases. In addition, there is an increase in particle size and decrease in the emission line widths as the reduction time decreases.

The tailing band-edge observed in the absorption spectra throughout the growth time (0 to 30 mins) for 6 hrs reduction time and, 5 mins growth time for 4 hrs reduction time confirms that increasing the initial monomer concentration leads to an increase in particle size. Such a feature is also seen in absorption spectra for 6 hrs reduction time (0 to 15 mins) at lower monomer concentration (Figure 2.8). This has been attributed to weak confinement effects characteristic of polydispersed particles.

With the exception of the PL spectrum for 5 mins (4 hrs reduction time) which consists of band-edge emission and a broad tail which is attributed to a trap state (Figure 2.18), all other PL spectra for 2 and 4 hrs exhibit only strong band-edge luminescence. The presence of symmetrically-shaped emission curves in contrast to those synthesized at lower concentration, suggest that increasing the monomer concentration reduces surface traps and leads to focusing of the size distribution. The intensity of the second peak on the lower energy side of the spectra (Figures 2.17 and 2.18), is sharper and higher when compared with those synthesized at lower concentration (Figures 2.9 - 2.11). This might indicate the emergence of particles with two different morphologies, the less prominent one having a smaller particle size. The roughness of the PL spectra for nanoparticles synthesized under 6 hrs reduction times (0.64 mmol) Figure 2.19, is attributed to insufficient passivation and annealing due to larger sized particles.

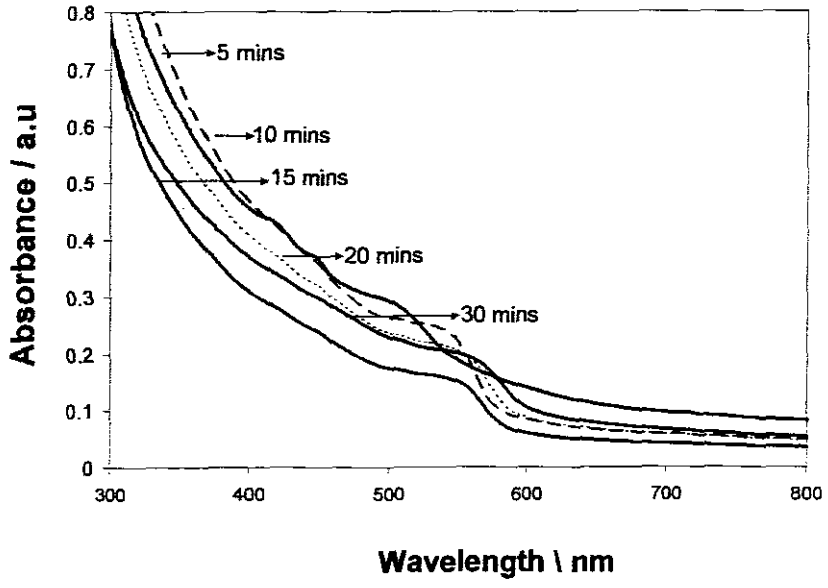


***Figure 2.14*** *Absorption spectra of HDA-capped CdSe under reduction time of 2 hrs for the growth time of 5, 10, 15, 20 and 30 mins using 0.64 mmol concentrations*

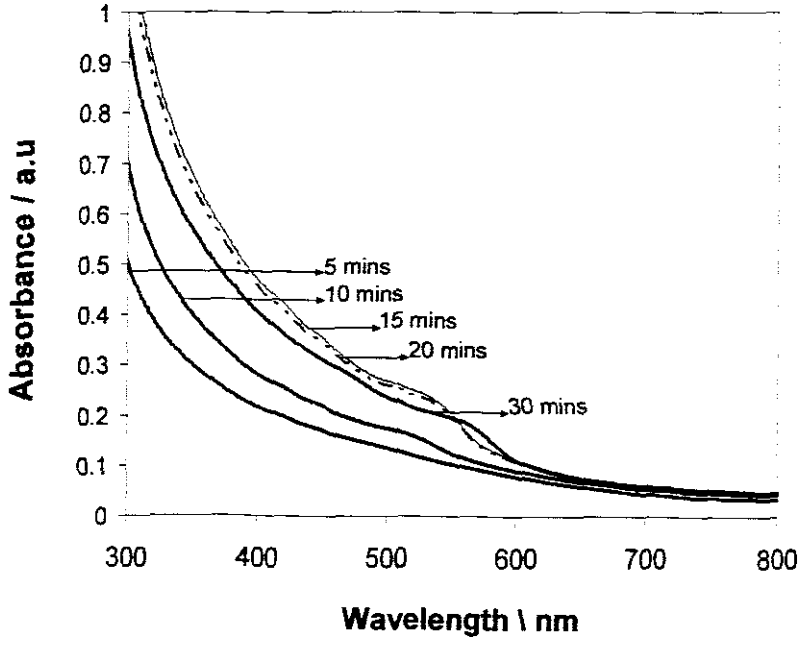


***Figure 2.15*** *Absorption spectra of HDA-capped CdSe under reduction time of 4 hrs for the growth time of 5, 10, 15, 20 and 30 mins using 0.64 mmol concentrations.*

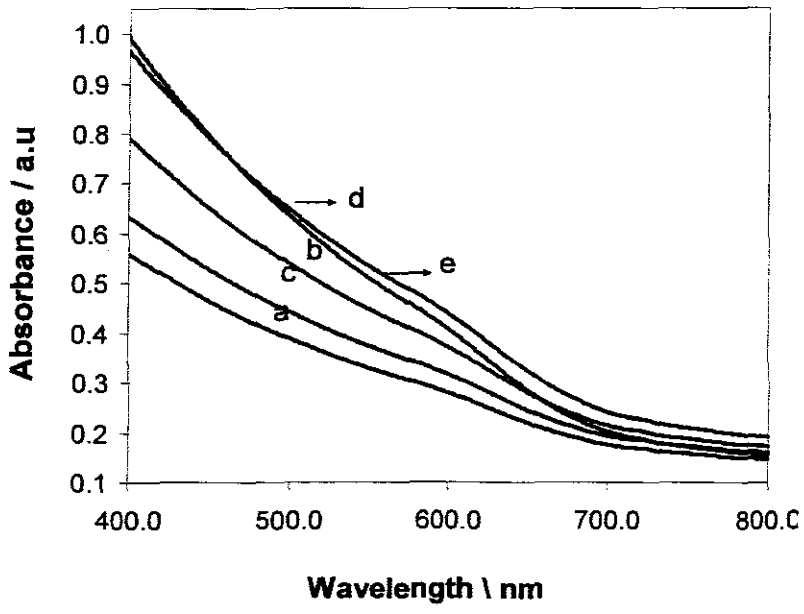


***Figure 2.16*** *Absorption spectra of HDA-capped CdSe under reduction time of 6 hrs for the growth time of (a) 5, (b) 10, (c) 15, (d) 20 and (e) 30 mins using 0.64 mmol concentrations.*

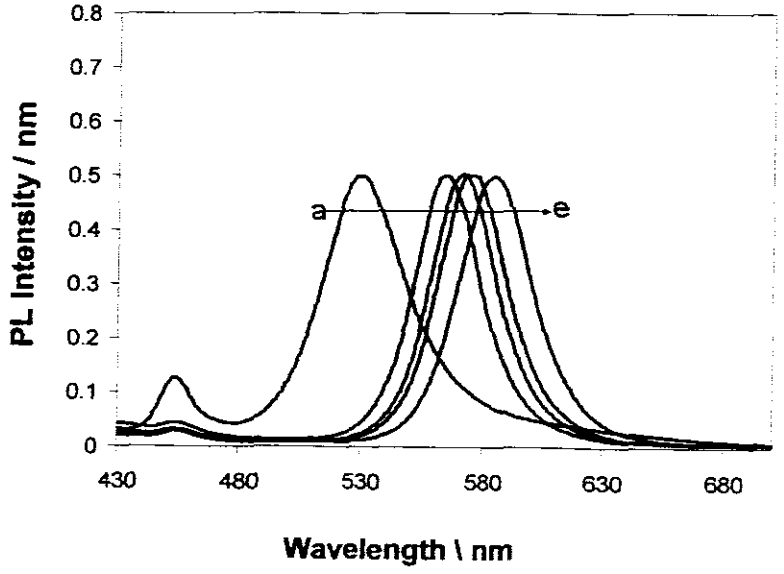


***Figure 2.17*** *Photoluminescence spectra ($\lambda_{400}$ nm) of HDA-capped CdSe under reduction time of 2 hrs for the growth time of (a) 5, (b) 10, (c) 15, (d) 20 and (e) 30 mins using 0.64 mmol concentrations.*

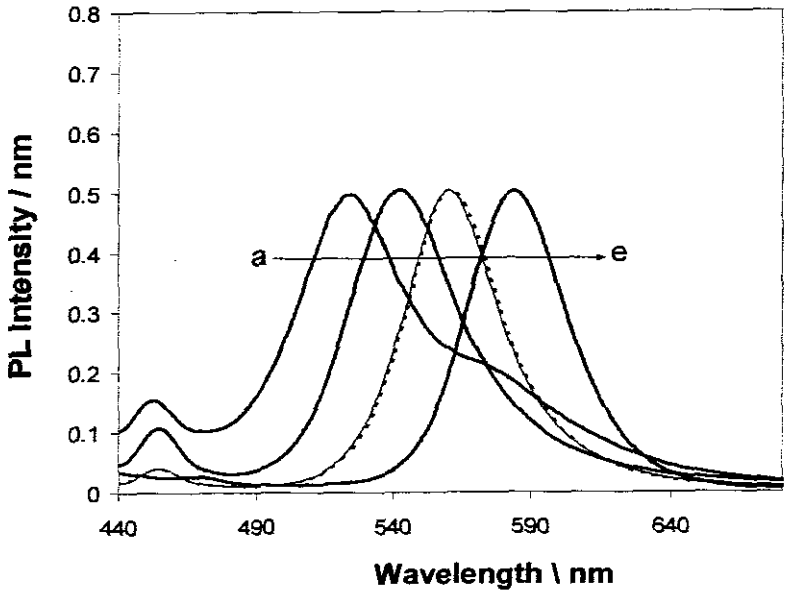


***Figure 2.18*** *Photoluminescence spectra ($\lambda_{400}$ nm) of HDA-capped CdSe under reduction time of 4 hrs for the growth time of (a) 5, (b) 10, (c) 15, (d) 20 and (e) 30 mins using 0.64 mmol concentrations.*

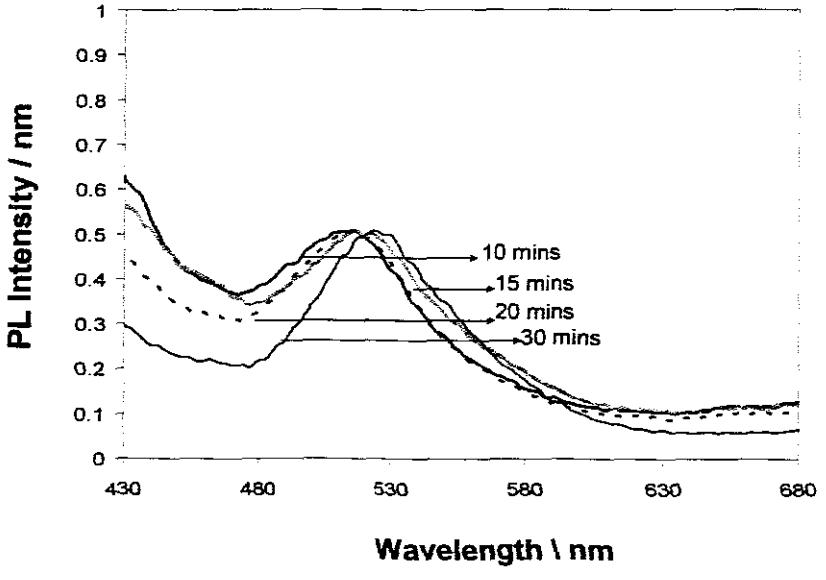


***Figure 2.19*** *Photoluminescence spectra ($\lambda_{400}$ nm) of HDA-capped CdSe under reduction time of 6 hrs for the growth time of 5, 10, 15, 20 and 30 mins using 0.64 mmol concentrations.*

TOPO-capped CdSe nanoparticles synthesized with 0.64 mmol (Figures 2.20 and 2.21) show optical properties similar to those produced at lower concentration under the same reduction time, with a few exceptions. The width of the exciton absorption is wider for those synthesized at higher concentration, indicating a larger size distribution. The emission spectra for all the reduction times exhibit only strong band-edge luminescence at higher monomer concentration, with symmetrically-shaped emission curves compared with those synthesized at lower concentration, confirming that increasing the monomer concentration reduces surface traps and leads to focusing of size distributions.

At higher concentration, the PL intensity of TOPO-capped CdSe is still lower than those synthesized at the same concentration with HDA as the passivating agent.

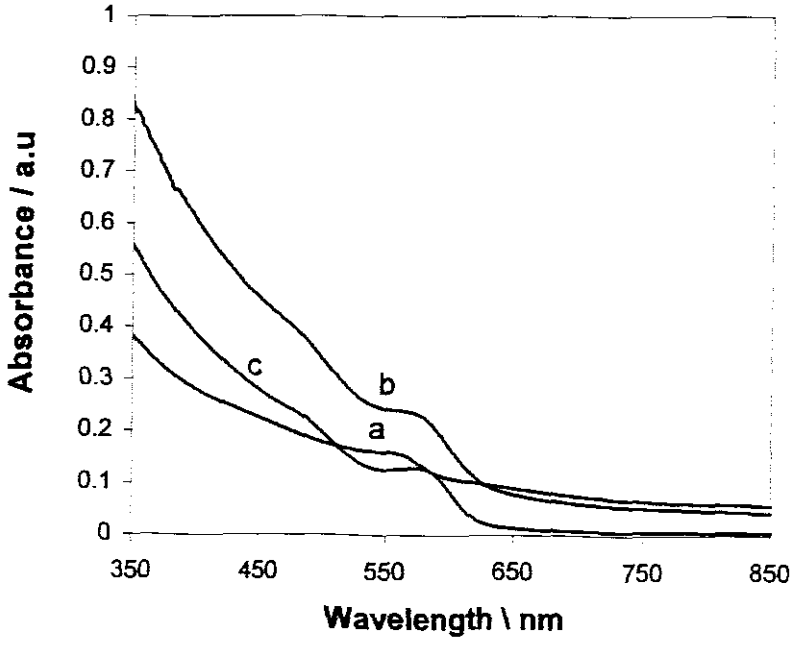


***Figure 2.20*** *Absorption spectra of TOPO-capped CdSe under reduction time of (a) 2, (b) 4 and (c) 6 hrs for the growth time of 30 mins using 0.64 mmol concentrations.*

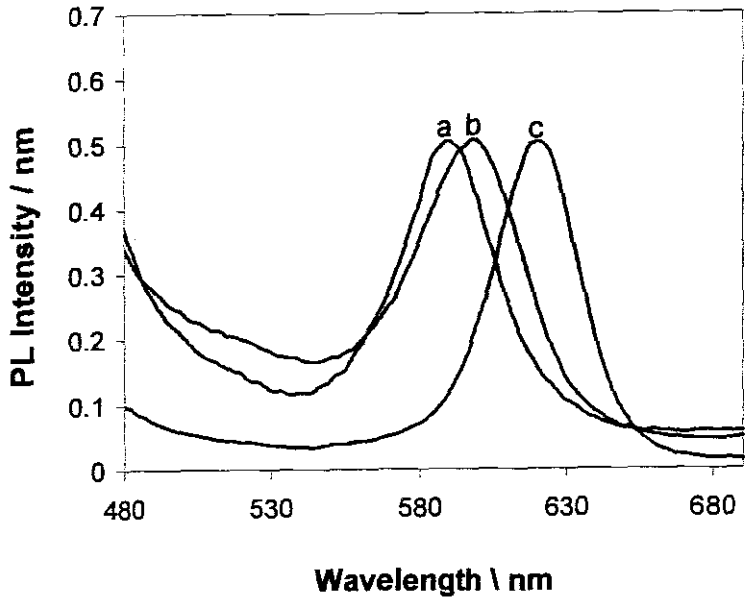


*Figure 2.21* *Photoluminescence spectra ($\lambda_{400}$ nm) of TOPO-capped CdSe under reduction time of (a) 2, (b) 4 and (c) 6 hrs for the growth time of 30 mins using 0.64 mmol concentrations.*

### 2.3.1.4 *Effect of Temperature*

Growth temperature has a major influence on the particle size, growth rate and luminescent properties. The initial period after the hot injection is usually characterized by rapid growth, which results in surface disorder and hence, low luminescence efficiency. Higher growth temperatures lead to faster growth rates and induce faster surface degradation. Therefore, the surface roughening and degradation compete with surface ordering. As the reaction time increases, the growth rates become slower and this reduces surface disorder and facilitates surface ordering and reconstruction during annealing, thus reducing the concentration of the defects.[6] Higher temperatures also favour the formation of larger particles and this has been attributed to the rate at which a ligand attaches and detaches from the surface.[34] A

higher rate of attaching and detaching at higher temperature results in a faster growth rate and thus, larger particles.

The absorption and emission spectra for the as-synthesized nanoparticles at temperatures of 110, 160 and 200 °C, are shown in Figures 2.22 - 2.29. The growth of the particles is confirmed by the shift of absorption and emission maxima to longer wavelengths as the temperature increases. The sharp absorption features are indicative of particles with narrow size distributions. The PL spectra also displayed sharp band-edge luminescence and weaker, broader luminescence peaks at lower temperatures. The relative intensities of the defect-associated luminescence, broad tail at lower energy side (higher wavelength) present in the PL spectra attributed to trap states, decrease with time at lower growth temperatures ($\geq$ 160 °C) and are completely absent at higher temperatures (> 160 °C), signifying effective passivation as the temperature increases.

In order to make the effect of the growth temperature more evident, the reactions were carried-out using the same monomer concentration (0.32 mmol) and reduction time (2 hrs). A substantial difference in the growth evolution was observed for the different growth temperatures. The FWHM of the emission peak will reflect the change in size distributions of the CdSe nanocrystals, thus it is a good indicator of size focusing and defocusing. The growth of the HDA-capped CdSe nanoparticles (Figures 2.22 - 2.27 ) evident by the shift of the absorption and emission maxima, is further supported by the colour of the solution which changes from yellow to orange and then to red after injection as the temperature increases from 110 to 160 °C and 200 °C respectively. This indicates an increase in particle size. The particle sizes

calculated from the first electronic absorption after 30 mins are 2.28 nm (110 °C), 2.98 nm (160 °C) and 4.58 nm (200 °C) with the particles emitting in the blue-red window.

At 110 °C (Figures 2.22 and 2.23.), the growth rate is very slow in the initial 10 mins of the reaction after injection, with the particles emitting in the blue region. As the reaction time increases, the growth rate accelerates at a faster rate and a regime of nanocrystal growth, accompanied with focusing of the size distribution, was observed with the particle emitting in the green region. This growth temperature gives the smallest particle size. The particle size ranges between 2.14 - 2.28 nm for the reaction time of 15 to 30 mins. Because of the lower reaction rate, the concentration of free monomer was high in the reaction mixture, forming nanoclusters in the early stages of the reaction, with a tailing band-edge as shown in Figure 2.22 (2 and 5 mins). As the reaction time increases, surface ordering occurs, resulting in nanoparticles with sharper sub-structures (15 to 30 min). Nanocrystals with sizes below ~ 2 nm usually have properties different from larger ones i.e., weak band-edge PL, deep trap emission and "magic" particle size.[34] So the distribution of PL efficiencies, immediately after the start of the reaction (2 to 5 mins) was complicated, due to the small size of the nanocrystals at early reaction stages.

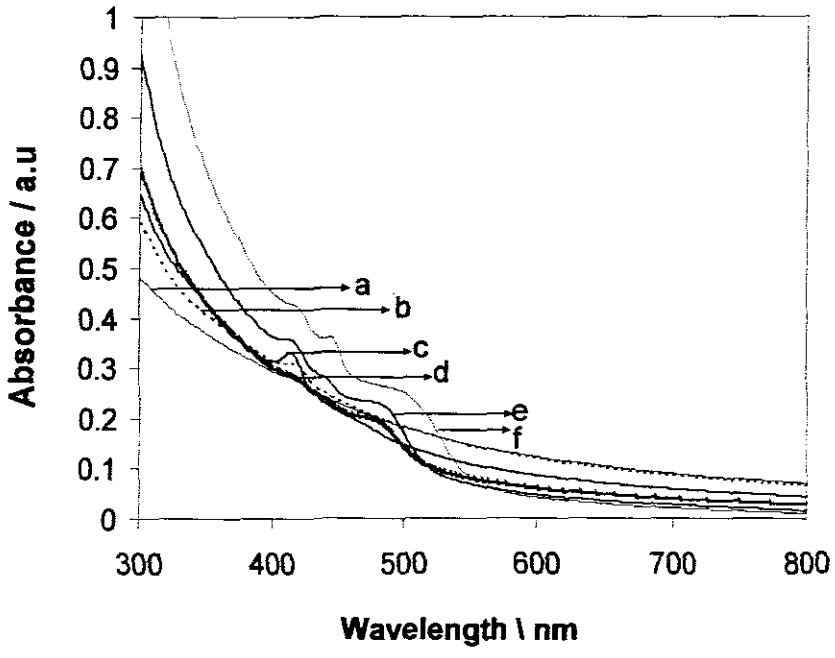


***Figure 2.22*** *Absorption spectra of HDA-capped CdSe at 110 °C for the reaction time of (a) 2, (b) 5, (c) 10, (d) 15, (e) 20 and (f) 30 mins*

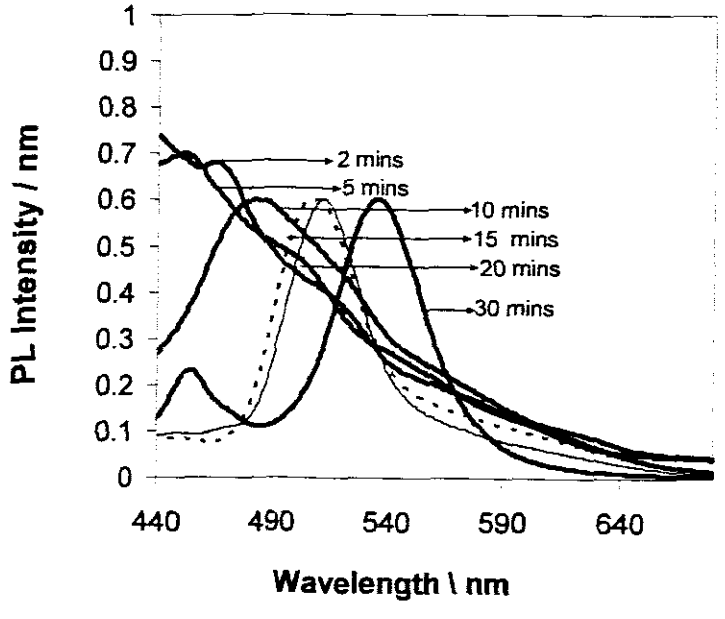


***Figure 2.23*** *Photoluminescence spectra ($\lambda_{400}$ nm) of HDA-capped CdSe at 110 °C for the reaction time of (a) 2, (b) 5, (c) 10, (d) 15, (e) 20 and (f) 30 mins.*

At 160 °C (Figures 2.24 and 2.25.), the growth rate is faster than at 110 °C. Growth rate and focusing increase rapidly in the initial 5 mins of the reaction after which, the focusing stops, stabilizing in a narrower size distribution than that achieved at 110 °C. After 10 mins, both the growth rate and size focusing accelerate although at a slower rate than the initial period. This temperature gives the narrowest size distribution between 0 to 30 mins reaction time, with the difference in FWHM being 10 nm. The particle size of the species ranges between 2.23 - 2.98 nm for the reaction time of 2 to 30 mins, with the particle emitting in the green-orange region.

The growth rate at 200 °C is the fastest (Figures 2.26 and 2.27.). At the beginning of the reaction, the growth rate and size focusing accelerate rapidly and after 10 mins, the focusing becomes stabilized while the growth proceeds at a slower rate. After 15 mins the growth rate and size focusing accelerate slowly and increase rapidly after 20 mins, leading to broad emission and size defocusing. The particle size at this temperature is the largest, with sizes ranging between 2.59 nm - 4.58 nm for the reaction time of 2 to 30 mins and, the particle emitting in the green-red region.

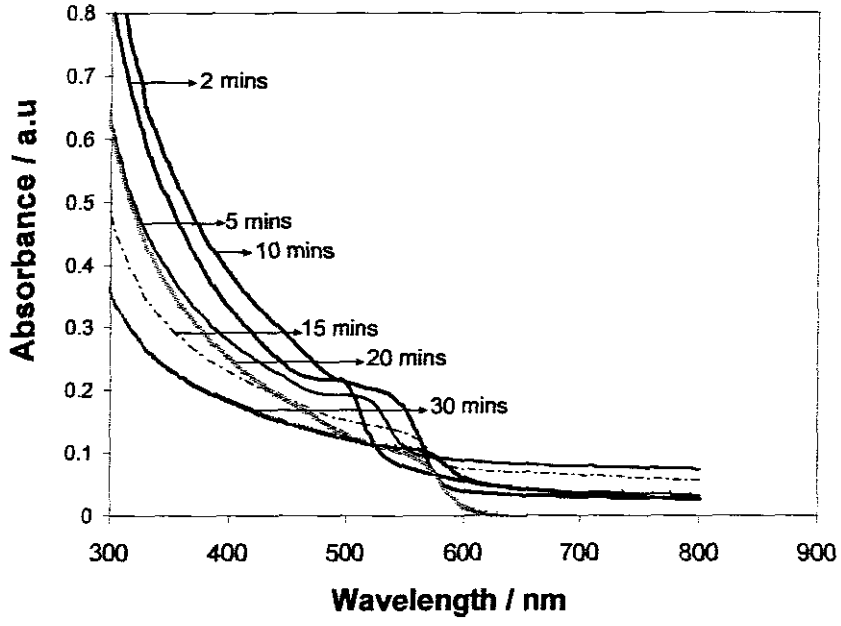


***Figure 2.24*** *Absorption spectra of HDA-capped CdSe at 160 °C for the reaction time of 2, 5, 10, 15, 20 and 30 mins.*

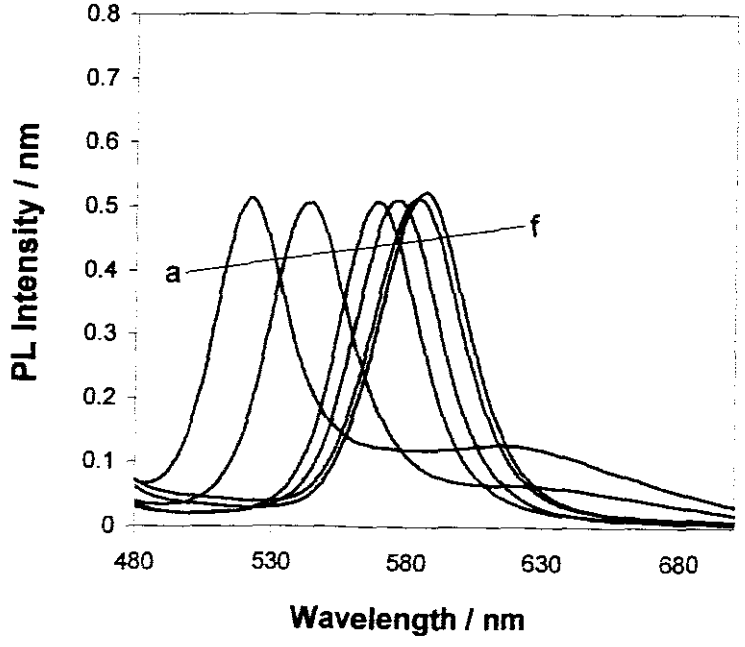


***Figure 2.25*** *Photoluminescence spectra ($\lambda_{400}$ nm) of HDA-capped CdSe at 160 °C for the reaction time of 2, 5, 10, 15, 20 and 30 mins*

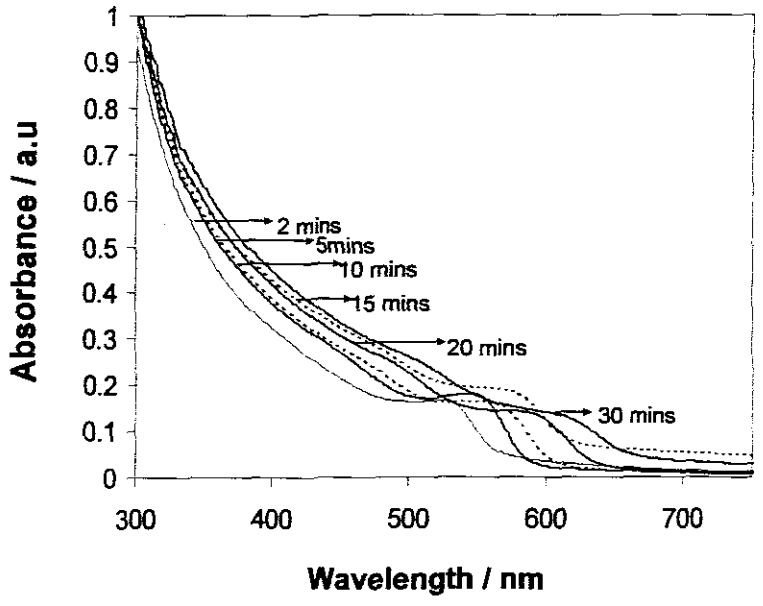


***Figure 2.26*** *Absorption spectra of HDA-capped CdSe at 200 °C for the reaction time of 2, 5, 10, 15, 20 and 30 mins*

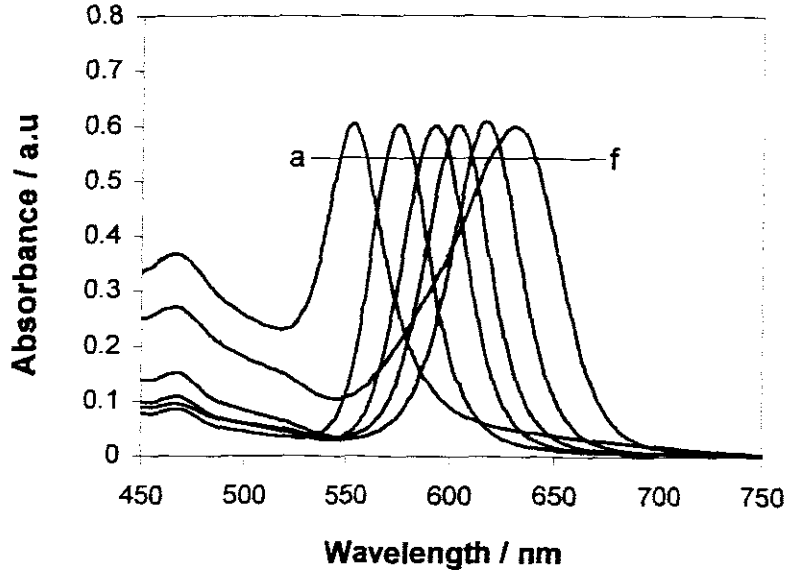


***Figure 2.27*** *Photoluminescence spectra ($\lambda_{400}$ nm) of HDA-capped CdSe at 200 °C for the reaction time of 2, 5, 10, 15, 20 and 30 mins.*

TOPO-capped CdSe nanoparticles (Figures 2.28 and 2.29) show the same trend as HDA-capped nanoparticles. The increase in particle size is confirmed by the shift of the absorption and emission maxima to higher wavelengths as the temperature increases from 170 to 250 °C. This is further supported by the change in the colour of the solution from light orange to red as the temperature increases. The sharpness of the band-edge luminescence and absorption features increase with increasing temperature. The size distribution becomes narrower as the temperature increases with particles emitting in the green-orange region. The sizes of the particle after 30 mins are 2.50 nm (170 °C), 3.08 nm (230 °C) and 3.68 nm (250 °C)

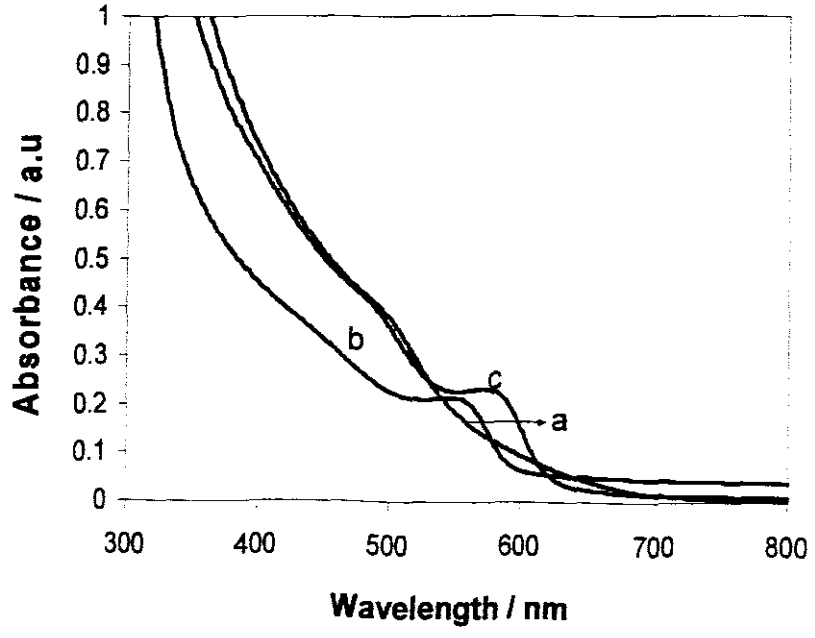


***Figure 2.28*** *Absorption spectra of TOPO-capped CdSe at 170 °C, 230 °C and 250 °C for the reaction time of 30 mins*

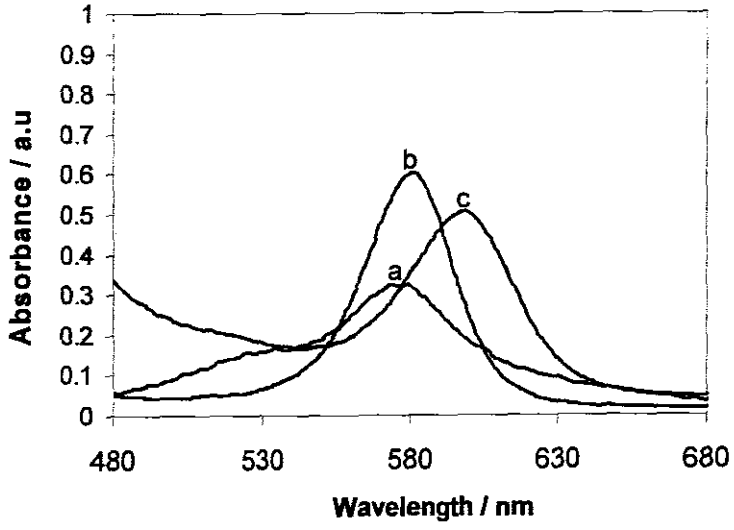


***Figure 2.29*** *Photoluminescence spectra ($\lambda_{400}$ nm) of TOPO-capped CdSe at 170 °C, 230 °C and 250 °C for the reaction time of 30 mins.*

### 2.3.1.5 *Growth Kinetics*

It is acknowledged that the temporal evolution of band gap absorption and emission is indicative of the growth kinetic of the nanocrystals; red-shifts indicate size growth, while the PL FWHM indicates change in size distribution. A large value of the FWHM usually suggests an increase in size distribution. The growth kinetics of the samples synthesized, was studied using 0.32 mmol monomer concentration, at 160 °C under a reduction time of two hours, with HDA as the capping agent.

The growth kinetics of nanocrystals grown by this new approach possesses a similar pattern to that of the highest quality CdSe nanocrystals formed by organometallic approaches.[31] The trends for the red-shifts of the absorption maxima and emission maxima in relation to the reaction time are shown in Figure 2.30. It is much easier to determine the peak position of the maximum band gap emission than that of

absorption (Figures 2.24 and 2.25), especially for the nanocrystals sampled at the late stage of growth. Thus, the shift of the emission peak should be more illustrative in the study of the size-growth kinetics than the absorption data. A study of the plot of the emission maxima and particle size as a function of reaction time (Figures 2.30 and 2.31), shows two distinct regions of growth: an early stage (2 to 10 min.) corresponding to a large red-shift in the emission peak, characterized by fast growth in size and at a later stage (after 10 minutes), corresponding to a slight red-shift in the emission peak characterized by slow growth in size. In comparison to the as-prepared CdSe nanoparticles reported previously, the CdSe particles synthesised by our approach exhibited a 20 nm red-shift of the emission peak in the 0 to 5 mins growth period, while a 60 nm red-shift of emission is observed in the 0 to 5 mins growth period for the non-organometallic approach reported previously.[4] Such a slower particle growth in size (especially in the late stage of our reaction) could be due to the decrease in surface roughness and defects, thereby leading to higher photoluminescence.[6]

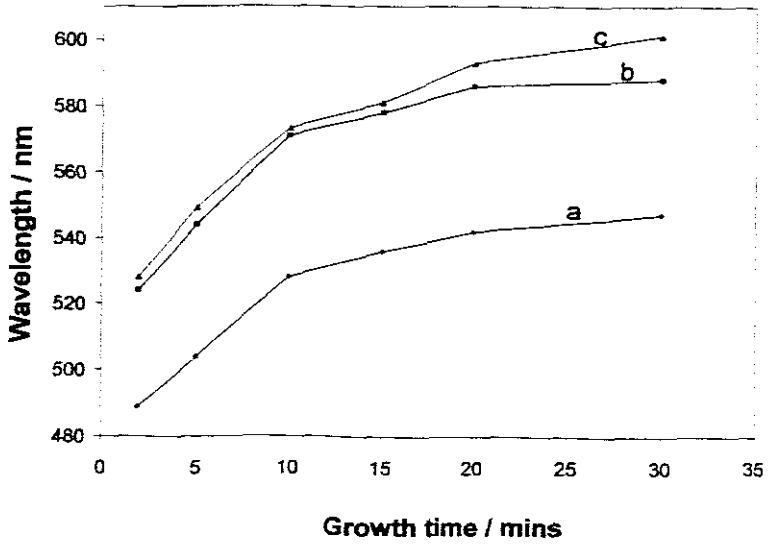


***Figure 2. 30*** *(a) excitonic peak (b) emission peak (c) absorption edge wavelengths of the HDA-capped CdSe nanoparticles at 160 °C as a function of time.*

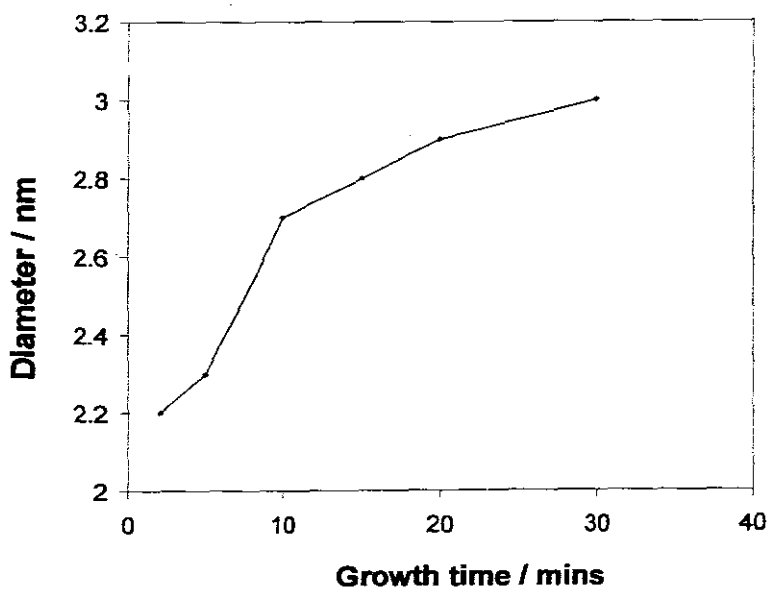


***Figure 2.31*** *Diameters of the HDA-capped CdSe at 160 °C as a function of time calculated using Yu's calibration data equation*[24]

A plot of the PL FWHM as a function of time (Figure 2.32) shows a trend of an increase in PL FWHM from 28 nm (2 min.) to 38 nm (30 min.). There is a rapid increase of the FWHM in the 2 to 5 min. growth period of the order of 5 nm with no increase in the 5 to 10 mins, indicating a zero growth rate (ZGR) period for size distribution. After 10 mins there is a gradual increase in the FWHM. The pattern of the temporal evolution of the PL FWHM further supports the two evident growth stages: an early stage (2 to 5 min.) and a later stage (after 15 min.), with a ZGR period between 5 and 10 min. This behaviour of growth kinetics had been observed and explained by Peng *et al.*, who attributed it to different particle growth modes.[31] In this case, there exists the presence of a large excess of monomer concentration after nucleation. Focusing of size distribution occurs because small nanocrystals present in the solution, are slightly larger than the critical size and grow faster than the larger ones. This accounts for the fast growth within the first 10 mins (Figures

2.31 and 2.32), of the reaction. The brief period of stability observed in the FWHM during the 5 to 10 mins growth period, is attributed to the presence of nanocrystals with a similar size distribution. As the reaction time increases, the monomer concentration is reduced and the critical size becomes larger than the average size present. Under these conditions, the smaller nanocrystals start shrinking and eventually disappear, providing the monomers for building the larger ones in the distribution which grow even bigger with the disappearance of the relatively smaller ones in the solution. At this point, the FWHM of the emission spectra begins to broaden after a period of stability (Figure. 2.32). The broadening indicates the onset of conventional Ostwald ripening, which causes a slow "defocusing" of the size distribution and accounts for the slow growth, increase in the FWHM and large particle size, for the remaining reaction time after 10 mins. This broadening at the later stage is more prominent in the sample synthesis, at 200 °C (Figure 2.27).

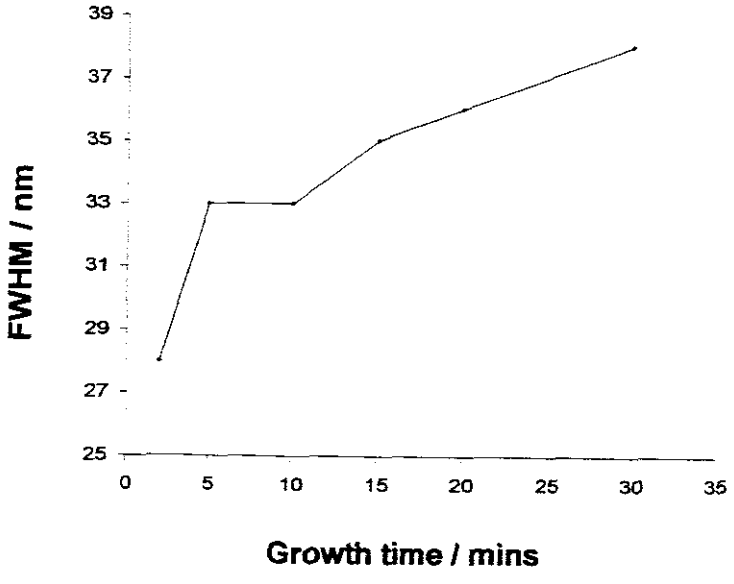


***Figure.2.32*** *FHWM of the HDA-capped CdSe at 160 °C as a function of time.*

In order to know which species are responsible for the emission, and to check for the purity of our sample, the photoluminescence spectra of the nanoparticles were measured at different excitation wavelengths from 350 to 480 nm (Figure 2.33). It is clear that while the florescence intensity changes with excitation wavelength, the fluorescence peak position remained unchanged. This indicates that the fluorescence involves the same initial and final state even though the excitation wavelength was varied between 350 and 450 nm, suggesting fast relaxation from the final state reached by photoexcitation to the state from which the fluorescence originates.[35] This lack of wavelength dependence of the fluorescence peak implies that the origin of the emitting state is similar in all species. In other words the samples do not contain any impurities such as, unreactive cadmium or selenium. [36] This observation was also reported by Banin *et al.* [37] and Wageh *et al.*[38] and been attributed as strong evidence for the purity of the samples. The same result was obtained for the TOPO-capped CdSe (Figure 2.34)

These type of measurements also shows that the as-synthesised samples have wider excitation spectra. This, together with the narrow emission bandwidth, indicates that the synthesised nanoparticles could be used as fluorescent biological probes, which can serve as an alternative to organic dyes usually characterised by wider emission bandwidth and narrow excitation, which limit its application. In addition, the synthesised nanoparticles emit green colour under the UV light suggesting that the nanoparticles produced, could be used in diagnosing through coupling to therapeutics agents (Figure 2.35).

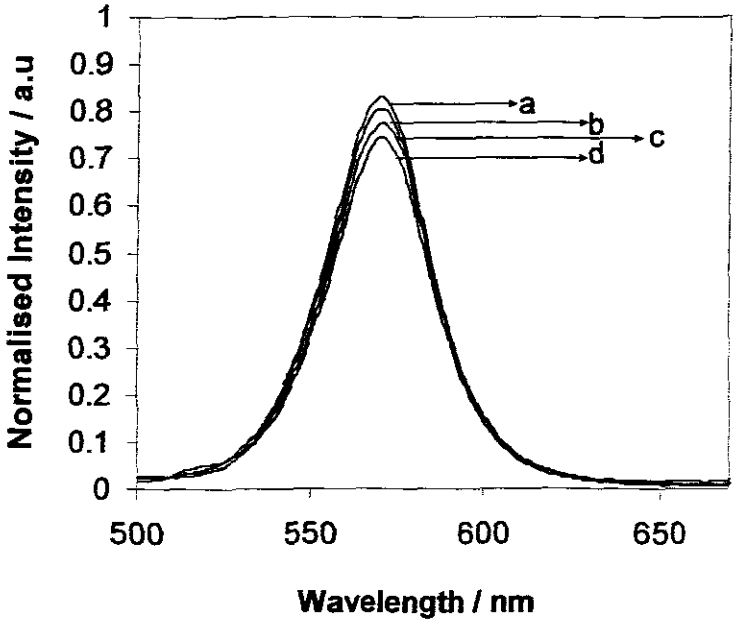


***Figure 2.33*** *Photoluminescence spectra of HDA-capped CdSe at different excitation wavelengths of (a) 350 nm, (b) 400 nm, (c) 450 nm and (d) 480 nm.*

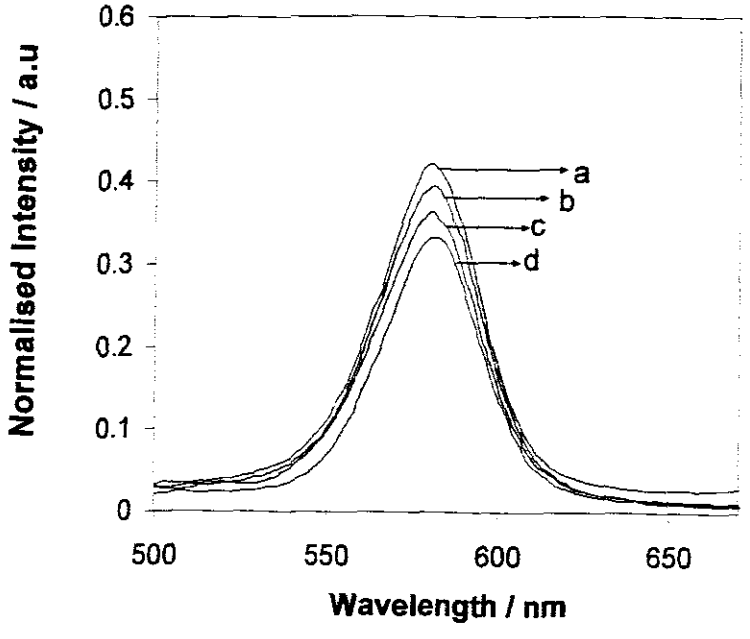


***Figure 2.34*** *Photoluminescence spectra of TOPO-capped CdSe at different excitation wavelengths of (a) 350 nm, (b) 400 nm, (c) 450 nm and (d) 480 nm.*

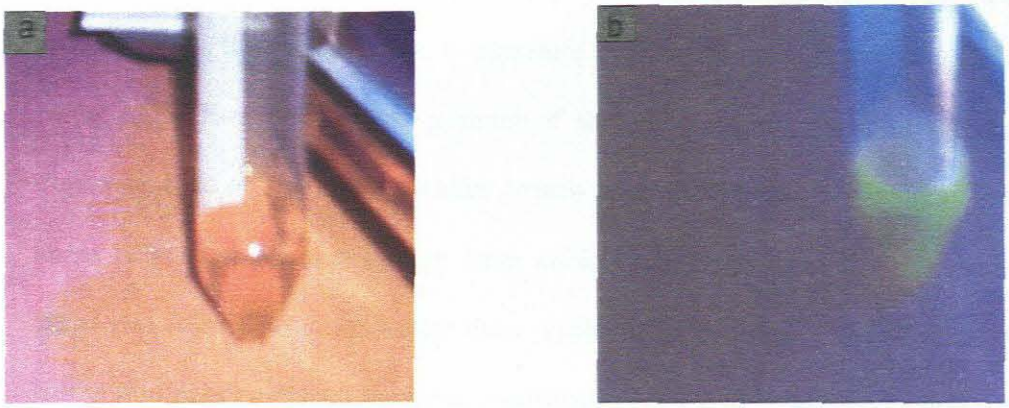

***Figure 2.35*** *HDA-capped CdSe at 160 °C after 30 mins under (a) fluorescent light and (b) UV light*

The peak position, intensity and the PL FWHM did not show any detectable change upon aging in air after one year, confirming the stability of our sample and effective passivation of the surface trapping state by the capping ligand. This is in contrast to the previous report that prolonged storage results in more rapid degradation in the PL intensity of nanoparticles, when HDA is used as capping agent.[14] This shows that there is optimal surface structure/reconstruction of the nanocrystals, grown under this synthetic route which minimizes the effect of the atomic configuration of the surface of the nanocrystals which would have a significant effect on the efficiency of the electronic passivation provided by the capping ligand.[4]

### 2.3.2 Structural Characteristics

#### 2.3.2.1 *Powder X-ray Diffraction*

The crystallinity of the particles was probed by X-ray diffraction (XRD). CdSe particles can exist as either the cubic or hexagonal phase. The existence of a mixture of cubic and hexagonal phase with the predominance of one over the other, is a possibility as reported by Bawendi *et al.*[17] The XRD pattern of the as-synthesised

nanoparticles ranges from cubic to hexagonal phases depending on the capping group, concentration, time of reduction, temperature and growth time. Figure 2.36 shows the wide angle X-ray diffraction patterns of the HDA-capped CdSe nanocrystals at reduction time of 2, 4 and 6 hrs after growth time of 30 mins. The results show that there is gradual phase transition from cubic to hexagonal, as the reduction time decreases from 6 to 2 hrs under these synthetic conditions. The position of the diffraction peaks matched the cubic modification of CdSe (zinc blende phase) better than the hexagonal for 6 hrs reduction time, while the hexagonal phase dominated the diffraction pattern obtained from 2 hrs reduction time. The XRD pattern of the prepared HDA-capped CdSe nanocrystals after reduction time of 6 hrs (Figure 2.36c), shows three diffraction peaks corresponding to the (111), (220) and (311) crystalline planes of cubic CdSe. The XRD patterns of the prepared HDA-capped CdSe nanocrystals after reduction time of 4 and 2 hrs (Figures 2.36 a & b), show four distinct diffraction peaks corresponding to the (002), (110), (103), and (112) crystalline planes of hexagonal CdSe. The stronger and narrower (002) peak in Figures 2.36a and b indicates that, the nanocrystals were elongated along the c-axis. The widths of diffraction peaks, broadened with increasing reduction time. This shows that the particle size decreases with increasing reduction time as expected from the absorption shift. For the larger particle sizes i.e., those produced at a reduction time of 2 and 4 hrs, a broad diffraction peak was observed at $2\theta = 45$ (103). This diffraction peak is characteristic of hexagonal wurtzite-type CdSe.[39] This diffraction was absent in the XRD pattern for the reduction time of 6 hrs, which showed the characteristic cubic zinc-blende type CdSe.[40] The disappearance of this peak for the reduction sample of 6 hrs, may be attributed to structural transformation from the wurtzite-type to the zinc-blende type upon decreasing crystal size. Omata *et al.*[41]

reported that, because the hexagonal wurtzite-type structure is strongly an anisotropic structure, the preservation of the wurtzite-type structure is difficult for small crystals hence, the structural transformation from the anisotropic wurtzite-type to isotropic cubic zinc-blende may occur if the crystal size is decreased. Due to the small particle size, the diffractograms of the as-synthesised particles at the early stage of growth, exhibit only very broad peaks from which a clear identification of the exclusive existence of either phase, is obviously difficult to assign with complete certainty (Figure 2.37). The SAD pattern (Figure 2.36a) consists of diffuse rings, which are indicative of the small size of the particles. The diffraction rings are indexed, with the (002), (110) and (103) planes confirming the wurtzite phase.

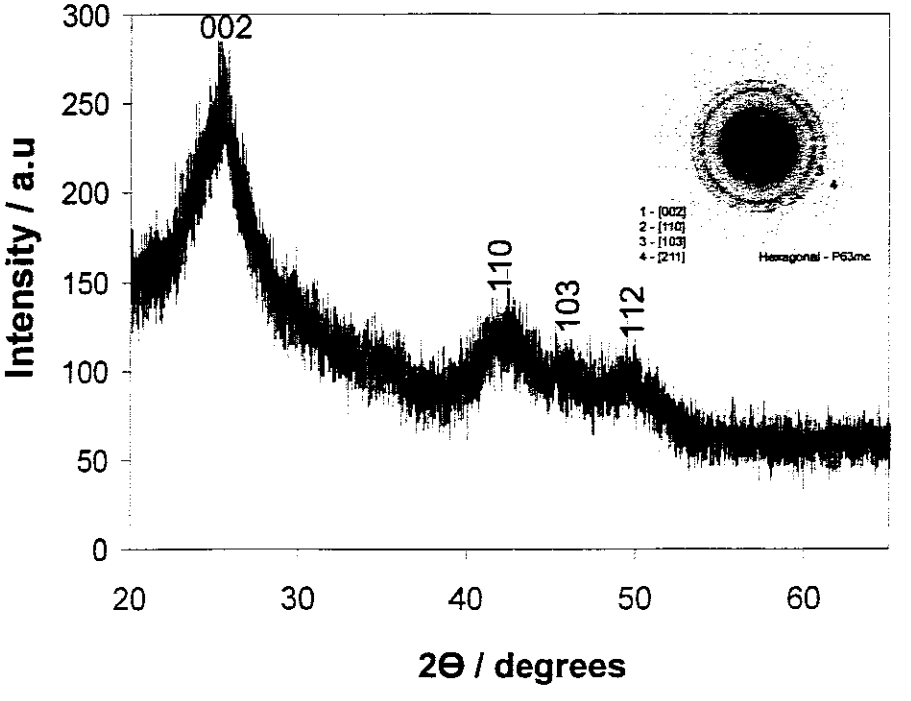


***Figure 2.36 (a)*** *XRD pattern and SAD (inlet) of HDA-capped CdSe under reduction time of 2 hrs using 0.32 mmol concentrations at 160 °C.*

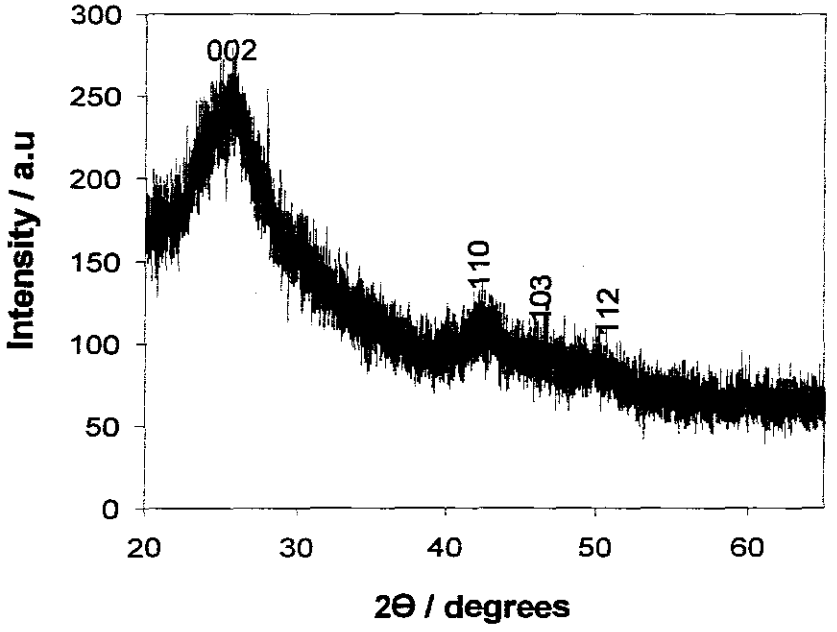


***Figure 2.36 (b)*** *XRD pattern of HDA-capped CdSe under reduction time of 4 hrs using 0.32 mmol concentrations at 160 °C.*

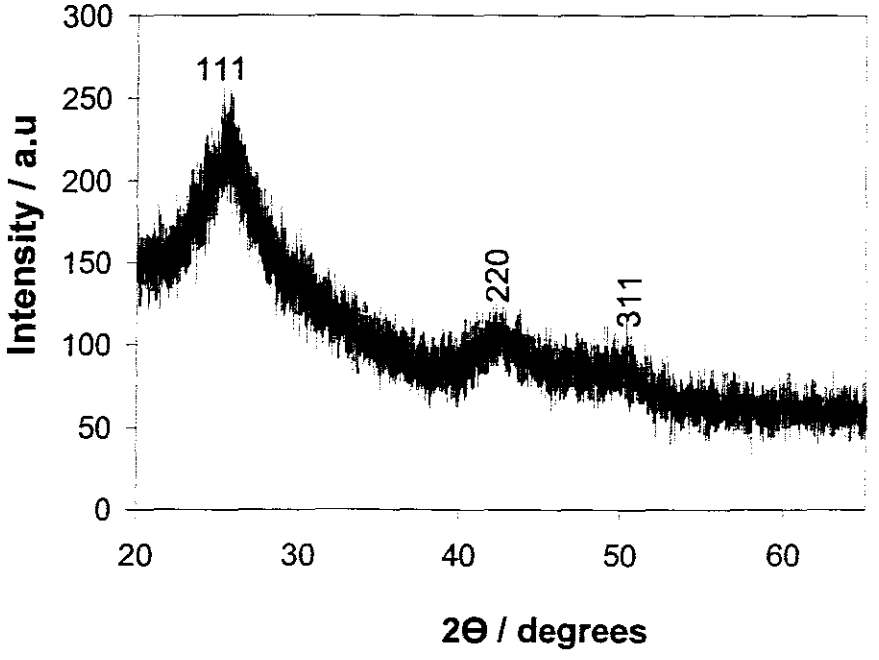


***Figure 2.36 (c)*** *XRD pattern of HDA-capped CdSe under reduction time of 6 hrs using 0.32 mmol concentration at 160 °C.*

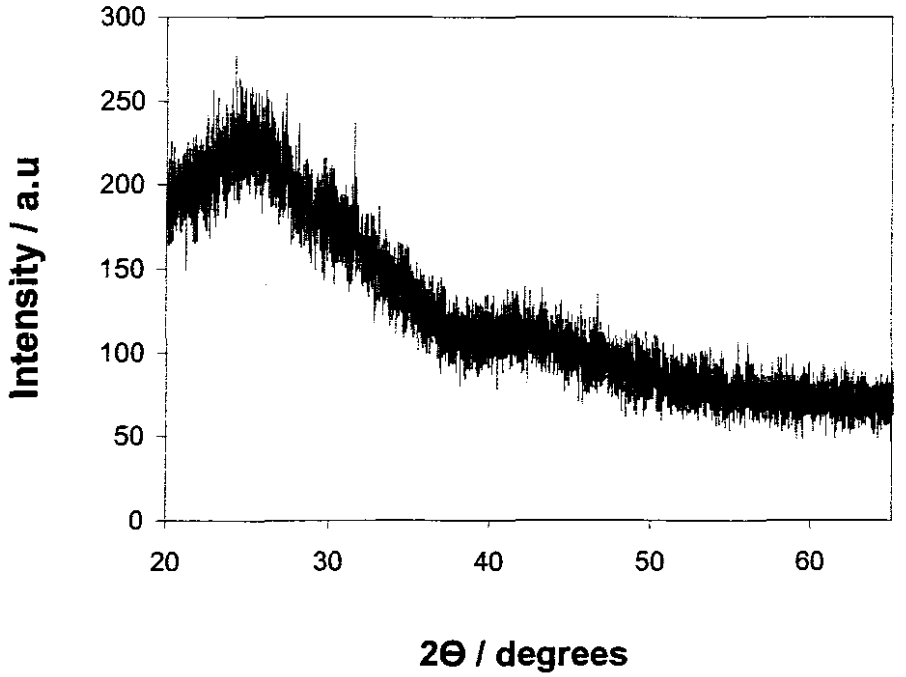


***Figure 2.37*** *XRD pattern of HDA-capped CdSe under reduction time of 2 hrs for the growth time of 5 mins using 0.32 mmol concentrations at 160 °C.*

Figure 2.38 shows the XRD pattern for the HDA-capped CdSe nanoparticles synthesised at different temperatures (110, 160 and 200 °C.) after 30 minutes growth time. The results also show a phase transition from cubic to hexagonal as the temperature increases from 110 to 200 °C. This might be attributed to the large particle sizes produced at higher temperature which is due to a faster growth rate that normally occurs at high temperatures. The results are in accordance with the previous report that, the thermodynamically-stable wurtzite phase is achieved at higher temperature, at which thermodynamics (rather than the reaction kinetics), governs the crystal growth.[17,42,43] The broad nature of the XRD peaks could be attributed to the nanocrystalline nature of the CdSe particles with the widths of diffractions becoming narrower with increasing temperature i.e., increasing particle size. The (110), (103) and (112) planes of wurtzite CdSe becomes more resolved as the temperature

increases. With increasing temperature, the intensity of the XRD peaks increased, which may indicate that the growth temperature has an important influence on the crystallinity of CdSe nanocrystals. This has also been observed by He *et al.*[34]

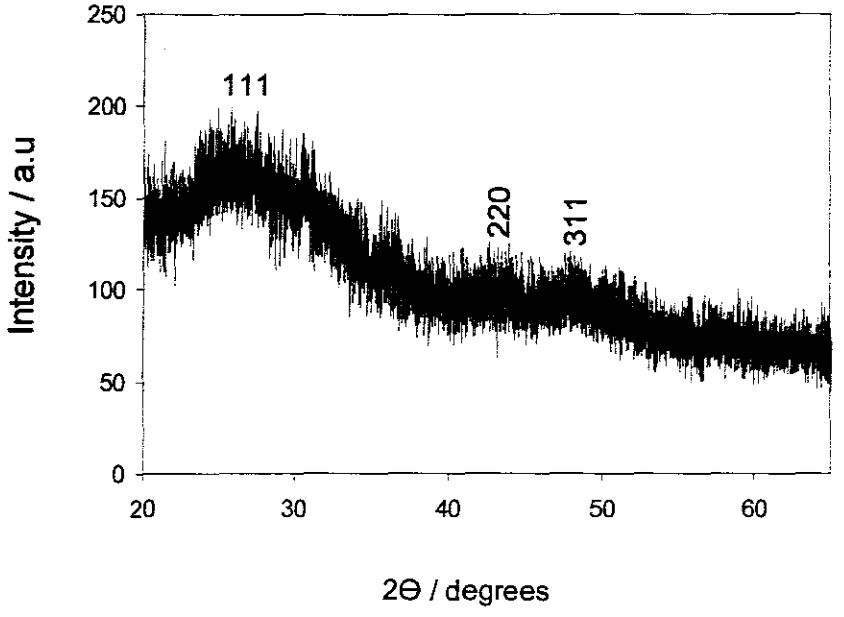


***Figure 2.38 (a)*** *XRD pattern of HDA-capped CdSe at 110 °C.*

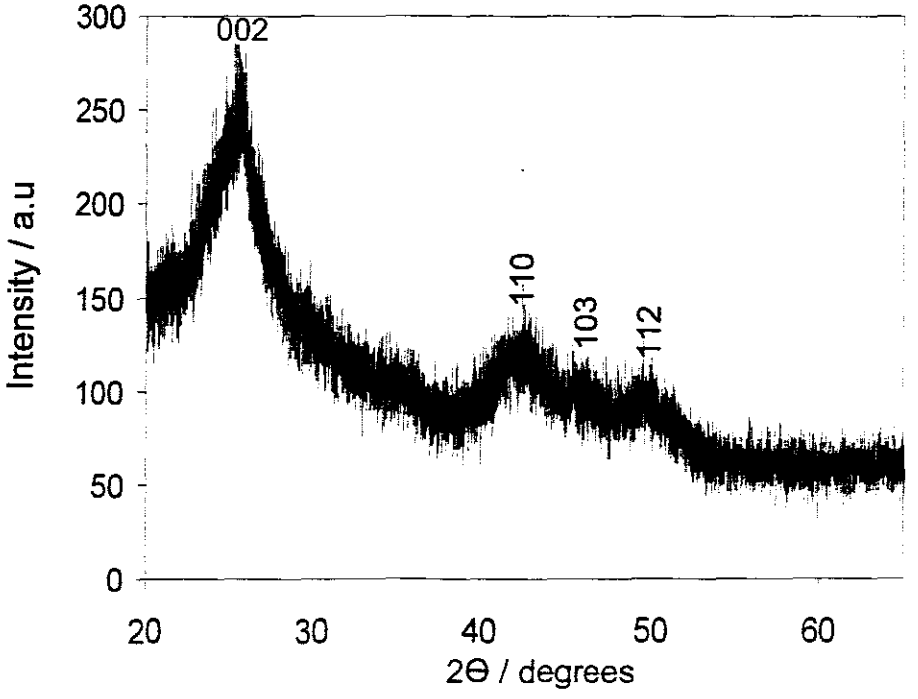


***Figure 2.38 (b)*** *XRD pattern of HDA-capped CdSe at 160 °C*

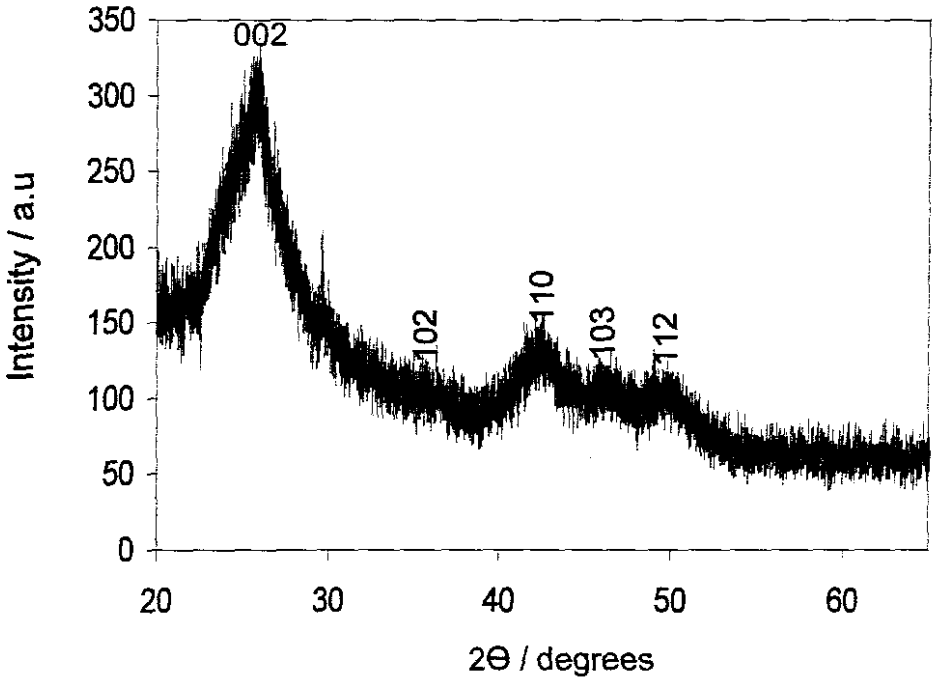


***Figure 2.38 (c)*** *XRD pattern of HDA-capped CdSe at 200 °C*

Figure 2.39 shows the XRD patterns of the HDA-capped CdSe at different monomer concentrations. The hexagonal phase of the CdSe, at lower monomer concentration, was still maintained at higher concentration for synthesis under the reduction time of 2 hrs (Figure 2.39a). However, the width of the diffraction peaks becomes narrower at higher monomer concentrations indicating an increase in particle size. This is consistent with the optical and TEM measurements. At higher monomer concentrations, the five diffraction peaks corresponded to the (002), (102) (110), (103), and (112) crystalline planes of hexagonal CdSe and were clearly resolved when compared to those obtained at lower concentration. In addition, the diffraction peak at $2\theta = 35$ (102) was clearly seen at higher concentration. However, this diffraction and the one at $2\theta = 45$ (103) was excessively attenuated. The attenuation of these diffractions has been attributed to the characteristic stacking faults along the (002) direction in the wurtzite-type structure.[17] At a reduction time of 6 hrs, there is a

Gtransformation from the cubic to hexagonal phase as the monomer concentration increases (Figure 2.39 b). This could be attributed to the stability of the hexagonal phase at higher particle sizes.[41]

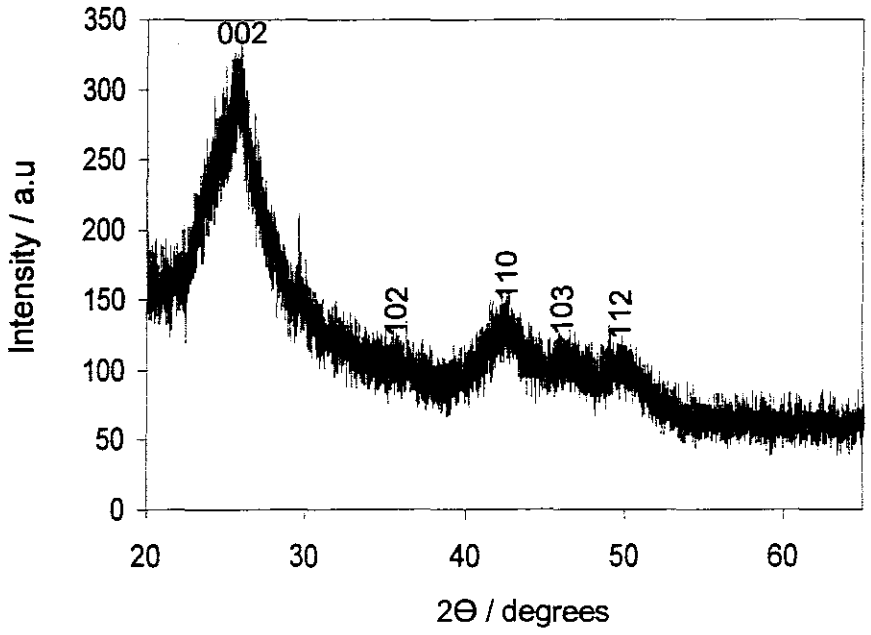


***Figure 2.39 (a)*** *XRD pattern of HDA-capped CdSe under reduction time of 2 hrs at 0.64 mmol concentrations.*

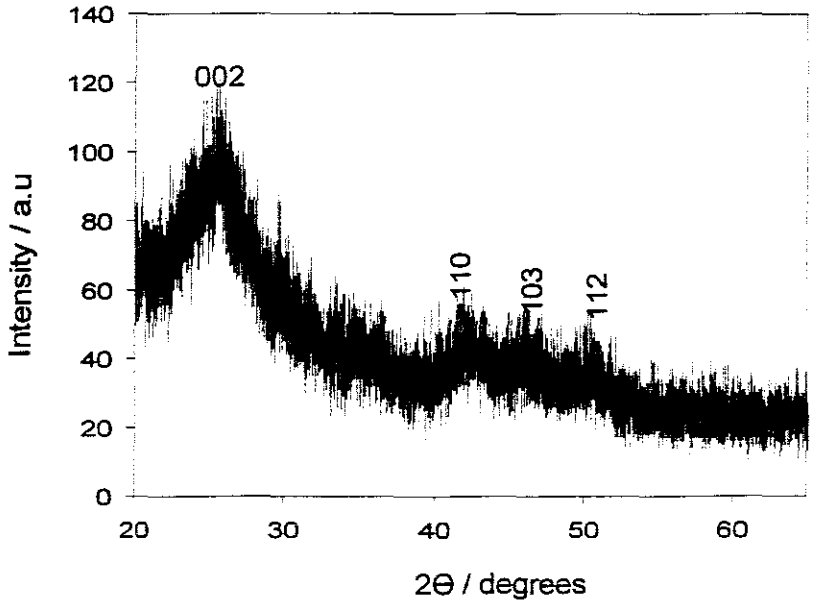


***Figure 2.39 (b)*** *XRD pattern of HDA-capped CdSe under reduction time of 6 hrs at 0.64 mmol concentrations.*

Figure 2.40 shows the XRD pattern for TOPO-capped CdSe nanocrystals at reduction times of 2 and 6 hrs after a growth time of 30 mins. Similar to HDA-capped nanoparticles, the results show gradual transformation from cubic to hexagonal phase as the reduction time decreases from 6 to 2 hrs. The hexagonal phase appears to be the dominant phase at lower reduction time. Unlike the HDA-capped, the (110), (103) and (112) planes of wurtzite CdSe are not well-defined due to the small overlap of the (110) and (103) peak (Figure 2.40a).

At higher monomer concentration (Figure 2.41) and the same temperature, there is no structural transformation. At a reduction time of 6 hrs, the cubic phase is maintained even though there is an increase in the particle size. However, the diffraction peaks are clearly resolved and narrower due to the increase in the particles size, resulting from the increase in the monomer concentration. Thus, the temperature cannot be the factor leading to changes in the crystal structure in the present case, as previously reported.[44] A significant factor to be noticed in this present case must be the reduction time, which favours the cubic phase at higher reduction time and the hexagonal phase at lower reduction time, in the presence of TOPO as the capping agent.

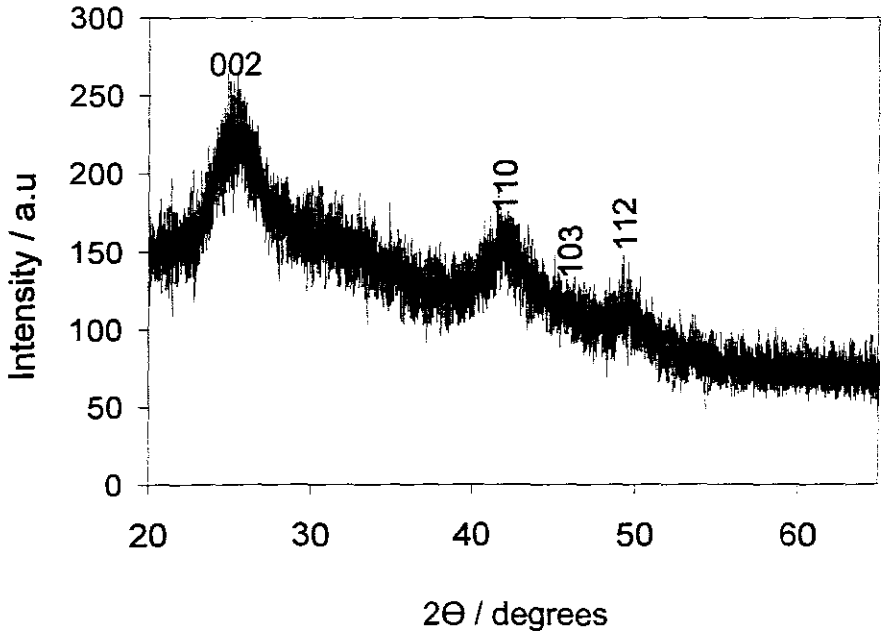


***Figure 2.40 (a)*** *XRD pattern of TOPO-capped CdSe under reduction time of 2 hrs at 0.32 mmol concentrations.*

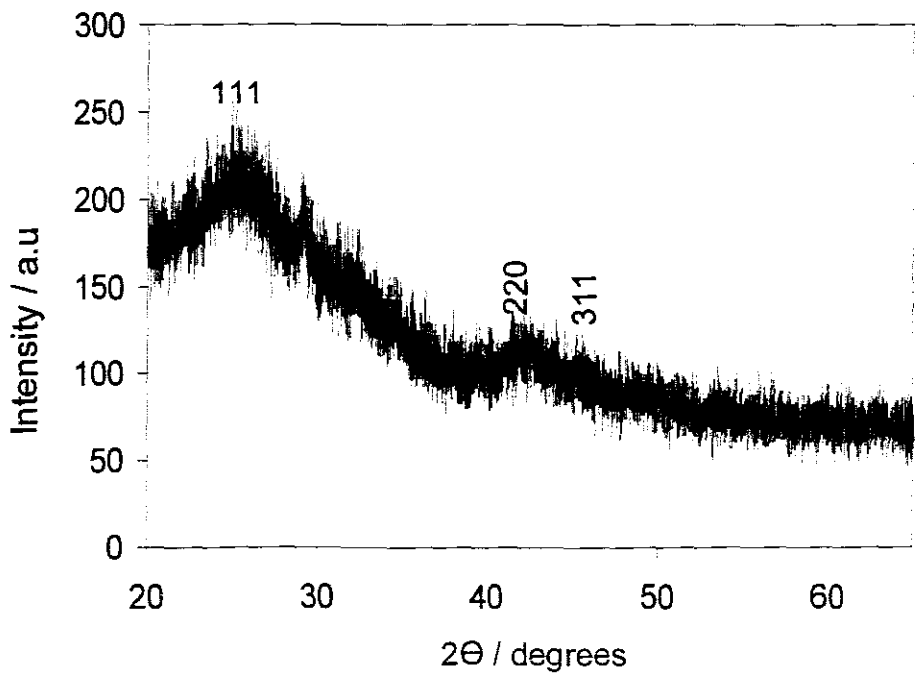


***Figure 2.40 (b)*** *XRD pattern of TOPO-capped CdSe under reduction time of 6 hrs at 0.32 mmol concentrations.*

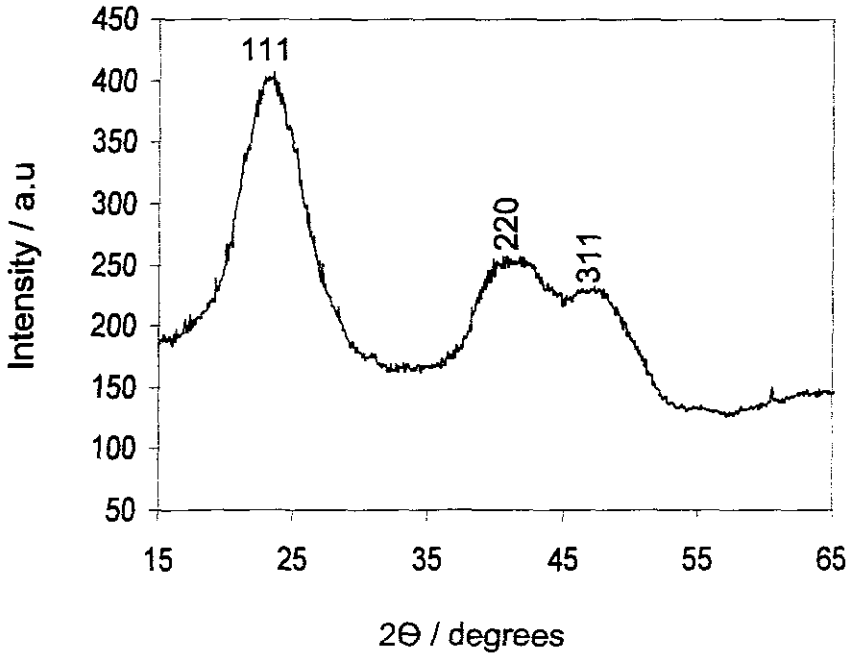


***Figure 2.41*** *XRD pattern of TOPO-capped CdSe under reduction time of 6 hrs at 0.64 mmol concentrations*

### 2.3.2.2 *Transmission Electron Microscope (TEM)*

The TEM and HRTEM are very useful tools in characterising the size and shape of the nanoparticles because, they provide two-dimensional images that give insight into shape, size and size distribution. Figure 2.42 shows the TEM images and particle size distribution of the HDA-capped CdSe synthesised at the reduction of 2, 4 and 6 hrs after the growth time of 30 mins. The TEM images show well-defined, monodispersed and mostly spherical particles. The average particle sizes, as determined from the TEM images for the reduction time of 2, 4 and 6 hrs respectively, are as follows : 3.00 ± 0.25 nm, 3.29 ± 0.28 nm and 2.96 ± 0.21 nm. The increase in the average diameter, as the reduction time decreases, is in agreement with the observed red-shift in the absorption spectra from 6 hrs to 2 hrs reduction time. The average particle diameter obtained from the TEM images, correlate with

the particle sizes calculated from the position of the first electronic transition in the UV-Vis absorption spectra for 2 hrs (2.98 nm) and 4 hrs (3.17 nm). However, the particle size for the 6 hrs sample as observed by the TEM, is larger than that calculated from the exciton absorption peak. Weller *et al.*[44] has reported a similar observation. This might be attributed to the fact that the electron microscopy in this regime of small sizes, may lead to an overestimation of the particle size due to loss of contrast in the TEM because of the presence of the passivating agent. The relative standard deviation of the size of the nanoparticles (± 8.27 %, 2 hrs; ± 8.55 %, 4 hrs and ± 7.09 %, 6 hrs) confirms the narrow size distribution of the nanoparticles. The TEM image also reveals the existence of elongated particles (especially for 2 hrs) which may be attributed to self-reorganisation occurring through adhesion between the nanoparticles. [29]

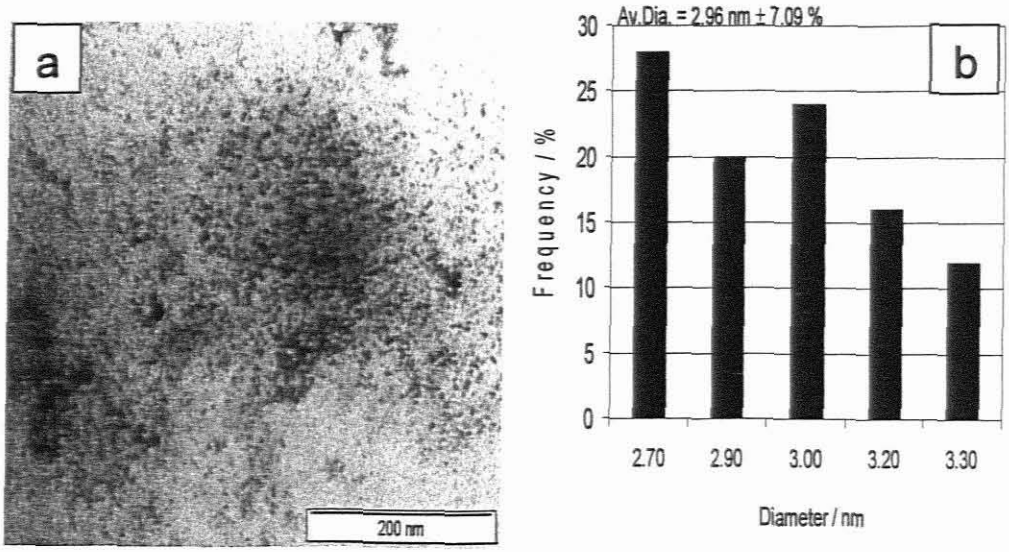


***Figure 2.42 (a)*** *TEM image and (b) Particle size distribution of HDA-capped CdSe at reduction time of 6 hrs using 0.32 mmol concentrations.*

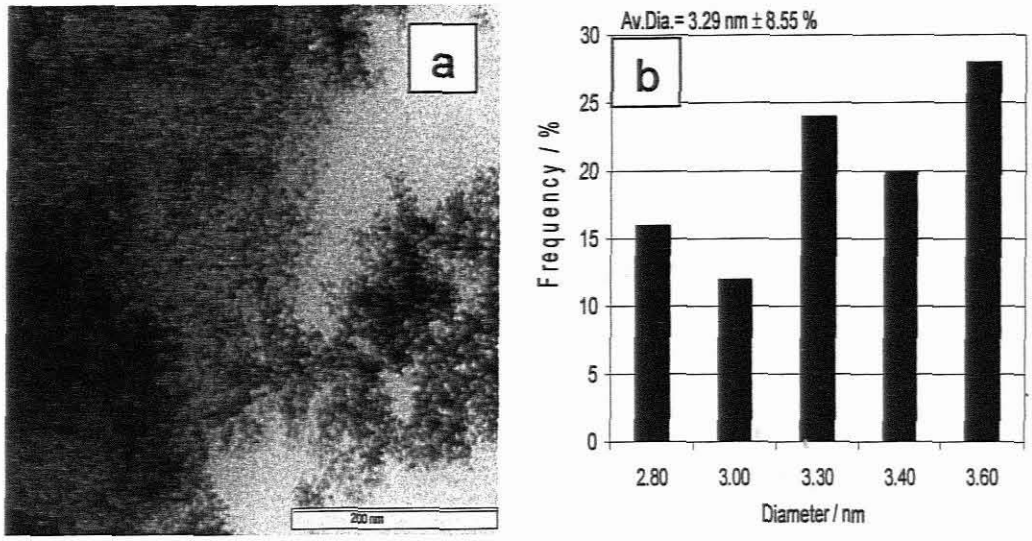


***Figure 2.42 (b)*** *TEM images and (b) Particle size distribution of HDA-capped CdSe at reduction time of 4 hrs using 0.32 mmol concentrations.*

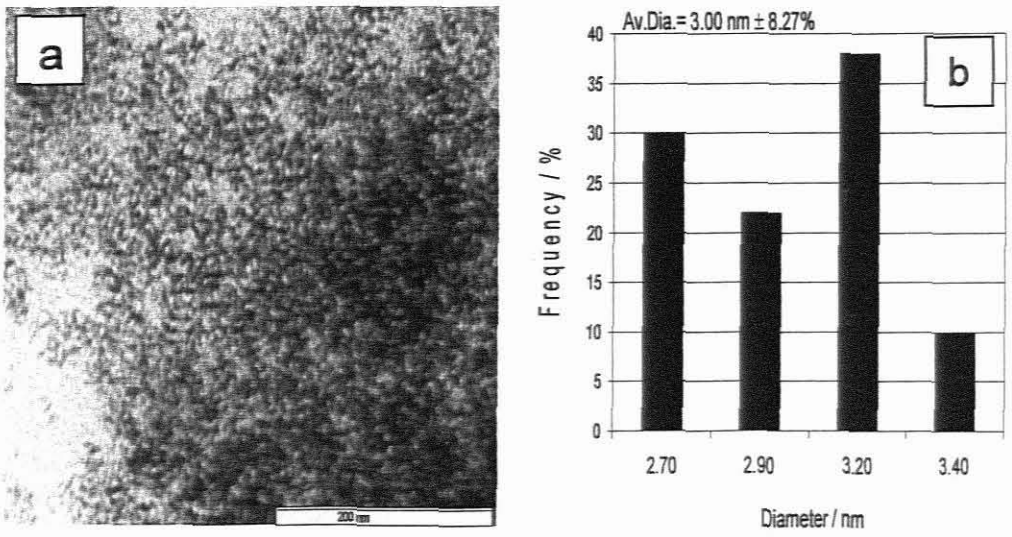


***Figure 2.42 (c)*** *TEM images and (b) Particle size distribution of HDA-capped CdSe at reduction time of 2 hrs using 0.32 mmol concentrations.*

The TEM images in Figure 2.43 show HDA-capped CdSe nanoparticles synthesised at different growth temperatures of 110, 160 and 200 °C. The TEM images consist of both spherical and elongated nanoparticles. The presence of the elongated

nanoparticles increases with the increase in temperature. The TEM images obtained at 200 °C consist mostly of rod-shaped particles of low aspect ratio, dot shaped particles and, a small percentage of multi-armed rods are also visible. The presence of the elongated particles could be attributed to the phenomenon of oriented attachment (self-assembly), due to dipole-dipole interactions between the highly charged surface of II-VI semiconductor nanocrystals.[45,46] Jun and co-workers reported similar observations for CdS nanoparticles. They pointed-out that at higher temperatures, the (001) face of the wurtzite crystal is more reactive than other faces hence, the formation of rods is favoured above that of spherically-shaped nanocrystals.[47] The formation of multi-armed rods is attributed to the different growth rates between the crystallographic surfaces. In Figure 2.43c, it could be seen that the rods are formed when two particles are joined together by a thin fusing section (marked as II); it also shows two dot particles about to join together but separated with a gap (marked as I), while the multi-arms could be seen to have emerged from differently sized dot particles (marked as III and IV). This observation confirmed our inference about the formation of elongated particles through self-assembly. The elongated nanocrystals obtained here, exhibit a wurtzite structure. This is similar to the results from the conventional organometallic method where the mono-rods obtained are of wurtzite phase structure. Manna and Peng gave insight into the mechanism for the formation of elongated particles.[30,32,33] They proposed that the arm(s) with the wurtzite structure grow(s) along the (001) axis direction after relatively reactive (001) face(s) is/are formed on the {111} face(s) of the zinc-blende core and nanocrystals evolve in the following order : dots, mono-rods and branched structures with an increase in monomer concentration. When the concentration of monomer present, just after nucleation is high, the difference in growth rates between

the unique *c*-axis of the wurtzite crystal and the other axis, is accentuated and rods are obtained.[30] This might be possible in this work because higher temperatures ensure that the monomer concentrations will be higher in the period of time just after nucleation. Recently, Wang and his co-workers reported that adhesion has a greater effect on the change of the size of the nanocrystals.[29] They believe that during the particle growth some of the remaining monomers which act as adhesives, play an important role in the adhesion of two nanocrystals and, without these "adhesives" their adhesion would be very difficult. They attributed the gap between the two parts, which should form a perfect rod or a perfect branch even after heating for several hours, to incomplete adhesion between the nanoparticle "adhesives". The large red-shift in the band gap (600 nm) of the nanoparticles produced at this temperature and the broadness of the spectrum compared to those produced at lower temperature (547 nm, 160 °C and 536 nm, 110 °C), could also be attributed to the contribution from the presence of elongated particles.

The average particle size calculated from the TEM images of the nanoparticles produced at 110 °C (mostly spherical), further supports adhesion among the nanoparticles. It is noted that the average particle size (3.44 ± 0.35 nm) obtained from the TEM images at this temperature is very large, compared to the particle sizes calculated from the optical measurements (2.28 nm). This difference in particle size can be attributed to the overestimation of the particle size from the electron microscopy, because of the closeness of the smaller particles arising as a result of adhesion.

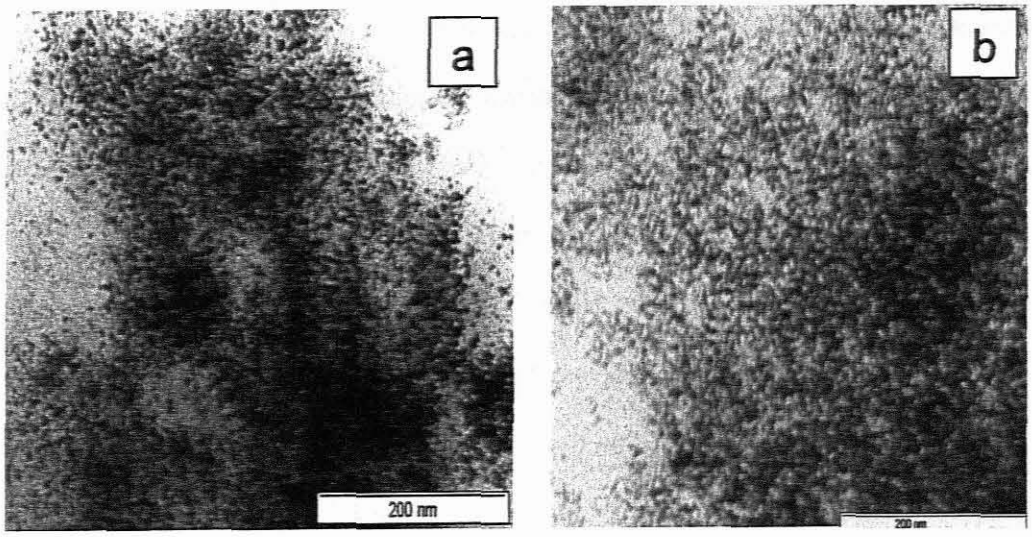


***Figure 2.43*** *TEM image of HDA-capped CdSe at (a) 120 °C and (b) 160 °C*

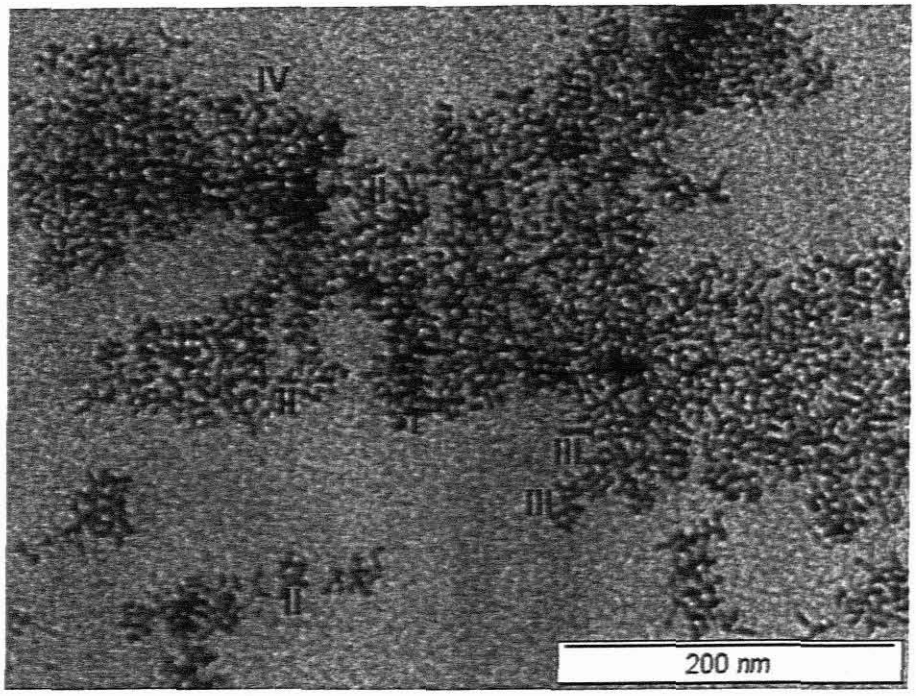


***Figure 2.43 (c)*** *TEM image of HDA-capped CdSe at 200 °C*

Figure 2.44 shows the TEM images of the HDA-capped CdSe synthesised at higher monomer concentration. Increasing the monomer concentration resulted in a change in particle size and morphology. The TEM images consist of a mixture of spherical and rod-shapes, with high aspect ratio. Formation of anisotropic-shaped particles by

increasing the monomer concentration, has been reported extensively and has been attributed to highly kinetically driven reaction conditions.[32,33,48-52] Nair and Scholes ascribed this to growth between different crystallographic surfaces, occurring under non-equilibrium conditions of a high flux of monomers and moderate supply of thermal energy.[52] Adam and Peng[32,33,48] and Lee *et al.*,[49,50] have elucidated the mechanism for the anisotropic growth and the shape evolution of nanocrystals in solution. They pointed out that the formation of elongated nanocrystals was a highly kinetic driven reaction and, shape evolution from long to shorter rods and even to spherical particles, was the result of the reaction system shifting from kinetically-driven control to thermodynamically-driven control, due to the situation change of nanocrystals and their reaction environment (high monomer concentration supplies the reaction system with high kinetic drive, while high reaction temperature provides it with high thermal energy (KT) and accelerated reaction rates).

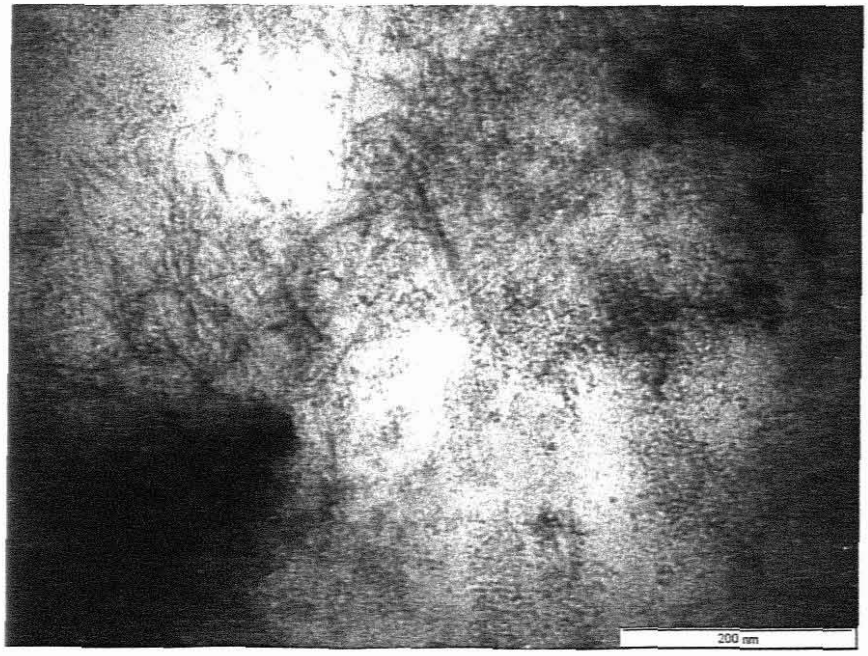


***Figure 2.44*** *TEM image of HDA-capped CdSe at reduction time of 2 hrs using 0.64 mmol concentrations.*

The TEM images in Figure 2.45 show the HDA-capped CdSe nanoparticles synthesised at 110 °C, under different growth times of 5, 15 and 30 mins. The TEM images show transformation in the nanoparticles shapes (dot &rod⟶rod⟶dot) as the growth time increases. The TEM image for the 5 mins sample consists mostly of non-uniform spherical particles with a small percentage of rods. At 15 mins the TEM image consists mostly of rod-shaped nanoparticles with low and high aspect ratios and some wires. The growth time of 30 mins consists mostly of dot-shaped particles and a small amount of rods. Manna *et al.*, attributed such transformation to the particle growth rate.[30] They reported that nanocrystals will eventually form nearly spherical shapes at slow growth rates, while rods would be formed at high growth rates by unidirectional growth of one face. From the optical results (Figure 2.22), two types of growth could be identified from these reactions : slower and faster growth rates. A slower growth rate occurs at the beginning of the reaction (0 to 10mins) due to lower injection temperature. This slow growth rate resulted in the high concentration of free monomer in the reaction mixture, forming nanoclusters in the early stage of the reaction with tailing band-edges. Hence, the shapes remain mostly non-uniformly spherical. As the reaction time increases (10 to 15 mins) surface ordering occurs, resulting in nanoparticles with sharper sub-structures. The growth rate increases rapidly between these times, resulting in the shift of exciton peak from 411 nm to 477 nm. Such a high growth rate could be attributed to the formation of elongated shapes (rods and wires) at this reaction time. As the reaction time increases the monomer concentration is reduced due to growth. Under these conditions, the larger nanocrystals in the distribution begin to grow larger with the disappearance of the relatively smaller ones in the solution. This leads to the onset of conventional Ostwald ripening and it accounts for the slower growth rate for the

remaining reaction time after 15 mins. This is also evident in the small shift of the exciton peak from 477 nm (15 mins) to 495 nm (30 mins). This slower growth rate, after a brief period of faster growth rate, could be attributed to the transformation of the nanoparticle shape from elongated to spherical particles, observed in the TEM image at 30 mins reaction time. Similar transformations have also been reported by Li *et al.*[51] They observed that longer periods of growth results in the transformation of the initially formed anisotropic crystals into a more thermodynamic stable shape. This transformation took many hours to occur however, in our reaction, the transformation takes only a few minutes.

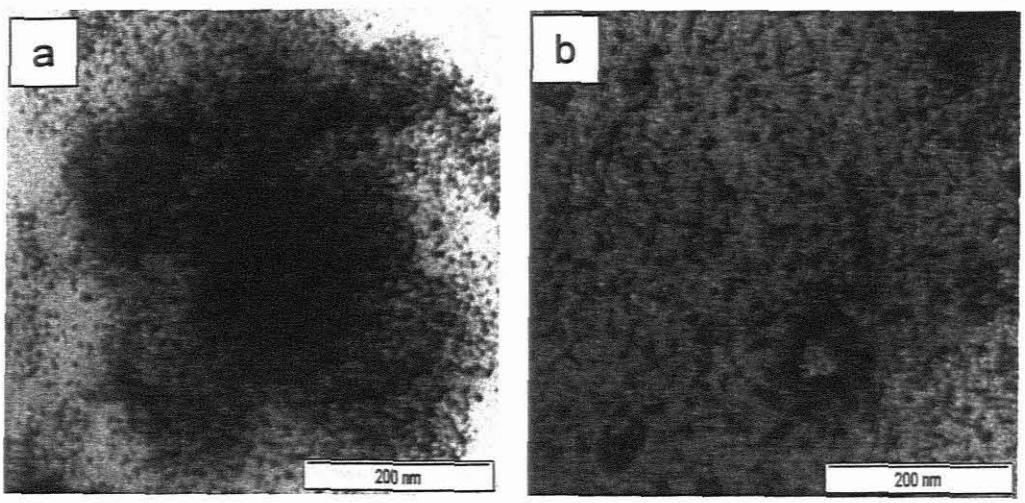


***Figure 2.45*** *TEM image of HDA-capped CdSe at 110 °C under (a) 5 mins and (b) 15 min.*

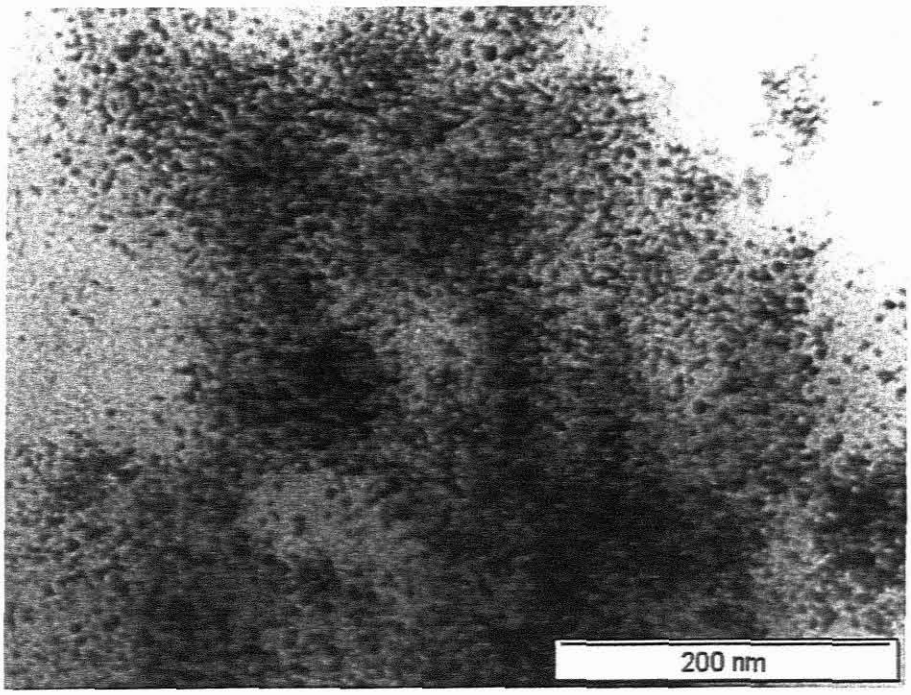


***Figure 2.45 (c)*** *TEM image of HDA-capped CdSe at 110 °C under 30 mins.*

Figure 2.46 and 2.47 show the TEM images and particle size distributions of TOPO-capped CdSe nanoparticles synthesised at different monomer concentrations (0.032 and 0.064 mmol), after the growth time of 30 mins. The TEM image shows well-defined, monodispersed, spherical particles at lower concentration and a mixture of dot and rods at higher concentration. The average particle size as determined from the TEM images for the lower monomer concentration is 3.00 ± 0.16 nm. This agrees well with the estimated size (3.07 nm) obtained from the absorption spectra. On increasing the monomer concentration the particle sizes increased to 5.1± 0.26 nm. The size is almost double that obtained from lower concentration. This could be attributed to the fact, that increase in monomer concentration leads to adhesion between the molecules as discussed earlier. The increase in the average particle diameter calculated from the TEM image, is consistent with the observed red-shift in the band-edge as the monomer concentration increases. However, the difference in

the particle size between the two samples as observed by the TEM, is larger than those obtained using the exciton absorption. The increase in the particle size shows only a little red-shift in the absorption spectra, as compared to those at lower concentration. It is noted from the TEM image, that the obvious changes in size mainly come from the elongation of the arms of nanocrystals and not from a slight increase in the diameter of the arms. This might be the reason for the discrepancy between the particle size calculated from the absorption spectra and, those obtained from the TEM images for particles synthesised at higher monomer concentration. Similar observations have been reported by Wang *et al.*,[29] who attributed the reason for the slight shift of absorption spectra to be that, the band gap of elongated particles depends more sensitively on their width than on their length.

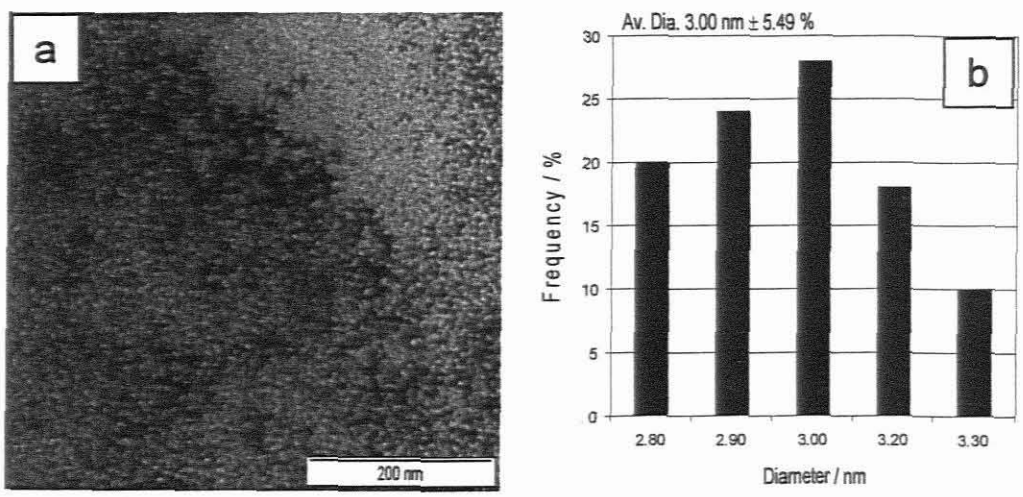


***Figure 2.46*** *(a) TEM images and (b) particle size distribution of TOPO-capped CdSe at 0.32 mmol concentrations.*

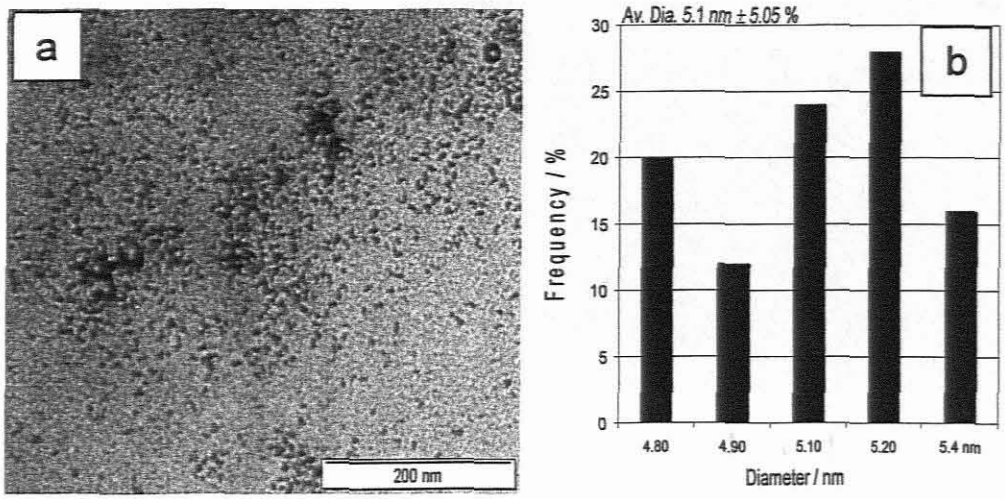


***Figure 2.47*** *(a) TEM images and (b) particle size distribution of TOPO-capped CdSe at 0.64 mmol concentrations.*

### 2.3.2.3 High *Resolution Transmission Electron Microscope (HRTEM)*

The HRTEM image of HDA-capped CdSe nanoparticles synthesized using 0.32 mmol monomer concentrations at 110 °C and after 30 mins in Figure 2.48, shows an array of CdSe nanoparticles. The image shows an ensemble of CdSe quantum dots assembled into a locally well-ordered close-parked array. The existence of lattice planes in the HRTEM image confirms the crystallinity of the sample. The HRTEM image can also be used as an indicator of the morphology of the particles. The particles in Figure 2.48a appear to be both spherical and reasonably elongated. This is in good agreement with the results obtained from the TEM images. Figure 2.48b shows the HRTEM of a single CdSe particle with a diameter of 3.64 nm. This is in agreement with the particle size calculated from the TEM image and further supports adhesion among the nanoparticles.

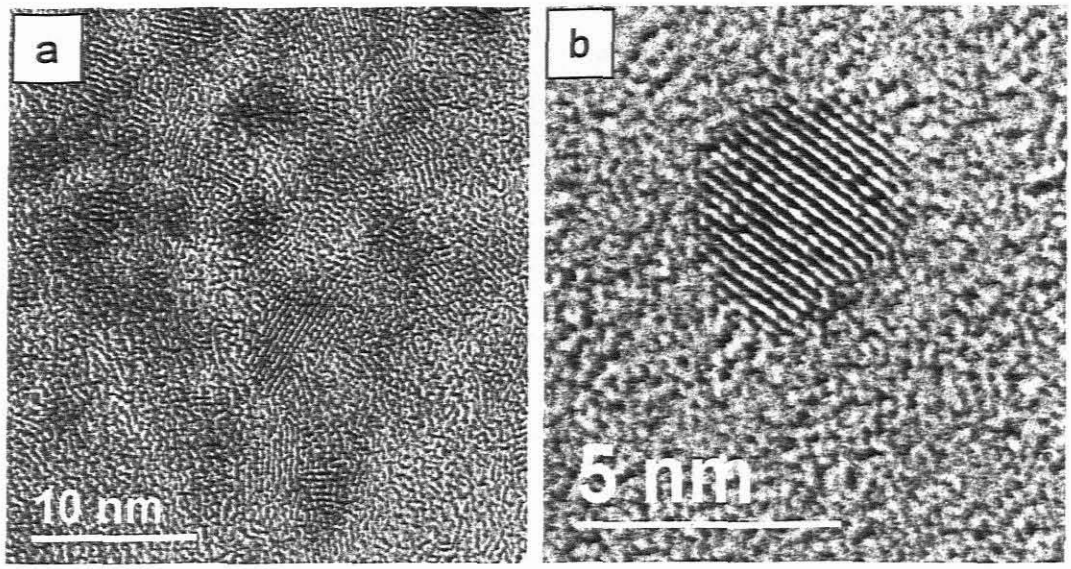


***Figure 2.48*** *HRTEM image of HDA-capped CdSe nanoparticles at 110 °C using 0.32 mmol concentration showing (a) an array of particles and (b) single quantum dot of CdSe.*

#### 2.3.2.4 *Energy Dispersive Spectroscopy (EDS)*

The EDS spectra in Figure 2.49 for the HDA- and TOPO-capped CdSe nanoparticles show the presence of Cd and Se, confirming the production of cadmium selenide nanocrystallites. The peak for the phosphorus in each case was due to the presence of TOP. The presence of a strong phosphorus peak in Figure 2.49b confirmed the passivation of the particle by TOPO while, the presence of nitrogen peak in Figure 2.49a confirmed the passivation by HDA. This nitrogen peak is absent in the TOPO-capped CdSe spectrum. In the case of the HDA-capped particles, the low intensity of the nitrogen peak is due to suppression from the high intensity of the carbon peak, whose source is the carbon tape used to suspend the powdered samples. The peak near 0.5 keV in Figure 2.50b is assigned to O, which is the oxygen atom from the TOPO.

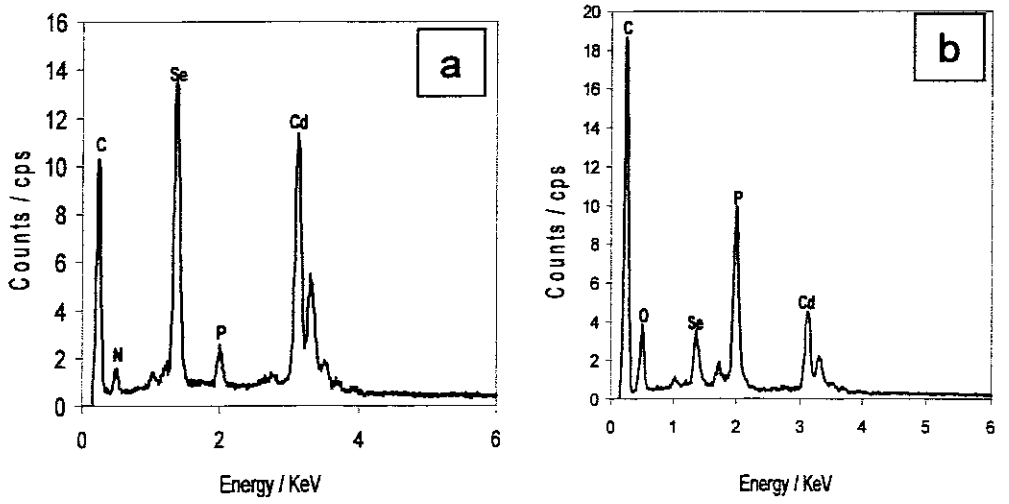


***Figure 2.49*** *EDS Spectra of (a) HDA and (b) TOPO-capped CdSe nanoparticles.*

### 2.3.2.5 *Fourier Transform Infrared Spectroscopy.*

The surface morphology of the CdSe was investigated by IR spectroscopy (Figure 2.50). TOPO absorbs strongly at 1466 $cm^{-1}$ and 1146 $cm^{-1}$ corresponding to $CH_2$ bending and P=O stretching respectively, the position of which depends on the attached group.[53] In this work, a shift of 14 $cm^{-1}$ ($\nu$ = 1452 $cm^{-1}$) to lower wavenumbers from the characteristic stretch of TOPO ($\nu_{sym}$, P=O=1466 $cm^{-1}$), is observed. This shift has been observed previously for TOPO bound CdSe-capped nanoparticles and, attributed to the binding of TOPO to $Cd^{2+}$ sites on the CdSe nanocrystallites surface.[19] The IR spectrum of HDA-capped CdSe show bands that are shifted to higher frequencies when compared to the free ligand. The band assignments are given in Table 1. This shift has been reported for amine bound to CdSe and may be due to coordination of the nanocrystallites.[54] The weak bands at 2676 $cm^{-1}$ and 2569 $cm^{-1}$ appearing in the HDA-capped CdSe, as well as C-N stretching band at 1176 $cm^{-1}$ are attributed to the coordination of the TOP and, the nanocrystallites to the nitrogen atom of the amine. The band at 1400 $cm^{-1}$ is assigned

to be P-$CH_2$ bending, due to the presence of the phosphine. The presence of phosphorus is also confirmed by the EDS spectra.

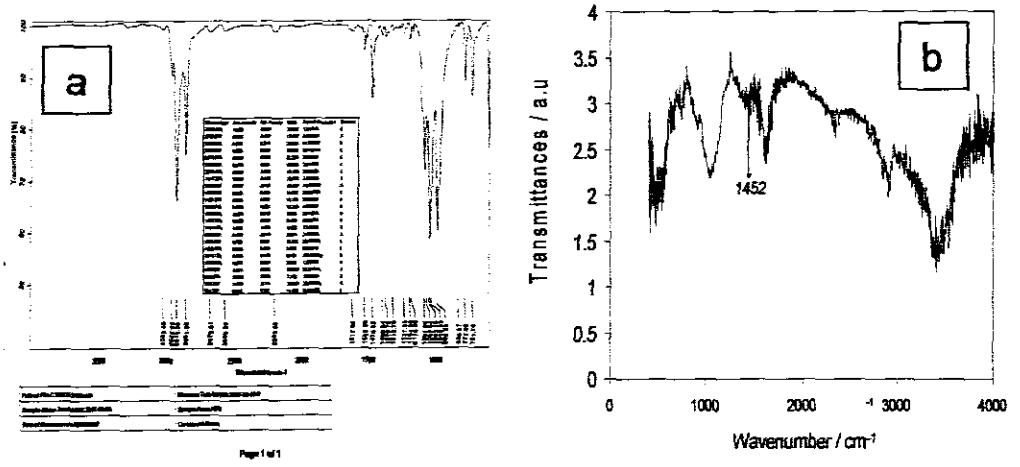


***Figure 2.50*** *IR Spectra of (a) HDA and (b) TOPO-capped CdSe nanoparticles.*

***Table 1.*** *Assignment of IR bands for HDA-capped CdSe nanoparticles*

| HDA | CdSe /HDA | BAND |
|---|---|---|
| 3331 (m) | 3334 (w) | N-H str |
| 2954 (m) | 2958 (m) | $CH_3$ ( C-H str) |
| 2916 (Vs) | 2919 (vs) | $CH_2$ ( C-H str) |
| 2847 (Vs) | 2851 (vs) | $CH_2$ (C-H str) |
| | 2676 &2569 (w) | $CH_2$ ( C-H str) |
| 1462 (s) | 1470 (s) | $CH_2/CH_3$ bend |
| 1363 (m) | 1376 (m) | $CH_3$ bend |
| 1058 (s) | 1062 (w) | C-N str |
| | 1176 | C-N str |
| 719 (s) | 721 (s) | $CH_2)_n$ rocking |
| | 1400 | P- $CH_2$ bend |

m = medium, w = weak, s = strong, vs = very strong

## 2.4 Conclusions

Monodispersed HDA- and TOPO-capped CdSe nanoparticles have been synthesised by a novel, greener, quick, facile and effective non-organometallic solution based method, using cadmium chloride and selenium powder as cadmium and selenide ion precursors respectively, without the use of additional stabiliser. The synthetic method is based on the reduction of selenium powder in water followed by the addition of $CdCl_2$. The CdSe nanoparticles produced are passivated, using TOPO and HDA. Optical and structural analysis show that the samples are of high quality with narrow full-width at half-maximum (FWHM) and narrow size distribution without any size-selective precipitation. The nanoparticles show band-edge luminescence and possess properties similar to those synthesized by conventional organometallic methods.

A systematic study of the effect of a capping group, growth time, temperature, reduction time and, monomer concentration on the absorption, size, emission properties and morphology of the as-synthesized nanoparticles, was also explored using this new approach. HDA-capped CdSe nanoparticles show high luminescence intensity compared to TOPO-capped CdSe nanoparticles, due to its high electron donating ability and capping density which enhances passivation. The absorption and emission maxima are shifted to higher band gap (lower wavelengths) as the reduction time increases from 2 to 6 hrs, indicating a decrease in particle size for the HDA-capped CdSe. The TOPO-capped CdSe show an increase in absorption and emission maxima as the reduction time increases from 2 to 4 hrs and decreases at the reduction time of 6 hrs. Increasing the monomer concentration and temperature, led to faster growth rates, increase in particles sizes, emission in the blue-red window, narrow

emission widths and focusing of the size distribution. The temporal evolution of the optical properties indicates two stages of growth : an early stage between 0 and 10 mins and a later stage after 10 mins.

The broad nature of the XRD diffraction peaks and diffuse diffraction of the SAD, confirm the nanocrystalline nature of the material with gradual phase transitions from cubic to hexagonal depending on the capping group, concentration, temperature, reduction time and growth time. The TEM images show well-defined, monodispersed, spherical and elongated (rod and multi-armed rod) particles. The formation of elongated particles was attributed to self-assembly between the nanoparticles, due to dipole-dipole interactions between the highly charge surface of II-VI semiconductor nanocrystals. The existence of lattice planes on the HRTEM image confirms the high crystallinity of the sample. The EDS pattern clearly confirmed the presence of the corresponding elements while, capping of the nanoparticles surface by HDA and TOPO was established by FT-IR and EDS spectroscopy.

## 2.5 References


1) J. M. Costa-Fernandez, R. Pereiro and A. Sanz-Medel, *Trends in Anal. Chem.*, 2006, **25** 207.

2) P. K. Khanna, R. M. Gorte and R. Gokhale, *Mater. Lett.*, 2004, **58**, 966.

3) C. J. Murphy, *J. Mater. Chem.*, 2008, **18**, 2173.

4) L. Qu and X. Peng, *J. Am .Chem. Soc.*, 2002, **124**, 2049.

5) L. Qu, W. W. Yu and X. Peng, *Nano. Lett.*, 2004, **4**, 465.

6) C. D. Donega, S. G. Hickey, S. F. Wuister, D. Vanmaekelbergh and A. Meijerink, *J. Phys.Chem.* B, 2003, **107**, 489.

7) D. V. Talapin, A. L. Rogach, E. V. Shevchenko, A. Kornowski, M. Haase, and H. Weller, *J. Am .Chem. Soc.*, 2002, **124**, 5782.

8) A. Eychmuller and A. L. Rogach, *Pure Appl. Chem.*, 2000, **72**, 179.

9) J. Hambrock, A. Birkner and R. A. Fischer, *J. Mater. Chem.*, 2001, **11**, 3197.

10) U. K. Gautam, M. Nath, and C. N. R. Rao, *J. Mater. Chem.*, 2003, **13**, 2845.

11) W. Wang, Y. Geng, P. Yan, F. Liu, Y. Xie and Y. Qian, *J. Am .Chem. Soc.*, 1999, **121**, 4062.

12) Z. A. Peng and X. Peng, *J. Am. Chem. Soc.*, 2001, **123**, 183.

13) X. G. Peng, L. Manna, W. D. Yang, J. Wickham, E. Scher, A. Kadavanich and A. P. Alivisatos, *Nature*, 2000, **404**, 59.

14) J. A. Gaunt, A. E. Knight, S. A. Windsor and V. Chechik, *J. Colloid and Interface Science*, 2005, **290**, 437.

15) J. McBride, J. Treadway, L. C. Feldman, S. J. Pennycook and S. J. Rosenthal, *Nano Lett.*, 2006, **6**, 1496.

16) K. Nose, H. Fujita, T. Omata, S. O. Y. Matsuo, H. Nakamura and H. Maeda, *J. Lumin.*, 2007, **126**, 21.

17) C. B. Murray, D. J. Norris and M. G. Bawendi, *J. Am. Chem. Soc.*, 1993, **115**, 8706.

18) M. A. Hines and P. J. Guyot-Sionnest, *J. Phys. Chem.* B, 1998, **102**, 3655.

19) J. E. Bowen Katari, V. L. Colvin, A. P. Alivisatos, *J. Phys. Chem.*, 1994, **98**, 4109.

20) K. Satoh, Y. Takahashi, T. Suzuki and K.Sawada, *J. Chem. Soc. Dalton Trans.*, 1989, 259.

21) D. V. Talapin, A. L. Rogach, A. Kornowski, M. Haase and H. Weller, *Nano. Lett.*, 2001, **1**, 207.

22) J. L. Pankove, *Optical Processes in Semiconductors*, Dover Publications, New York. 1990.

23) M. G. Bawendi, M. L. Steigerwald and L. E. Brus, *Annu. Rev. Phys. Chem.*, 1990, **41**, 477.

24) W. W. Yu, L. Qu, W. Guo and X. Peng, *Chem. Mater.*, 2003, **15**, 2854.

25) L. E. Brus, *J.Chem. Phys.*, 1984, **80**, 4403.

26) X. Peng, M.C. Schlamp, A. Kadavanich, A. P. Alivisatos, *J. Am. Chem. Soc.*, 1997, **106**, 9869.

27) S. N. Sarangi and S. N. Sahu, *Physica E*, 2004, **23**, 159.

28) K. Yu, S. Singh, N. Patrito and V. Chu, *Langmuir*, 2004, **20**, 11161.

29) Q. Wang, D. Pan, S. Jiang, X. Ji, L. An and B. Jiang, *J. Cryst. Growth*, 2006, **286**, 83.

30) L. Manna, E. C. Scher and A. P Alivisatos, *J. Am. Chem. Soc.*, 2000, **122**, 12700.

31) X. Peng, J. Wickham, P. A. Alivisatos, *J. Am. Chem. Soc.,* 1998, **120**, 5343.

32) Z. A. Peng and X. Peng, *J. Am. Chem. Soc.*, 2001, **123**, 1389.

33) Z. A. Peng and X. Peng, *J. Am. Chem. Soc.*, 2002, **124**, 3343.

34) R. He and H. Gu, *Colloids and Surfaces A: Physicochem. Eng. Aspects*, 2006, **272**, 111.

35) J. Joo, H. B. Na, T. Yu, Y. W. Kim, F. Wu, J. Z. Zhang and T. Hyeon, *J. Am. Chem. Soc.*, 2003, **125**, 11100.

36) O. S. Oluwafemi and N. Revaprasadu, *New J. Chem.*, 2008, **10**. 1432.

37) V. N. Soloviev, A. Eichhofer, D. Fenske and U. Banin, *J. Am. Chem. Soc.*, 2001, **123**, 2354.

38) S. Wageh, L. Shu-Man, F. T. You and X. X. Rong, *J. Lumin.*, 2003, **102-103**, 768.

39) Y. N. Xu and W. Y. Ching, *Phys. Rev. B*, 1993, **48**, 4335.

40) P. D. Lao, Y. Guo, C. C. Siu, and S. C. Shen, *Phys. Rev. B*, 1993, **48**, 11701.

41) T. Omata, K. Nose, S. O. Y. Matsuo, H. Nakamura and H. Maeda, *J. Apply. Phys.*, 2005, **44**, 452.

42) L. Qu, Z. A. Peng and X. Peng, *Nano. Lett.*, 2001, **1**, 333.

43) T. Vossmeyer, L. Katsikas, M. Giersig, I. G. Popovic, K. Diesner, A. Chemseddine, A. Eychumuller and H. Weller, *J. Phys. Chem.*, 1994, **98**, 7665.

44) A. L. Rogach, A. Kornowski, M. Gao, A. Eychmuller and H. Weller, *J. Phys. Chem.*, 1999, **103**, 3065.

45) Q. Yang, K. Tang, C. Wang, Y. Qian and S. Zhang, *J. Phys. Chem.* B, 2002, **106**, 9227.

46) Z. Tang, N. A. Kotov and M. Giersig, *Science*, 2002, **297**, 237.

47) Y. W. Jun, S. M. Lee, N. J. Kang and J. Cheon, *J. Am. Chem. Soc.*, 2001, **123**,5150.

48) X. G. Peng, *Adv. Mater.*, 2003, **15**, 459.

49) S. M. Lee, S. N. Cho, J. W. Cheon, *Adv. Mater.*, 2003, **15**, 441.

50) S. M. Lee, Y. W. Jun, S. N. Cho, J. W. Cheon, *J. Am. Chem. Soc.*, 2002, **124**, 11244.

51) Y. Li, X. Li, C. Yang and Y. Li, *J. Phys. Chem.* B, 2004, **108**, 16002.

52) P. S. Nair and G. D. Scholes. *J. Mater. Chem.*, 2006, **16**, 467.

53) N. B. Colthup, L. H. Daly, S. E. Wiberley, *Introduction to Infrared and Raman Spectroscopy*, 3rd ed; Academic Press Inc: San Diego, 1990, 364.

54) T. Trindade and P. O'Brien, *Adv. Mater.*, 1996, **8**, 161.

# *CHAPTER THREE*

## *SYNTHESIS OF ORGANICALLY SOLUBLE ZINC SELENIDE NANOPARTICLES*

## 3.1 Introduction

Zinc selenide (ZnSe) is a light yellow binary solid compound. It is an intrinsic direct band gap semiconductor, with a band gap of 2.58 eV (480 nm) at 25 °C. It has a standard enthalpy of formation of 177.6 kJ/mol at 25 °C and is a suitable material for red, blue and green light-emitting diodes, diode lasers, photovoltaic, laser screen, thin film transistors and photochemical cells. It emits blue light and is susceptible to n-type doping with for instance, halogen elements while its p-type doping is more difficult, but can be achieved by introducing nitrogen.[1-3] ZnSe doped with chromium (ZnSe:Cr) has been used as an infrared laser gain medium. While ZnSe, doped with tellurium (ZnSe (Te)) is a scintillator with an emission peak at 640 nm, it is suitable for matching with photodiodes and is significantly different from the ZnS ones. It's very low absorption of energy, makes it useful for optical components in high power laser windows and multi-spectral applications, providing good imaging characteristics. ZnSe is also useful in high resolution thermal imaging systems, where it is used to correct colour distortion which is often inherent in other lenses used in the system.[4-6]

Among the II-VI family of semiconductors, ZnSe is of special interest as it exhibits, via quantum confinement effects, tunable blue-ultraviolet (UV) luminescence. This UV range is practically difficult to obtain for cadmium-based systems such as CdSe, for which the toxicity of cadmium represents an additional disadvantage. As an important semiconductor material and of low toxicity, when compared to CdSe,[7,8] ZnSe has attracted extensive interest because of its wider band gap and transmittance range (0.5-22 μm), higher luminescence efficiency, lower absorption coefficient and its excellent transparency to infrared.[4-6,9] It has long been a material of choice for

blue diode lasers and an important material with high potential, for various device applications. These include optoelectronic devices such as optical limiters for eye protection and optically-controlled switching, owing to non-linear optical properties,[10] biomedical labeling and sensors resulting from photoluminescence.[11,12] It is also a promising candidate for the replacement of the toxic CdS in the buffer layer, due to its wider band gap (2.58 eV) than that of CdS (2.4 eV) and good lattice match with $Cu(In,Ga)(S,Se)_2$.[13] Although a lot of work has been reported on the synthesis of II-VI nanoparticles, CdSe has so far been the most studied nanocrystal colloid system while, relatively little work has been done on ZnSe nanocrystals. With the controlled growth of particles of diameters between 1.7 nm and 12 nm, a CdSe size-dependent absorption edge covers the entire visible spectrum. However, the small CdSe nanocrystals with an absorption edge in the UV-blue, remains very difficult to passivate and exhibits low quantum yields and broad emission. This limits CdSe in the blue[14] and justifies the development of other materials like ZnSe nanoparticles.

ZnSe nanoparticles have been prepared by most of the methods used to prepare CdSe nanoparticles by simply replacing the cadmium source with its zinc analogue. Hence, the methods of preparation experienced the limitations similar to those for the preparation of CdSe nanoparticles, as described in chapter one. The synthesis of ZnSe nanoparticles, similar to the cadmium analogue, started by means of arrested precipitation techniques. However, these earlier reports only provide optical absorption with no luminescence information,[15] The improved methods for the synthesis of ZnSe include, the use of a supersaturated glass solution which did not give any optical spectra,[16] a sol-gel process which resulted in defected particles with

large size distribution and broad heavily red-shifted emission,[17] non-aqueous solution *synthesis*,[15] *organometallic routes*,[14,18] *solvothermal routes*,[19-21] *single source* precursor routes,[22-26] molecular beam epitaxy (MBE),[27] metal organic chemical vapour deposition (MOCVD),[28] pulse nitrogen laser,[29] thermochemical methods,[30] liquid-solid-solution process,[31] hydrothermal method,[32] and most recently, the aqueous route.[33]

This chapter describes the synthesis of ZnSe nanoparticles using our proposed new, safe, inexpensive, facile and non-organometallic synthetic route. A systematic study of the effect of reduction time, monomer concentration, temperature, zinc precursor and capping group on the size, optical properties and the morphology of the as-synthesized nanoparticles, were also explored.

### 3.2 Synthetic method

Zinc selenide nanoparticles were synthesised by the addition of an aqueous solution of $ZX_2$ (X=Cl or $CH_3COO^-$) to a freshly prepared oxygen-free NaHSe solution, as described in chapter two. Hines *et al.*, found in their studies of ZnSe nanoparticles, that the TOP/TOPO coordination solvent combination did not work successfully in the synthesis of ZnSe, using $Et_2Zn$ and TOPSe.[14] By varying the TOP/TOPO ratios, the resulting reactions yielded either small particles which could not be isolated by standard solvent/non-solvent techniques or, there was formation of large aggregates of ZnSe nanoparticles. This was attributed to TOPO binding too strongly to Zn and TOP too weakly. As a result they chose HDA as the capping agent because of its high boiling point (330 °C), larger capping density as a result of its reduced steric hindrance and, the fact that it is a slightly weaker base than the

phosphine oxide. Revaprasadu *et al.* in contrast to this, reported the synthesis of TOPO-capped ZnSe by the thermolysis of the single source complex $EtZn(Se_2CNEt_2)_2$ in TOPO.[22]

Our synthetic approach accommodates the use of these two versatile coordinating solvents. The ZnSe produced was dispersed in TOP and after continuous stirring, the TOP-CdSe was injected into hot coordinating solvent (TOPO or HDA) under nitrogen flow. A decrease in temperature was observed by rapid introduction of the reagent mixture. The temperature was raised and maintained for 20 mins. The isolation of the particles is similar to that of CdSe as reported in chapter two. The addition of methanol to the pale-yellow reaction mixture resulted in a flocculant precipitate, which could be redissolved in toluene.

The quality of the synthesised nanoparticles was confirmed using absorption and photoluminescence spectroscopy, fourier transform infrared spectroscopy (FT-IR), powder x-ray diffraction (XRD) and transmission electron microscopy (TEM). In the same manner as CdSe nanoparticles, all measurements were performed without any post-preparative size separation of the nanoparticles.

### 3.3 Result and discussion

The addition of the aqueous $ZnCl_2$ to the freshly prepared NaHSe resulted in a pale-yellow reaction mixture, with the colour intensity depending on the reduction time of the selenium powder and monomer concentrations. The reaction scheme is shown below.

$$4NaBH_4 + 2Se + 7H_2O \longrightarrow 2NaHSe + Na_2B_4O_7 + 14H_2 \quad (2:1)$$

$$NaHSe + ZnCl_2 \longrightarrow ZnSe + NaCl + HCl \quad (2:2)$$

$$ZnSe + TOP \xrightarrow{HDA\,/\,TOPO} HDA/\,TOPO\text{-capped ZnSe} \quad (2.3)$$

***Scheme 1*** *The reaction scheme for the synthesis of ZnSe nanoparticles.*

### 3.3.1 Optical properties

#### 3.3.1.1 *Effect of reduction time*

The reduction was monitored between the periods of 2, 4 and 6 hrs with initial monomer concentration of the precursors being 0.32 mmol. The intensity of the colour of the reaction solution increases as the reduction time increases. The effect of these reduction times on the size and optical properties of the CdSe nanoparticles was studied, using HDA as the coordinating solvent at 160 °C.

Figures 3.1 - 3.3 show the temporal evolution of the absorption and photo-luminescence spectra of HDA-capped ZnSe nanoparticles, synthesized at reduction times of 6, 4 and 2 hrs. The absorption band-edge and emission maxima, of all the nanoparticles synthesized within these periods, are blue-shifted from the bulk band gap clearly showing quantum confinement. The spectra for particles synthesized within the period of 6 and 4 hrs reduction times, show sharp absorption edges and excitonic shoulders (Figure 3.1a and 3.2a) signifying monodispersed particles. The excitonic shoulder becomes broadened as the reduction time decreases and, is absent in the spectrum for the reduction time of 2 hrs (Figure 3.3a). The absence of the excitonic peak in the spectrum for 2 hrs reduction time, might be attributed to weak confinement because of the presence of particles with larger particle sizes.[34,35]

The shift of absorption band-edge and emission maxima to higher band gap (lower wavelength) increases with increasing reduction time, indicating decrease in particle sizes as the reduction time increases. The absorption band-edges, as calculated using the direct band gap method,[36] are as follows: 368 nm (3.37 eV) for the particles synthesised at 6 hrs reduction time which has the smallest particles sizes; 395 nm (3.14 eV) for 4 hrs and 401 nm (3.09 eV) for the largest particle sizes synthesized at 2 hrs, all blue-shifted in relation to bulk ZnSe, 480 nm (2.58 eV). This is contrary to the prediction from the colour of the solution, after addition of $ZnCl_2$ which increases in intensity as the reduction time increases signifying an increase in the particle size.

The emission maximum (Figures 3.1b - 3.3b), shows a slight red-shift in relation to the corresponding absorption band-edge, suggesting that near band-edge emission (shallow trap emission) is present. The emission maxima are 381 nm, 3.25 eV, (6 hrs); 402 nm, 3.08 eV, (4 hrs) and 407 nm, 3.05 eV, (2 hrs). The closeness of the emission maxima to the absorption edge increases as the reduction time decreases. The narrowing of the emission width and the sharpness of the luminescence increases as the reduction time decreases. The unevenness of the curve at 6 and 4 hrs reduction time suggests the presence of surface defects. As the particles size decreases the surface/volume ratio increases, thereby increasing the number of surface traps. It might also imply that the optimal surface structure/reconstruction of the nanocrystals, grown under this synthetic route, decreases (more surface defects) as the reduction time increases. This increases the effect of the atomic configuration on the surface of nanocrystals and thus, significantly affects the efficiency of the electronic passivation provided by the capping ligand.[37] The narrowest emission width and sharpest luminescence obtained under 2 hrs reduction times, indicates the growth of the

crystallites with few electronic defect sites attributed to the efficiency of the capping group in electronically passivating the surface states or defects, which are normally associated with semiconductor nanoparticles.[38-40]

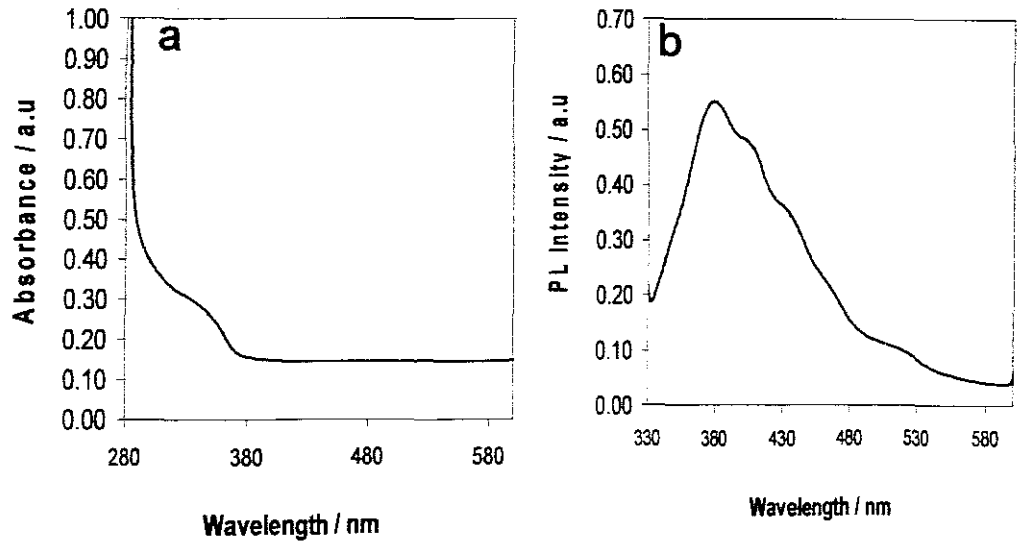


***Figure 3.1*** *(a) Absorption and (b) photoluminescence spectra of HDA-capped ZnSe nanoparticles under reduction time of 6 hrs*

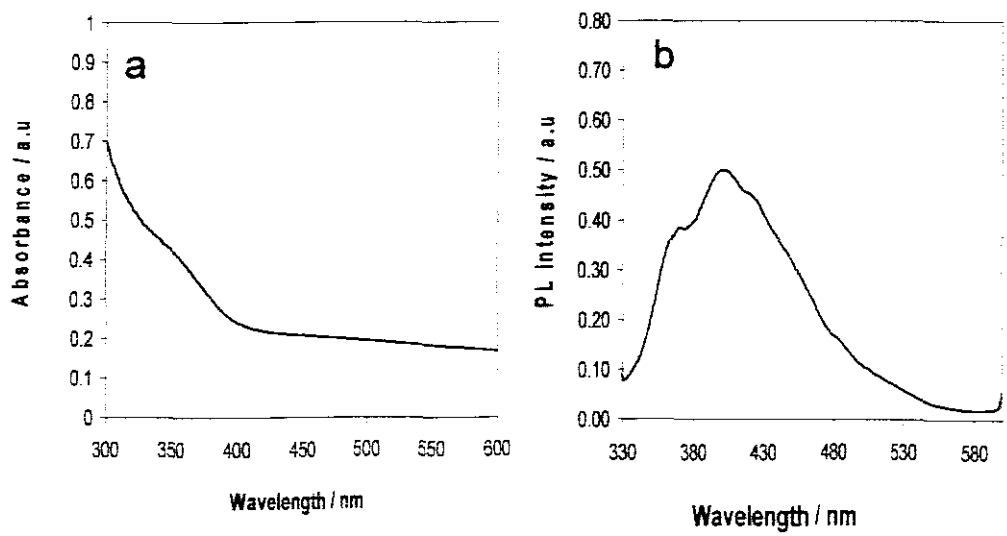


***Figure 3.2*** *(a) Absorption and (b) photoluminescence spectra of HDA-capped ZnSe nanoparticles under reduction time of 4hrs*

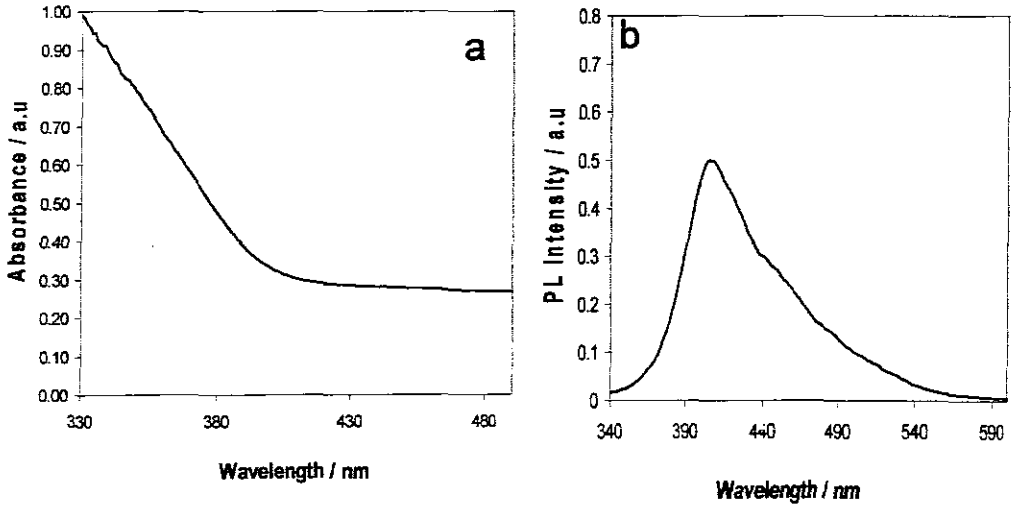


***Figure 3.3*** *(a) Absorption and (b) photoluminescence spectra of HDA-capped ZnSe nanoparticles* under *reduction time of 2 hrs*

### 3.3.1.2 *Effect of temperature*

Studies have shown that growth temperature has a major influence on the particle size and luminescent properties. The initial period after the hot injection is usually characterized by rapid growth, which results in surface disorder. Higher growth temperature leads to faster growth rates, which favours the formation of larger particle sizes and induces faster surface degradation. The effect of growth temperature was monitored by carrying-out the reactions at different temperatures of 110, 160 and 200 °C, under constant initial monomer concentration of 0.32 mmol and a reduction time of 2 hrs, using HDA and TOPO as the capping agents.

Figures 3.4 - 3.6 show the absorption and emission spectra of HDA-capped ZnSe nanoparticles, synthesized at different temperatures of 110, 160 and 200 °C. The shifts of the absorption band-edge and emission maxima to longer wavelengths as the temperature increases, clearly indicate the growth of the particles. Hence, higher

temperature favours the formation of larger particles. This has been attributed to the rate at which the ligand attaches and detaches the surface.[41] The absorption band-edges and emission maxima are all blue-shifted from the bulk band gap due to quantum confinement. The absorption band-edges as calculated, using the direct band gap method, are as follows: 365 nm, 3.40 eV (110 °C); 401 nm, 3.09 eV (160 °C) and 415 nm, 2.99 eV (200 °C). The spectra for particles synthesized at 110 and 200 °C show sharp absorption edges and excitonic shoulders (Figures 3.4a and 3.6a), indicative of monodispersed particles. The absence of an excitonic shoulder at 160 °C (Figure 3.5a), might be attributed to the disparity between the growth rate and size focusing at the reaction time (20 mins), which leads to growth via Ostwald ripening. The reoccurrence of excitonic shoulder at 200 °C is attributed to the higher growth rate at this temperature with a pronounced focusing, which leads to stability in the size distribution and sharp luminescence.[42]

The photoluminescence spectra (Figures 3.4b - 3.6b) of the as-synthesized particles exhibit band-edge luminescence at all three temperatures. The emission maxima are 367 nm, 3.38 eV (110 °C); 407 nm, 3.05 eV (160 °C) and 408 nm, 3.04 eV (200 °C). The emission maxima show a red-shift in relation to the corresponding absorption edge at 110 and 160 °C, while it is blue-shifted for the nanoparticles synthesized at 200 °C. This blue-shift of the emission maxima, in relation to absorption edge, has been observed for ZnSe synthesised at high temperatures[14,26] and is very prominent for CdSe nanoparticles. The narrow emission line widths and sharp luminescence indicate the efficiency of the capping group, in electronically passivating the surface states or defects located in the band gap of the nanocrystals, which acts as the trapping state for the photogenerated charges. The absence of broad tail, towards the

lower energy side normally associated with defect-luminescence, indicates the absence of deep- trap emission.

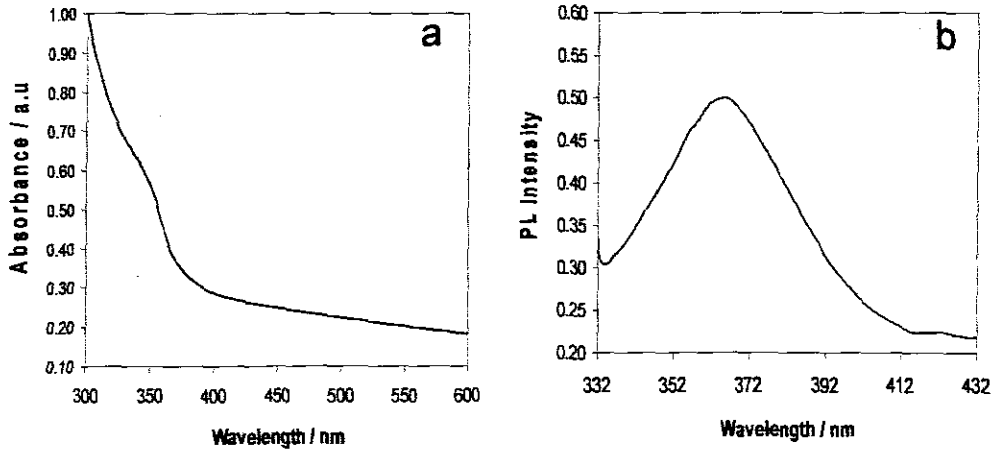


*Figure 3.4 (a) Absorption and (b) photoluminescence spectra of HDA-capped ZnSe nanoparticles at 110 °C.*

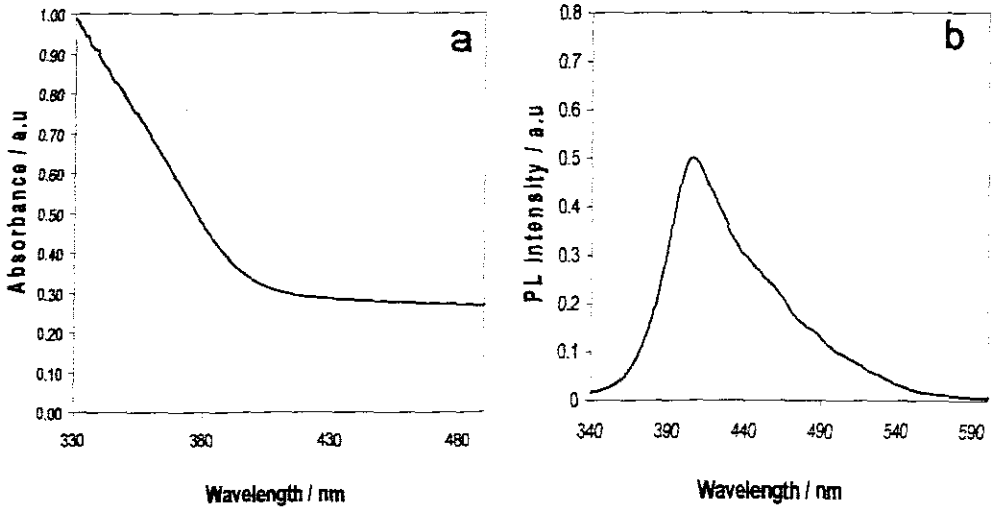


*Figure 3.5 (a) Absorption (b) photoluminescence spectra of HDA-capped ZnSe nanoparticles at 160 °C.*

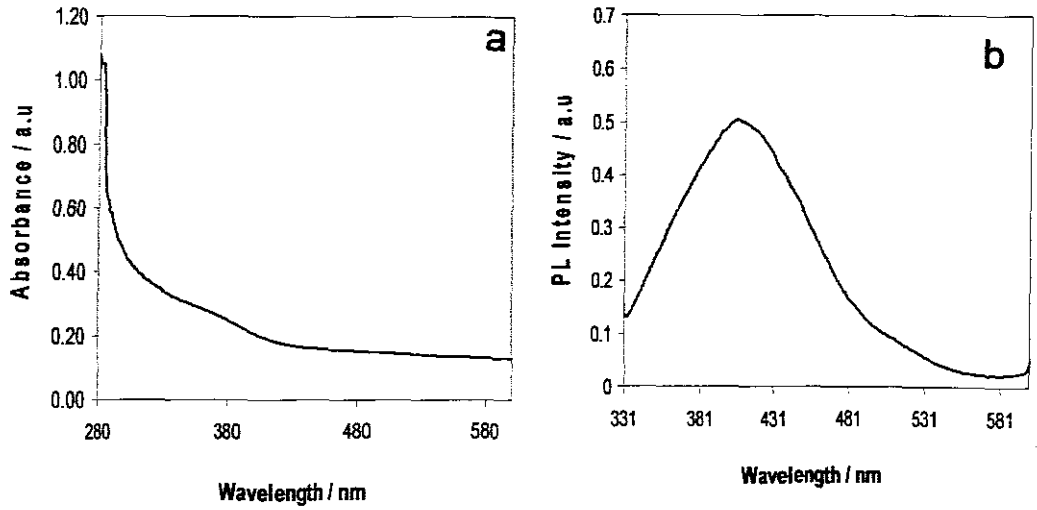


***Figure 3.6*** *(a) Absorption and (b) photoluminescence spectra of HDA-capped ZnSe nanoparticles at 200 °C*

The absorption and photoluminescence spectra shown in Figures 3.7 and 3.8 indicate that the absorption band-edge and emission maxima of TOPO-capped CdSe at different temperatures of 160 and 200 °C, are also blue-shifted from the bulk sample. The absorption band-edges (Figures 3.7a and 3.8a) as calculated, using the direct band gap method, are 3.67 eV (338 nm) and 3.12 eV (398 nm) for 160 and 200 °C respectively. The shifts of the absorption band-edge to lower band gap as the temperature increases, indicates an increase in the particle size. The absorption band-edge of the TOPO-capped particles is blue-shifted, as compared to the HDA-capped particles synthesized at the same temperature, indicating decrease in particle size. This might be due to the high molecular weight of HDA compared to TOPO, which suppresses the crystal growth of the ZnSe nanoparticles. The amine forms Zn-amine complexes in the source solution, which decreases the diffusion rate of the complexes in the product solution, leading to larger particle sizes. Unlike the HDA-capped

ZnSe, there is an absence of an excitonic shoulder in the spectra for TOPO-capped particles. This might be due to either the overlap of absorption by TOPO in this region or a large size distribution.

The emission maxima shown in Figures 3.7b and 3.8b are red-shifted as the temperature increases due to the increase in the particle size. The emission spectra for samples synthesized at 160 °C (Figure 3.7b) show two maxima peaks at 348 nm (3.56 eV) and 362 nm (3.43 eV), while the emission spectra for the particles synthesized at 200 °C (Figure 3.8b) show a single emission maximum at 388 nm (3.20 eV). Similar to the HDA-capped ZnSe at 200 °C, the emission maximum is also blue-shifted in relation to the absorption edge. The absence of the defect emission at 200 °C could be attributed to higher growth temperature. This higher temperature encourages prolonged annealing, which allows surface ordering and reconstruction to subsequently take place and hence, reduces the concentration of defects.[42]

Unlike CdSe nanoparticles described in chapter two, there is no significant difference between the PL intensity of the HDA-capped and TOPO-capped ZnSe nanoparticles prepared under this synthetic route. This confirms that the surface states present in the ZnSe nanocrystals, were sufficiently passivated by the two capping groups

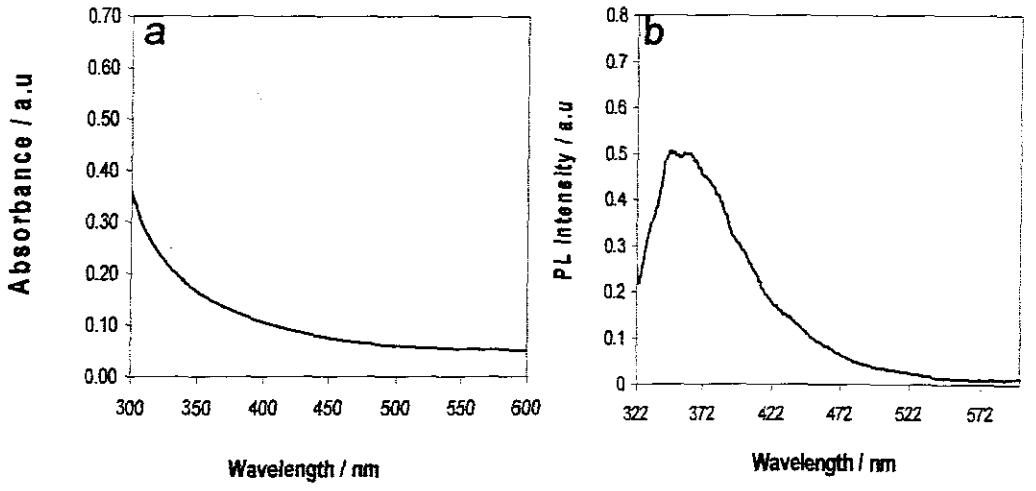


***Figure 3.7*** *(a) Absorption and (b) photoluminescence spectra of TOPO-capped ZnSe nanoparticles at 160 °C.*

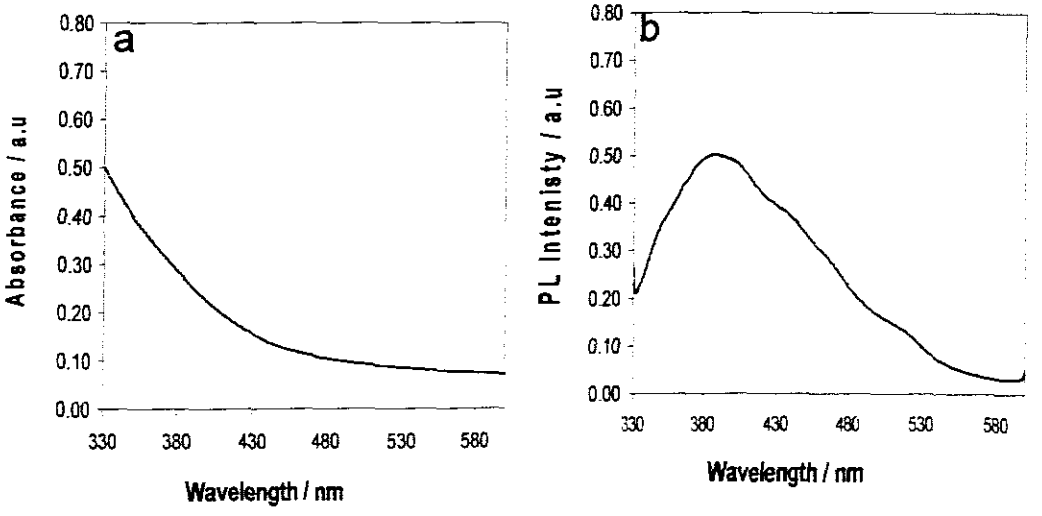


***Figure 3.8*** *(a) Absorption and (b) photoluminescence spectra of TOPO-capped ZnSe nanoparticles at 200 °C*

### 3.3.1.3 *Effect of monomer concentration*

The amount of precursor concentration injected into the hot coordinating solvent, is considerably important to determine the growth and size of the nanocrystals. Increasing the initial precursor concentration may lead to a significant

change in size, morphology and emission properties of the as-synthesized nanoparticles. Higher monomer concentration usually leads to an increase in particle size and narrowing of the size distribution.[43-47] The effect of monomer concentration was studied by increasing the monomer concentration from 0.32 mmol to 0.64 mmol and carrying out the reactions at different temperatures of 110, 160 and 200 °C, under the reduction time of 2 hrs with HDA and TOPO as the capping agent.

The absorption spectra for the HDA-capped nanoparticles synthesized, using 0.64 mmol at different temperatures, are shown in Figures 3.9a - 3.11a. All the absorption band-edges are blue-shifted in relation to the bulk band gap, indicating quantum confinement. The absorption band-edges as calculated, using the direct band gap method are as follows : 416 nm, 2.98 eV (110 °C); 420 nm, 2.95 eV (160 °C) and 431 nm, 2.88 eV(200 °C). The absorption band-edge increases as the temperature increases, signifying an increase in the particle size. In general, there is an increase in the particle size of the nanoparticle synthesized with 0.64 mmol when, compared with those synthesized using 0.32 mmol. This is confirmed by the shifting of the absorption band-edge to higher wavelengths. The particles synthesized at higher monomer concentration show no visible excitonic features but, a tailing band-edge is present. This might be due to large particle sizes produced as a result of the increase in the monomer concentration. Higher monomer concentration leads to a large number of smaller nuclei immediately after hot injection and these quickly grow into larger particles, hence the presence of the tailing band-edge.

Figures 3.9b - 3.11b show the emission spectra for the ZnSe nanoparticle synthesized at higher monomer concentration. All the emission maxima are blue-shifted in

relation to the bulk band gap. The emission maxima are 429 nm, 2.89 eV (110 °C); 444 nm, 2.79 eV (160 °C) and 454 nm, 2.73 eV (200 °C). These are red-shifted in relation to the corresponding absorption band-edges, signifying band-edge emission. Similar to the absorption band-edge, all the emission maxima increase as the temperature increases and are shifted to higher wavelengths, as compared to those synthesized at lower monomer concentration. This also confirms that, increasing the monomer concentration leads to larger particle sizes. The emission widths are narrow but the spectra are not symmetrical, suggesting the presence of surface defects. These might be attributed to insufficient passivation of the surface state located in the band gap of the nanocrystals, as a result of a faster growth rate at a higher monomer concentration.

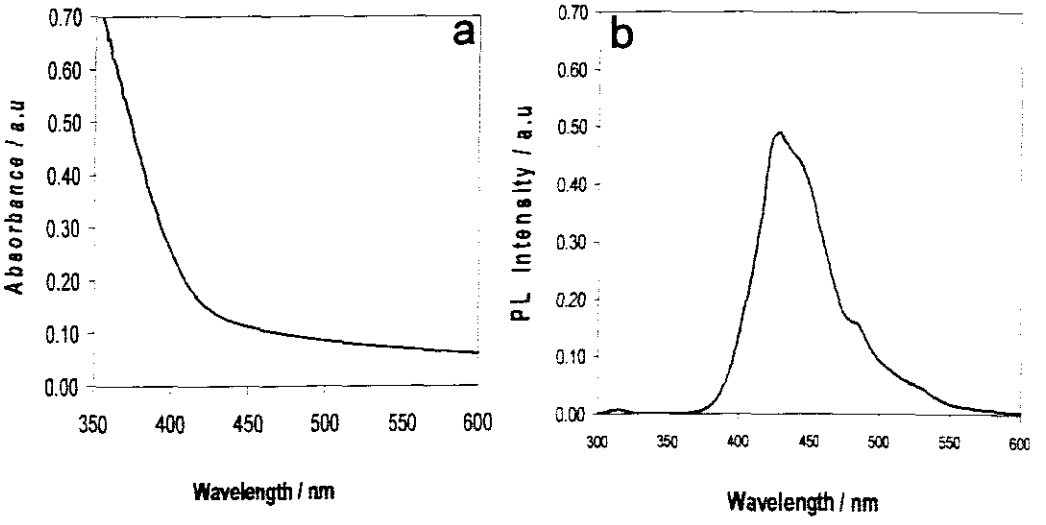


***Figure 3.9*** *(a) Absorption and (b) photoluminescence spectra of HDA-capped ZnSe nanoparticles at 110 °C, under 0.64 mmol monomer concentrations.*

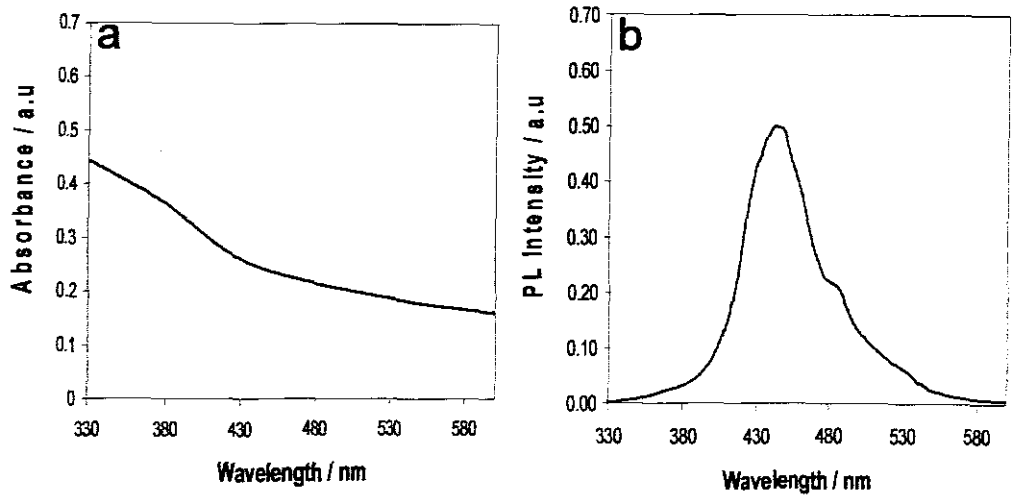


***Figure 3.10*** *(a) Absorption (b) photoluminescence spectra of HDA-capped ZnSe nanoparticles* at *160 °C under 0.64 mmol monomer concentrations.*

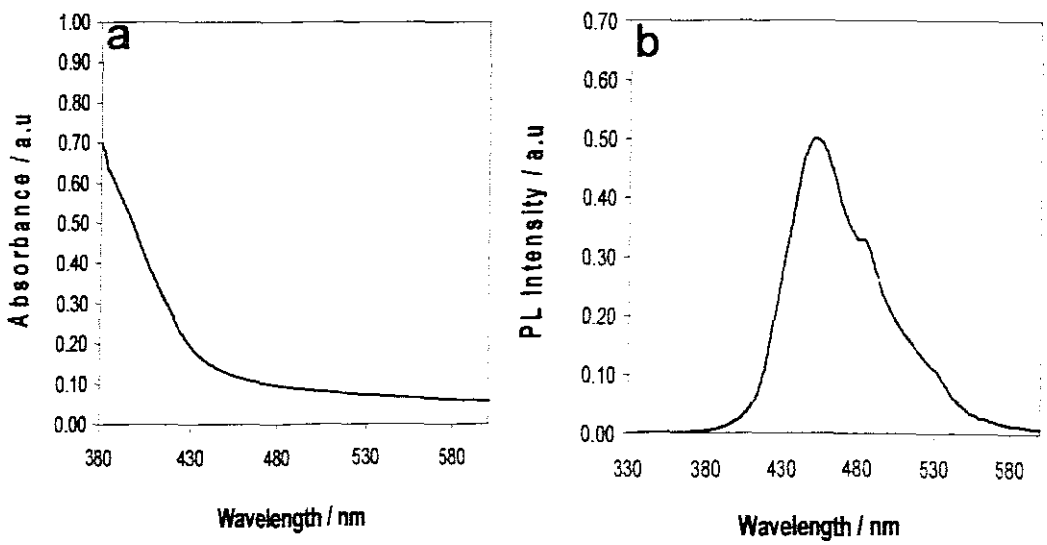


***Figure 3.11*** *(a) Absorption spectra and (b) Photoluminescence of HDA-capped ZnSe nanoparticles* at *200 °C under 0.64 mmol monomer concentrations.*

The absorption band-edge and emission maxima of the TOPO-capped ZnSe at higher monomer concentration and at different temperatures, as shown in Figures 3.12 and

3.13, are all blue-shifted from the bulk band gap. The absorption band-edges (Figures 3.12a and 3.13a) as calculated, using the direct band gap method are : 369 nm, 3.36 eV (160 °C) and 425 nm, 2.92 eV (200 °C). The absorption band-edge increases as the temperature increases and the results obtained at higher monomer concentration, are larger than the values calculated at lower concentration signifying an increase in the particle size. However, similar to the results obtained at lower monomer concentration, the absorption band-edge of the TOPO-capped particles at higher concentration, are also blue-shifted as compared to the HDA-capped particles synthesized at the same temperature, indicating a decrease in particle size.

The emission spectra for the TOPO-capped ZnSe nanoparticles synthesized at higher monomer concentration (Figures 3.12b and 3.13b), also exhibit band-edge luminescence. The emission maxima are 385 nm, 3.22 eV (160 °C) and 433 nm, 2.86 eV (200 °C). The emission maxima follow a similar trend to the absorption band-edge; they increase as the temperature increases, are shifted to lower band gap compared to those synthesized at lower monomer concentration and, are blue-shifted as compared to the HDA-capped particles synthesized at the same temperature. The emission spectra at 200 °C are smoother and narrower than those synthesized at 160 °C. This might be attributed to the fact that higher temperatures allow surface ordering and reconstruction to take place, thereby reducing the concentration of defects.[42]

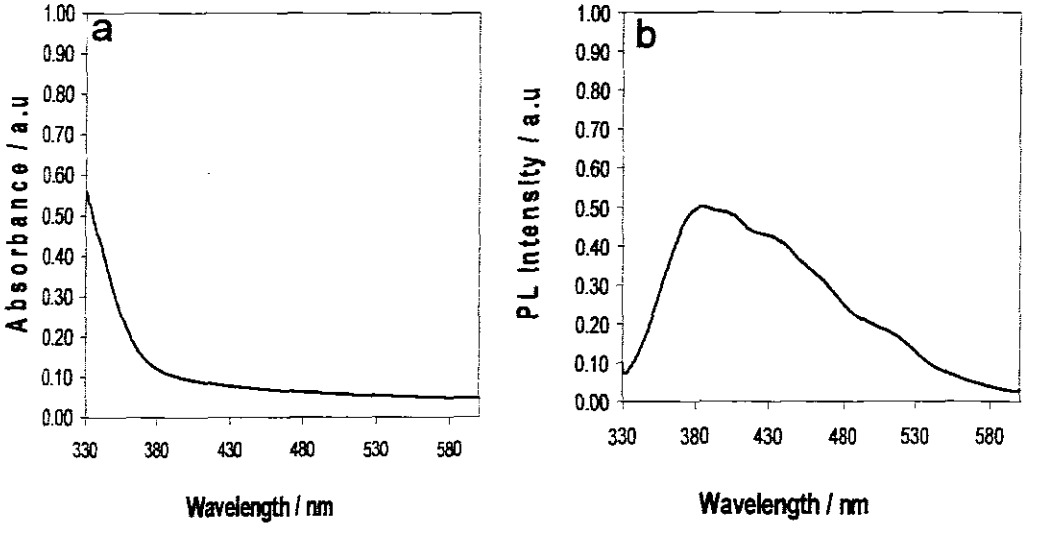


*Figure 3.12 (a) Absorption and (b) photoluminescence of TOPO-capped ZnSe nanoparticles at 160 °C under 0.64 mmol monomer concentrations.*

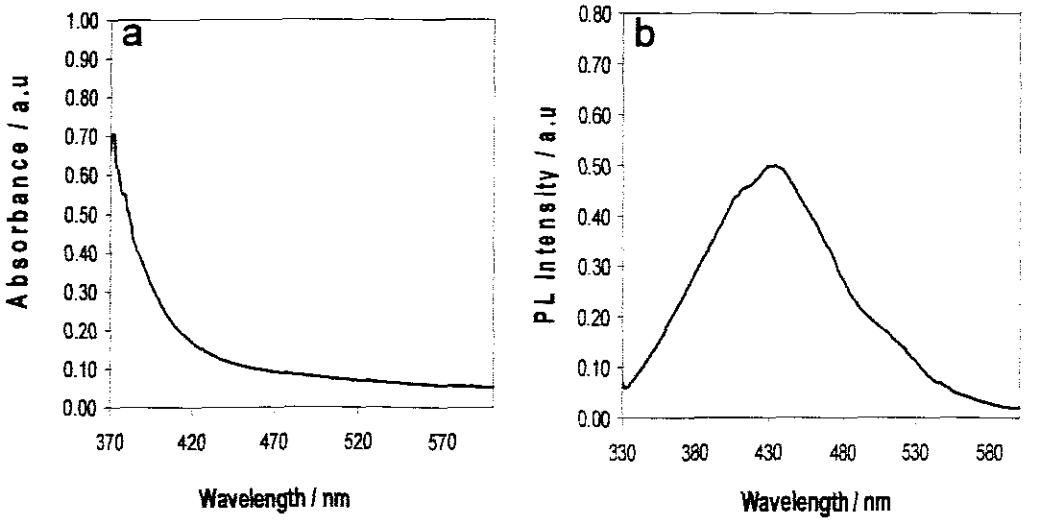


*Figure 3.13 (a) Absorption and (b) photoluminescence of TOPO-capped ZnSe nanoparticles at 200 °C under 0.64 mmol monomer concentrations.*

### 3.3.1.4 *Synthesis using $Zn(CH_3COO)_2$*

Studies have shown that different sources of precursors sometimes have a significant influence on the size, optical and morphological properties of nanocrystals. Under this reaction regime, we have used $Zn(CH_3COO)_2$ in place of $ZnCl_2$ as the zinc source. Our approach was based on two motives. Firstly, of all three temperatures (110, 160 and 200 °C) studied at lower monomer concentration (0.32 mmol) and under reduction time of 2 hrs, the nanocrystals produced at 160 °C did not show any excitonic shoulders. This prompted us to see if there will be any significant difference in the optical properties of the ZnSe nanoparticles synthesised, by changing the zinc source. Secondly, to investigate whether this synthetic route can also accommodate the use of another precursor, such as $Zn(CH_3COO)_2$ as its cadmium analogue had proved to be an excellent precursor in place of CdO.[48]

The absorption and emission spectra of the ZnSe nanoparticles synthesised, using $Zn(CH_3COO)_2$ as the zinc precursor, are shown in Figure 3.14. The absorption band-edge as calculated using the direct band gap method is 375 nm (3.31 eV), which is blue-shifted in relation to the one synthesised using $ZnCl_2$ as the zinc source, signifying a smaller particle size. Unlike the $ZnCl_2$ produced nanoparticles, the spectrum (Figure 3.14a) shows the presence of an excitonic peak at 334 nm and a sharp absorption edge, such as those synthesized at 110 and 200 °C, which is indicative of particles with a narrow size distribution. The emission maximum is at 410 nm (3.02 eV) and is red-shifted from the absorption band-edge, without any deep-trap emission. The emission spectrum (Figure 3.14b) is symmetrical, smoother and narrower than the one obtained using $ZnCl_2$ as precursor. This signifies the presence of fewer electronic defect sites hence, an increase in the capping efficiency.

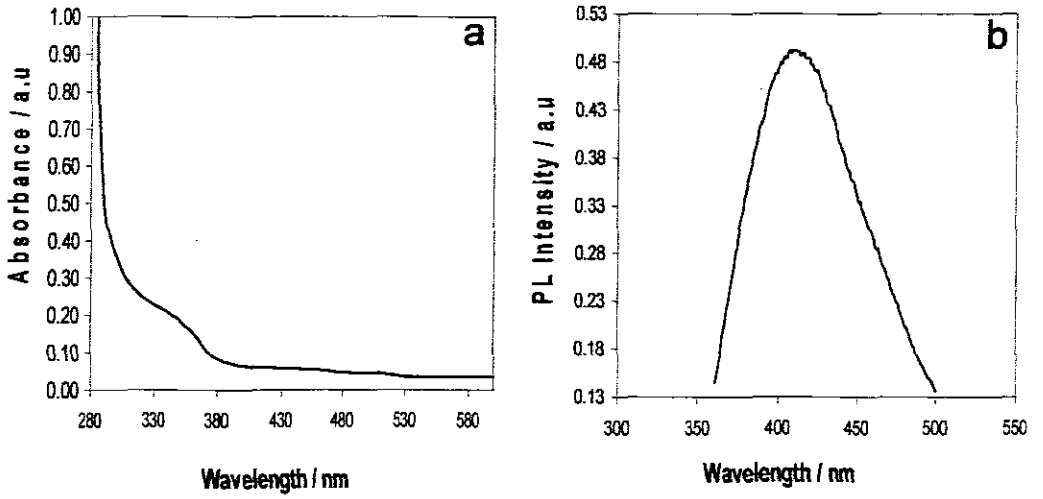


***Figure 3.14*** *(a) Absorption (b) photoluminescence of HDA-capped ZnSe nano-particles at 160 °C using 0.32 mmol of $Zn(CH_3COO)_2$ as the zinc precursor.*

### 3.3.2 Structural characteristics

#### 3.3.2.1 *Transmission electron microscope (TEM)*

The size, shape and size-distribution of some of the nanoparticles were examined using TEM. Figures 3.15 - 3.17, show the TEM images and particle size distribution of the HDA-capped ZnSe synthesised under reduction times of 2, 4 and 6 hrs after the growth time of 20 mins. The TEM (Figures 3.15 and 3.16) images of the selected fractions under reduction times of 6 and 4 hrs show well-defined, monodispersed spherical particles, while those under the reduction time of 2 hrs show larger particles (Figure 3.17) which are very close to each other, appearing as aggregates. This might be responsible for the absence of the excitonic shoulder in the absorption spectra under this reduction time. The average particle sizes as determined from the TEM images for the reduction time of 2, 4 and 6 hrs are, 3.71 ± 0.40 nm 3.26 ± 0.37 nm and 2.95 ± 0.32 nm respectively. The increase in the average

diameter, as the reduction time decreases, corresponds with the observed red-shift in the absorption band-edge from 6 hrs to 2 hrs reduction time. The relative standard deviation of the size of the nanoparticles (± 10.82 %, 6 hrs; ± 11.25 %, 4 hrs and ± 10.74 %, 2 hrs), confirms the narrow size distribution of the nanoparticles.

The TEM image and particle size distribution of HDA-capped ZnSe nanoparticles, synthesised at a higher monomer concentration (0.64 mmol) under reduction time of 2 hrs, is shown in Figure 3.18. The particles are spherical in shape, well-dispersed and larger, with a narrow size distribution compared to those synthesised at lower monomer concentration. The average particle size as determined from the TEM images for the selected fraction, is 4.41 nm ± 0.40 nm. The relative standard deviation of the size of the nanoparticles (± 9.14 %,), confirms the narrow size distribution of the nanoparticles.

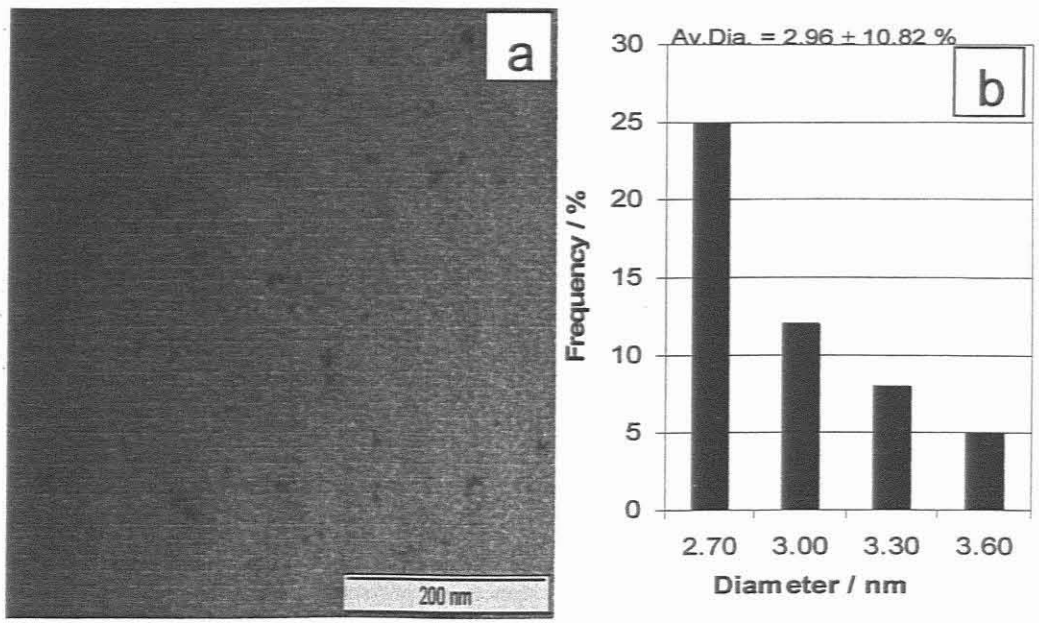


***Figure 3.15*** *(a) TEM and (b) particle size distribution of HDA-capped ZnSe nano-particles synthesised at reduction time of 6 hrs.*

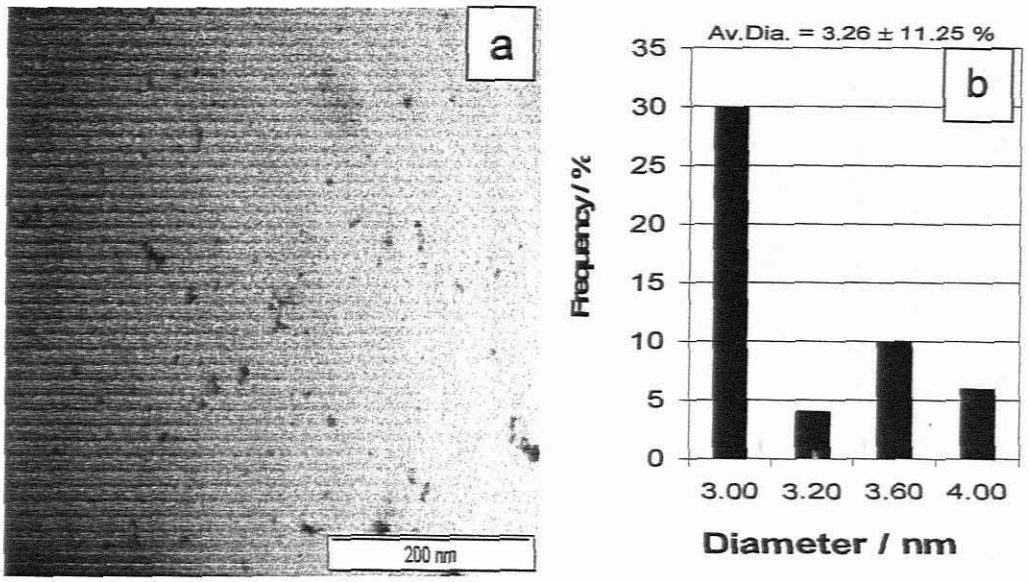


***Figure 3.16*** *(a) TEM and (b) particle size distribution of HDA-capped ZnSe nanoparticles synthesised at reduction time of 4 hrs.*

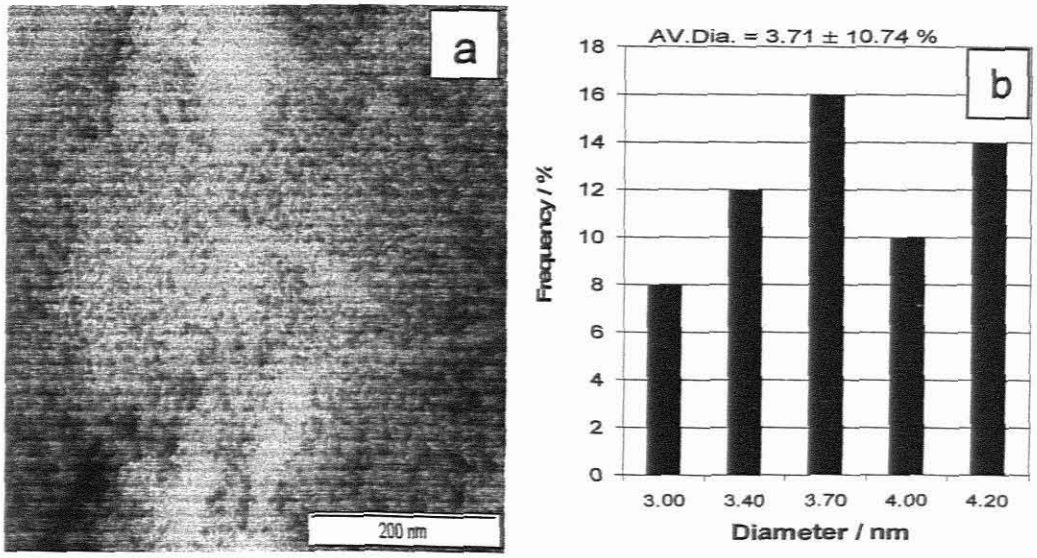


***Figure 3.17*** *(a) TEM and (b) particle size distribution of HDA-capped ZnSe nanoparticles synthesised at reduction time of 2 hrs.*

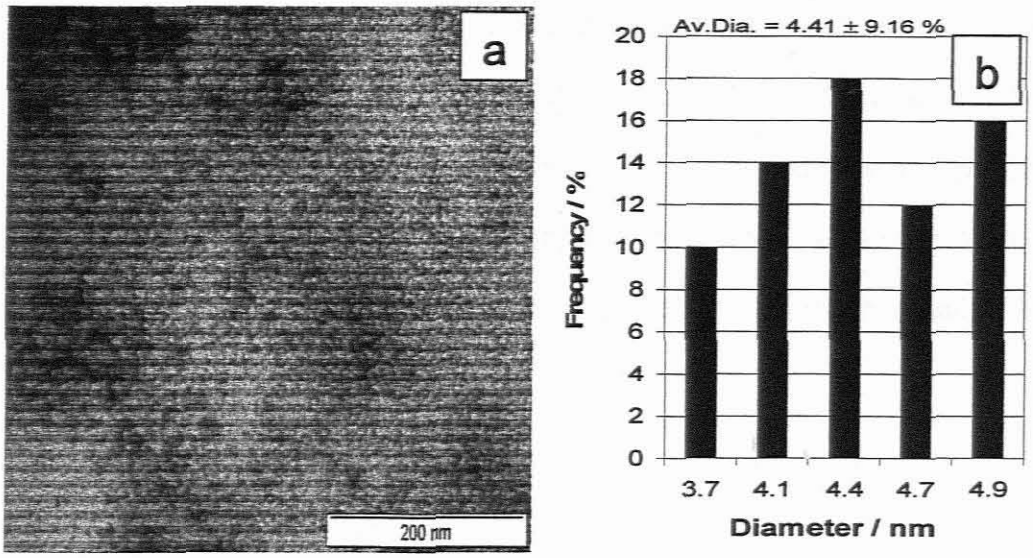


***Figure 3.18*** *(a) TEM and (b) particle size distribution of HDA-capped ZnSe nano-particles under reduction time of 2 hrs at 0.64 mmol monomer concentration.*

Figure 3.19 shows the TEM image and particle size distribution of TOPO-capped ZnSe nanoparticles synthesised, using a higher monomer concentration (0.64 mmol) under a reduction time of 2 hrs at 200 °C. The TEM image consists of both spherical and a small amount of elongated nanoparticles. The average particle sizes for the selected fraction, as determined from the TEM images, is 4.54 nm ± 0.35 nm. The slight increase in the particle size, as compared to the HDA-capped particles at 160 °C under the same monomer concentration, is consistent with observed slight red-shift in the absorption band-edge, 420 nm, 2.95 eV(160 °C, HDA) and 425 nm, 2.92 eV(200 °C, TOPO). The presence of elongated particles could be attributed to the phenomenon of oriented attachment (self -assembly), due to dipole-dipole interactions between the highly charge surface of II-VI semiconductor nanocrystals.[49,50] Figure 3.19 shows that the elongated particles consist of short and long rods. The shorter ones are formed by the fusion between two dots particles (marked as I), while the longer rods are formed as a result of the fusion between three

or more dot particles (marked as II). It also shows two dot particles about to join together but separated with a gap (marked as III). According to Wang and his co-workers, adhesion between nanocrystals can induce a significant change on their morphology and hence, cause a transition from dot to rod shape.[43] They attributed the gap between the two dots which should form a perfect rod, to incomplete adhesion between the nanoparticle "adhesives".

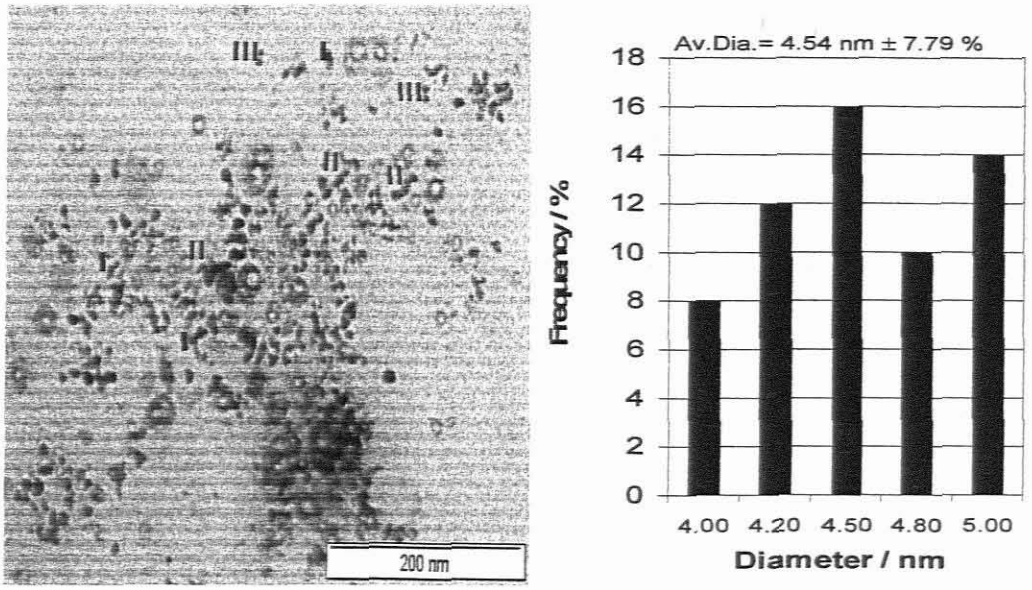


***Figure 3.19*** *(a) TEM and (b) particle size distribution of TOPO-capped ZnSe nano-particles at 200 °C using 0.64 mmol monomer concentration.*

### 3.3.2.2 *X-ray diffraction pattern (XRD)*

The crystallinity and phases of the synthesised nanoparticles was explored by X-ray diffraction (XRD). Figures 3.20 - 3.22 show the wide angle X-ray diffraction patterns of the HDA-capped ZnSe nanocrystals, at a reduction time of 2, 4 and 6 hrs after 20 mins of growth. Due to the small particle size, the diffractograms of the as-synthesised particles at higher reduction time (Figures 3.20 and 3.21) show broad peaks from which a clear identification, of the exclusive existence of either phase, is

obviously difficult to assign with complete certainty. As the reduction time decreases, the crystallinity improves and the diffraction peaks becomes more clearly resolved (Figure 3.22). This shows that particle size increases with decreasing reduction time as expected from the absorption shift.

The XRD pattern of the prepared HDA-capped ZnSe nanocrystals after reduction time of 2 hrs at 160 °C, shows three diffraction peaks corresponding to the (111), (220) and (311) planes of sphalerite cubic ZnSe with a lattice constant of a = 5.667, which is consistent with the JCPDS card number 80-0021 for cubic ZnSe. The mean particle diameter was calculated to be 3.2 nm from the Scherrer equation.[51] a value smaller than that obtained from the TEM analysis. This difference could be attributed to the fact that the scherrer equation probes only the crystalline region and does not take into account the thickness of the capping layer.[52]

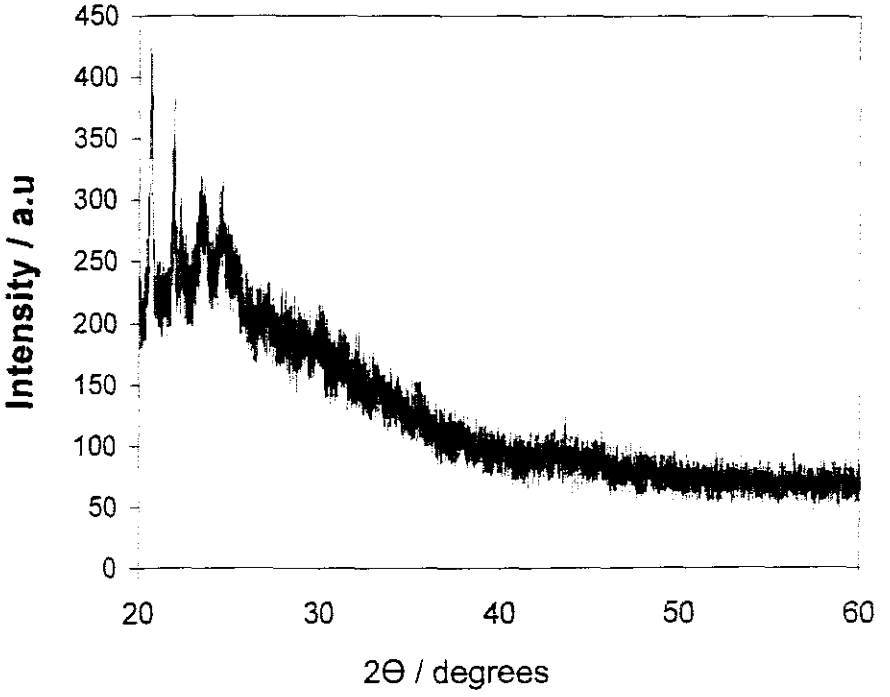


***Figure 3.20*** *XRD pattern of HDA-capped ZnSe under reduction time of 6 hrs at 160 °C using 0.32 mmol concentration*

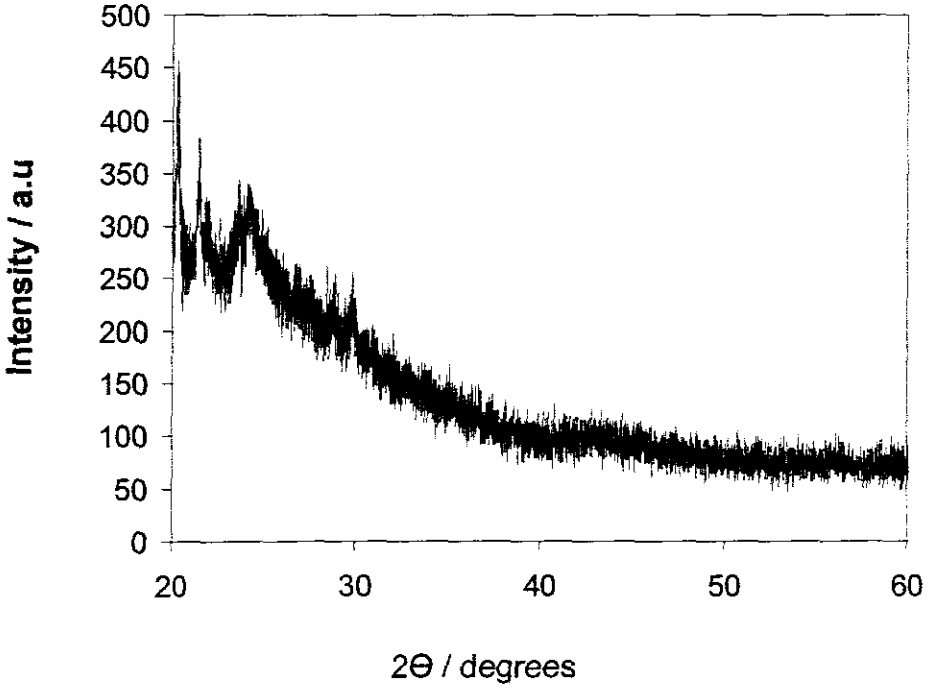


***Figure 3.21*** *XRD pattern of HDA-capped ZnSe under reduction time of 4 hrs at 160 °C using 0.32 mmol concentration.*

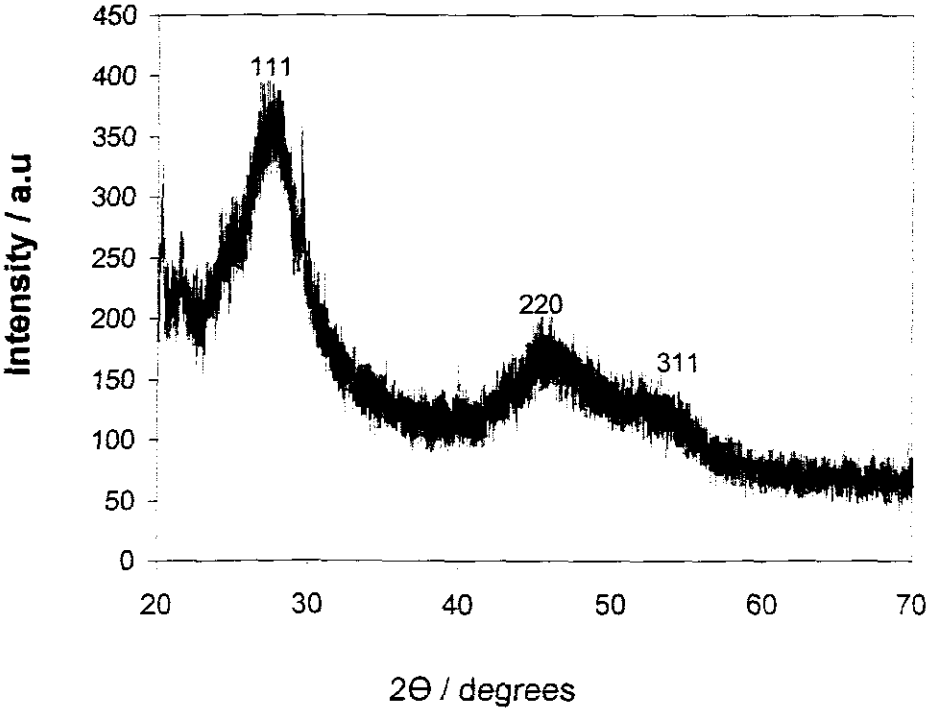


***Figure 3.22*** *XRD pattern of HDA-capped ZnSe under reduction time of 2 hrs at 160 °C using 0.32 mmol concentration.*

The XRD pattern of the HDA-capped ZnSe nanocrystals synthesised at 160 °C using a higher monomer concentration (0.64 mmol) and, at different growth times, are shown in Figures 3.23 and 3.24. The results show that there is gradual phase transition from the face centred cubic to the hexagonal phase, as the growth time increases. The XRD pattern of the nanoparticles after 2 mins of growth (Figure 3.23), shows three diffraction peaks corresponding to the (111), (220) and (311) planes of sphalerite cubic crystalline ZnSe with a lattice constant of a=5.667. While the nanoparticles synthesised at 20 mins, Figure 3.24 shows diffraction peaks at 2θ values of 22.3°, 23.5°, 27.9°, 37.8°, 46.2°, 50.2° and 54.4°, corresponding to the respective (100), (002), (101), (102), (110), (103) and (112) diffraction planes of hexagonal wurtzite-type ZnSe with a lattice constant of a = 3.974, c = 6.506, consistent with the JCPDS card number 89-2940 for hexagonal ZnSe. Excessive attenuation in the (102) and (103) planes has been attributed to the characteristic stalking faults in the wurtzite-type structure.[38] The mean particle diameter as calculated using Scherrer's equation are 4.3 nm ( 2 mins) and 5.5 nm (20 mins).

Figure 3.25 shows the XRD pattern of the TOPO-capped ZnSe nanocrystals prepared at 160 °C, using higher monomer concentration (0.64 mmol) and in 20 mins time of growth. The three diffraction peaks in the XRD patterns at (111), (220) and (311) correspond to the reflection of sphalerite cubic crystalline ZnSe with a lattice constant of a = 5.667.

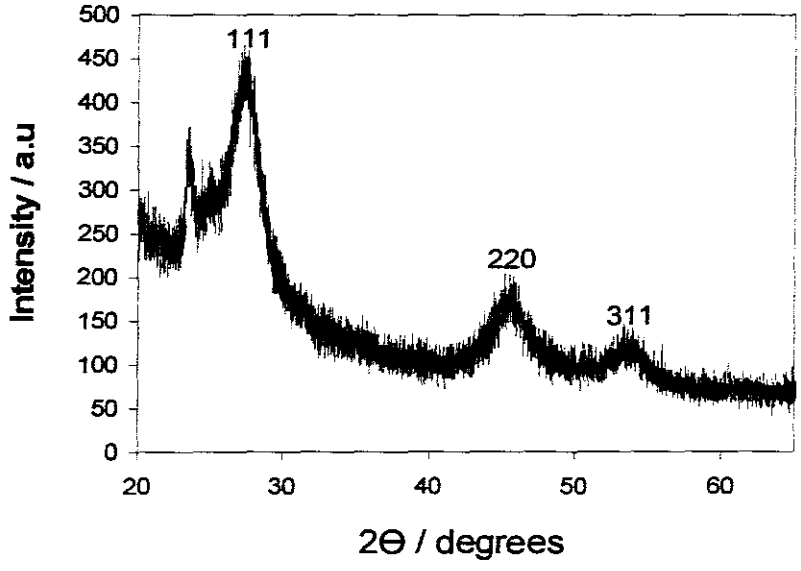


***Figure 3.23*** *XRD pattern of HDA-capped ZnSe prepared using 0.64 mmol monomer concentration, under reduction time of 2 hrs at 2 mins growth time.*

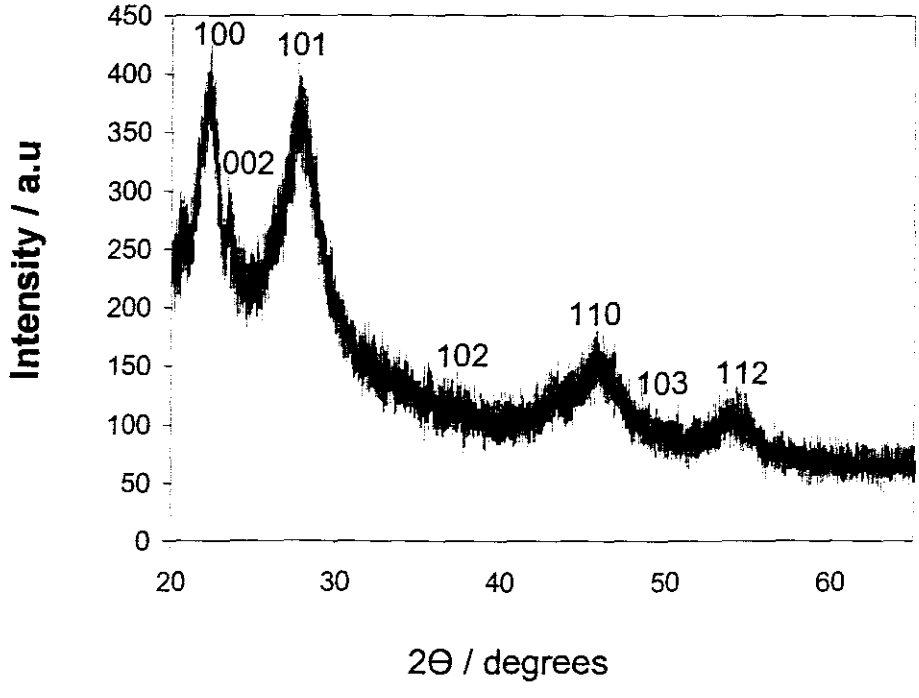


***Figure 3.24*** *XRD pattern of HDA-capped ZnSe prepared using 0.64 mmol monomer concentration, under reduction time of 2hrs at 20 mins growth time.*

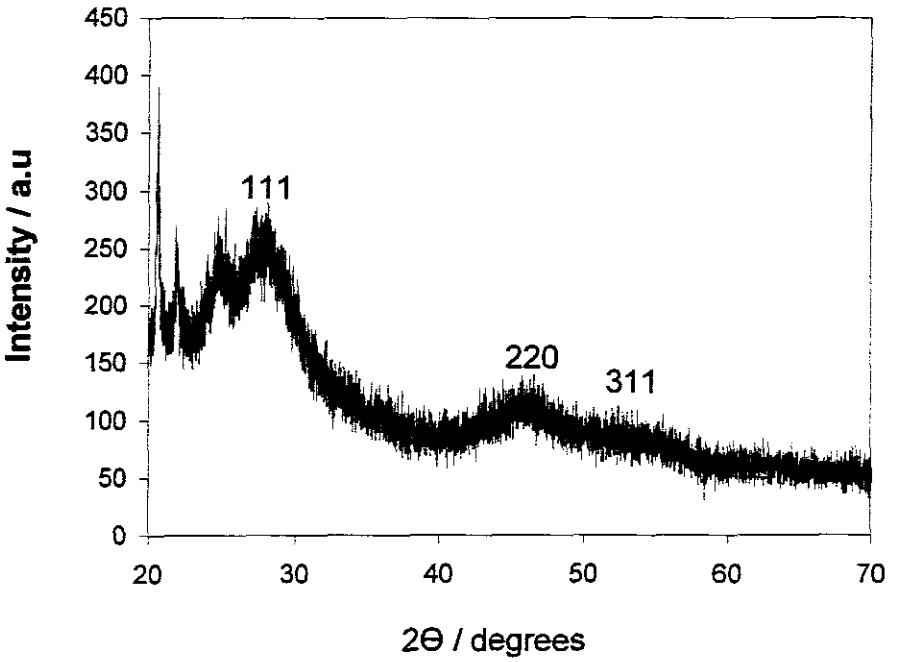


***Figure 3.25*** *XRD pattern of TOPO-capped ZnSe prepared using 0.64 mmol monomer concentrations at 160 °C.*

### 3.3.2.3 *Infrared spectroscopy (IR)*

The IR spectrum of HDA-capped ZnSe nanoparticles shows bands that are shifted to higher frequencies and, are of low intensity when compared with the free ligand. This shift has been reported for amine bound to nanocrystals and was attributed to the coordination between amine and the nanocrystallites.[52] The appearance of a peak at 467.72 $cm^{-1}$ and 350.07 $cm^{-1}$ associated with ZnSe which are absent in the free ligand, further confirmed the coordination of ZnSe to the HDA-capping group.

### 3.4 Conclusions

Good quality HDA- and TOPO-capped ZnSe nanoparticles have been synthesised, using our newly-developed, safe, inexpensive, facile and non-organometallic synthetic route. Zinc chloride and selenium powder were used as zinc and selenide ion precursors respectively, without the use of any additional stabiliser. The ZnSe nanoparticles produced are passivated using TOPO and HDA. Optical and structural analysis show the samples are of high quality and are all blue-shifted in relation to the bulk band gap, clearly showing quantum confinement. The nanoparticles have a narrow size distribution and exhibit band-edge luminescence.

A systematic study of the effect of reduction time, temperature, monomer concentration, capping group and zinc precursors on the absorption, size, emission properties and morphology of the as-synthesized nanoparticles, was also explored. Absorption and emission maxima are shifted to lower band gap (higher wavelengths), as the reduction time decreases from 6 to 2 hrs, indicating an increase in particle size. Increasing the monomer concentration and temperature, led to a faster growth rate, increase in particle sizes and narrowing of the size distribution. The PL intensity of the HDA- and TOPO-capped ZnSe show no significant difference. However, the absorption band-edge of the TOPO-capped particles are blue-shifted, as compared to the HDA-capped particles synthesized at the same temperature, reduction time and monomer concentration. This has been attributed to the high molecular weight of HDA compared to TOPO, which suppresses the crystal growth of the ZnSe nanoparticles. The use of Zn $(CH_3COO)_2$ as zinc precursor, improved the optical properties of ZnSe nanoparticles and showed that this synthetic route, is not limited to only one precursor.

The TEM images of the selected fractions under reduction times of 6 and 4 hrs, show well-defined, monodispersed, spherical particles, while those synthesised under the reduction time of 2 hrs, show larger particles that are very close to each other, appearing as aggregates. The mean average particle diameter are, 3.71 ± 0.40 nm 3.26 ± 0.37 nm and 2.95 ± 0.32 nm for the reduction time of 2, 4 and 6 hrs respectively. Increasing the monomer concentration produced larger particles that are spherical in shape, well-dispersed and with a narrow size distribution. The TEM image of TOPO-capped ZnSe nanoparticles, synthesised at higher monomer concentration, consists of both spherical and small amounts of elongated nanoparticles. The formation of elongated particles was attributed to the phenomenon of oriented attachment, due to dipole-dipole interactions between the highly charged surface of II-VI semiconductor nanocrystals. The broad nature of the XRD peaks, confirm the nanocrystalline nature of the material, with phase transitions from sphalerite cubic to wurtzite hexagonal phase, on increasing the monomer concentration. The appearance of peaks, associated with ZnSe in the IR spectrum which are absent in the free ligand and, the appearance of IR bands at higher frequency in relation to the free ligand, confirmed the coordination of ZnSe to the HDA-capping group.

## 3.5 References


1) R. R. Alfano, O. Z. Wang, J. Jumbo and B. Bhargava, *J. Phys. Rev. A*, 1987, **35**, 459.

2) A. Ennaoui, S. Siebntrit, M. C. Lux-Steiner, W. Riedl and F. Karg, *Solar Energy Mater. Solar Cells*, 2001, **67**, 31.

3) K. R. Murali, K. Thilakvathy, S. Vasantha and Rachel Ooomen, *Chalcogenide Lett.*, 2008, **5**, 111.

4) A. P. Alivisatos, *Science*, 1996, **271**, 933.

5) H. Luo and J. K. Furdyna, *Semicond. Sci. Technol.*, 1995, **10**, 1041.

6) P. Qi, Y. J. Dong and Y. D. Li, *Angew. Chem. Int. Ed.*, 2003, **42**, 3027.

7) M. A. Haase, J. Qiu, J. M. Depuydt and H. Cheng, *Appl. Phys. Lett.*, 1991, **58**, 1272.

8) H. Jeon, J. Ding, W. Patterson and A. V. Nurmiko, *Appl. Phys. Lett.*, 1991, **59**, 3619.

9) L. Li, W. Q. Sheng, D. Y. Ping and W. P. Ming, *Mater. Lett.*, 2005, **59**, 1623.

10) N. Kouklin, L. Menon, A. Z. Wong, D. W. Thompson, J. A. Woollam and P. F. Williams, *Appl. Phys. Lett.*, 2001, **79**, 4423.

11) C. C. Kim, S. Sivananthan, *Phys. Rev. B*, 1996, **53**, 1475.

12) G. F. Neumark, R. M. Park and J. M. Depuydt, *Phys. Today*, 1994, **47**, 26.

13) C. D. Lokhande, P.S. Patil, H. Tributsch and A. Ennaousi, *Solar Energy Mater.*,1998, **55**, 379.

14) M. A. Hines and P. J. Guyot-Sionnest, *J. Phys. Chem.* B, 1998, **102**, 3655.

15) N. Chestnoy, R. Hull and L. E. Brus, *J. Chem. Phys.*, 1986, **85**, 2237.

16) V. J. Leppert, S. H. Risbud and M. J. Fendorf, *Philos. Mag. Lett.*, 1997, **75**, 29.

17) G. Li and M. J. Nogami, *Appl. Phys.*, 1994, **75**, 4276.

18) P. Reiss, G. Quemard, S. Carayon, J. Bluese, F. Chandezon and A. Pron, *Mater. Chem. Phys.*, 2004, **84**, 10.

19) W. Wang, Y. Geng, P. Yan, F. Liu, Y. Xie and Y. Qian, *Inorg. Chem. Commun.*, 1999, **2**, 83.

20) W. Wang, Y. Geng, P. Yan, F. Liu, Y. Xie and Y. Qian, *J. Am .Chem. Soc.*, 1999, **121**, 4062.

21) M. S. Selim, R. Seoudi and A. A. Shabaka, *Mater. Lett.*, 2005, **59**, 2650.

22) N. Revaprasadu, M. A. Malik, P. O'Brien, M. M. Zulu and G. Wakefield, *J. Mater. Chem.*, 1988, **8**, 1885.

23) B. Ludolph, M. A. Malik, P. O'Brien and N. Revaprasadu, *Chem. Commun.*, 1998, 1849.

24) M. Afzaal, S. M. Aucott, D. Crouch, P. O'Brien, J. D. Woollins and J. H. Park, *Chem. Vap. Deposition*, 2002, **8**, 187.

25) M. Afzaal, D. Crouch, M. A. Malik, M. Motevalli, P. O'Brien, J. H. Park and J. D. Woollins, *Eur. J. Inorg. Chem.*, 2004, 171.

26) S. L. Cumberland, K. M. Hanif, A. Javier, G. A. Khitrov, G. F. Strouse, S. M. Woessner and C. S. Yun, *Chem. Mater.*, 2002, **14**, 1576.

27) B. P. Zhang, T. Yasuda, Y. Segawa, H. Yaguchi, K. Onabe, E. Edamatsu and T. Itoh, *Apply. Phys. Lett.*, 1997, **70**, 2413.

28) C. E. D. Bourrait, *Appl. Phys. Lett.*, 1996, **68**, 2418.

29) H. Jorkaala and H. Stennenen, *J. Opt. A, Pure Appl. Opt.*, 2002, **4**, 366.

30) Y. C. Zhu and Y. Bando, *Chem. Phys. Lett.*, 2003, **377**, 367.

31) X. Wang, J. Zhuang, Q. Peng and Y. D. Li, *Nature*, 2005, **437**, 121.

32) Y. Jiao, D. Yu, Z. Wang, K. Tang and X. Sun, *Mater. Lett.*, 2007, **61**, 1541.

33) S. Xiong, S. Huang, A. Tang and F. Teng, *Mater. Lett.*, 2007, **61**, 5091.

34) S. N. Sarangi and S. N. Sahu, *Physica E*, 2004, **23**, 159.

35) K. Yu, S. Singh, N. Patrito and V. Chu, *Langmuir*, 2004, **20**, 11161.

36) J. L. Pankove, *Optical Processes in Semiconductors*, Dover Publications, New York. 1990.

37) L. Qu and X. Peng, *J. Am .Chem. Soc.*, 2002, **124**, 2049.

38) C. B. Murray, D. J. Norris and M. G. Bawendi, *J. Am. Chem. Soc.*, 1993, **115**, 8706.

39) X. G. Peng, L. Manna, W. D. Yang, J. Wickham, E. Scher, A. Kadavanich and A. P. Alivisatos, *Nature*, 2000, **404**, 59.

40) K. Nose, H. Fujita, T. Omata, S. O. Y. Matsuo, H. Nakamura and H. Maeda, *J. Lumin.*, 2007, **126**, 21.

41) R. He and H. Gu, *Colloids and Surfaces A: Physicochem. Eng. Aspects*, 2006, **272**, 111.

42) C. D. Donega, S. G. Hickey, S. F. Wuister, D. Vanmaekelbergh and A. Meijerink, *J. phys.Chem.* B, 2003, **107**, 489.

43) Q. Wang, D. Pan, S. Jiang, X. Ji, L. An and B. Jiang, *J. Cryst. Growth*, 2006, **286**, 83.

44) L. Manna, E. C. Scher and A. P Alivisatos, *J. Am. Chem. Soc.*, 2000, **122**, 12700.

45) X. Peng, J. Wickham, P. A. Alivisatos, *J. Am. Chem. Soc.*, 1998, **120**, 5343.

46) Z. A. Peng and X. Peng, *J. Am. Chem. Soc.*, 2001, **123**, 1389.

47) Z. A. Peng and X. Peng, *J. Am. Chem. Soc.*, 2002, **124**, 3343.

48) L. Qu, Z. A. Peng and X. Peng, *Nano. Lett.*, 2001, **1**, 333.

49) Q. Yang, K. Tang, C. Wang, Y. Qian and S. Zhang, *J. Phys. Chem.* B, 2002, **106**, 9227.

50) Z. Tang, N. A. Kotov and M. Giersig, *Science*, 2002, **297**, 237.

51) B. Cullity, *Handbook of Elements of X-ray Diffraction*, 2nd ed., Addison–Wesley Reading, MA, 1978.

52) S. Wageh, L. Shu-Man, F. T. You and X. X. Rong, *J. Lumin.*, 2003, **102-103**, 768

53) T. Trindade and P. O'Brien, *Adv. Mater.*, 1996, **8**, 161.

# *CHAPTER FOUR*

## SYNTHESIS OF WATER SOLUBLE CADMIUM AND ZINC SELENIDE NANOPARTICLES

## 4.1 Introduction

The unique size and surface-dependent properties of quantum dots, have stimulated research on their surface modification with an aim to broaden their potential applications. Intensive research on nanoparticles, over the past decades, has focused on the study of their optical and electrical properties for possible applications in biological labels, opto-electronic devices, photovoltaic cells and lasers.[1,2] Recently, the conjugation of semiconductor nanoparticles with biomolecules through biosynthesis and biological surface modification of semiconductors[3,4] and, metal nanoparticles[5] with biomolecules such as starch, proteins and nucleic acids,[6] has added a new dimension to research at the nanoscale. This conjugation represents convolution of nanotechnology and biotechnology, where novel hybrid materials can be synthesised by incorporating the unique optical and electronic properties of nanoparticles and highly selective binding of protein and oligonucleotides. The bio-functionality of the nanoparticles enables selective interaction with target molecules or biochemical species, thereby extending the area of applications to biological or chemical systems. Examples of these applications include the preparation of non-radioactive biological labels[7,8] and chemical opto-sensors[9] for labelling in bioanalysis and diagnostics, tags for protein and DNA immunoassays, biocompatible labels for *in vivo* imaging studies, recognition of specific antibodies or antigens through luminescence emission measurements and the potential development of biosensors.

Many authors have stressed the distinct advantages of quantum dot (QD) bioconjugates over conventional organic dyes (such as rhodamine, fluorescein, perylene *etc.*) for use in biological imaging. These advantages include bright fluorescence, greater analytical sensitivity, narrow emission, broad UV excitation and

high photostability.[8-16] However, the difficulty in producing stable QD-biomolecules complexes has slowed down the development of QD biological labelling.[10] It is essential that the quantum dots be in a water-dispersible form for their use in any biological applications. The main limitation of organic nanoparticles in biological systems is their lack of water solubility and, several techniques have been offered to confer water solubility. The most common method for producing water-soluble selenide nanoparticles is through surface modification of organic soluble nanoparticles, which can be achieved by altering the nature of passivating ligands or augmenting the crystal with a shell material that is biocompatible.[7,8] The surface modification of QDs can increase their luminescent quantum yields, improve their stability, prevent aggregation and make them available for interaction with target analytes, which is of crucial interest for chemical sensors or biosensor applications.[9,17,18] Since the pioneering work of Chan *et al.*[7] and Alivisatos,[8] where QDs were made biocompatible and water-soluble via surface coating, various methods have been developed, in which hydrophobic QDs are first prepared and their surfaces then made hydrophilic by further modification with mercaptoacetic acid (MAA), 3-(mercaptopropyl)tri methyloxysilane (MPS), mercaptopropionic acid (MPA), mercaptoethylamine (MEA), β-mercaptoethanol (MBE), dihydrolipotic acid or dithiothreitol.[19-22] In fact, any molecule which binds to the surface of the particle and is water-soluble can be used thus, allowing for a range of surface chemistry to be explored.

The ligand exchange techniques involves a number of variations however, the basic principles remain the same. First, the nanoparticles are dried to remove unreacted ligand and the organic solvent. This can be accomplished by using either rotary

evaporator or precipitation in a counter-solvent. In the case of TOPO-capped particles, the addition of anhydrous methanol will cause flocculation of the particles, followed by separation through centrifugation.[23] Next, the particles are added into a solution containing an excess of the new ligand. After incubation for several hours, exchange occurs. With MAA as the exchange ligand, the binding occurs through the sulphur group at the molecule's terminus, while the carboxyl end provides water-solubility. This technique allows the use of high quality particles produced by organic synthesis in a biological context however, there are still some disadvantages. For example, all the limitations described in chapter one for the synthesis of organically soluble nanoparticles, are still present. In addition, the surface coating itself is tedious, time consuming (involving many processing steps) and involves wastage of anxiliary materials (solvent and processing aids) used for the reaction. Moreover, most of the particles produced have a short period of stability indicating possible loss of ligand coverage over time and, the fluorescence yields are lower than those of the original dots in the organic solvent. Furthermore, if the ligands are toxic like MBE or bioactive, MEA desorption can have damaging effects on the cells in contact with the particles.

An obvious route to water-soluble nanoparticle synthesis is their production in an aqueous solvent.[24-28] Rogach *et al.*[24] reported the direct synthesis of selenide nanoparticles in an aqueous solution using $H_2Se$ produced by titration as the selenium source, while mercapto-alcohols and mercapto acids were used as stabilizers. Recently there has been the use of selenosulphate as the selenium source for the direct synthesis of water-soluble selenide nanoparticles. The flexibility of the reaction allows the use of different passivating agents such as MAA,[29] starch,[30] and polymers

like PVA and PVP.[31-34] However, the production of the selenosulphate takes a longer reaction time and, the reaction sometimes involves the use of high intensity ultrasonic sound or sonochemical techniques.[35] In general, the direct synthesis of water-soluble nanoparticles is very efficient, flexible and several thiol ligands and polymers could be used as stabilizers. In addition, most of the reactions have the unique ability of being manufactured using simple bench-top chemistry, requiring only a fume hood which is easily available in most laboratories. Furthermore, particle surfaces may be readily altered through the use of biomolecules and polymers or, by performing post-synthetic conjugation chemistry on a ligand functional group. However, reduced optical properties, large particle size distributions, low quantum yields and deep trapped emission are the main limitations of these procedures, in addition to the toxic $H_2Se$ used as a selenium source in some cases. These boundaries have slowed down the production of stable QD-biomolecules complexes, hence limiting its biological applications.

Though many methods for preparing these highly functionalised materials have been reported, greener sustainable methods with less toxic starting materials, smaller number of reagents, a single synthetic step, mild temperature synthesis and the use of water – an essential material for its biological application as solvent, is still a significant challenge. As part of our efforts towards green synthesis of nanoparticles, in order to minimise chemical hazards to health and the environment which usually occur both during the synthesis and applications of these materials, we have put forward a facile and environmentally benign, one step synthetic route[36,37] that would fulfil almost all the conditions for the green synthesis of biocompatible nanoparticles, using different water dispersable ligands.

This chapter describes the synthesis, surface chemistry and characterisation of high quality water-soluble cadmium and zinc selenide nanoparticles through a novel, greener, facile and environmentally benign, one step synthetic method. Studies have revealed that subtle variation in synthesis parameters such as pH, reaction time, concentration, reactant ratio, passivating ligand and temperature, affects the quality and dispersibility of nanoparticles synthesised by the aqueous route. Therefore, the systematic study of some of these parameters on the nanocrystal size, optical properties and morphology are also investigated.

## 4.2 Synthetic Method

A direct aqueous-phase synthesis of semiconductor nanocrystals provides a convenient, economical and environmentally-friendly alternative to the labour-intensive, ligand exchange method of organic phase synthesis. This synthetic approach involves addition of an appropriate volume of selenide ion, produced via reduction of selenium powder in water for 2 hrs as described in chapter two, to an aqueous solution of the ligand and metal salt ($MCl_2$ M = Zn or Cd) without an additional stabilizing agent. The particle size and optical properties were controlled by varying the pH of the solution (between acidic, neutral and basic medium), capping ligand, temperature, concentration and reaction time. The pH of the solution was adjusted prior to the addition of the freshly prepared selenide ion solution, to the aqueous solution of the ligand and metal salt for synthesis at room temperature. Whereas for the synthesis at high temperature, the pH of the solution was adjusted after the addition of aqueous solution of the ligand and metal salt to freshly prepared selenide ion solution, in an inert environment. The capping ligands used are L-cysteine ethyl ester hydrochloride, methionine, ascorbic acid, starch, polyvinyl

alcohol (PVA) and poly (vinylpyrrolidone) (PVP), which function as agents of solubilisation, stabilization and conjugation. Compared with organometallic precursor methods, the key chemicals used in this method are non-toxic, safe and inexpensive. The reactions were carried-out at a maximum temperature of about 90 °C, which is easy to control and is very reproducible, implying high energy efficiency a preferred condition for green synthesis.

The as-synthesised nanoparticles were characterised by absorption and photoluminescence spectroscopy, fourier transform infrared spectroscopy (FT-IR), powder x-ray diffraction (XRD), transmission electron microscopy (TEM), high resolution transmission electron microscopy (HRTEM), selected area diffractometry (SAD) and, energy dispersive spectroscopy (EDS).

## 4.3 Results and Discussion

### 4.3.1 *Synthesis of Water-soluble CdSe Nanoparticles*

#### 4.3.1.1 Synthesis *at High Temperature*

In this synthetic procedure, colloidal CdSe nanoparticles have been synthesized by the simultaneous addition of an aqueous solution of cadmium chloride and ligand, to a freshly prepared oxygen-free NaHSe solution. The reactions were then refluxed at 90 °C for 5 hrs under inert atmosphere. Excessive prolonged heating resulted in the growth of bulk cadmium chloride hence, a shorter period of time was necessary. The capping ligands used are L-cysteine ethyl ester hydrochloride, methionine and starch. The reaction scheme is shown below :

$$4NaBH_4 + 2Se + 7H_2O \xrightarrow[2\ hrs,\ N_2]{R.T} 2NaHSe + Na_2B_4O_7 + 14H_2 \quad (1)$$

$$NaHSe + CdCl_2 \xrightarrow[90\ ^{o}C,\ 5\ hrs,\ N_2]{Ligands} \text{Ligand - capped CdSe} + NaCl + HCl \quad (2)$$

***Scheme 1.*** *Equation for the formation of Ligand-capped CdSe nanoparticle at high temperature (R.T= room temperature).*

#### 4.3.1.1.1 *Cysteine-capped CdSe nanoparticles*

In this synthetic procedure, L-cysteine ethyl ester hydrochloride ($C_5H_{11}NO_2S.HCl$) was used as our source of cysteine. We have chosen to cap the CdSe nanoparticles with cysteine for the following reasons, cysteine is one of the water-soluble amino acids that can be found in the human body and contains $COO^-$ and $NH_3^+$ groups through which it can easily conjugate with other biomolecules in an aqueous solution. In addition, it passivates the surface states of nanoclusters more effectively than other thiols, thereby enhancing their emission properties and it has high suitability for conjugation with different classes of biomolecules, ranging from smaller molecules and peptides to antibody conjugates.[38-41] Furthermore, the amino acid L-cysteine readily binds to the surface of CdSe via a thiolate linkage and the polar $COO^-$ and $NH_3^+$ groups render it water-soluble (Figure 4.1).

The simultaneous addition of aqueous solution of cadmium chloride and L-cysteine ethyl ester hydrochloride to a freshly prepared oxygen-free NaHSe solution, changes the colour of the solution. The solution changes from colourless to brownish-red, orange and light orange as the pH of the solution changes from 4 to 7 and 11 respectively.

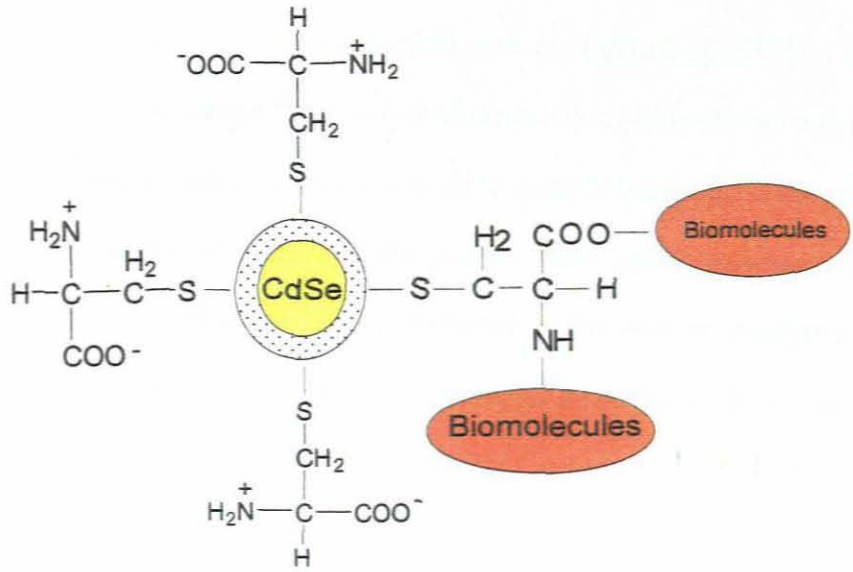


***Figure 4.1*** *Schematic diagram of cysteine-capped CdSe nanoparticles showing the attachment of cysteine to the surface of CdSe via a thiolate linkage and its covalent binding to biomolecules through the amino and the carboxyl group.*

#### 4.3.1.1.1.1 *Optical Properties*

The absorption and photoluminescence spectra of an aqueous solution of cysteine-capped CdSe at different pH under 5 hrs of refluxing, are shown in Figures 4.2 to 4.4. The absorption band-edges are all blue-shifted (Figures 4.2a – 4.5a) in relation to the bulk band gap indicating quantum confinement. The absorption band-edges as calculated using the direct band gap method [42] are 588 nm, 2.11 eV (pH 4); 540 nm, 2.30 eV (pH 7) and 535 nm, 2.32 eV (pH 11). The shift of the absorption band-edge to a higher energy as the pH of the solution increases from 4 to 11, indicates a decrease in particle size. The particles show an absorption shoulder at 535 nm (pH 4) and 450 nm (pH 7 and 11). The absorption shoulder becomes narrower as the pH of the solution increases, indicating narrowing of the particle size distributions. The particle diameters as estimated, using the effective mass

approximation (EMA) model[43] are, 3.14 nm (pH 4), 2.57 nm (pH 7) and 2.52 nm (pH 11), signifying that the smallest particle size is obtained at pH 11. This is in agreement with the change in the colour of the solution as the pH increases from 4 to 11. The largest particle size obtained at pH 4 could be attributed to the contribution from a large number of unreacted thiol groups, which remain un-ionised at this pH. These unreacted thiol groups also contributed to the broader absorption shoulder obtained at this pH. Optical spectroscopy studies on cadmium thiol complexes has revealed that, the ionisation of thiol groups and subsequent complexation with the nanoparticle surface, dramatically decreases as the pH of the solution decreases from neutral to the acidic range and, no complexation occurs at pH < 4.[44-46] Recently, Chatterjee *et al.*[47] and Green *et al.*[48] have shown that the rate of ionisation and complexation of the thiol group increases as the pH of the solution increases. As the pH of the solution increases the ionisation of the thiol group is enhanced, the particle size becomes smaller and absorption shoulder becomes narrower, because there is little influence from the unreacted thiol group. The occurrence of an absorption shoulder at the same wavelength for the nanoparticles produced at pH 7 and 11 with different particle sizes, suggests the formation of the particles through thermodynamically-controlled crystal growth. Similar features have been observed previously for CdSe,[24] CdS,[25,49] and CdTe.[26-27] The presence of an absorption maximum in the UV region of the spectrum located at 255 nm (pH 4), is attributed to $Cd^{2+}$-cysteine (thiolate) complex. Chatterjee *et al.* reported a similar observation for water-soluble cysteine-capped CdS nanoparticles.[47] This peak has very low intensity at pH 4, due to low ionisation of the thiol group. As the pH increases the peak disappears and, reappears at a new wavelength (269 nm) with the curve becoming more symmetrical in shape. The low intensity at pH 7 suggests high ionisation and

low complexation at this pH and, as the pH increases the complexation of the thiol groups on the surface of the CdSe nanoparticle increases hence, high intensity of this peak at pH 11. The high intensity of this absorption maximum at pH 11 as compared to the one at pH 7 might also be responsible for the low intensity of its absorption shoulder at 450 nm, as compared to the same shoulder at pH 7.

The absorption spectra at 3 hrs of refluxing did not show any significant difference compared to the result obtained at 5 hrs. In addition, under this refluxing time, the photoluminescence obtained at higher pH, was very low and no luminescence was detected at pH 4.

The emission maxima of the particles at different pH (Figures 4.2b to 4.4b) are 408 nm, 3.04 eV (pH 4); 520 nm, 2.38 eV (pH 7) and 530 nm, 2.34 eV (pH 11). They are all blue-shifted in relation to the bulk band gap of 713 nm (1.74 eV). As the pH of the solution increases, the emission maximum shifts to red, with the particle emitting in the blue (pH 4) and green region (pH 7 and 11), while the emission line widths become narrower. This indicates an increase in particle size and a narrower size distribution. It therefore supports our inference that the largest particle size and size distribution obtained at pH 4, is attributed to the presence of a large number of unreacted thiol groups, which remain un-ionised at this pH. The emission line widths are narrower at higher pH which indicates the growth of the crystallite with few electronic defects. This is attributed to the high degree of ionization of the thiol group and its complexation on the nanoparticle surface as the pH increases, which consequently leads to a higher passivation rate. The relatively broad emission width obtained at pH 4 could be attributed to recombination from surface defects, due to a

lower degree of passivation by the thiol group. The abrupt shift in the emission maxima as the pH increases implies that ionisation and complexation of the thiol groups, have significant influences on the growth rate of the particle.

It is worth mentioning that increasing the cadmium to cysteine ratio systematically from 1:10 to 1:60 at different pH did not have any significant effect on the luminescence intensity of the nanoparticles. In addition, the synthesis at higher reduction time (4 and 6 hrs) produced large particle sizes close to the bulk cadmium chloride and no photoluminescence was observed.

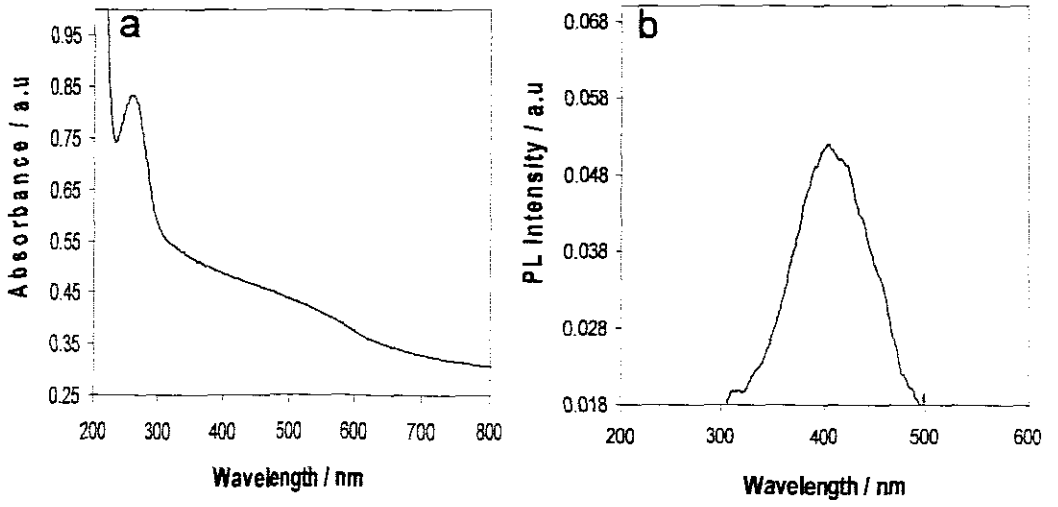


***Figure 4.2*** *(a) Absorption and (b) photoluminescence spectra of cysteine-capped CdSe nanoparticles at pH 4.*

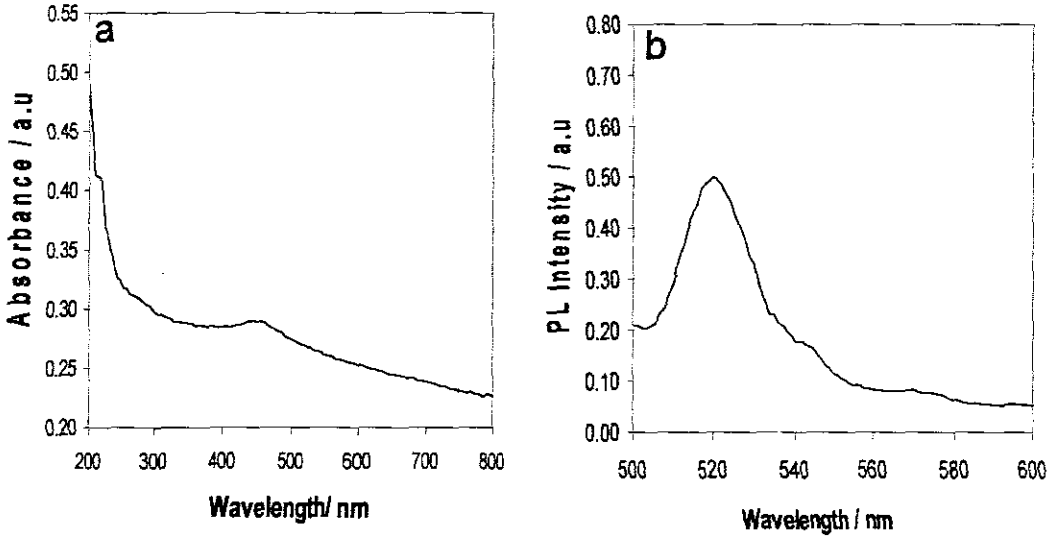


***Figure 4.3*** *(a) Absorption and (b) photoluminescence spectra of cysteine-capped CdSe nanoparticles at pH 7.*

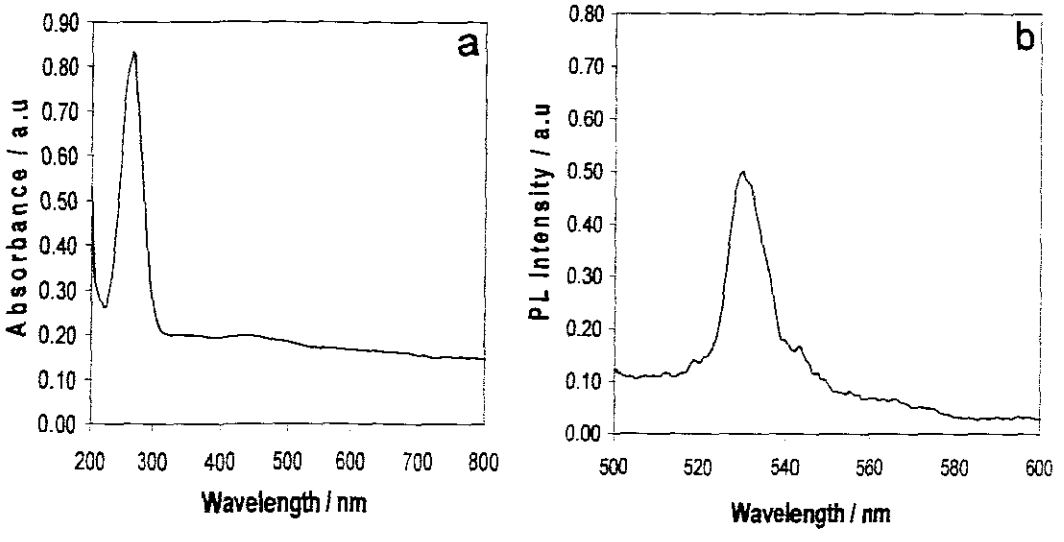


***Figure 4.4*** *(a) Absorption and (b) photoluminescence spectra of cysteine-capped CdSe nanoparticles at pH 11.*

#### 4.3.1.1.1.2 *Structural Properties*

##### 4.3.1.1.1.2.1 *Fourier-Transform infrared spectroscopy (FT-IR)*

The surface morphology of nanoparticles was investigated by IR spectroscopy to confirm the capping of the CdSe nanoparticles by cysteine. Figure 4.5 shows the FTIR spectra of L-cysteine ester and a representative cysteine-capped CdSe sample. Generally, amino acids exist as zwitterions (internal salts) and exhibit spectra, characteristic of both the carboxylate and primary amine salt. They show a $NH_3^+$ stretch (very broad), N-H bend (asymmetric/symmetric) and $COO^-$ (carboxylate ion) stretch (asymmetric/symmetric) as characteristic vibrations.[50] The amino acid L-cysteine is water-soluble and would readily bind to the surface of CdSe via a thiolate linkage. When comparing the two spectra, the most significant observation is the band at 2546 and 950 $cm^{-1}$ corresponding to the S-H stretching and bending mode, which is distinctly visible for the free cysteine molecule but absent in the spectrum for cysteine-capped CdSe particles. This provides strong evidence for the surface binding of cysteine to CdSe nanoparticles via a Cd-S linkage. This may be attributed to the cleavage of the S-H bond and the formation of a new S-Cd bond of the Cd thiolate complex on the nanoparticle surface. It can also be observed that the band at 1754 and 1294 $cm^{-1}$ of cysteine, which corresponds to the $COO^-$ asymmetric and symmetric stretch, a band at 1592 $cm^{-1}$ corresponding to N-H asymmetric bend, the very broad band of $NH_3^+$ stretch observed in the 3000-3500 $cm^{-1}$ and a band at 1064 $cm^{-1}$ corresponding to C-N stretch respectively, are shifted to slightly lower wavenumbers in the cysteine passivated CdSe nanoparticles. The shift in the $COO^-$ and $NH_3^+$ stretching position is probably due to a change in the dipole moment, when cysteine binds on the metal surface with high electron density.[51] These observations confirm the capping of nanoparticles surface by L-cysteine i.e., the ester has been

hydrolysed during the reaction to produce the parent amino acid which coordinates to the CdSe via the thiolate group. Any free cysteine would have been removed during the filtration process. The other two functional groups -$NH_2$ and -$COO^-$ are available for conjugation with suitable biomolecules.

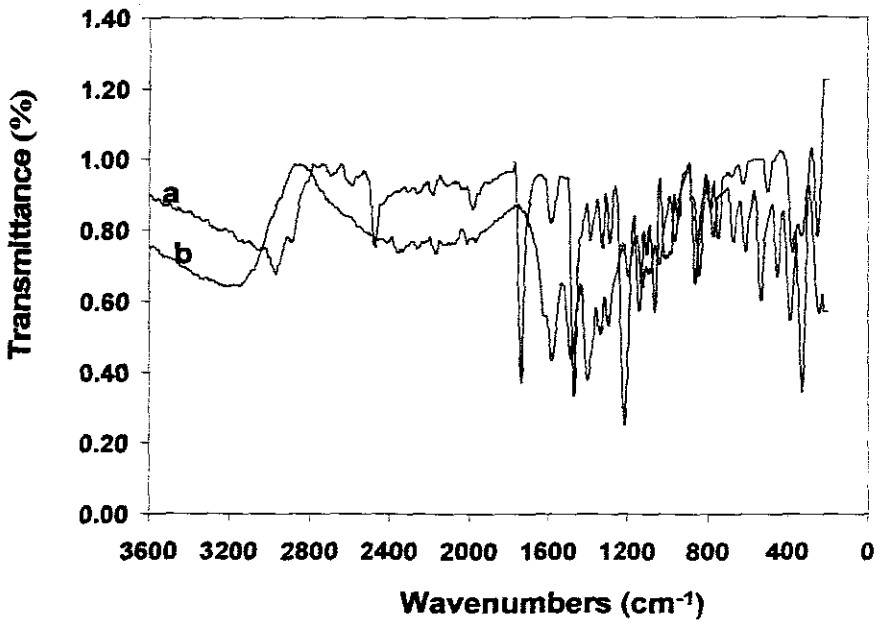


***Figure 4.5*** *FTIR spectra (a) L-cysteine ethyl ester hydrochloride and (b) cysteine-capped CdSe nanoparticles at pH 11 under 5 hrs refluxing time.*

#### 4.3.1.1.1.2.2 *Transmission Electron Microscope (TEM)*

The TEM image of the cysteine-capped CdSe at different pH under 5 hrs of refluxing is shown in Figure 4.6. The image confirms the extent of ionisation and complexation of the thiol groups on the surface of the nanoparticles. At pH 4 (Figure 4.6a), the TEM image of the material shows monodispersed, spherical particles of CdSe within the matrix of the cysteine capping agent. Particle size estimation is difficult, due to apparent aggregation within the capping matrix as a result of large presence of un-ionised thiol groups. At pH 7 the TEM image (Figure 4.6b) shows that there is no network or aggregate patterns among the particles. This is due to high

ionization and low degree of complexation at this pH. The image confirmed that the particles are small, monodispersed and spherical in shape. At pH 11 the TEM image shows small, monodispersed, spherical particles that are joined together in a network pattern (Figure 4.6c). This network pattern can be attributed to the Cd-thiolate end-to-end linkage as a result of complexation of the thiol groups on the surface of the nanoparticles. Such metal-thiolate end-to-end linkages have been reported for the interaction between metals and cysteine.[51-53]

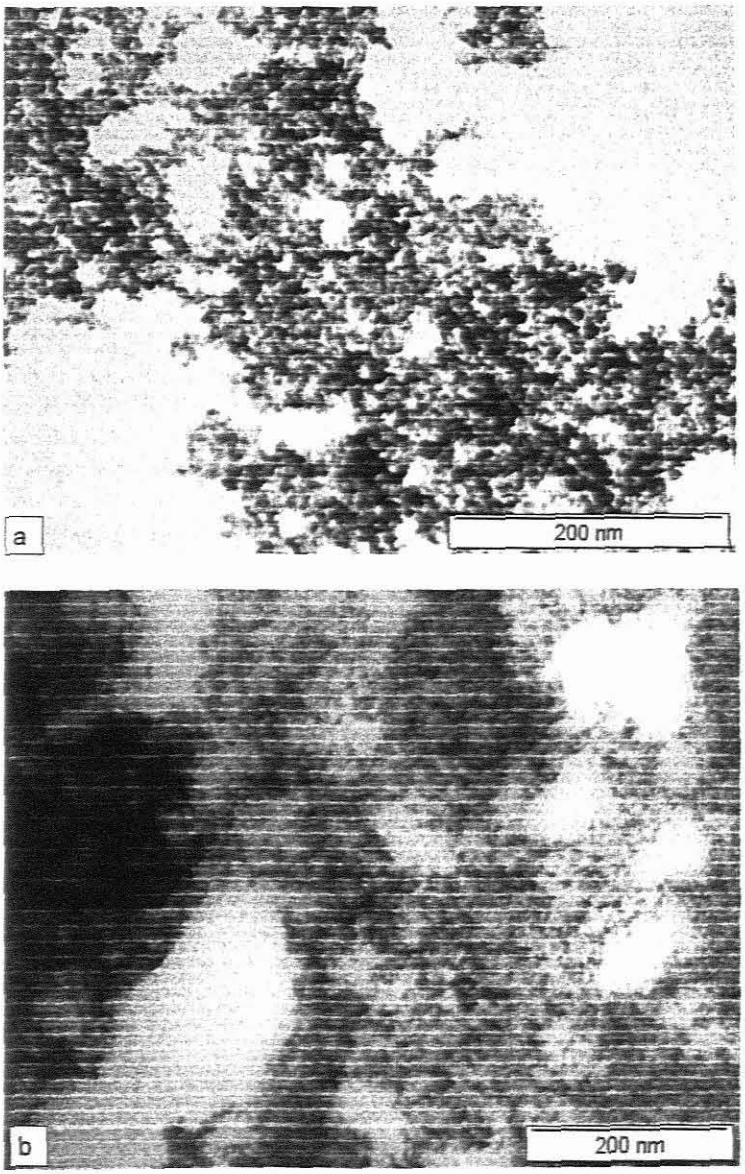

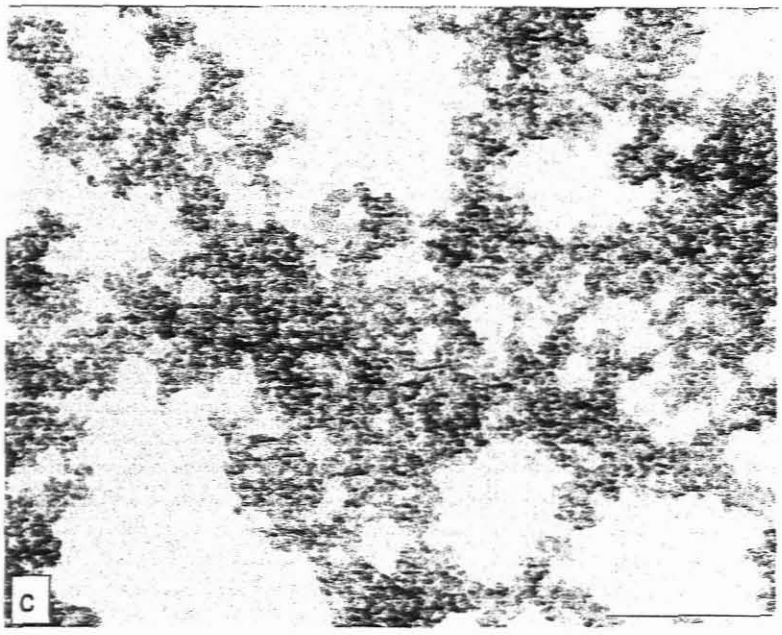


***Figure 4.6*** *TEM images of cysteine-capped CdSe nanoparticles at (a) pH 4, (b) pH 7 and (c) pH 11*

#### 4.3.1.1.1.2.3 *High Resolution Transmission Electron Microscope (HRTEM)*

A typical representative HRTEM image of the cysteine-capped CdSe nanoparticles and its corresponding Fast-Fourier-Transformation (FFT), is shown in Figure 4.7. The existence of lattice planes in the HRTEM image further confirms the crystallinity of the CdSe nanoparticles. The lattice spacing of approximately 3.7 $A^{o}$ corresponds with the (100) plane of the hexagonal phase of CdSe. The Selected Area Diffraction (SAD) pattern (Figure 4.7c) consists of distinct rings, confirming that the particles are crystalline. The pattern can be indexed to hexagonal CdSe.

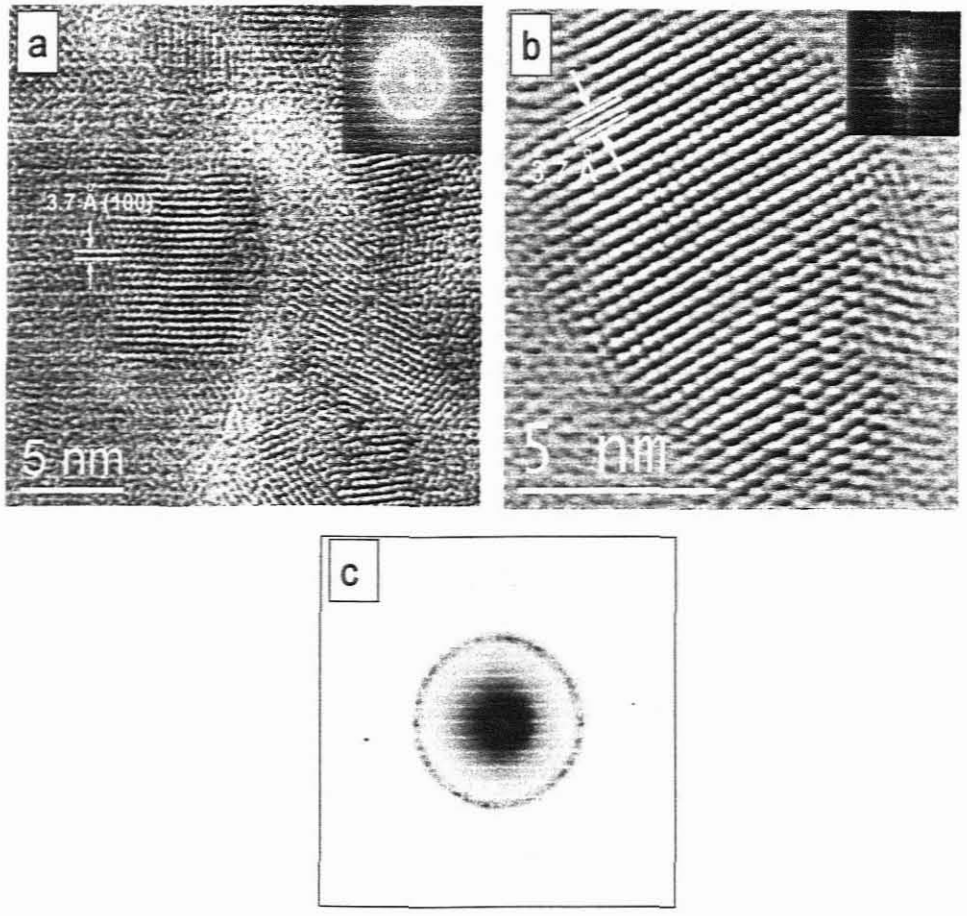


**Figure 4.7** *HRTEM images of (a) cysteine-capped CdSe nanoparticles at pH 11 under 5 hrs refluxing time, with FFT (inlet), (b) showing the interplanar spacing with corresponding FFT (inset) and (c) selected area diffraction.*

#### 4.3.1.1.1.2.4 *Powder X-ray Diffraction (XRD)*

The XRD diffraction pattern of the as-synthesised particles are broadened due to the nanocrystalline nature of the particles. The broadness of the diffraction peak increases gradually, with increasing pH signifying decreases in particle size, as the pH increases. This is inconsistent with the optical measurements. The position of the diffraction peaks for all the particles at the different pHs (4, 7 and 11), corresponds to the crystalline plane of hexagonal-wurtzite-type CdSe, with lattice constant a = 4.3 and c = 7.010, which is inconsistent with the JCPDS card number 8-459 for

hexagonal CdSe.[54] The result is also in agreement with the SAD results. This is a remarkable difference to the previously reported phases of CdSe nanoparticles synthesised via an aqueous method. It should be mentioned in this context that aqueous synthesis of CdSe nanoparticles mostly yield cubic-zinc blende phase,[24,29-35] whereas, a hexagonal-wurtzite phase is usually obtained under high-temperature organometallic synthesis.[23,55-57] Since thermodynamically-stable wurtzite phase is achieved at high temperature, at which thermodynamics (rather than the reaction kinetics) governs the crystal growth, it is concluded that the cysteine-capped nanoparticles are formed under thermodynamically controlled crystal growth. This then confirms our inference about the presence of absorption shoulder at the same wavelength in the optical spectra for the nanoparticles, produced at pH 4 and 11 with different particle size.

A typical representative XRD pattern of the cysteine-capped CdSe nanoparticles is shown in Figure 4.8. Five distinct diffraction peaks at 2θ values of 24.4°, 34.5°, 42.5°, 45.0° and 49.1°, are observed corresponding to the respective (002), (102), (110), (103) and (112) diffraction planes of hexagonal CdSe. The high intensity of (002) peak indicates that the nanocrystals are elongated along the c-axis and the particles contain a large number of (002) planes, thus making that peak the dominant reflection in the first diffraction feature.

The greater coherence length in that direction, results in the narrowing of (002) reflection and a smaller overlap with the neighbouring (100) and (101) reflection. The mean particle diameter was calculated to be 2.7 nm from the Scherrer equation.[58]

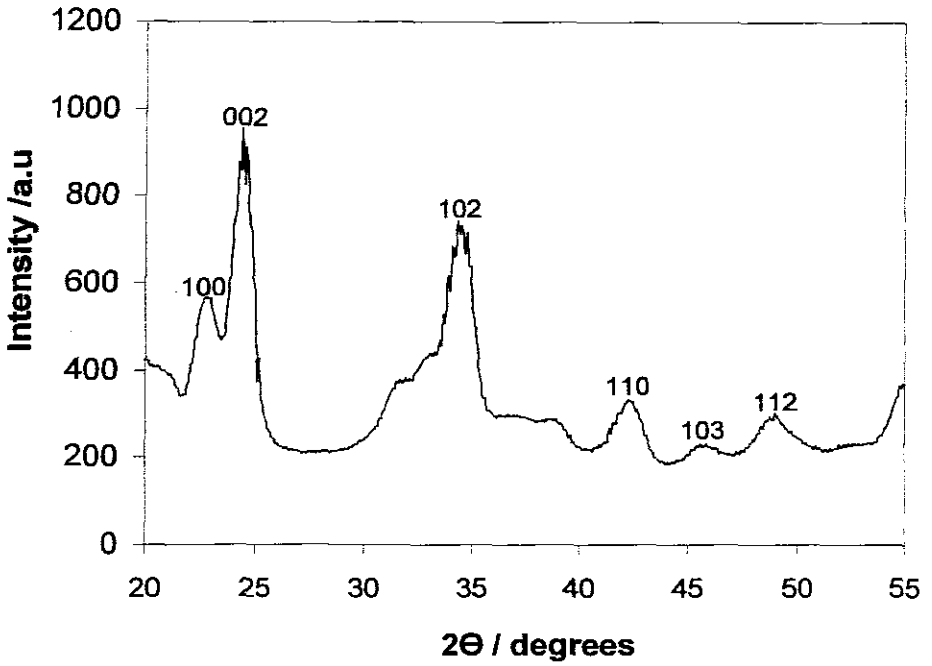


***Figure 4.8*** *XRD pattern of cysteine-capped CdSe nanoparticles at pH 11 under 5 hrs refluxing time.*

#### 4.3.1.1.1.2.5 *Energy Dispersive spectroscopy (EDS)*

The EDS spectrum of the synthesised cysteine-capped CdSe particles at all the pHs confirms the presence of cadmium, selenium and sulphur. A typical representative pattern is shown in Figure 4.9. The high intensity of the sulphur peak in the EDS spectrum is attributed to the presence of thiol group on the surface of the nanocrystals. This correlates with the increase of surface-to-volume ratio when the particles become smaller, which corresponds to a larger amount of stabilizing thiol molecules (S atoms) on the particle surfaces, relative to the number of Se atoms in the particle core. This increased S/Se ratio has previously been reported for thiol stabilised CdSe nanocrystals.[24]

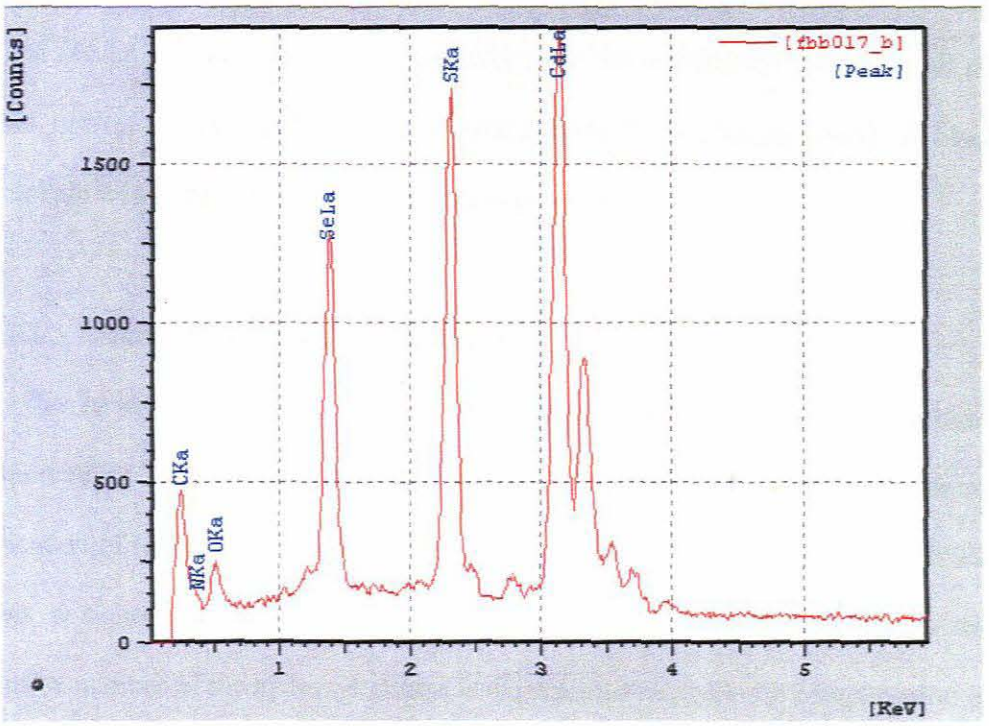


***Figure 4.9*** *EDS spectrum of cysteine-capped CdSe nanoparticles at pH 11 under 5 hrs refluxing time.*

#### 4.3.1.1.2 *Methionine-capped CdSe nanoparticle.*

Methionine was chosen as the capping agent because it belongs to the same group, with cysteine as the only two-sulphur-containing amino acids that can be found in the human body. In fact, it aids the synthesis of cysteine in a human body when available in sufficient quantity. Unlike cysteine, it belongs to a group of hydrophobic amino acids because of its hydrophobic side-chain. However, similar to cysteine, it is expected to passivate the surface states of nanoclusters via its thiolate linkage, while its polar $COO^-$ and $NH_3^+$ groups should enhance the solubility of the nanoparticles in water, as well as for covalent coupling to various biomolecules thus making it easier to conjugate with other biomolecules in the body.

The synthesis of methionine-capped CdSe at high temperature, did not give any optical results nor produce any nanoparticles after the purification process at all pH (basic, neutral and acid medium) and refluxing times (3, 5 or longer hours). A black precipitate was obtained after the purification process.

#### 4.3.1.1.3 *Starch-capped CdSe nanoparticles*

We have used starch as one of the capping agents because it is the main component of carbohydrate food and would be a perfect carrier for the direct application of CdSe nanoparticles in food processing. It is a renewable polymer and adopts a right-handed helical conformation in aqueous solutions, in which the extensive number of the hydroxyl groups is expected to facilitate the complexation of metal ions to the molecular matrix and its solubility in water.

The synthesis of starch-capped nanoparticles under these reaction conditions also produced large size particles, close to the bulk cadmium chloride and no photoluminescence was observed.

As a result of the generally low luminescence intensity of the cysteine-capped CdSe nanoparticles and the unpleasant result obtained from using methionine and starch as capping agent under high temperature, we decided to carry out the whole reaction at room temperature with slight modifications to the reaction conditions.

### 4.3.1.2 *Synthesis at Room Temperature*

In this synthetic procedure, water-soluble CdSe nanoparticles were synthesized by the addition of a freshly prepared, oxygen-free, NaHSe solution to an aqueous

solution of cadmium chloride and the ligand. The capping ligands used are L-cysteine ethyl ester hydrochloride, methionine, ascorbic acid, starch and polyvinyl alcohol (PVA). The reaction scheme is given below:

$$4NaBH_4 + 2Se + 7H_2O \xrightarrow{2\ hrs,\ N_2} 2NaHSe + Na_2B_4O_7 + 14H_2 \quad (1)$$

$$Ligands + CdCl_2 + NaHSe \xrightarrow{R.T} Ligand\text{-}capped\ CdSe + NaCl + HCl \quad (2)$$

***Scheme 2.*** *Equation for the formation of Ligand-capped CdSe nanoparticles at room temperature (R.T= room temperature).*

#### 4.3.1.2.1 *Cysteine-capped CdSe nanoparticles*

##### 4.3.1.2.1.1 *Optical properties*

The temporal evolution of the absorption and photoluminescence spectra of an aqueous solution of cysteine-capped CdSe, synthesised at room temperature under different pH and reaction time, is shown in Figures 4.10 to 4.15. The absorption and emission maxima of all the nanoparticles are strongly blue-shifted from the bulk band gap, clearly showing quantum confinement. The shift of absorption and emission maxima to lower wavelength for the first 3 hrs of reaction time increases as the pH increases from 4 to 11, indicating decrease in particle size. This is in agreement with the colour of the solution which changes from light-orange to light-yellow, as the pH increases. This has been attributed to the high rate of ionisation and complexation which occurs at higher pH as discussed earlier. In contrast with those synthesised at higher temperature as reported earlier, all the particles show sharp excitonic shoulders and absorption edges, signifying smaller particles with narrower size distributions. The absorption shoulder becomes narrower as the pH increases, indicating that the

size distribution becomes much narrower with increasing pH. The presence of distinct excitonic features is attributed to the first electronic transition (1s-1s) occurring in CdSe nanoparticles.[59,60] The narrowing of the size distribution of the particles led to a better resolution of the 1s-1s electronic transitions. As expected for quantum-sized particles, the position of the first electronic transition was shifted to higher photon energies and became more pronounced with decreasing particle sizes, in accordance with the size quantization effect. Higher electronic transitions were also clearly resolved for those synthesized at pH 11. The first exciton absorption peak appears at a wavelength as low as 415 nm, with a clearly resolved higher energy electronic transition, an impossible task with the $Cd(CH_3)_2$ and CdO-related approach.[23,55,56] It is observed that, unlike the absorption spectra for the synthesis under refluxing (Figures 4.2a–4.4a), the high intensity peak at lower wavelength (< 270 nm) is completely absent at all the pHs investigated. In addition, all the particle sizes are less than 2 nm and smaller than those synthesized under refluxing. This is advantageous in incorporating them into cells or electronic devices for diagnostic or therapeutic studies. These two observations show that the presence of heat affects the size and quality of the nanoparticles under this new synthetic method.

Another striking observation is the presence of high luminescence intensity, with no evidence of trap emission at room temperature, without any refluxing at a short period of time (1 hour). This is a significant advantage of this synthetic route. To the best of our knowledge, there have been no reports of such luminescence without refluxing for water-soluble CdSe nanoparticles. All the particles emit strongly in the blue region and the luminescence intensity is very high (Figures 4.12 to 4.14), increasing about four times in intensity when compared to the nanoparticles synthesized under

refluxing, as discussed earlier. The high luminescence intensity, narrow emission line widths and sharp luminescence as the pH increases, indicates the growth of crystallites with few electronic defects. This signifies the efficiency of the capping group as the pH increases in electronically passivating the surface states or defects present in the band gap of the nanocrystals, which act as trapping states for photogenerated charges. The emission properties can be explained using two factors, (i) increase in the amount of free thiols from the cysteine ester and, (ii) increase in the rate of thiol complexation. At higher pH, the rate of ionisation and complexation of the thiol group is very high[47,48] hence, there is an increase in the coverage of the nanoparticle surface by the thiol groups, due to the presence of a large number of ionised thiol groups and its concurrent complexation on the surface of CdSe nanoparticles, as the pH increases. As a result, more trap sites on the CdSe surface will be removed thus, dramatically improving the fluorescence intensity. This enhanced thiol complexation also improves the stability of the nanoparticles. In addition, in the basic medium the excess thiol anions, together with cadmium ions, can form complexes on the surface of CdSe particles due to high rate of complexation at this pH. In this way, a thick layer of cadmium thiol complexes may be formed on the surface of CdSe, which may have a higher potential for ground-state electrons. This makes the shell of cadmium thiol complexes analogous to the CdS and ZnS shells around the CdSe core.[61,62] Gao *et al.* has reported similar observations for the synthesis of water-soluble CdTe capped by thiols.[28]

These two factors are responsible for the high luminescence intensity, narrow emission line width and sharp luminescence seen in the emission spectra at pH 11 (Figure 4.13). At pH 7 (Figure 4.14), the luminescence intensity is a bit lower and the

spectrum is broad, with defects as compared to pH 11. This is attributed to high ionisation but low complexation at this pH. At pH 4 (Figure 4.15), the luminescence intensity is low and the spectrum is broader with few defects. This could be attributed to the lower degree of thiol ionisation and complexation on the surface of CdSe nanoparticles at this pH. Hence, there is insufficient passivation of the large number of non-radiative surface states present in the bandgap of the nanocrystals at this pH. The nanoparticles show no luminescence until after 5 hrs of reaction time at pH 4. This shows that ionisation and complexation of the thiol group has significant impact on the luminescence of the as-synthesised particles under this synthetic condition. At pH 4 the ionisation and complexation rate is very low hence, for the first few hours of the reaction there is a large number of un-ionised thiol groups, with simultaneous formation of CdSe nanoparticles. This leads to a large number of surface states which traps the excited electron due to poor passivation. As the reaction time increases the rate of ionisation and complexation increases, more thiol groups become ionised and complexation on the nanoparticle surface, also occurs concurrently. This then reduces some of the surface states present in the nanocrystals and is responsible for the luminescence obtained at 24 hrs (Figure 4.15). The particle size calculated at 24 hrs reaction time is the same as the particle size obtained at 3 hrs. This might imply that there is no significant increase in the number of surface defects arising from the uncapped CdSe particles after 3 hrs.

Figure 4.10 shows a set of absorption spectra recorded at pH 11, between the reaction times of 1 to 24 hrs. All the spectra in the first 5 hrs of the reaction, show a well-developed maximum near the onset of absorption, which is ascribed to the first (1s-1s) transition and the presence of a very sharp, clearly resolved, lower energy

transition at 363 nm, which increases in optical density as the reaction time increases and is absent in the spectrum obtained after 24 hrs. The presence of this peak (363 nm) indicates a very narrow size distribution of the CdSe nanocrystals during the first 5 hours of the reaction.[63] It also implies that excitation at shorter wavelength is possible. This is an important feature for biological applications because, it allows simultaneous excitation of multicolour QDs with single light source.[64] In addition, the presence of this peak in the spectrum after 1 hour reaction time (3 and 5 hrs) suggests the preferential thermodynamic stability of the particles produced at 1 hour thus, making them an intermediate stage in the growth of CdSe nanocrystallite.[25,26] With increasing time, i.e. with successive particle growth, this peak disappears.

The first excitonic shoulder (1s-1s transition) is shifted to higher wavelength as the growth time increases for the first 5 hrs at pH 11, signifying an increase in particle size. The sizes of the particles as calculated, using Yu's calibration data equation,[65] are 1.68 nm (1 hr), 1.73 nm (3 hrs) and 1.78 (5 hrs). The smaller size of the particle is also reflected in the colour of the solution, which was light-yellow and showed no visible difference to the eye throughout the reaction times, indicating that there is very little difference in the particle size. The increase in particle size shows that nucleation and growth occurs simultaneously. The possibility of these two reaction stages taking place without a clear boundary, has been reported for the synthesis of CdSe nanoparticles.[66,67] With increasing reaction time, the absorption spectra appeared atypical as the absorption shoulder disappeared and then reappeared, as a very small broad peak at a lower wavelength at 24 hrs, signifying broader size distribution and decrease in particle size (1.37 nm).

In a similar trend to the absorption spectra, the emission maximum is red-shifted as the reaction time increases for the first 5 hrs and becomes blue-shifted at 24 hrs (Figure 4.13). The emission maxima are 441 nm (1 hr), 446 nm (3 hrs), 460 nm (5 hrs) and 432 nm (24 hrs). In addition, the luminescence intensity at 24 hrs is higher than that of the sample at 5 hrs. This blue-shift in the absorption and emission spectra (reduction in particle size) is contrary to existing reports on the growth of CdSe quantum dots and, suggests a process other than the typical particle growth mode. The only similar observation was reported recently by Green *et al.* for the synthesis of water-soluble CdTe nanoparticles and the reaction occurred under refluxing.[48] In their report, they observed the presence of two emission maxima in the spectra of the solution after refluxing at 600 nm and 700 nm which they assigned to the presence of two different materials (nanodots, 600 nm and nanorods, 700 nm), in the TEM image. They attributed the atypical spectra to digestive ripening phase, whereby the rods were totally digested (evidence by the disappearance of the emission maxima at 700 nm) and the spherical particles modestly affected. Another explanation given was that, the rods grew too big to remain soluble and precipitated out as bulk, leaving only the spherical particles.

In this case, the smaller increase in the average particles size as reaction time increases for the first 5 hrs implies that, moderation of growth is better achieved at this pH. This slight increase in the particle size, with the occurrence of a well-defined absorption maxima appearing reproducibly at the same wavelength (363 nm) as the reaction time increases, suggests that the growth did not occur via Ostwald ripening. However, we propose the following particle growth mode. At the beginning of the reaction there is low concentration of thiol anions from the cysteine ester hence, it is

the size determining factor. As the reaction time increases, the amount of thiol anions increase, leading to an increase in particle size. When its concentration exceeds the $Cd^{2+}$ ions, the role is taken over by $Cd^{2+}$ which is now the limiting reactant. At this point the amount of free $Cd^{2+}$ available would be shared by the selenide ion in the solution and the free thiol anions for the formation of the nanoparticles and $Cd^{2+}$-thiol complex respectively. This leads to a decrease in the particle size and therefore, blue-shifting of the absorption and emission maxima. The formation of $Cd^{2+}$-thiol complex produced further passivation for the nanoparticles hence, the resultant enhanced luminescence intensity of the nanoparticles obtained at 24 hrs as compared to those obtained at 5 hrs of the reaction time.

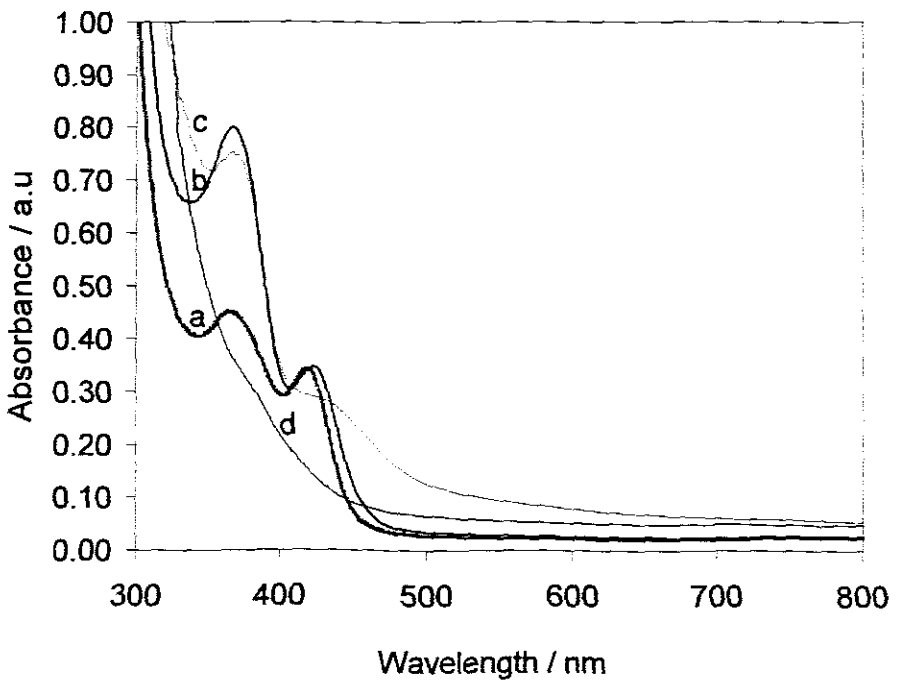


***Figure 4.10*** *Absorption spectra of cysteine-capped CdSe nanoparticles at pH 11 for the reaction time of (a) 1 hr (b) 3 hrs (c) 5 hrs and (d) 24 hrs*

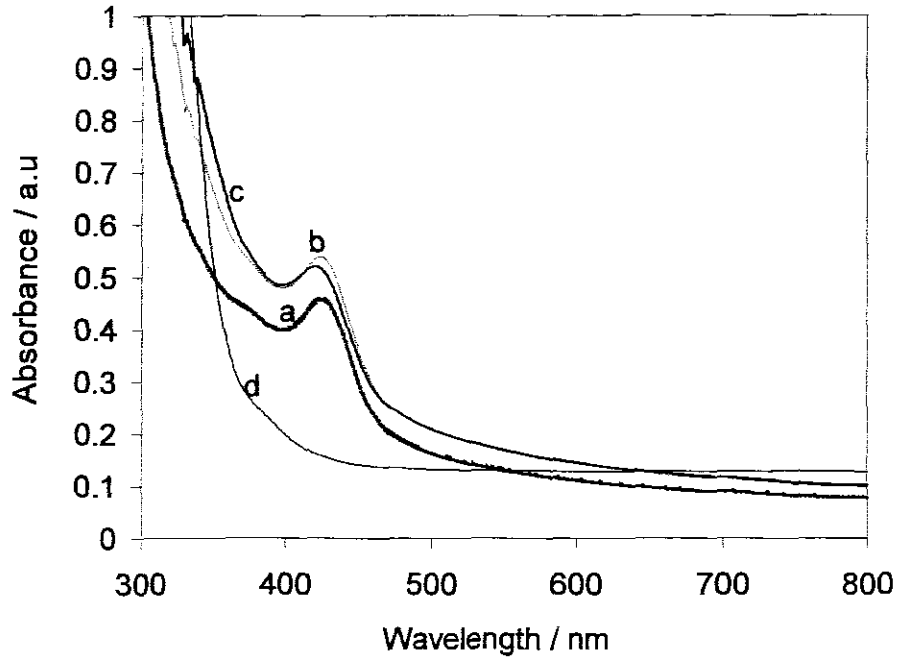


***Figure 4.11*** *Absorption spectra of cysteine-capped CdSe nanoparticles at pH 7 for the reaction time of (a) 1 hr (b) 3 hrs (c) 5 hrs and (d) 24 hrs*

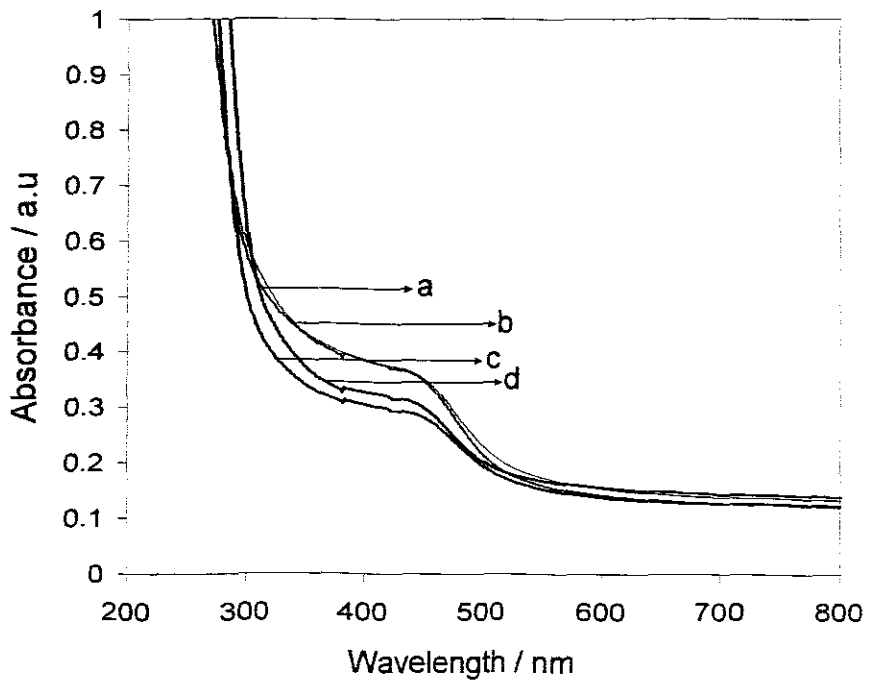


***Figure 4.12*** *Absorption spectra of cysteine-capped CdSe nanoparticles at pH 4 for the reaction time of (a) 1 hr (b) 3 hrs (c) 5 hrs and (d) 24 hrs*

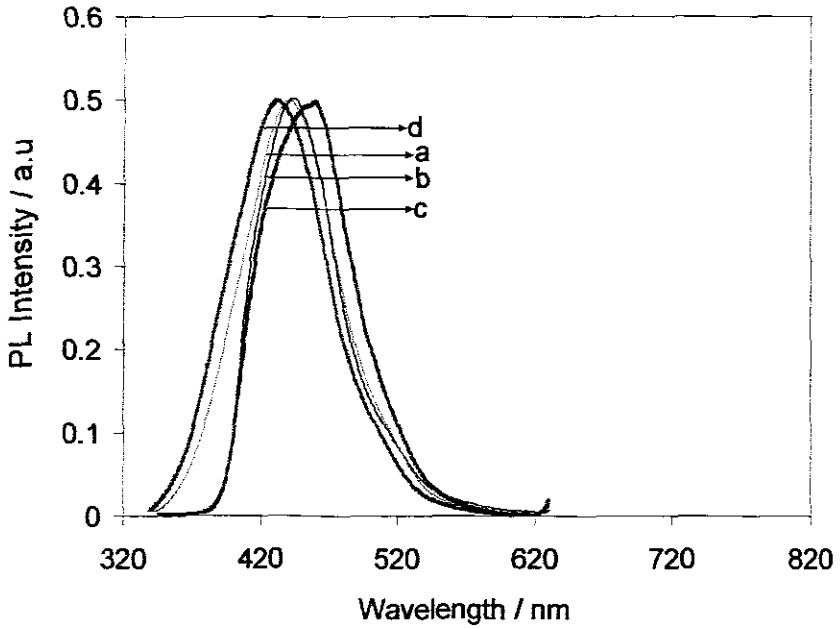


***Figure 4.13*** *Photoluminescence spectra ($\lambda_{320\ nm}$) of cysteine-capped CdSe nanoparticles at pH 11 for the reaction time of (a) 1 hr (b) 3 hrs (c) 5 hrs and (d) 24 hrs*

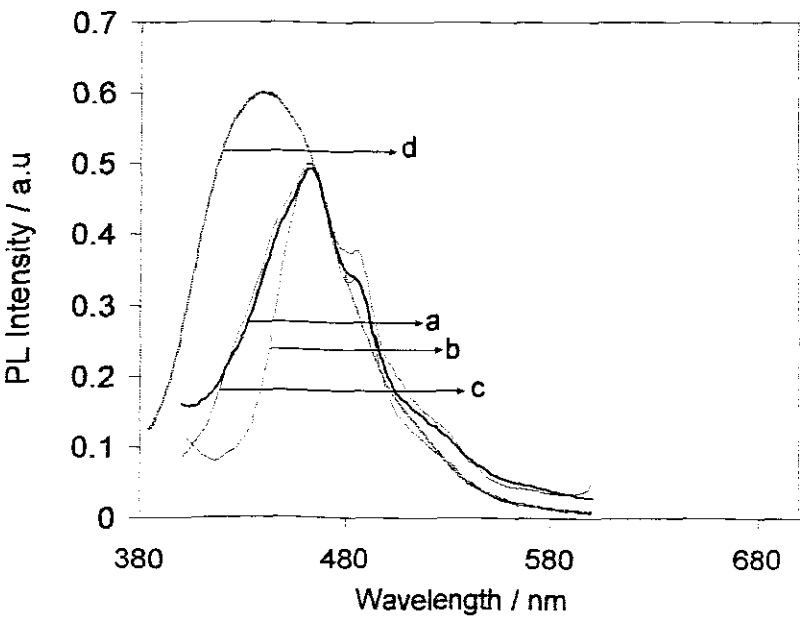


***Figure 4.14*** *Photoluminescence spectra ($\lambda_{320\ nm}$) of cysteine-capped CdSe nanoparticles at pH 7 for the reaction time of (a) 1 hr (b) 3 hrs (c) 5 hrs and (d) 24 hrs*

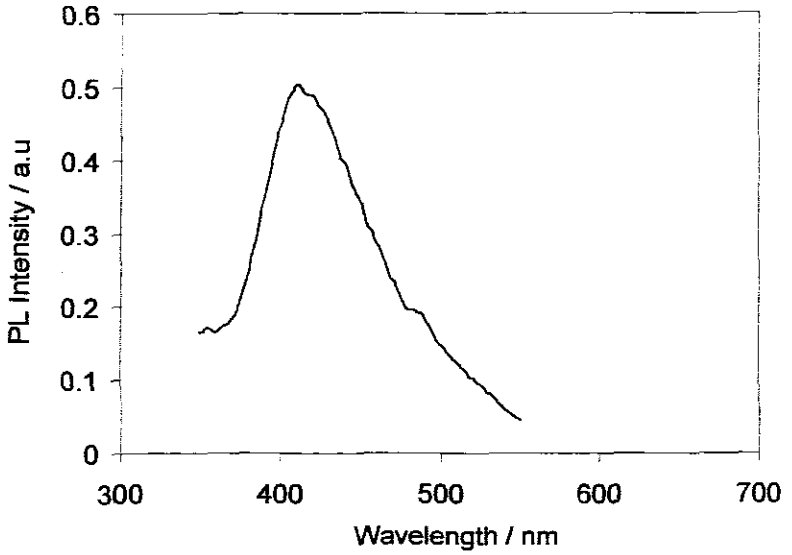


***Figure 4.15*** *Photoluminescence spectra ($\lambda_{320\ nm}$) of cysteine-capped CdSe nano-particles at pH 4 for the reaction time of 24 hrs*

The absorption and emission spectra of the nanoparticles at pH 7 is shown in Figures 4.11 and 4.14. The absorption spectra show an excitonic shoulder that is blue-shifted as the reaction time increases for the first 5 hrs, indicative of monodispersed particles with smaller particle sizes. The spectrum at 1 hour also contains higher energy transitions. As the reaction time increases, the excitonic shoulder becomes broad and the particle decreases further in size, indicating that the size distribution becomes large with decreasing particle size and increasing reaction time. The particle sizes as calculated at different reaction times are 1.74 nm (1 hr), 1.73 nm (3 hrs), 1.71 nm (5 hrs) and 1.69 nm (24 hrs). The emission maximum appears at the same wavelength (464 nm) with improved luminescence as the reaction time increases for the first 5 hrs and, becomes blue-shifted at 24 hrs (440 nm) with improved luminescence. The slight increase in the particle size of the nanoparticles, obtained at 1 hour under this pH (1.74 nm) as compared to the one at pH 11 (1.68 nm), shows that the growth rate is higher at this pH. The decrease in the particle size after 1 hour as the reaction time

increases indicates that, the growth of the particle ceased before 3 hrs. We propose two factors for this, (i) lower $Cd^{2+}$ ions concentrations (limiting reactant) as the reaction time increases, (ii) digestive ripening. Digestive ripening is a mode of particle growth, where smaller particles grow at the expense of larger ones and is essentially the opposite of Ostwald ripening.[48] It usually occurs through breaking into smaller fragments or digestion of a layer at a time, which re-grows at a later stage. The decrease in particle size, without any significant change in the emission maxima, suggests that the first factor is not responsible for the decrease in the particle sizes for the first 5 hours of reaction times. The constant emission maxima indicate that the emission must come from particles of the same size. Hence the reduction might be through digestive ripening. The improved luminescence obtained as the reaction time increased is in agreement with the fact that (i) the rate of ionisation and complexation increases with the reaction time; (ii) at a longer period, the formation of $Cd^{2+}$-thiol complex produced further passivation for the nanoparticles which improves the luminescence. The decrease in the absorption and emission maxima at 24 hrs hours, together with an enhanced, improved luminescence, further supports our particle growth mode whereby, the increase in the thiol anions as the reaction time increases leads to a decrease in particle size, with an improved luminescence as discussed earlier.

Figure 4.12 shows the absorption spectra at pH 4. All the spectra show a well-developed absorption maximum near the onset of absorption which is ascribed to the first electronic transition. The absorption maximum is broad when compared to the spectra obtained at higher pH, indicating that the particles at this pH have a broader size distribution. The absorption maximum is initially slightly blue-shifted after 1

hour reaction time (decrease in particle size), then red-shifted after 3hrs (increase in particle size) and finally, remains the same throughout the reaction time. The particle sizes as calculated are 1.84 nm (1 hr), 1.80 nm (3 hrs) and 1.88 nm (5 & 24 hrs). The large increase in the particle size of the nanoparticles obtained at 1 hour under this pH (1.84 nm) as compared to the one at higher pH (1.74 nm, pH 7 and 1.68 nm, pH 11), shows that highest growth rate occurs at this pH. The decrease in the particle size, as the reaction time increases to 3 hrs, indicates that the particle growth ceases before 3 hrs, after which digestive ripening takes place. The digestion also ceased before 5 hours and the particles grew via Ostwald ripening. This type of decrease in particle size, followed by Ostwald ripening, has also been reported by Vossmeyer *et al.*[25] for CdS nanoparticles of smaller particle sizes. The absence of luminescence in the spectra for the first 5 hrs of the reaction is attributed to the rate of ionisation and complexation, which is very low at the beginning of the reaction under this pH. As discussed earlier, this rate increases as the reaction time increases and leads to improved passivation of the nanoparticles after 24 hrs. A similar particle size obtained at 5 and 24 hrs reaction time indicates that there is no increase in particle size, as the reaction time increases after 5 hrs. This might also imply that there is no significant increase in the number of surface defects arising from the uncapped CdSe particles after 3 hrs, but that only ionisation and complexation occurred for the remaining part of the reaction. Hence, the thiol complex is able to passivate the surface state more efficiently and improve the luminescence.

#### 4.3.1.2.1.2 *Structural properties*

The TEM images of the cysteine-capped particles show that they are small (with particle size less than 2 nm), monodispersed, spherical and their sizes decrease

as the pH increases. A representative sample of the TEM image is shown in Figure 4.16.

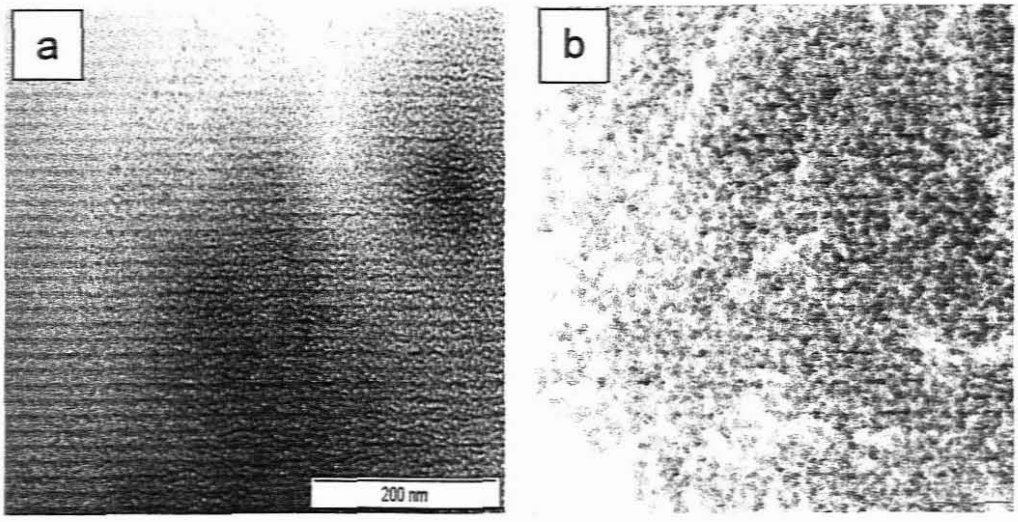


***Figure 4.16*** *TEM image of cysteine-capped CdSe nanoparticles at (a) pH 11 (5 hrs) and (b) pH 4 (5 hrs).*

#### 4.3.1.2.2 *Methionine-capped CdSe nanoparticles*

##### 4.3.1.2.2.1 *Optical properties*

The absorption and emission spectra of methionine-capped CdSe nanoparticles, are shown in Figures 4.17 to 4.20. The absorption edges decreases as the pH increases from 4 to 7 and then increases again when the pH of the solution changes to 11. The emission maxima increased with increasing pH for the first 3 hours and no luminescence was observed at pH 7. This trend in the absorption and emission spectra indicates that the pH of the solution greatly affects the nature of this amino-acid which in turn, influences the optical properties of the particles. The decrease in the particle size and non-luminescence at pH 7 might be attributed to the fact that, the thiol group of the methionine amino acid is not attached to any proton, unlike cysteine which is a hydrophilic amino acid. Hence, we propose that pH 7 might be its isoelectric point where it exits mainly as zwitterions, i.e. the charge $NH_3^+$ and $COO^-$

neutralise each other (equilibrium stage). Under this condition, the rate of ionisation and complexation of the thiol group would be greatly reduced. In general all the absorption shoulders and emission line widths at all the pH studied are broad, which are indicative of particles with large size distributions. Since all the particles (at pH 4 and 11) emit in the blue region, it can be deduced that the broad absorption shoulder might be due to the presence of the bulky hydrophobic side chain of the amino acid.

The absorption spectra of methionine-capped CdSe particles at pH 11, shows a tailing band-edge due to a large size of the particles. The emission maxima (Figure 4.17) are 406 nm (1 hrs), 407 nm (3 hrs) and 409 nm (5 & 24 hrs). The high luminescence at this pH is attributed to the increase in the rate of ionisation and complexation. The luminescence intensity increases with time and remains stable after 3 hours for the rest of the reaction time.

The absorption spectra at pH 7 are shown in Figure 4.18. The particle sizes, as calculated from the absorption band-edges are 2.83 nm (1 hr), 2.89 nm (3 &5 hrs) and 2.80 nm (24 hrs). This shows that the particle grows in size within the first 3 hrs and decreases in size after some period of stability.

Figures 4.19 and 4.20 show the absorption and emission spectra at pH 4. The particle sizes, as calculated from the absorption band-edges are 2.59 nm (1 and 3 hrs), 2.89 nm (5 hrs) and 2.95 nm (24 hrs). This shows that, unlike the growth trend for pH 7 and 11, the particle size increases with reaction time. The emission spectra show maxima at 336 nm (1 hr), 407 nm (3 hrs) and 419 nm (5 and 24 hrs). The lower wavelength of the emission maxima at 1 hour, together with a broad tail toward lower

energy, normally assigned to a trap state, could be attributed to the inefficiency of the capping group in passivating effectively the surface state at the beginning of the reaction. This is due to the lower rate of ionisation and complexation at this pH. As the reaction time increases the ionisation and complexation rate increase and the surface state becomes more passivated. The presence of an emission maximum at higher energy (364 nm) in the spectra for 3, 5 and 24 hours, might be an indication of the presence of two emitting species with different shapes.

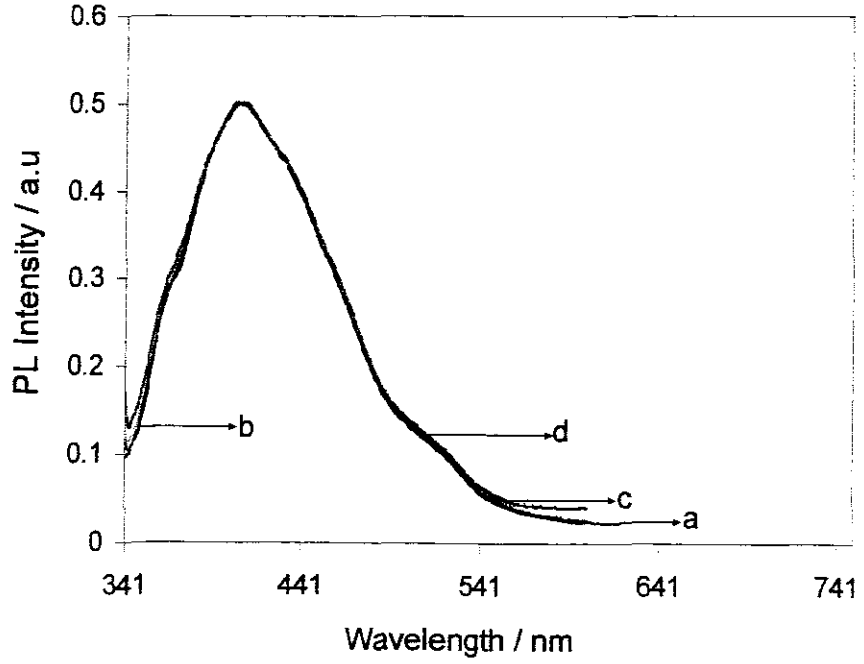


***Figure 4.17*** *Photoluminescence spectra ($\lambda_{300\ nm}$) of methionine-capped CdSe nano-particles at pH 11 for the reaction time of (a) 1 hr (b) 3 hrs (c) 5 hrs and (d) 24 hrs*

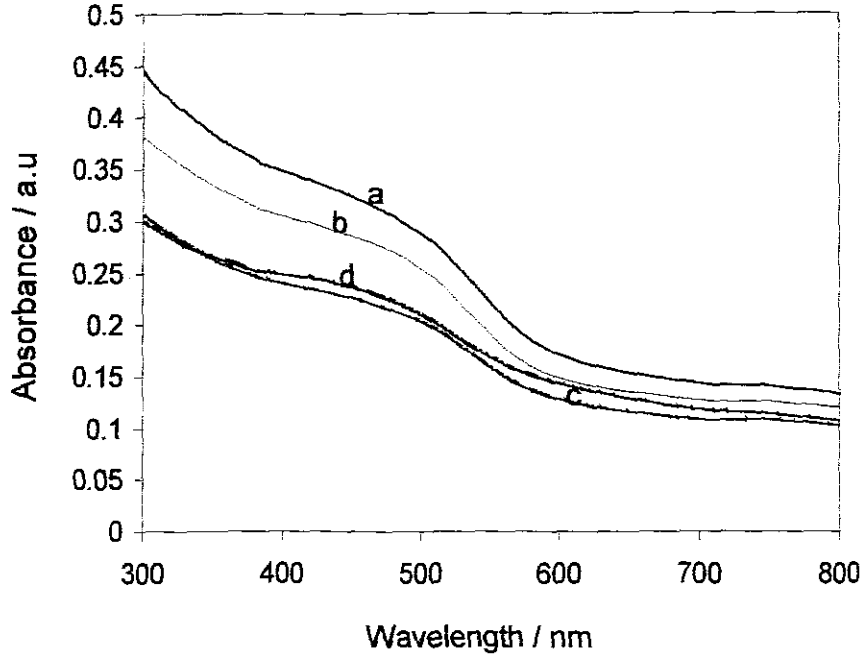


***Figure 4.18*** *Absorption spectra of methionine-capped CdSe nanoparticles at pH 7 for the reaction time of (a) 1 hr (b) 3 hrs (c) 5 hrs and (d) 24 hrs*

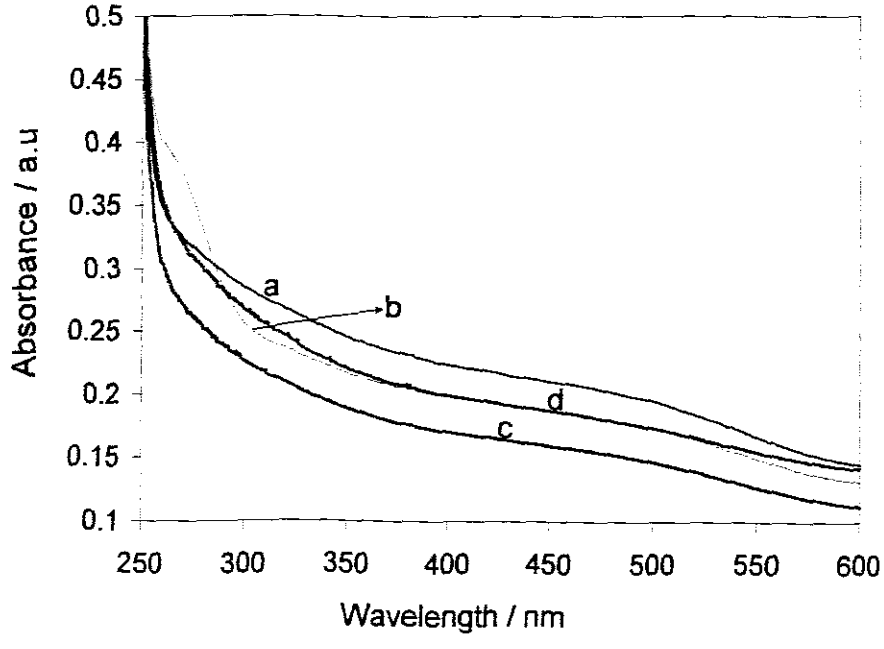


***Figure 4.19*** *Absorption spectra of methionine-capped CdSe nanoparticles at pH 4 for the reaction time of (a) 1 hr (b) 3 hrs (c) 5 hrs and (d) 24 hrs.*

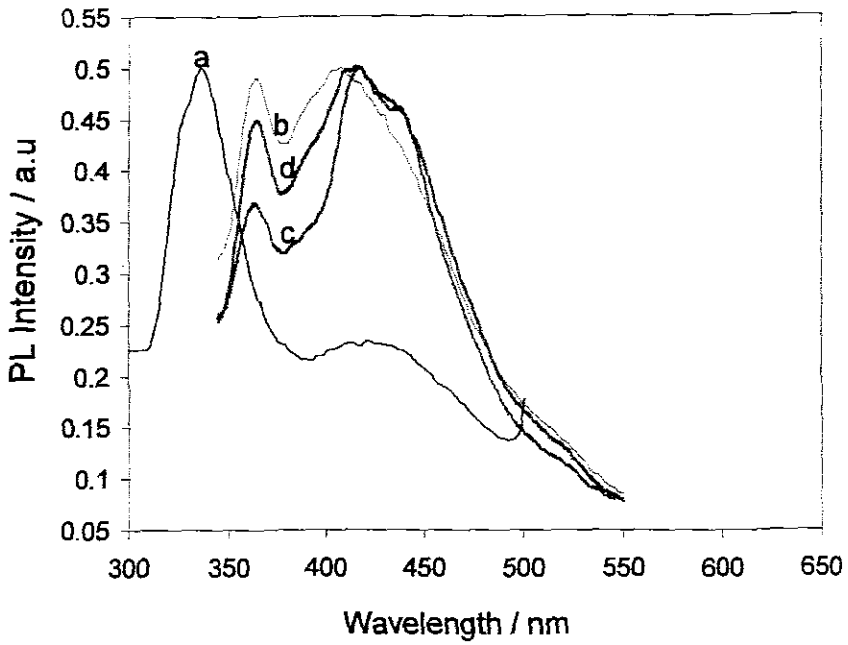


***Figure 4.20*** *Photoluminescence spectra ($\lambda_{300\ nm}$) of methionine-capped CdSe nano-particles at pH 4, for the reaction time of (a) 1 hr (b) 3 hrs (c) 5 hrs and (d) 24 hrs.*

#### 4.3.1.2.2.2 *Structural Properties*

A typical representative of the TEM images is shown in Figure 4.21. At pH 7, the TEM image shows that the particles are spherical and more dispersed when compared to pH 4, where the image shows aggregated particles. This pattern of the particle makes it difficult to identify the presence of other shapes apart from spherical at pH 4, as indicated by the emission spectra (Figure 4.21). At pH 11, the particle appears as aggregates forming larger particles.

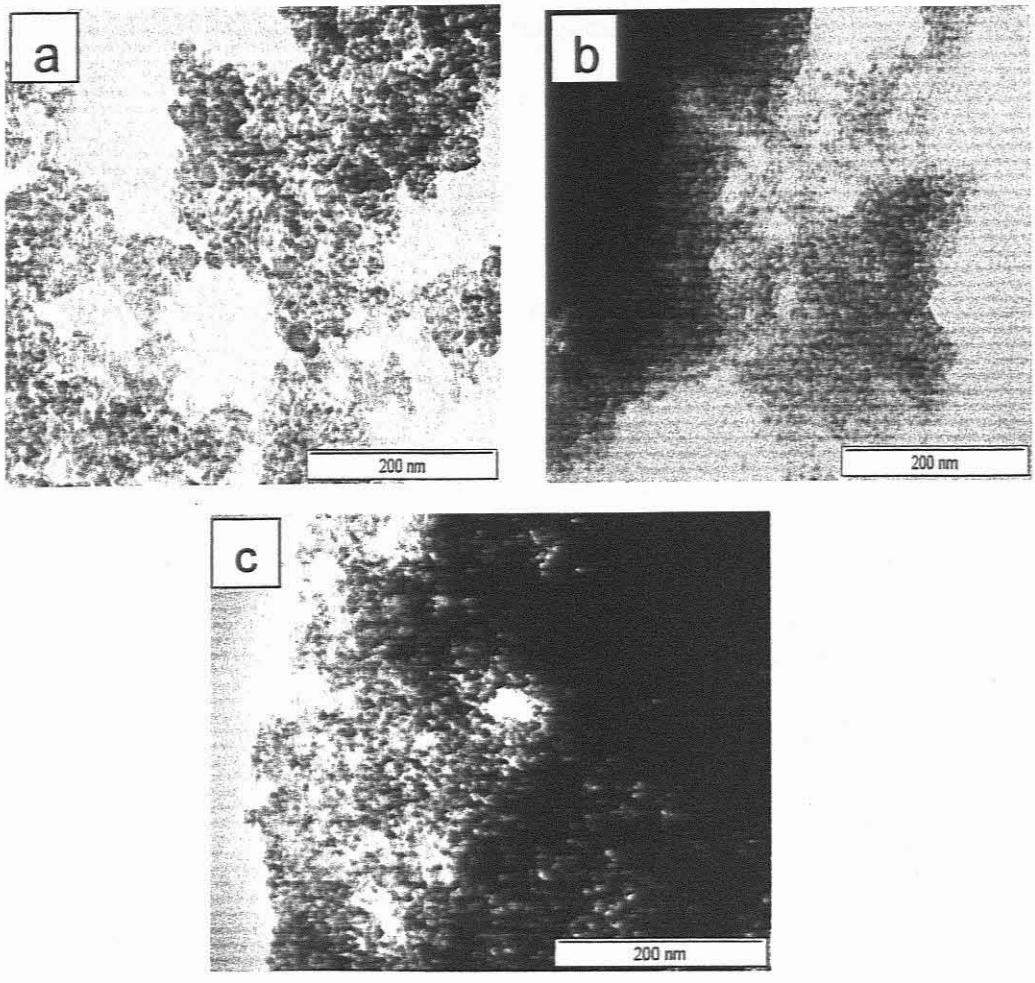


***Figure 4.2*** *TEM image of methionine-capped CdSe nanoparticles at (a) pH 11 (3 hrs), (b) pH 7 (3 hrs) and (c) pH 4 (3 hrs).*

#### 4.3.1.2.3 *Ascorbic acid-capped CdSe nanoparticles.*

We have chosen ascorbic acid (also known as vitamin C), a water-soluble vitamin and an antioxidant, as one of the capping agents because studies have shown that the cytotoxicity of CdSe and ZnS capped CdSe was increased significantly by exposure to light and/or air,[68,69] which means that degradation of semiconductor nanoparticles proceeds via oxidative pathways. Hence, we hope that the antioxidant properties of ascorbic acid will slow the process and improve stability, being a very efficient oxygen scavenger. In addition it is a water-soluble vitamin with hydroxyl

groups that are expected to facilitate its complexation of metal ions and its solubility in water.

#### 4.3.1.2.3.1 *Optical Properties.*

The absorption and emission spectra of ascorbic acid-capped CdSe nanoparticles are shown in Figures 4.22 to 4.26. The absorption band-edges and emission maxima are all blue-shifted in relation to the bulk band gap. The absorption band-edges decrease with increasing sharpness of the absorption shoulder as the pH increases from 4 to 11, signifying a decrease in particle size. The emission spectrum shows no luminescence at pH 4 and as the pH increases, the emission width becomes narrower with increase in luminescence intensity,

Figure 4.22 shows the optical properties at pH 4. The absorption shoulders are very broad and the band-edges are very close to the bulk band gap, indicating large particle sizes. This is also reflected in the colour of the solution which gives an intense red colouration immediately after the addition of the selenide ion. The size decreases slightly before 3hrs, after which the growth process stops and no luminescence is observed throughout the reaction time. This might be due to the high stability of ascorbic acid in acidic medium hence, a low complexation with the metal. The particle sizes as calculated, using the EMA model, are 7.48 nm (1 hr) and 7.32 nm (3 hrs).

The absorption and emission spectra at pH 7 are shown in Figures 4.23 and 4.24. All the absorption spectra for the first 5 hours show, a broad absorption shoulder close to the band-edge without any significant shift in the band-edges, as the reaction time

increases. This indicates that the particle sizes are nearly the same throughout these periods. The particle size as calculated, using the EMA model, is 4.23 nm. The presence of an absorption peak appearing at the same wavelength (350 nm) with increases in the optical density as the reaction time increases for the first 5 hours, suggest a preferential thermodynamic stability of the particles after one hour. It might also be responsible for the even distribution of the particles at this pH, as shown in the TEM image (Figure 4.28). As the reaction time increases, this peak disappears and a tailing band-edge is observed at 24 hours.

The emission spectrum shows a broad emission with low intensity at the start of the reaction and an obvious tail towards higher energy, which is attributed to the formation of small nanocrystals with poor surface quality. As the reaction time increases (3 hrs), the emission intensity increases and the obvious tail towards lower energy, becomes less pronounced and eventually disappears in the spectrum obtained at 24 hours, which gives a narrow emission with high intensity at higher wavelength.

Figures 4.25 and 4.26 show the absorption and emission spectra at pH 11. The absorption spectra for the first 5 hours show a sharp absorption shoulder close to the band-edge, when compared with spectra obtained at lower pH. This might be attributed to the small size of the particles at this pH. The absorption shoulders appear at the same position (488 nm, 2.54 eV) with increase in optical density, as the reaction time increases without any significant shift in the absorption edge. The particle size calculated, using the EMA model, is 2.64 nm. As the reaction time increases the absorption shoulder disappears and reappears as a small, broad shoulder

at 556 nm, 2.23 eV with a new band-edge at 623 nm, signifying an increase in particle size. The particle size calculated, was 3.79 nm at this period (24 hrs).

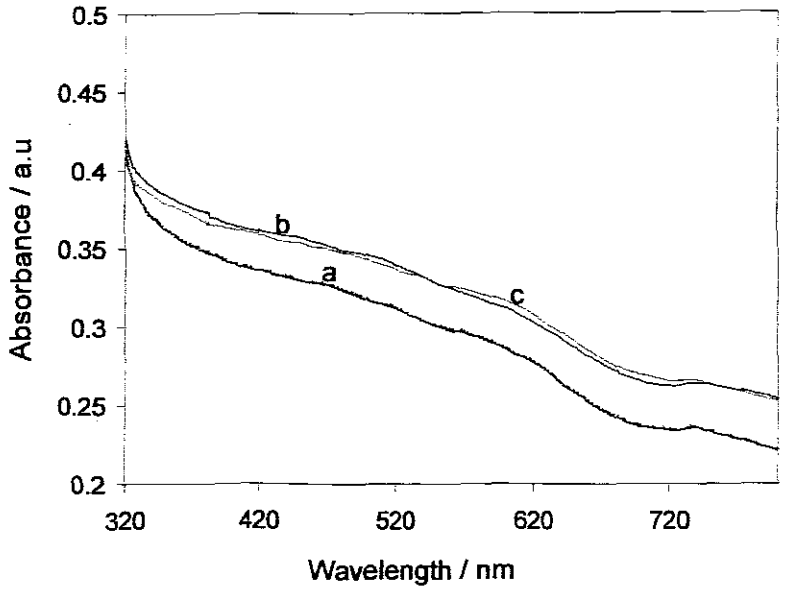


***Figure 4.22*** *Absorption spectra of ascorbic acid-capped CdSe nanoparticles at pH 4 for the reaction time of (a) 1 hr (b) 3 hrs (c) and 5 hrs*

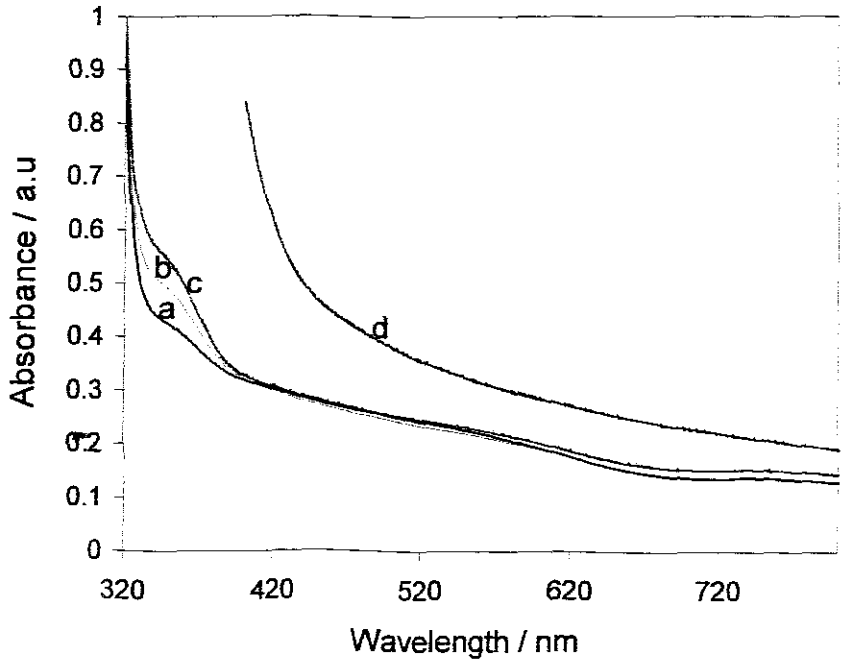


***Figure 4.23*** *Absorption spectra of ascorbic acid-capped CdSe nanoparticles at pH 7 for the reaction time of (a) 1 hr (b) 3 hrs (c) 5 hrs and (d) 24 hrs*

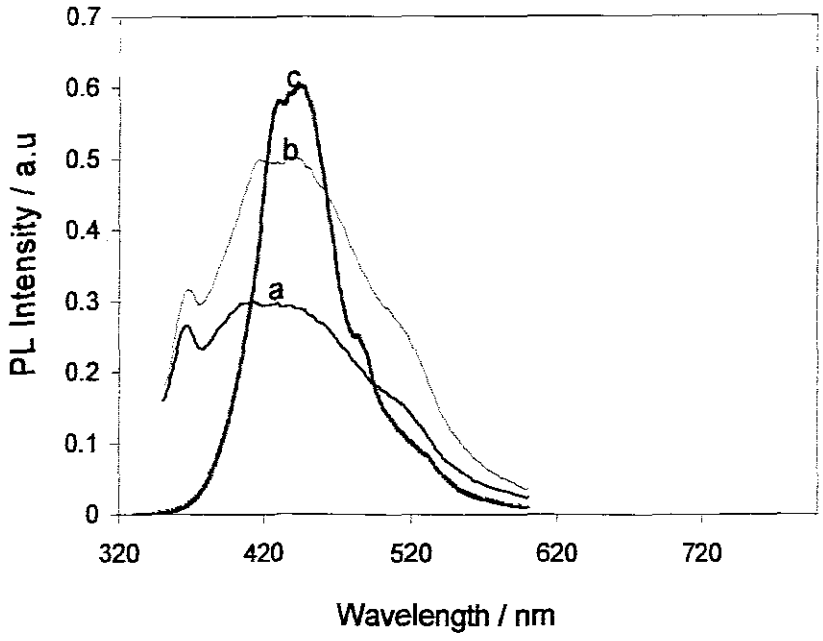


***Figure 4.24*** *Photoluminescence spectra ($\lambda_{340\ nm}$) of ascorbic acid-capped CdSe nanoparticles at pH 7, for the reaction time of (a) 1 hr (b) 3 hrs and (c) 24 hrs*

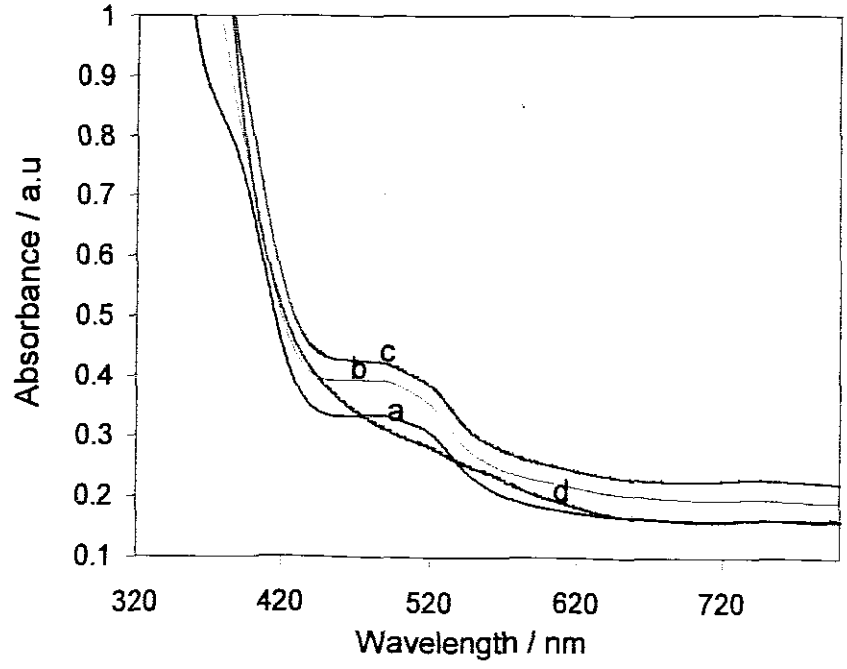


***Figure 4.25*** *Absorption spectra of ascorbic acid-capped CdSe nanoparticles at pH 11 for the reaction time of (a) 1 hr (b) 3 hrs (c) 5 hrs and (d) 24 hrs*

The emission maxima at pH 11 appear at the same wavelength but the emission width becomes slightly narrower as the reaction time increases for the first 5 hours. At 24 hours, the emission curve is typical of particles with defects, which may be attributed to the large particle size at this time, leading to insufficient passivation of the surface states.

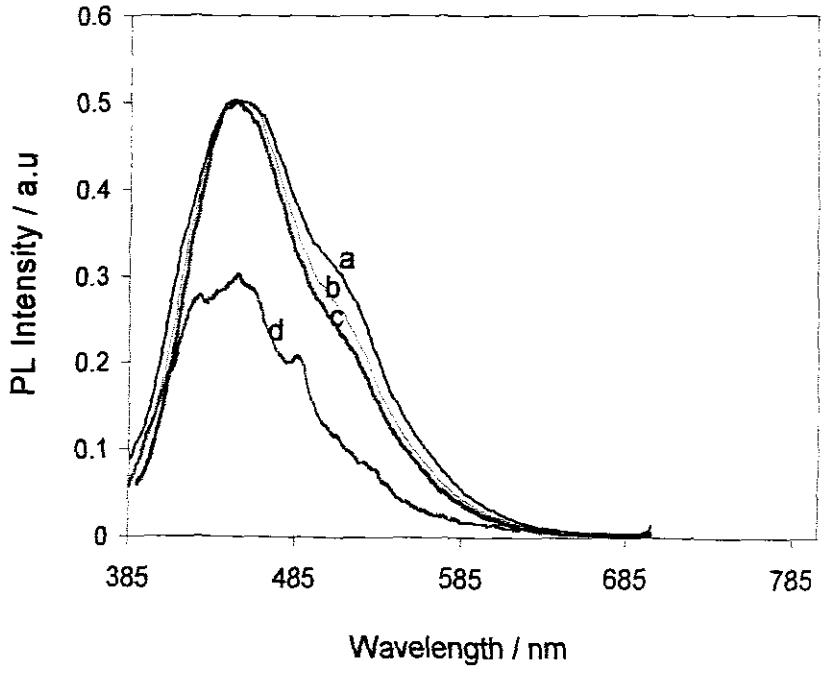


***Figure 4.26*** *Photoluminescence spectra ($\lambda_{340\ nm}$) of ascorbic acid-capped CdSe nanoparticles at pH 11 for the reaction time of (a) 1 hr (b) 3 hrs (c)5 hrs and (d) 24 hrs*

#### 4.3.1.2.3.2 *Structural Properties*

A typical representative TEM image of ascorbic acid-capped CdSe nanoparticles is shown in Figure 4.27 and 4.28. At pH 4 (Figure 4.27a), the TEM shows particles of different shapes (dots and elongated) that are very close to each other in the form of an aggregate. The diameter and particle size distributions of the

solution at pH 7 (3hrs), are shown in Figures 4.28a & b. The TEM image shows large spherical particles spaciously distributed without any aggregation. The average particle size, as determined from the TEM image, is 4.22 nm. This correlates with the particle size calculated from the absorption band-edge (640 nm and 4.23 nm), using the EMA model. The relative standard deviation of the size of the nanoparticles shown in Figure 4.28b is 1.236 nm (29 %) indicating a broad size distribution. This is attributed to the large difference (4.1 nm) in the size distribution between the biggest and smallest particles present in the TEM image, within the selected fraction. At pH 11 (Figure 4.27b), the TEM shows the presence of small, spherical, nearly monodispersed particles. Short elongated particles (mono rods) are also present, as a result of fusion between the spherical particles.

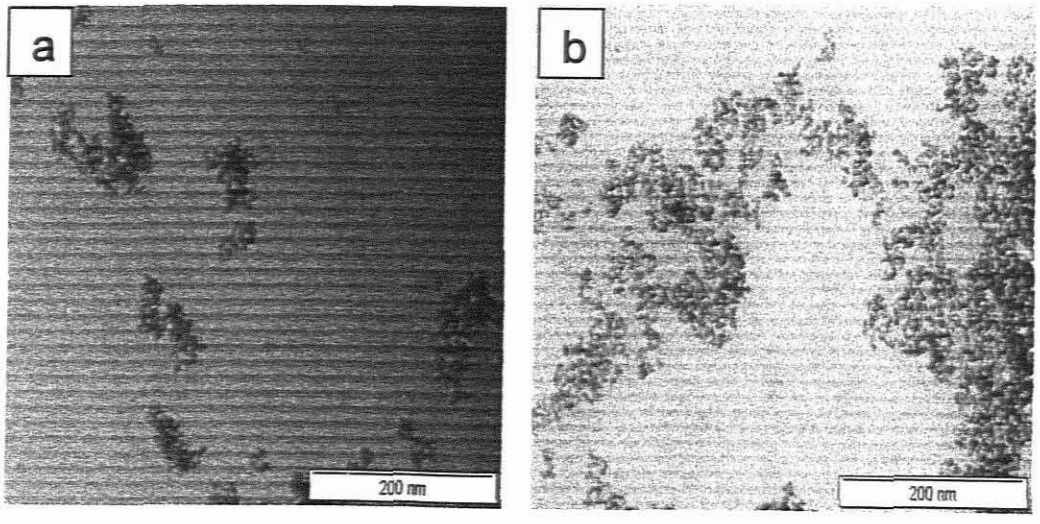


***Figure 4.27*** *TEM images of ascorbic acid-capped CdSe at (a) pH 4 (3 hrs) and (b) pH 11 (3hrs)*

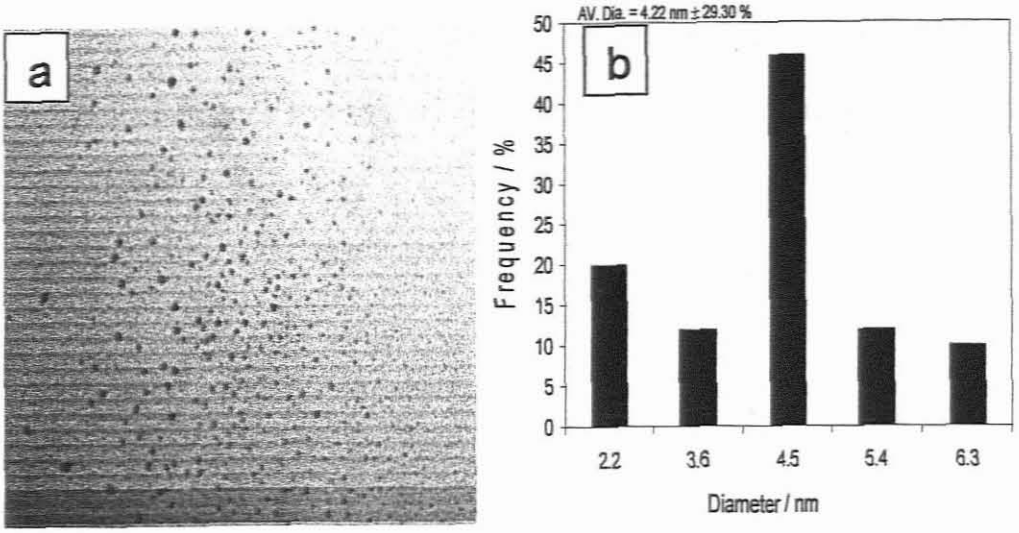


***Figure 4.28*** *(a) TEM images and (b) particle size distribution of ascorbic acid-capped CdSe at pH 7 (3 hrs)*

#### 4.3.1.2.4 *Starch-capped CdSe nanoparticles*

##### 4.3.1.2.4.1 *Optical Properties*

The absorption and emission spectra of starch-capped CdSe nanoparticles, synthesized with 0.05 wt/% of starch using 0.16 mmol monomer concentration, is shown in Figure 4.29. The absorption spectrum (Figure 4.29a) consist of two absorption shoulders which indicate the presence of particles with two different sizes or morphology[48] and an absorption edge at 670 nm (1.85 eV), which is blue-shifted from the bulk band gap due to quantum confinement. From the TEM image (Figures 4.31) the sharp, narrow, higher energy transition (263 nm), is attributed to monodispersed, small, spherical-shape particles, while the broad lower energy transition (602 nm) is attributed to elongated (nanorods and nanowires) particles. Estimation of the size of the rods, using the effective mass approximation (EMA) model (using a shifted band gap of 0.12 eV) suggested particles with a diameter of 5.59 nm. Estimation of the spherical particle size could not be made as the absorption

of the rods masked that of the dots. The emission maximum at 337 nm (Figure 4.29b) is attributed to emission from the smaller particles. The sharp luminescence and narrow emission width is indicative of a particle with few electronic defects attributed to the efficiency of the starch, in electronically passivating the surface states or defects normally associated with nanoparticles.[56,57,70]

The absorption and emission spectra of starch-capped CdSe nanoparticles synthesized with 0.05 wt/% of starch, using a higher mmol monomer concentration (0.32 mmol), is shown in Figure 4.30. The absorption spectrum (Figure 4.30a) also consists of two absorption shoulders which indicates the presence of particles with two different sizes or morphology and, an absorption edge at 652 nm (1.90 eV). Similar to the synthesis at lower concentration, the narrow, sharp, higher energy transition (285 nm) is attributed to monodispersed, small, spherical-shaped particles, while the broad lower energy transition (558 nm) is attributed to the elongated (short rods) particles. Estimation of the size of the rods, using the effective mass approximation (EMA) model (using a shifted band gap of 0.17 eV), suggest particles with a diameter of 4.70 nm. However, in comparison to the particles at lower monomer concentration, it is noted that the peak at higher energy transition is red-shifted while the one at lower energy transition is blue-shifted. It is expected that an increase in monomer concentration should result in larger anisotropic particles.[67,71-74] Therefore, the red-shift at higher energy is attributed to the increase in monomer concentration, while the blue-shift at lower energy transition is attributed to the influence of the capping group. This might arise from the same wt/% of starch (0.05) used for the two different concentrations which may not be sufficient for effective passivation at higher concentration.

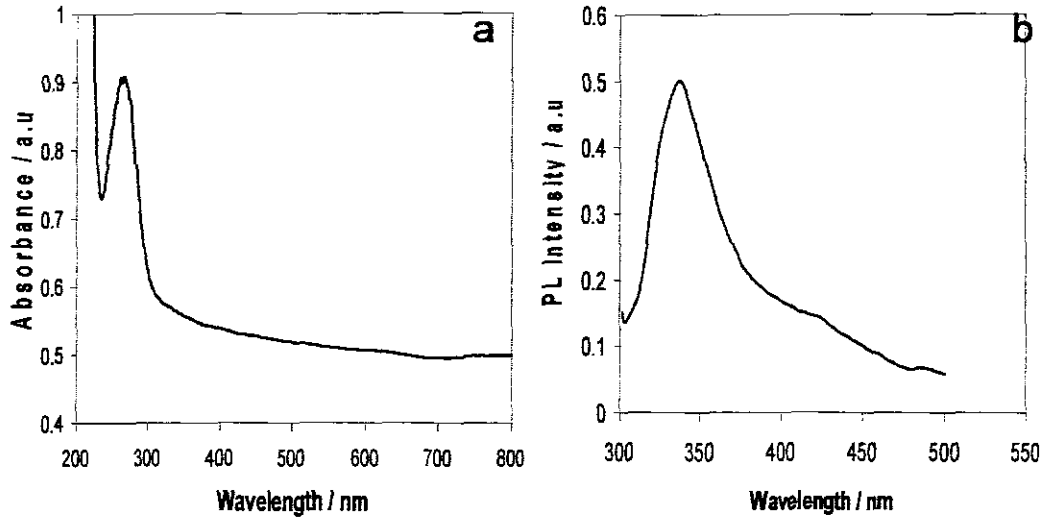


***Figure 4.29*** *(a) Absorption and (b) photoluminescence spectra of starch-capped CdSe nanoparticles synthesised using 0.16 mmol monomer concentration*

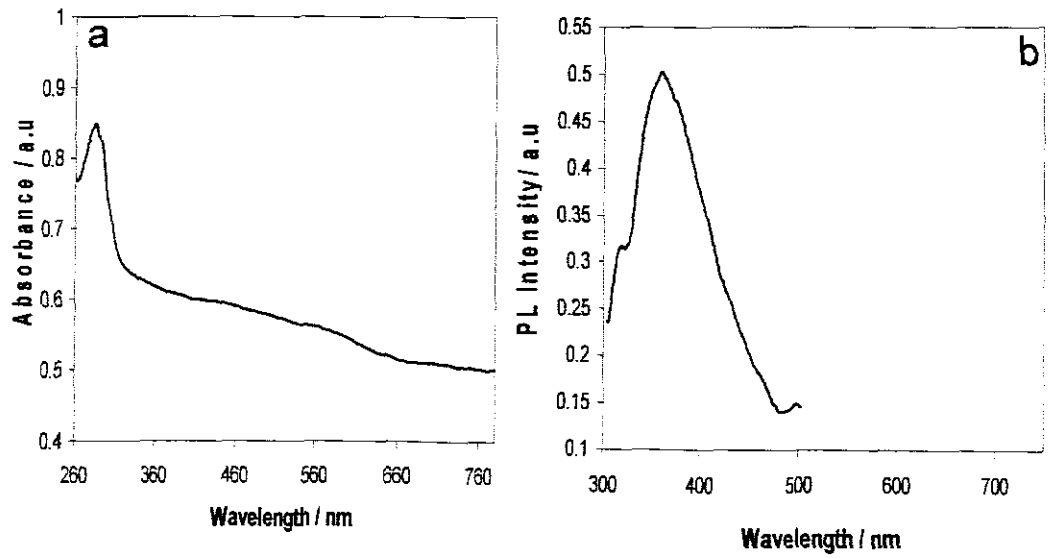


***Figure 4.30*** *(a) Absorption and (b) photoluminescence spectra of starch-capped CdSe nanoparticles synthesised using 0.32 mmol monomer concentration*

The emission maximum at 361 nm (Figure 4.30b) attributed to the spherical particles, is red-shifted in relation to the emission maxima at lower concentration, supporting the fact that an increase in the monomer concentration leads to an increase in particle size.

#### 4.3.1.2.4.2 *Structural Properties*

The TEM images of the starch-capped CdSe nanoparticles synthesised, using 0.16 mmol monomer concentrations, is shown in Figure 4.31. The image consists of nanorods and nanowires of very high aspect ratio, together with monodispersed smaller spherical particles. This elucidates the presence of the two absorption shoulders observed in the absorption spectrum. On increasing the monomer concentrations (0.32 mmol), the TEM image (Figure 4.32) shows the presence of monodispersed spherical particles together with elongated particles of low aspect ratios. Figure 4.32b shows the different patterns of how the dot particles arrange themselves into elongated ones. The following patterns are visible (I) tripod, (II) sinusoidal and (III) S-shaped. The larger-sized spherical particles and elongated particles of low aspect ratio obtained at higher concentration, indicates that the wt/% of starch used, greatly influences the transformation of the particle shape from dots to elongated particles.

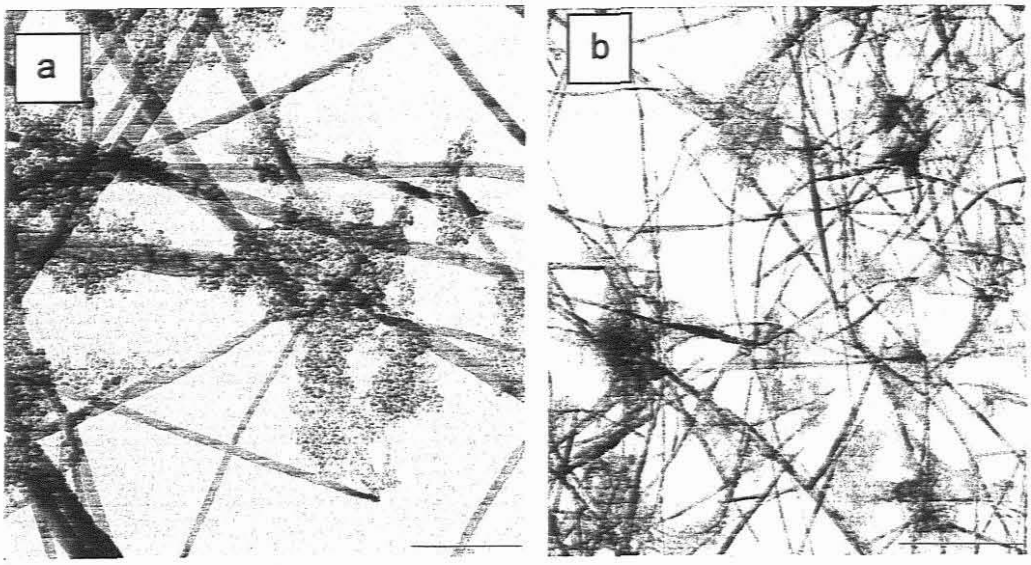


***Figure 4.31*** *The TEM image of starch-capped CdSe synthesised using 0.16 mmol monomer concentrations showing (a) nanorods and (b) nanowires, both samples containing smaller spherical/dots-shaped particles*

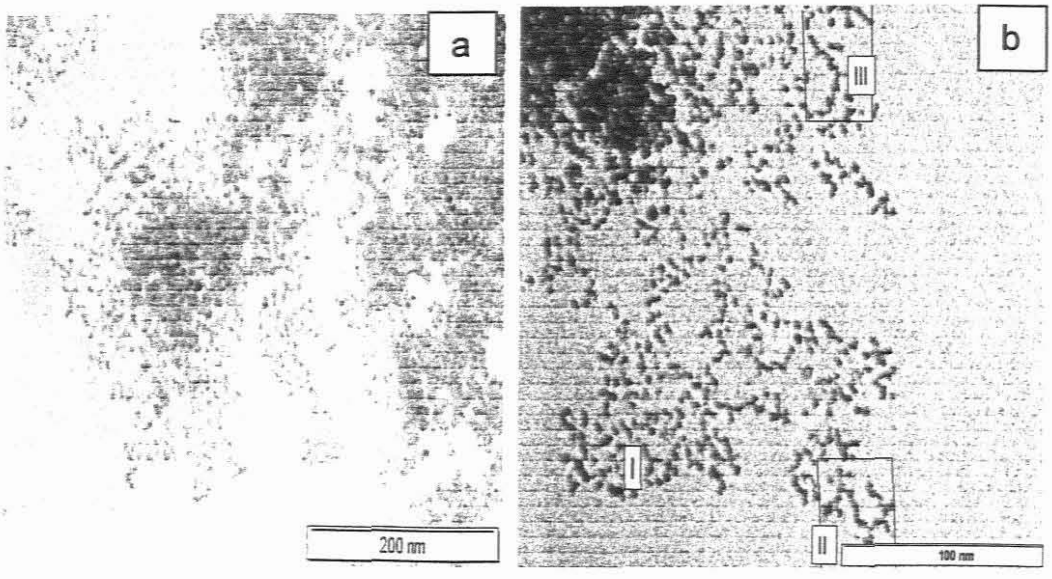


***Figure 4.32*** *The TEM image of starch-capped CdSe synthesised using 0.32 mmol monomer concentrations showing (a) mixture of dot and elongated particles and (b) different pattern of elongated arrangement,(I)tripod (11)sinusoidal and (III) S-shaped.*

Figures 4.33 and 4.34 show the XRD patterns of the starch-capped CdSe nano-particles, synthesised at different monomer concentrations. The patterns show five diffraction peaks corresponding to the crystalline planes of hexagonal CdSe. The results are in accordance with literature reports on elongated particles.[23,25,75] The sharp X-ray diffraction pattern of the 0.16 mmol monomer concentration samples (Figure 4.33), suggests that the diffraction is predominantly due to the presence of nanorods and nanowires of a very high aspect ratio. This also accounts for the slight shift of the diffraction peaks to higher 2θ value. The presence of a double peak at 2θ = ~ $30.4^0$ in the two XRD patterns is attributed, to the starch crystalline peak.

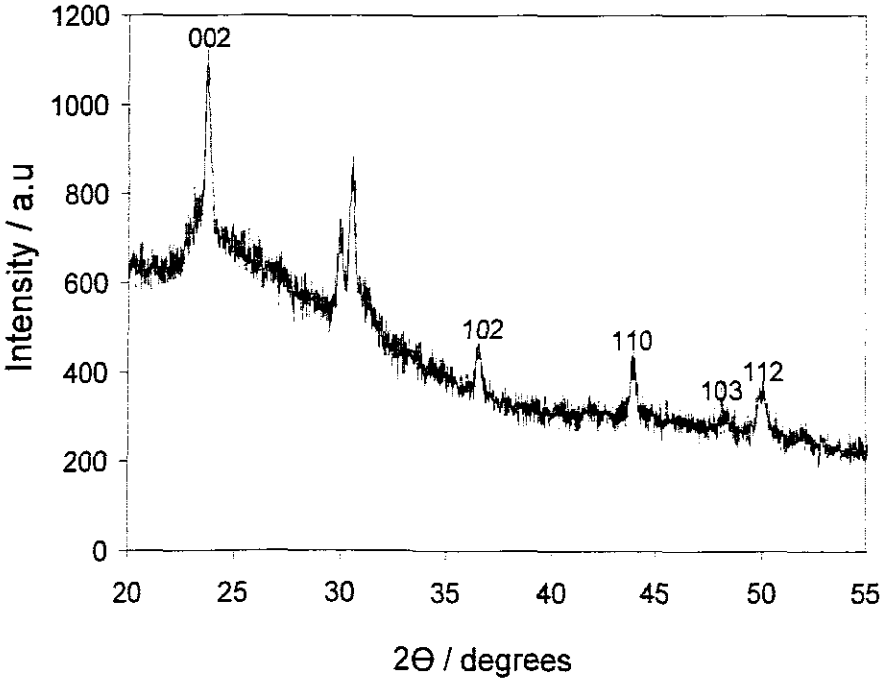


***Figure 4.33*** *XRD patterns of starch-capped CdSe using 0.16 mmol monomer concentrations*

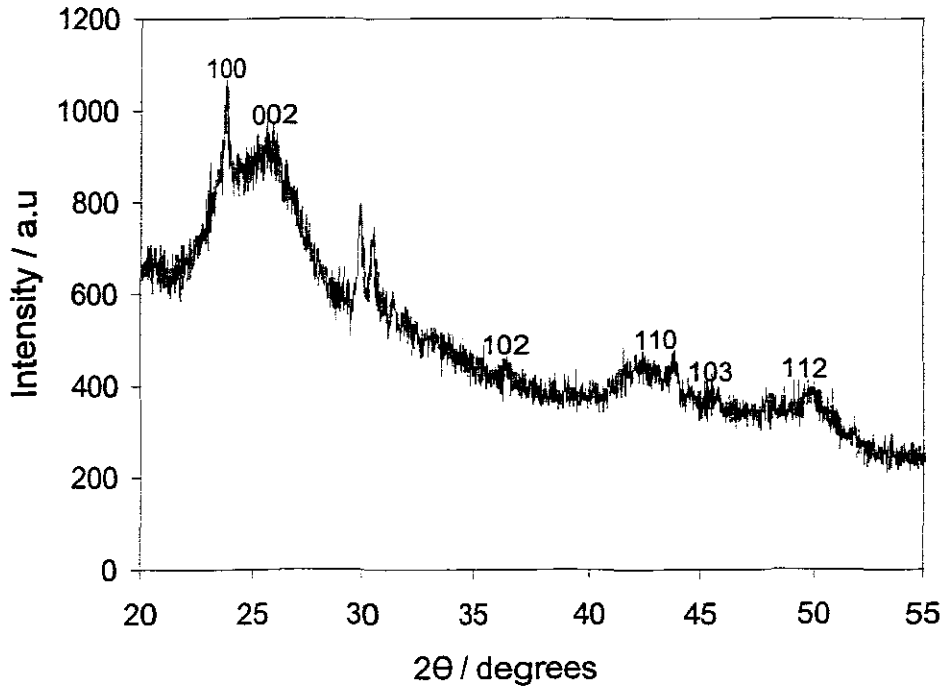


***Figure 4.34*** *XRD patterns of starch-capped CdSe using 0.32 mmol monomer concentrations*

#### 4.3.1.2.5 *Polymer-capped CdSe nanoparticles*

Polymer-capped nanoparticles have been increasingly studied because of their enhanced optical and electronic properties. They are good choices as stabilizers, because they can interact with metal ions by complex or ion-pair formation and, can be designed to certain physical properties of semiconductor nanoparticles.[76-78] We have chosen polyvinyl alcohol (PVA) as a capping agent in addition to aforementioned reasons because, (i) the high viscosity of the polymer solution would be helpful in controlling the growth of selenide nanoparticles and, prevent particles from aggregating hence, no additional stabilizer would be needed, (ii) they have high aqueous solubility and (iii) from applications point of view, the polymer matrix would protect the selenide against photo-oxidation.

#### 4.3.1.2.5.1 *PVA-capped CdSe nanoparticles*

##### 4.3.1.2.5.1.1 *Optical properties*

The absorption and emission spectra of PVA-capped CdSe nanoparticles, using 0.32 mmol monomer concentration, is shown in Figures 4.35 and 4.36. The absorption shoulders are all blue-shifted in relation to the bulk band gap. The particle sizes as calculated, using the EMA model, are 4.70 nm (1 hr), 4.57 nm (3 hrs), 4.04 nm (5 hrs) and 3.60 nm (24 hrs). This indicates a decrease in particle size as the reaction time increases and could be attributed to digestive ripening, considering the fact that (i) the emission maxima appear nearly at the same position and, (ii) the spectra show higher energy transitions at the same position (299 nm and 315 nm) throughout the reaction time. The presence of two bands in the UV region of the spectrum located at 269 nm and 278 nm, appearing at the same position in the entire spectrum, is attributed to *n*- $\pi^*$ excited transition of the CdSe-PVA nanocomposite.[79]

Figures 4.37 and 4.38 show the absorption and emission spectra of PVA-capped CdSe, at lower monomer concentration (0.16 mmol). The absorption band-edges and emission maxima are blue-shifted, as compared to those synthesised at higher monomer concentration indicating decrease in the particle size. Similar to the absorption spectrum at higher monomer concentration, all the absorption spectra show the presence of two bands in the UV region, attributed to the *n*- $\pi^*$ excited transition of CdSe-PVA nanocomposite. In addition, the entire spectrum shows the presence of higher energy transitions at 299 nm and 315 nm, signifying particles with narrow size distributions. Furthermore, the shifts in the particle sizes, as the reaction time increases, are the same for both concentrations. The particle sizes as calculated,

using the EMA model, are 3.95 nm (1 hr), 3.73 nm (3 hrs), 3.66 nm (5 hrs) and 3.37 nm (24 hrs).

The emission line width becomes narrower with an increase in intensity, as the reaction time increases. All particles emit in the blue region without any significant change in the emission maxima, which is at 406 nm.

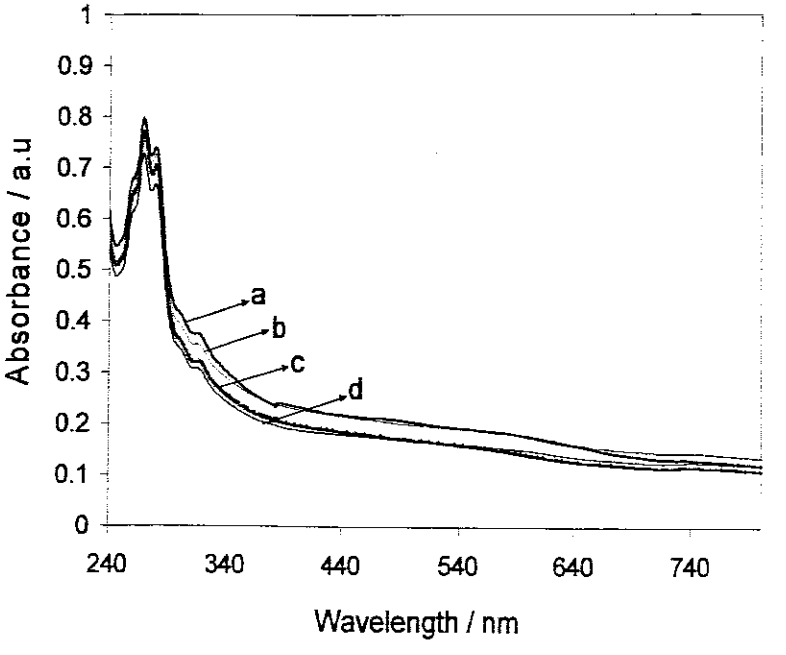


***Figure 4.35*** *Absorption spectra of PVA-capped CdSe using 0.32 mmol monomer concentrations at (a) 1 hr, (b) 3 hrs, (c) 5 hrs and (d) 24 hrs reaction times*

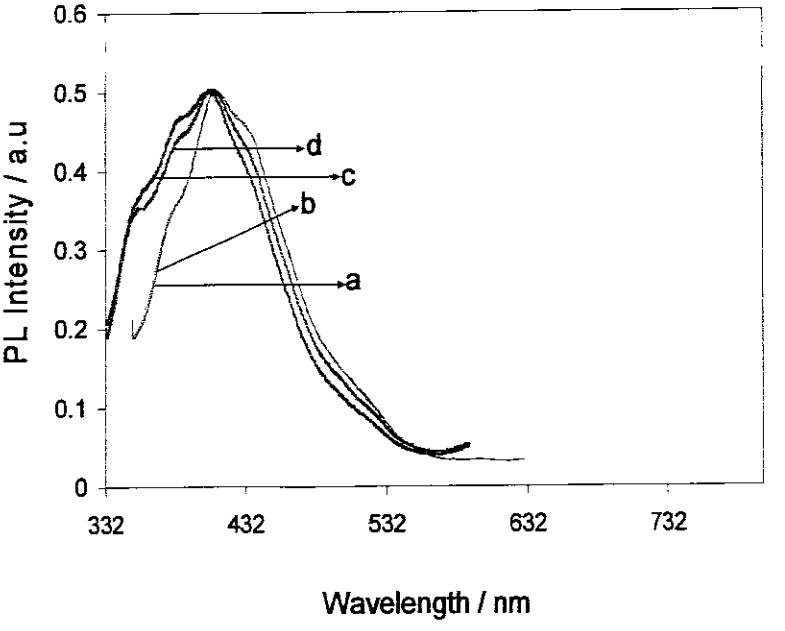


***Figure 4.36*** *Photoluminescence spectra ($\lambda_{300\,nm}$) of PVA-capped CdSe using 0.32 mmol monomer concentrations at (a) 1 hr, (b) 3 hrs, (c) 5 hrs and (d) 24 hrs reaction times*

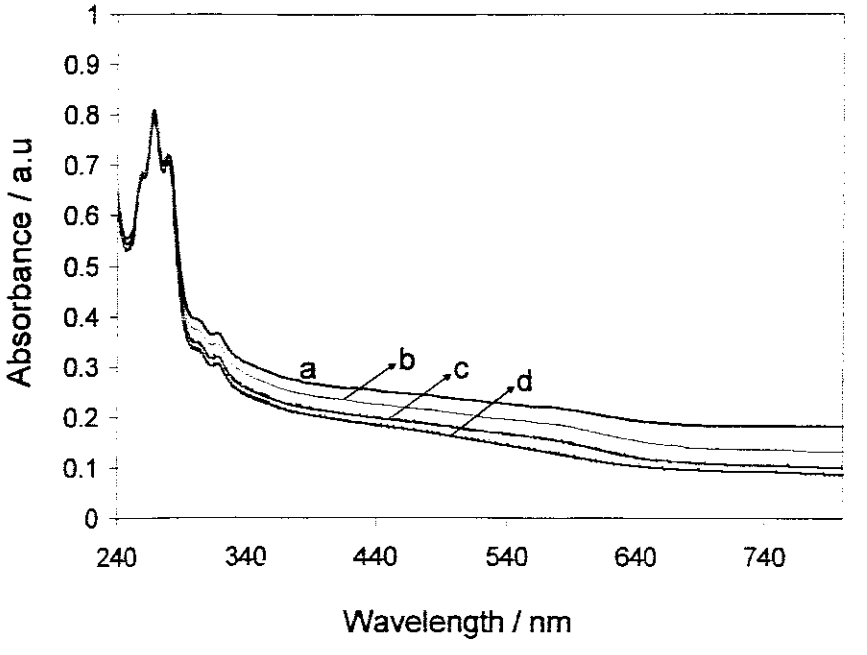


***Figure 4.37*** *Absorption spectra of PVA-capped CdSe using 0.16 mmol monomer concentrations at (a) 1 hr, (b) 3 hrs, (c) 5 hrs and (d) 24 hrs reaction times*

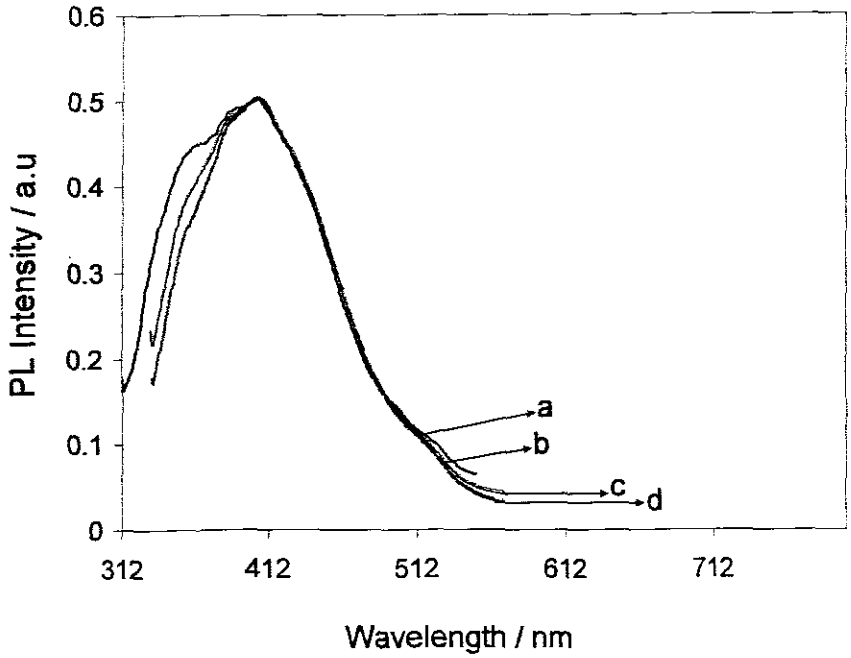


***Figure 4.38*** *Photoluminescence spectra ($\lambda_{280\ nm}$) of PVA-capped CdSe using 0.16 mmol monomer concentrations at (a) 1 hr, (b) 3 hrs, (c) 5 hrs and (d) 24 hrs reaction times*

#### 4.3.1.2.5.1.2 *Structural properties*

The diameter and particle size distribution of a typical representative TEM image, at higher monomer concentration (0.32 mmol) and 3 hrs reaction time, is shown in Figure 4.39. The image shows well-defined, monodispersed, spherical particles. The average particle size, as determined from the TEM image, is 4.51 nm. This correlates with the particle size calculated from the absorption edge (648 nm; 4.57 nm), using the EMA model. The relative standard deviation of the size of the nanoparticles shown in Figure 4.37b is 0.37 nm (8 %) indicating a narrow size distribution.

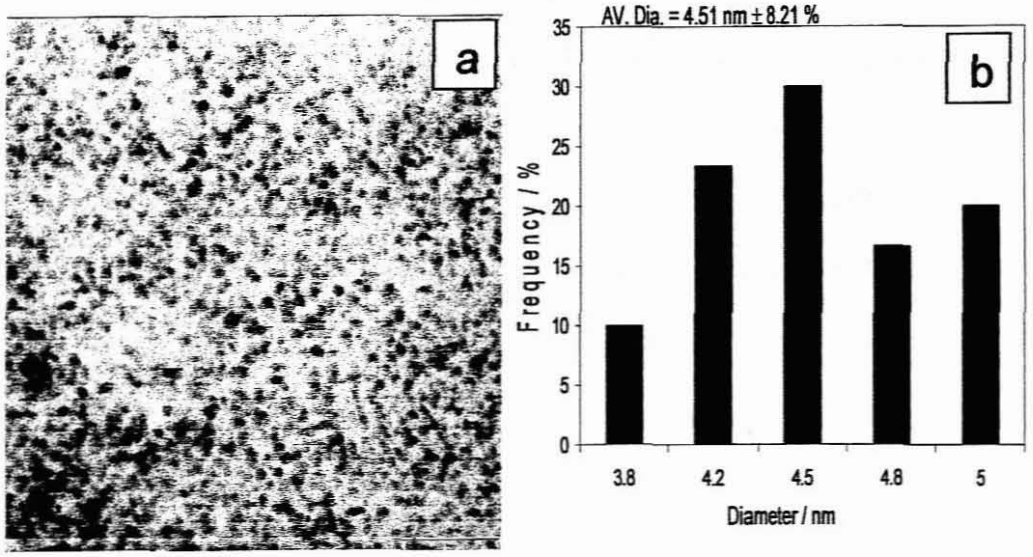


***Figure 4.39*** *(a) TEM images and (b) particle size distribution of PVA-capped CdSe nanoparticles using 0.32 mmol monomer concentrations at 3 hrs.*

### 4.3.2 *Synthesis of Water-soluble ZnSe Nanoparticles*

As a result of excellent results obtained from the room temperature synthesis of water-soluble CdSe nanoparticles, water-soluble ZnSe nanoparticles were synthesised at room temperature, following the same procedure used for the CdSe nanoparticles with $ZnCl_2$ replacing $CdCl_2$. The following biomolecules and polymer were used as capping agents which served as agents of stabilization, solubilisation and conjugation with biomolecules, L-cysteine ethyl ester hydrochloride, ascorbic acid and poly (vinylpyrrolidone) (PVP). The reaction schemes are shown below:

$$4NaBH_4 + 2Se + 7H_2O \xrightarrow[2\ hrs,\ N_2]{R.T} 2NaHSe + Na_2B_4O_7 + 14H_2 \qquad (1)$$

$$Ligands + ZnCl_2 + NaHSe \xrightarrow{R.T} Ligand\text{-}capped\ ZnSe + NaCl + HCl \qquad (2)$$

***Scheme 3.*** *Equation for the formation of Ligand-capped ZnSe nanoparticles at room temperature (R.T = room temperature).*

#### 4.3.2.1 *Cysteine-capped ZnSe nanoparticles*

The temporal evolution of the absorption and photoluminescence spectra of cysteine-capped ZnSe at pH 7 and 11 at different reaction times, are shown in Figures 4.40 to 4.43. The absorption band-edges and emission maxima of all the nanoparticles are blue-shifted from the bulk band gap (480 nm). The absorption and emission maxima at the start of the reaction shift to higher wavelength as the pH increases from 4 to 11, indicating an increase in particle size. This is in agreement with the intensity of the colour of the solution (pale yellow) which increases as the pH increases. The absorption shoulder becomes narrower as the pH increases, indicating narrowing of the size distribution. It is observed that unlike all the spectra obtained at higher temperatures, using TOPO and HDA, the spectra obtained at pH 11 show distinct sharp excitonic shoulders, an indication of the high monodispersity of the particles.

The emission spectra increase in intensity and the emission line widths become narrower as the pH increases from 4 to 11, with the exception of the spectra obtained at pH 7 which shows the presence of surface defects. This indicates the efficiency of the thiol group, as the pH increases, in electronically passivating the surface states or defects present in the band gap of the nanocrystals which act as trapping states for photogenerated charges and has been attributed to the high rate of ionisation and complexation of the thiol group as pH increases. All the emission maxima are slightly red-shifted from their corresponding absorption band-edges, suggesting band-edge emission.

Figures 4.40a and 4.41 show the absorption and emission spectra at pH 11. The spectra show well-defined, sharp absorption shoulders near the absorption band-edges at 366 nm (1 & 3 hrs) and 360 nm (5 hrs), attributed to the first electronic transition (1s-1s). This distinct excitonic shoulder increases in optical density as the reaction time increases. The absorption band-edges as calculated, using the direct band gap method, are 433 nm (1 and 3 hrs), 401 nm (5 hrs) and 394 nm (24 hrs), indicating a decrease in the particle sizes as the reaction time increases. This shows that the growth of the particles occur within one hour of the reaction and becomes stable for about 3 hrs after which, the particle size decreases. The shift in emission maxima follows the same trend as the absorption maxima. The emission maxima are 433 nm (1 and 5 hrs), 415 nm (5 hrs) and 411 nm (24 hrs).

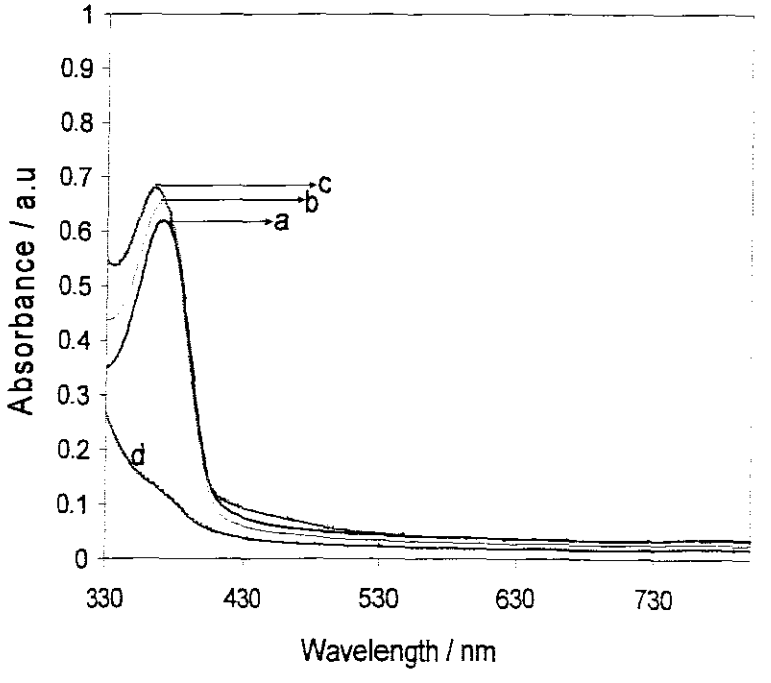


***Figure 4.40a*** *Absorption spectra of cysteine-capped ZnSe nanoparticles at pH 11 for the reaction time of (a) 1 hr (b) 3 hrs (c) 5 hrs and (d) 24 hrs*

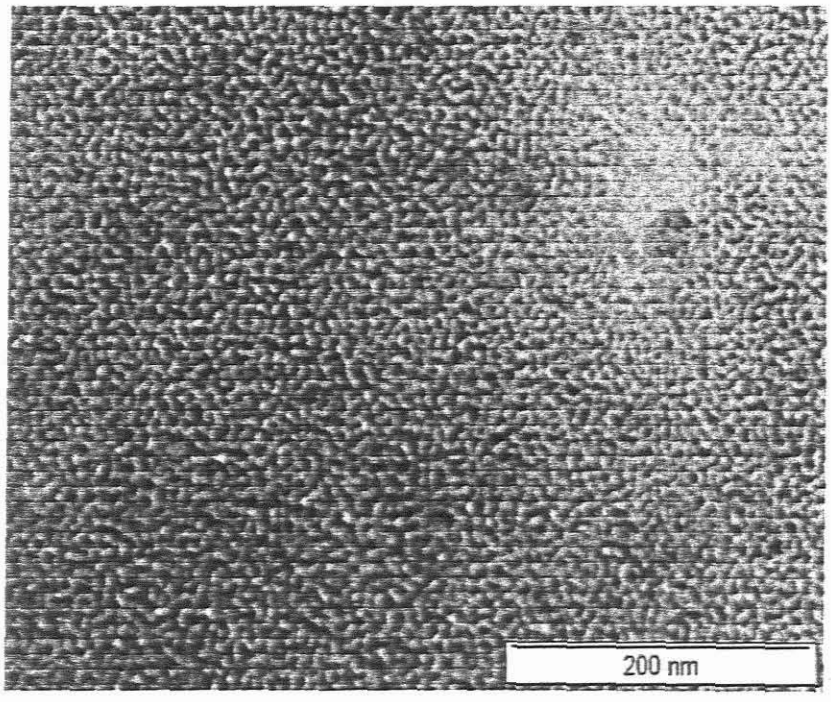


***Figure 4.40b*** *TEM image of cysteine-capped ZnSe nanoparticles at pH 11 for the reaction time of 1 hour*

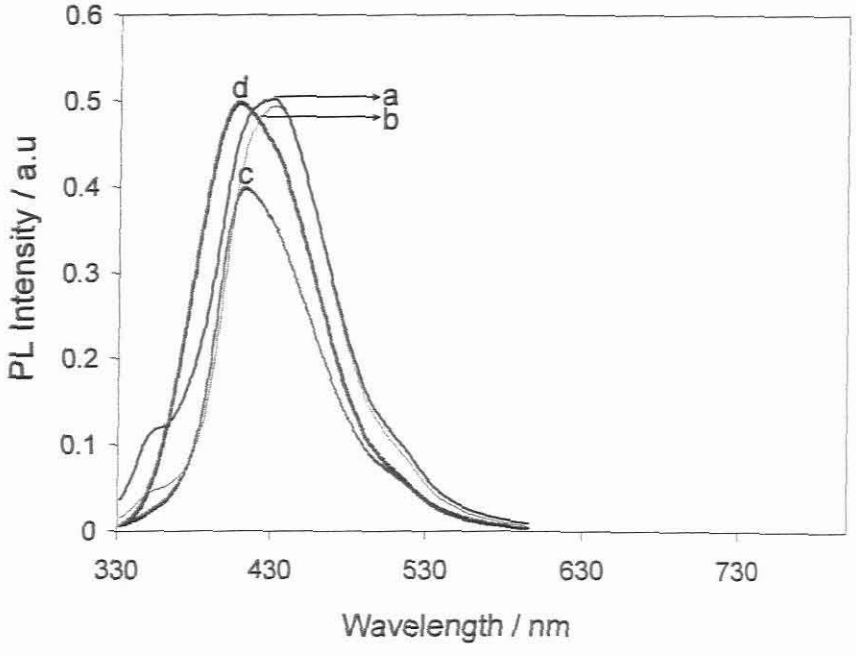


***Figure 4.41*** *Photoluminescence spectra ($\lambda_{300\ nm}$) of cysteine-capped ZnSe nanoparticles at pH 11 for the reaction time of (a) 1 hr (b) 3 hrs (c) 5 hrs and (d) 24 hrs.*

At pH 7, the absorption spectra (Figure 4.42) show broad excitonic shoulders with an increase in the absorption band-edges (i.e. particle size) for the first 3 hrs of the reaction time, after which the band-edges decrease slightly and, increase significantly without any shoulder at 24 hrs. The absorption band-edges, as calculated are 358 nm (1 hr), 432 nm (3 hrs), 416 nm (5 hrs) and 436 nm (24 hrs). The emission spectra (Figure 4.43) are broad and are indicative of particles that contain defects. The emission maxima are 387 nm and 416 nm (1 hr), 448 nm (3 hrs), 438 nm (5 hrs) and 458 nm (24 hrs). The smooth curve obtained at 5 hrs is attributed to the smaller size of the particle, coupled with an increasing rate of thiol ionisation and complexation as the reaction time increases. This rate of ionisation and complexation was overcome by the large size of the particle at 24 hrs thus, leading to broad and defect emission.

The absorption spectra at pH 4 show sharp absorption band-edges, which increase with the reaction time signifying increase in particle size. This pH gives the smallest particle size. The emission spectra are broad with little defects signifying large size distributions and, the intensity decreases as the reaction time increases.

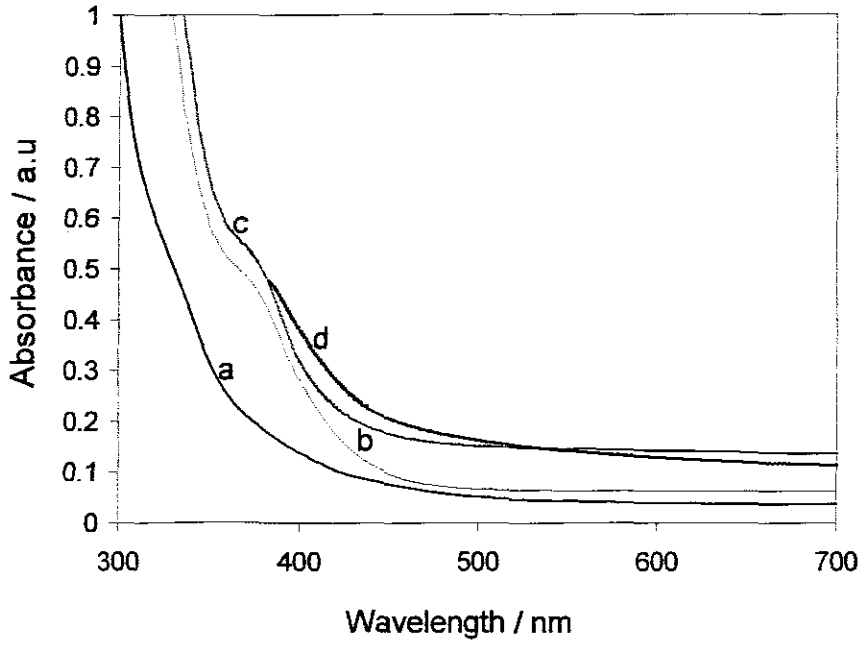


***Figure 4.42*** *Absorption spectra of cysteine-capped ZnSe nanoparticles at pH 7 for the reaction time of (a) 1 hr (b) 3 hrs (c) 5 hrs and (d) 24 hrs*

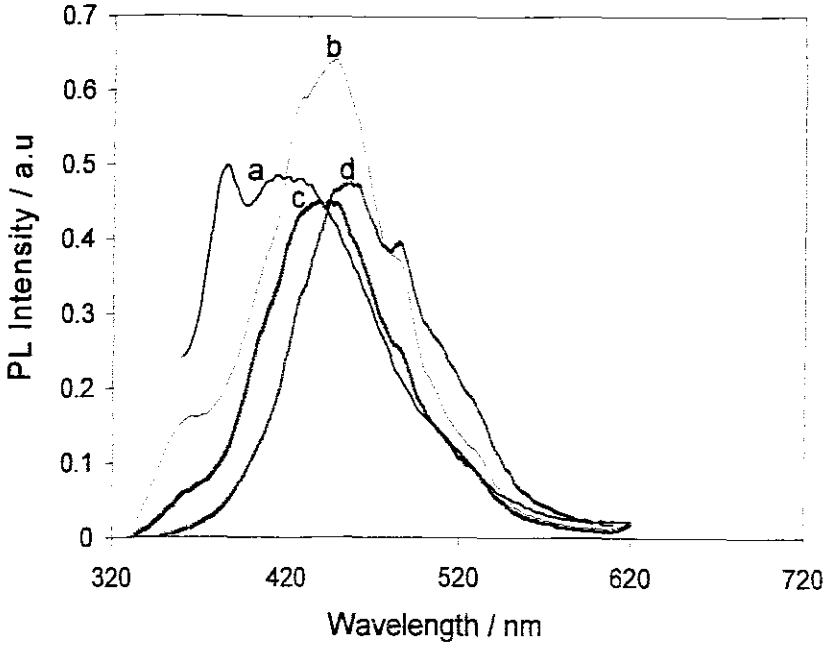


***Figure 4.43*** *Photoluminescence spectra ($\lambda_{270\ nm}$) of cysteine-capped ZnSe nano-particles at pH 7 for the reaction time of (a) 1 hr (b) 3 hrs (c) 5 hrs and (d) 24 hrs*

#### 4.3.2.2 *Ascorbic acid-capped ZnSe nanoparticles*

##### 4.3.2.2.1 *Optical properties*

The absorption and photoluminescence spectra of ascorbic acid-capped ZnSe at different pH is shown in Figures 4.44 to 4.49. The absorption band-edges and emission maxima of all the nanoparticles are blue-shifted from the bulk band gap. The absorption and emission maxima are red-shifted as the pH increases from 4 to 11, indicating an increase in particle size. The emission spectra intensity increases as the pH increases and, all the particles show band-edge emission.

Figures 4.44 and 4.45 show the absorption and emission spectra at pH 4. The absorption band-edges are very sharp and increase slightly, as the reaction time increases. The absorption band-edges are 372 nm (1 hr), 375 nm (3 hrs) and 382 nm (5 and 24 hrs). This indicates that the particle size increases as the reaction time increases for the first 5 hours after which, the growth stops and becomes stable throughout the reaction time. The emission maxima follow the same trend as the absorption band edges and, decrease slightly in intensity as the reaction time increases. The roughness of the curves is attributed to the incomplete passivation of the surface defects.

The absorption and emission spectra at pH 7 are shown in Figures 4.46 and 4.47. The absorption spectrum shows no distinctive excitonic features. The absorption band-edges of the particles are 396 nm (1 hr), 386 nm (3 and 5 hrs) and 411 nm (24 hrs). This shows that the size of the particles begins to decrease after 1 hour and then increases after 5 hrs. The TEM images of the particles which will be discussed later, gives a better understanding of the growth process. The emission spectra show the

presence of two maxima peaks for the first 5 hrs, which may be attributed to the presence of particles with two different morphologies and a single peak at 24 hrs that is significantly red-shifted from the spectra at 5 hrs.

The absorption and emission spectra of the solution at pH 11, are shown in Figures 4.48 and 4.49. The absorption edges are 422 nm (1 hr), 417 nm ( 3 and 5 hrs) and 381 nm (24 hrs). This signifies that the size of the particles decreases with increasing reaction time. In contrast to the absorption band-edges, the emission maxima are shifted to red after 1 hour and become blue-shifted after 5 hrs. The emission maxima are 424 nm (1 hr), 426 nm (3 & 5 hrs) and 395 nm (24 hrs). The luminescence intensity increases as the reaction time increases.

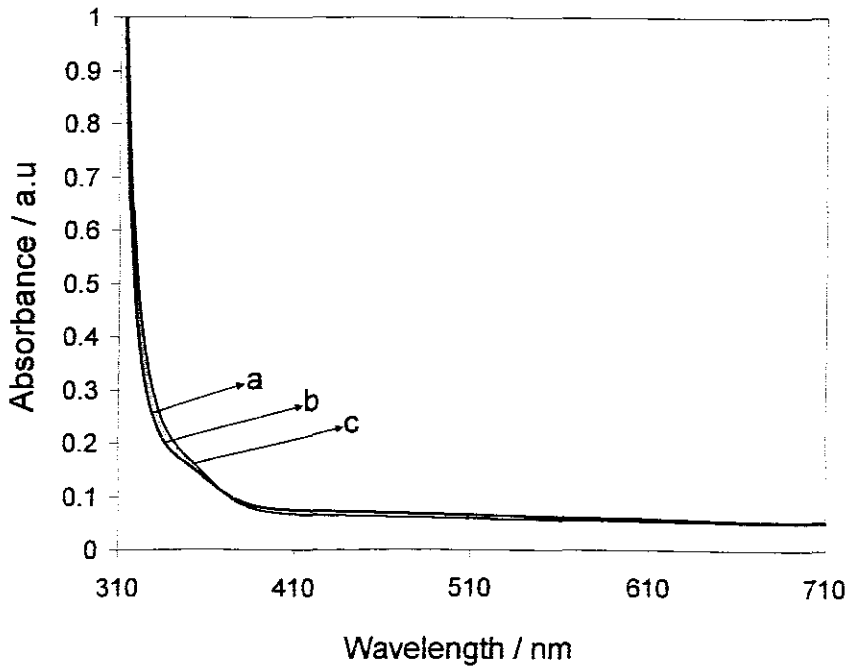


***Figure 4.44*** *Absorption spectra of ascorbic acid-capped ZnSe nanoparticles at pH 4 for the reaction time of (a) 1 hr (b) 3 hrs and (c) 5 hrs*

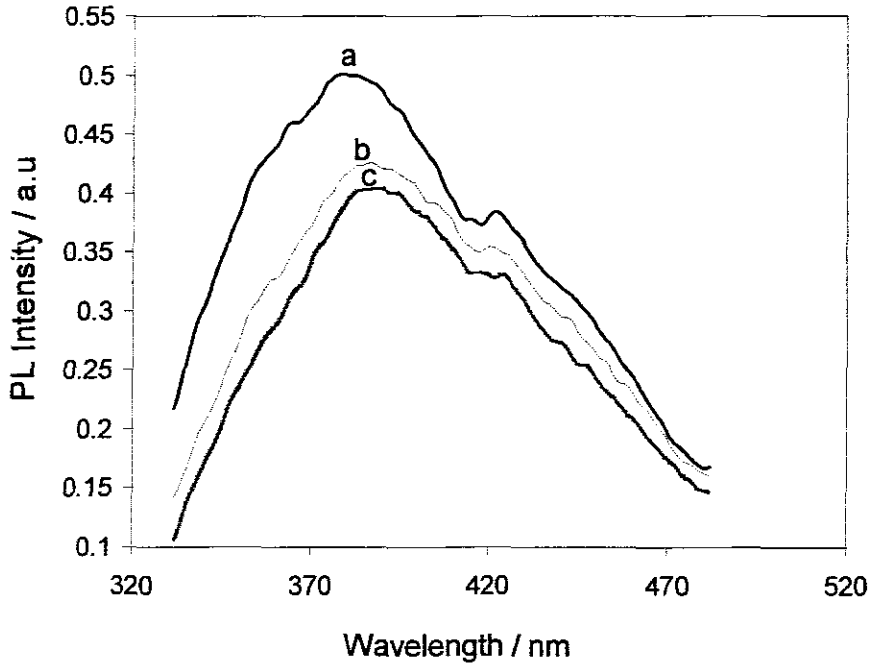


***Figure 4.45*** *Photoluminescence spectra ($\lambda_{300\ nm}$) of ascorbic acid-capped ZnSe nanoparticles at pH 4 for the reaction time of (a) 1 hr (b) 3 hrs and (c) 5 hrs*

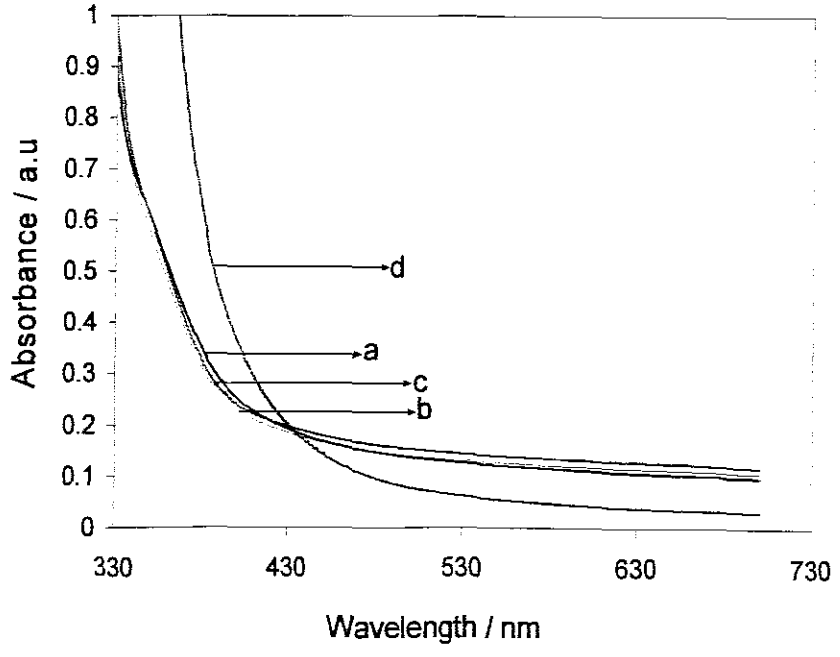


***Figure 4.46*** *Absorption spectra of ascorbic acid-capped ZnSe nanoparticles at pH 7 for the reaction time of (a) 1 hr, (b) 3 hrs, (c) 5 hrs and (d) 24 hrs*

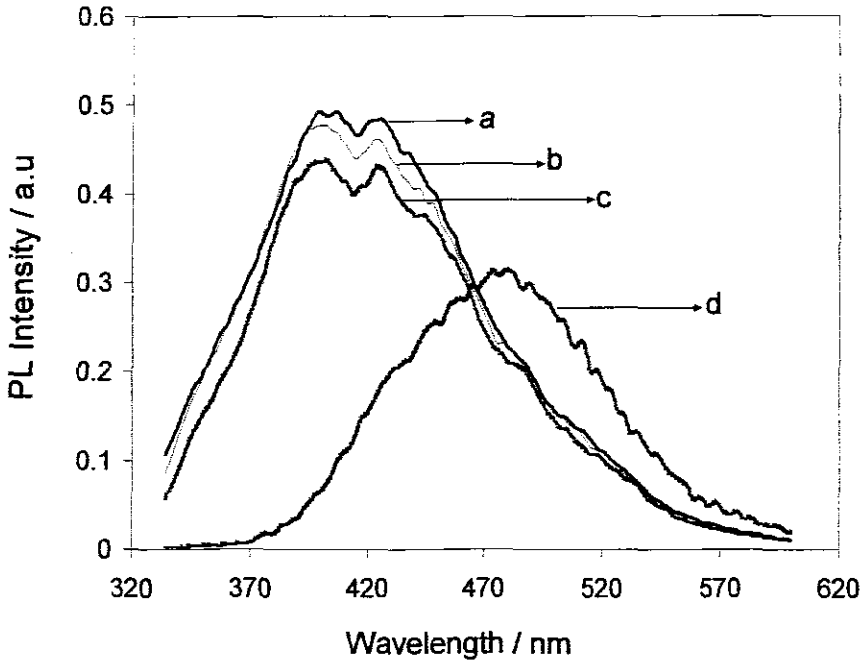


***Figure 4.47*** *Photoluminescence spectra ($\lambda_{300\ nm}$) of ascorbic acid-capped ZnSe nanoparticles at pH 7 for the reaction time of (a) 1 hr, (b) 3 hrs, (c) 5 hrs and (d) 24 hrs*

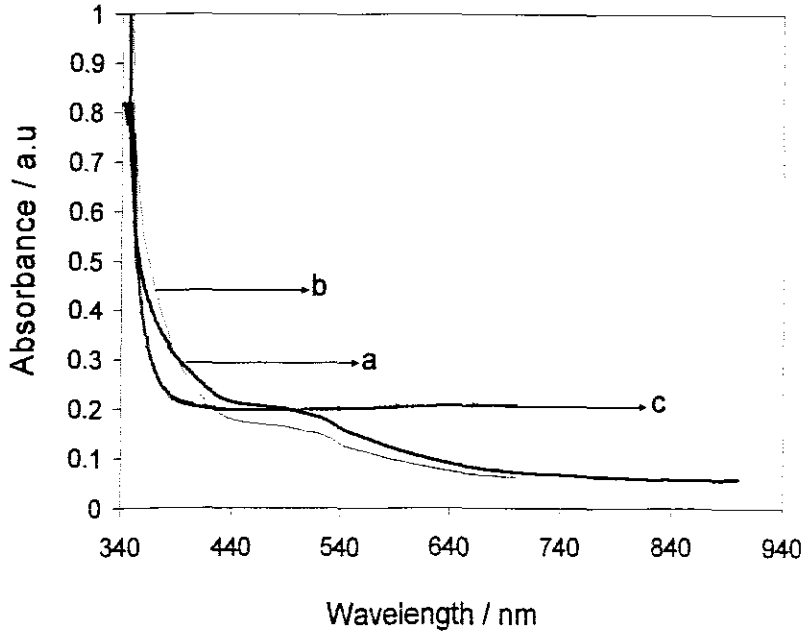


***Figure 4.48*** *Absorption spectra of ascorbic acid-capped ZnSe nanoparticles at pH 11 for the reaction time of (a) 1 hr, (b) 3 hrs, and (c) 24 hrs*

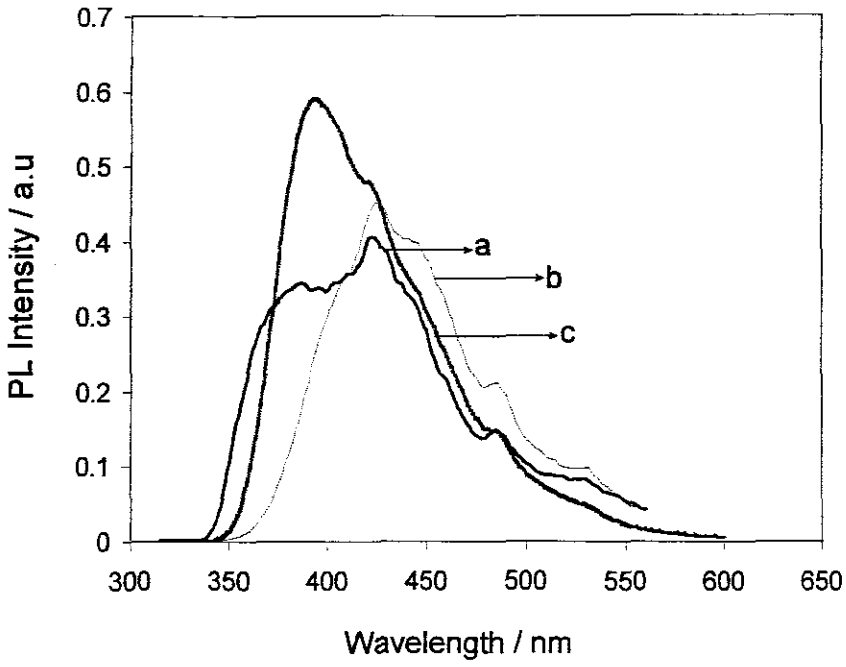


***Figure 4.49 :*** *Photoluminescence spectra ($\lambda_{300\ nm}$) of ascorbic acid-capped ZnSe nanoparticles at pH 11 for the reaction time of (a) 1 hr (b) 3 hrs and (c) 24 hrs*

#### 4.3.2.2.2 *Structural properties*

Typical representative TEM images of ascorbic acid-capped ZnSe nanoparticles are shown in Figures 4.50 to 4.53. At pH 4, the diameter and particle size distributions of the solution at 1 and 24 hrs are shown in Figures 4.50 and 4.51. The TEM images of the particles show well-defined, small spherical particles mostly of homogenous size distribution. As the reaction time increases, the TEM images of the particles show an increase in the particle sizes, which is in agreement with the optical results. The average particle diameters, as determined from the TEM images, are 2.15 nm (1 hr) and 2.44 nm (24 hrs). The relative standard deviations of the particles (± 6.4 %, 1 hr and ± 8.8 %, 24 hrs) confirms the narrow size distribution of the nanoparticles.

The TEM image of the particles, synthesised at pH 7, is shown in Figure 4.52. The TEM image of the solution taken at 1 hour shows an agglomerated material, consisting mostly of spherical particles and a small amount of nanorods formed by the fusion of the dot particles. The presence of two maxima peaks in the emission spectra for the first 5 hrs has been ascribed to this. As the reaction time increases, most of the spherical particles are converted into rods of variable lengths and aspect ratios. We propose this might be the basis for the reduction in the particle size, as the reaction time increases after 1 hour. The TEM image at 24 hrs is dominated by the presence of rods with variable lengths and aspect ratios. This transformation might be responsible for the increase in the absorption edge (particle size) and a single, red-shifted emission maximum peak at 24 hrs.

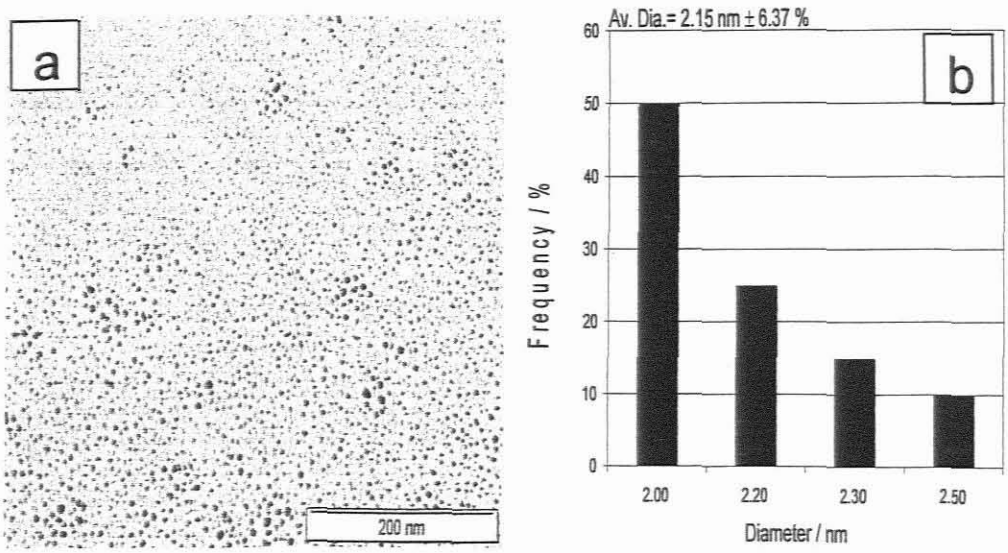


***Figure 4.50*** *(a) TEM images and (b) particle size distribution of ascorbic acid-capped ZnSe nanoparticles at pH 4 for the reaction time of 1 hr*

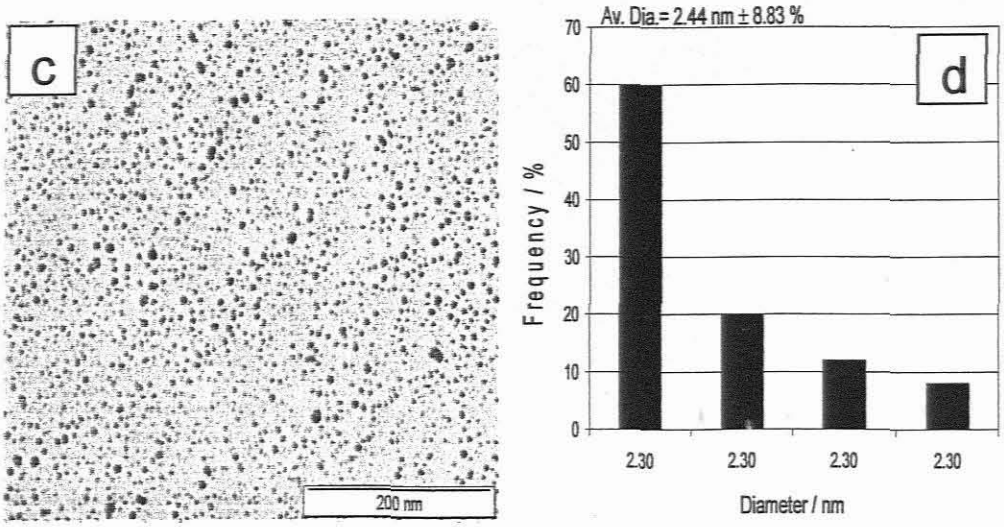


***Figure 4.51*** *(c) TEM images and (d) particle size distribution of ascorbic acid- capped ZnSe nanoparticles at pH 4 for the reaction time of 24 hrs*

Figure 4.53 shows the TEM image of the particle synthesised at pH 11. The TEM image of the solution at 5 hrs, show well-defined monodispersed, spaciously distributed spherical particles, with an average diameter of 2.80 nm. At 24 hrs the TEM image show well-defined homogenously distributed spherical particles of smaller sizes, with an average diameter of 2.34 nm as compared to those synthesised at 5 hrs (2.80 nm). This decrease in particle size is in accordance with the optical results.

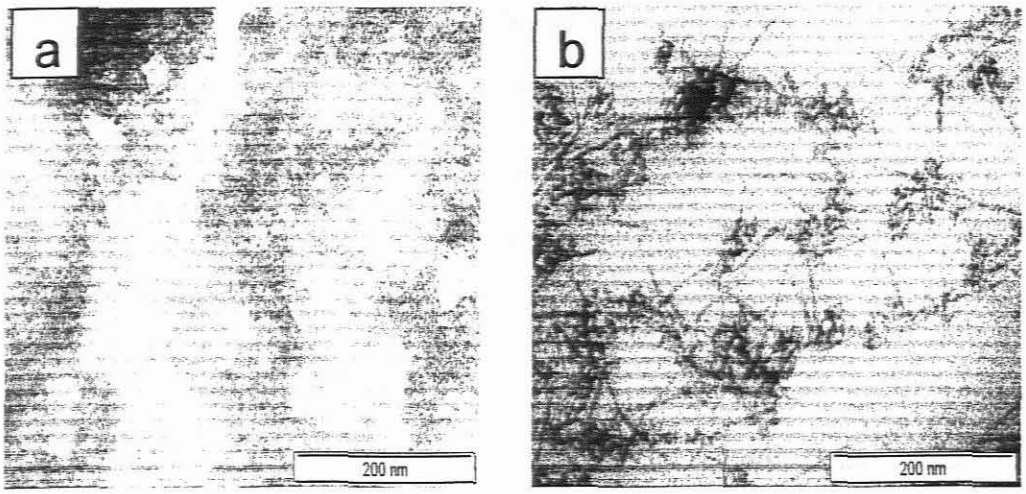


***Figure 4.52*** *TEM image of ascorbic acid-capped ZnSe nanoparticles at pH 7 for the reaction time of (a) 1 hr and (b) 24 hrs*

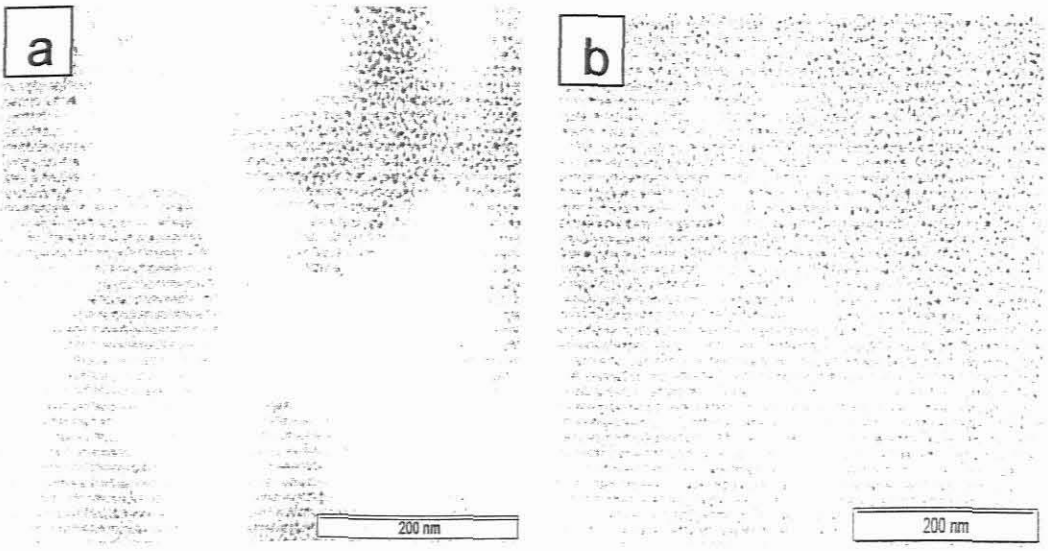


***Figure 4.53*** *TEM image of ascorbic acid-capped ZnSe nanoparticles at pH 11 for the reaction time of (a) 5 hrs and (b) 24 hrs.*

#### 4.3.2.3 *PVP-capped ZnSe nanoparticles*

The absorption and emission spectra of PVP-capped ZnSe nanoparticles at different reaction times are shown in Figures 4.54 and 4.55. The absorption band-edges and emission maxima are slightly blue-shifted from the bulk band gap. The

absorption spectra are characterised by tailing band-edges at the start of the reaction (1–3 hrs). As the reaction progresses, a distinctive excitonic shoulder appears in the spectra, without any changes in the absorption band-edges of the particles at 5 hrs. This suggests monodispersity of the particles as the reaction progresses. At 24 hrs the band-edge was slightly blue-shifted, signifying a decrease in the particle size.

The emission spectra of the particles show band-edge luminescence. The emission maxima appear at the same position as the reaction time increases for the first 3 hrs and, decreases slightly as the reaction time increases. The emission maxima appear at 446 nm (1 and 3 hrs), 435 nm (5 hrs) and 427 nm (24 hrs) with high luminescence intensity at 5 hrs. The sharp luminescence of the emission spectra, show the efficiency of the capping group.

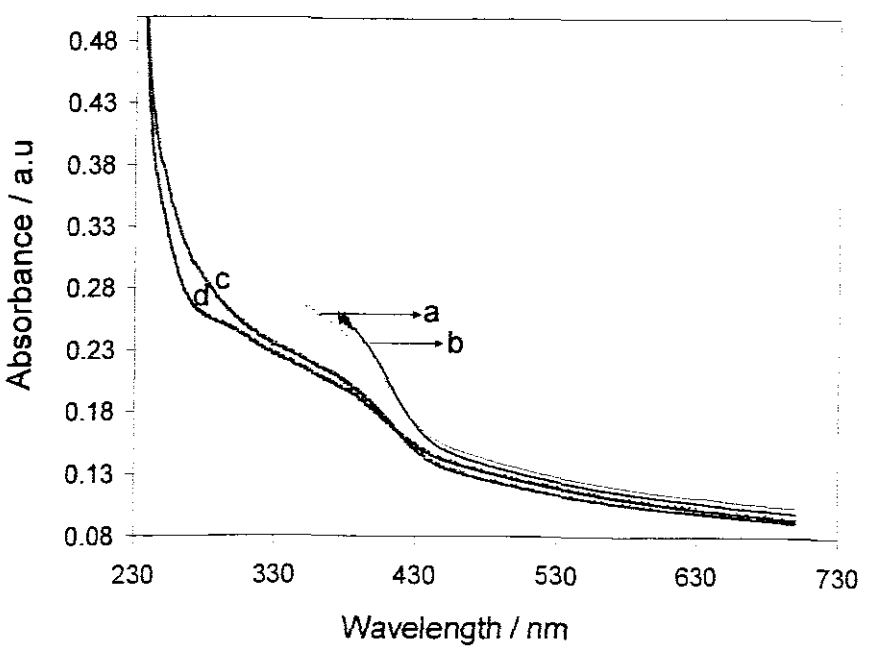


***Figure 4.54*** *Absorption spectra of PVP-capped ZnSe nanoparticles at reaction time of (a) 1 hr, (b) 3 hrs, (c) 5 hrs and (d) 24 hrs*

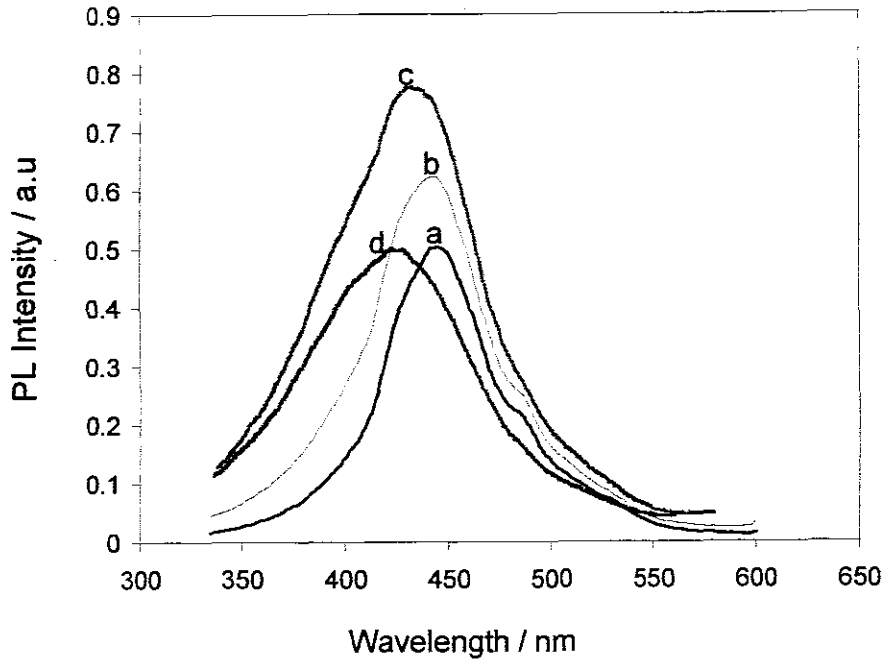


***Figure 4.55*** *Photoluminescence spectra ($\lambda_{300\ nm}$) of PVP-capped ZnSe nanoparticles at reaction time of (a) 1 hr, (b) 3 hrs, (c) 5 hrs and (d) 24 hrs.*

## 4.4 Conclusions

We report a novel, greener, cheaper, facile and environmentally benign, one-step synthetic method for the synthesis of water-soluble CdSe and ZnSe nanoparticles. The synthesis was carried-out at elevated and room temperatures, using biomolecules and polymers as passivating agents. A systematic study of the effects of parameters such as pH, reaction time, concentration, reactant ratio, passivating ligand and temperature on dispersibility, size, optical properties and morphology of the nanoparticles, was also investigated.

The synthesis of CdSe nanoparticles at high temperatures, were carried-out using L-cysteine ethyl ester hydrochloride, methionine and starch as the capping agent at different pH, Cd: cysteine ratio, monomer concentration and refluxing time. For the

cysteine-capped CdSe nanoparticles under refluxing time of 5 hrs, the particle size decreases while the luminescence properties improves with increasing pH. The absorption spectra at 3 hrs of refluxing did not show any significant difference with the results obtained at 5 hrs. In addition, the luminescence obtained at higher pH was very low and no luminescence was detected at pH 4. Increasing the cadmium to cysteine ratio systematically from 1:10 to 1:60 at different pH did not have any significant effect on the luminescence intensity of the nanoparticles. While the synthesis at higher reduction time (4 and 6 hrs) produced large particle sizes close to the bulk cadmium chloride and no luminescence was observed.

The structural properties of the nanoparticles were investigated using XRD, TEM, HRTEM and SAD. The FT-IR study confirmed the capping of the nanoparticles by cysteine, while the EDS spectrum confirmed the presence of Cd, Se and S in the nanoparticles. The XRD study shows that all the particles, at different pH studies, are of the hexagonal phase. This is in contrast to the previously reported cubic phases of CdSe nanoparticles, synthesised via the aqueous method. The use of methionine as capping agent did not give any optical results for the entire pH studied, while the use of starch produced large size particles close to bulk cadmium chloride.

The synthesis of CdSe nanoparticles at room temperatures was carried-out, using L-cysteine ethyl ester hydrochloride, methionine, ascorbic acid, starch and PVA as the capping agent at different pH, monomer concentrations and reaction times of 1 to 24 hrs. In contrast to the cysteine-capped CdSe nanoparticles synthesised at higher temperature, all the cysteine-capped nanoparticles synthesized at room temperature, show very sharp excitonic shoulders and absorption edges, signifying particles with

narrower size distributions. Higher electronic transitions were also clearly resolved for the synthesized at pH 11 and the first exciton absorption peak appears at a wavelength, as low as 415 nm, with a clearly resolved higher energy electronic transition, an impossible task with the $Cd(CH_3)_2$ and CdO-related approach. Another striking observation and a significant advantage of this synthetic route, is the presence of high luminescence intensity with no evidence of trap emission at room temperature, without any refluxing at a short period of time (1 hour). There have been no reports of such luminescence without refluxing for water-soluble CdSe nanoparticles, to the best of our knowledge thus, showing the quality of this synthetic route. All the particles are of smaller sizes (< 2 nm), a significant advantage for diagnostic or therapeutic studies and, emit strongly in the blue region with luminescent intensity that is about four times higher than the ones produced under refluxing. The high quality of the emission properties was attributed to (i) increase in the amount of free thiols from the cysteine ester and (ii) increase in the rate of thiol complexation. An unusual growth mode was seen during the course of the reaction, i.e. decrease in particle size with increasing reaction time. Two factors were proposed for this: (i) lower $Cd^{2+}$ ion concentration, as the reaction time increases, which produced a decrease in both absorption and emission peak positions and (ii) digestive ripening, which produced a decrease in particle size without any significant change in emission peak position.

The optical analysis of methionine-capped CdSe nanoparticles indicates that the pH of the solution greatly affects the nature of this amino-acid, which in turn influences the optical properties of the particles. The particle size decreases as the pH increases from 4 to 7 and then increases again on increasing the pH to 11. The emission

maxima increase with increasing pH (4 and 11) for the first 3 hours and no luminescence was observed at pH 7. The TEM image at pH 7 shows particles that are spherical and monodispersed, while pH 4 and 11 produced aggregated particles.

At pH 4, ascorbic acid-capped CdSe nanoparticles produced large sized particles which decreased slightly before the 3 hrs reaction time, after which the growth process stopped and no luminescence was observed throughout the reaction time. This was attributed to the high stability of ascorbic acid in the acidic medium. As the pH increased, the particle size decreased and the optical properties improved in quality, showing a sharp absorption shoulder and, high luminescence properties at pH 11. The TEM image at pH 7 shows small and large spherical particles with homogenous distribution.

The optical results of starch-capped CdSe nanoparticles show two absorption shoulders and two emission maxima peaks, attributed to the presence of particles with two different morphologies. The TEM image of the particles at lower monomer concentrations consists of nanorods and nanowires, of very high aspect ratios, together with smaller spherical particles while at higher concentrations, the image consists of spherical particles together with elongated particles, of low aspect ratios. The presence of larger sized spherical particles and elongated particles of low aspect ratios at higher concentration indicates that the wt/% of starch, greatly influences the transformation from dots to elongated particles. The XRD patterns of the particles also confirmed the presence of elongated particles.

The PVA-capped CdSe nanoparticles increase in particle size as the monomer concentration increases, but decreases with increasing reaction times. The absorption spectrum shows two bands in the UV region at 269 nm and 278 nm appearing at the same position, in the entire spectrum assigned to $n$- $\pi^*$ excited transition of CdSe-PVA nanocomposite. The TEM image at 3 hrs under higher monomer concentrations shows well-defined, monodispersed, spherical particles with a relative standard deviation of 8 %.

The synthesis of ZnSe nanoparticles at room temperatures was carried-out, using L-cysteine ethyl ester hydrochloride, ascorbic acid and PVP as capping agents at different pH, monomer concentration and reaction time of 1 to 24 hrs. Similar to the cysteine-capped CdSe nanoparticles synthesised at room temperature, cysteine-capped ZnSe nanoparticles show high quality optical properties with band-edge emission as the pH of the solution increases. However the absorption and emission maxima at the start of the reaction shift to higher wavelength as the pH increases from 4 to 11, indicating an increase in particle size. At pH 11, absorption spectra show distinct excitonic shoulders at higher energy, indicating high monodispersity of the particles. This is a difficult task under preparation at higher temperatures, using TOPO and HDA as the capping agent.

The optical spectra of ascorbic acid-capped ZnSe nanoparticles show red-shifted absorption and emission maxima as the pH increases. The TEM images at pH 4 show well-defined, monodispersed, small spherical particles mostly of homogenous size distribution, which increase in size as the reaction time increases with relative standard deviations as low as ± 6.4 % (1 hr) and ± 8.8 %, (24 hrs). At pH 7, the TEM

image shows the presence of spherical and elongated particles with increased length and aspect ratios, as the reaction time increases. While at pH 11, the image show well-defined, spaciously distributed, spherical particles which decrease in size with reaction time.

The optical spectra of the PVP-capped ZnSe nanoparticles show that the quality of the particles increase with reaction times and the surface states of the nanocrystals are well-passivated, exhibiting band-edge emission.

Without any further post preparation, the qualities of the particles formed by this new method are comparable, to that of the best CdSe and ZnSe nanocrystals reported in the literature, synthesised by the high temperature conventional organometallic methods. This new synthetic route is safe, inexpensive, involves the use of non-toxic chemicals, reproducible and can be readily used for large scale synthesis.

## 4.5 References


1) M. Gao, C. Lesser, S. Kirstein, H. Mohwald, A. L. Rogach and H. Weller, *J. Appl, Phys.*, 2000, **87**, 2297.

2) K. Barnham, J. L. Marques, J. Hassard and P. O'Brien, *Appl. Phys. Lett.*, 2000, **76**, 1197.

3) S. Wang, N. Mamedova, N. A. Kotov, W. Chen and J. Studer, *Nano Lett.*, 2002, **2**, 817.

4) A. Ahmad, P. Mukherjee, D. Mandal, S. Senapati, M. I. Khan, R. Kumar and M. Sastry, *J. Am. Chem. Soc.*, 2002, **124**, 12108.

5) Y. Xiao, F. Patolsky, E. Katz, J. F. Haintfeld and I. Willner, *Science,* 2003, **299**, 1877.

6) A. J. Sutherland, *Curr. Opinion Solid State Mater. Sci.*, 2002, **6**, 365.

7) W. C. W. Chan and S. M. Nie, *Science,* 1998, **281**, 2016.

8) M. Bruchez, M. Moronne, P. Gin, S. Weiss and A. P. Alivisatos, *Science,* 1998, **81**, 2013.

9) C. J. Murphy, *Anal. Chem.*, 2002, **74**, 520A.

10) J. M. Costa-Fernandez, R. Pereiro and A. Sanz-Medel, *Trends in Anal. Chem.*, 2006, **25**, 207.

11) M. Ozkan, *DDT*, 2004, **9**, 1065.

12) A. M. Derfus, W. C .W. Chan and S. N. Bhatia, *Nano. Lett.*, 2004, **4**, 11.

13) M. Stroh, J. P. Zimmer, D. G. Duda, T. Levchenko, K. S. Cohen, E. B. Brown, D. T. Scadden, V. P. Torchilin, M. G. Bawendi, D. Fukumura and R. K. Jain, *Nat. Med.*, 2005, **11**, 578.

14) B. C. Lagerholm, M. Wang, L. A. Ernst, D. H. Ly, H. Liu, M. Bruchez and A. S. Waggomer, *Nano Lett.*, 2004, **4**, 2019.

15) J. McBride, J. Treadway, L. C. Feldman, S. J. Pennycook and S. J. Rosenthal, *Nano Lett.*, 2006, **6**, 1496.

16) E. L. Bentzen, F. House, T. J. Utley, J. E. Crowe and D. W. Wright, *Nano. Lett.*, 2005, **5**, 591.

17) X. peng, M. C. Schlamp, A. V. Kadavanich and A. P. Alivisatos, *J. Am. Chem. Soc.*, 1997, **119**, 7019.

18) A. R. Koran, R. Hull, R. I. Opila, M. G. Bawendi, M. I. Steigerwald, P. J. Carroll and L. E. Brus, *J. Am. Chem. Soc.*, 1990, **112**, 1327.

19) W. C. W. Chan, T. L. Prendergast, M. Jain, and S. Nie, *SPIE. Proc.*, 2000, **2**, 3924.

20) J. A. Schneider, B. Katz, and R. B. Melles, *Pediatr. Nephrol.*, 1990, **4**, 645.

21) H. Mattoussi, J. *Am. Chem. Soc.*, 2000, **122**, 12142.

22) S. Pathak, *J. Am. Chem. Soc.*, 2001, **123**, 4103.

23) C. B. Murray, D. J. Norris and M. G. Bawendi, *J. Am. Chem. Soc.*, 1993, **115**, 8706.

24) A. L. Rogach, A. Kornowski, M. Gao, A. Eychmuller and H. Weller, *J. Phys. Chem.*, 1999, **103**, 3065.

25) T. Vossmeyer, L. Katsikas, M. Giersig, L. G. Popovic, K. Diesner, A. Chemseddine, A. Eychumuller and H. Weller, *J. Phys. Chem.*, 1994, **98**, 7665.

26) A. L. Rogach, L. Katsikas, A. Kornowski, D. S. Su, A. Eychmuller and H. Weller, *Ber.Bunsenges. Phys. Chem.*, 1996, **100**, 1772.

27) A. L. Rogach, L. Katsikas, A. Kornowski, D. S. Su, A. Eychmuller and H. Weller, *Ber.Bunsenges. Phys. Chem.*, 1997, **101**, 1668.

28) M. Gao, S. Kirstein, H. Mohwald, A. L. Rogach, A. Kornowski, A. Eychmuller and H. Weller, *J. Phys. Chem.* B, 1998, **102**, 8360.

29) H. Y. Han, Z. H. Sheng and J. G. Liang, *Mater. Lett.*, 2006, **60**, 3782.

30) J. H. Li, C. L. Ren, X. Y. Liu, Z. D. Hu and D. S. Xue, *Mater. Sci. Eng.* A, 2007, **458**, 319.

31) X. D. Ma, X. F. Qian, J. Yin, H. A. Xi and Z. K. Zhu, *J. Colloid and Interface Science*, 2002, **252**, 77

32) X. D. Ma, X. F. Qian, J. Yin and Z. K. Zhu, *J. Mater. Chem.*, 2002, **12**, 663.

33) Y. Badr and M. A. Mahmoud, *Physica* B, 2005, **369**, 278.

34) Y. J. Yang and B. J. Xiang, *J. Cryst. Growth*, 2005, **284**, 453.

35) J. Ge, Y. Li and G. Yang, *Chem. Commun.*, 2002, **17**, 1826.

36) O. S. Oluwafemi and N. Revaprasadu, *Mater. Res. Soc. Symp. Proc.*, 2007, **951** E03.

37) S. O. Oluwafemi, N. Revaprasadu and A. J. Ramirez, *J. Cryst. Growth*, 2008, **310**, 3230.

38) J. Li, X. Hong, D. Li, K. Zhao, L. Wang, H. Wang, Z. Du, J. Li, Y. Bai and T. Li *Chem. Commun.*, 2004, 1740.

39) X. Cao, C. M. Li, H. Bao, Q. Bao and H. Dong, *Chem. Mater.*, 2007, 19, 3773.

40) S. Sapra, J. Nanda, D. D. Sarma, F. Abed El-Al and G. Hodes, *Chem. Commun.*,2001, 2188.

41) N. N. Mamedova, N. A. Kotov, A. L. Rogach and J. Studer, Nano Lett., 2001, **1**, 281.

42) J. L. Pankove, *Optical Processes in Semiconductors*, Dover Publications, New York. 1990.

43) L. E. Brus, *J. Chem. Phys.*, 1984, **80**, 4403.

44) H. B. Burgi, *Chim, Acta.*, 1974, **57**, 513.

45) D. Hayes, O. L. Micic, M. T. Nenadovic, V. Swayambunathan and D. Meisel, *J. Phys. Chem.*, 1989, **93**, 4603.

46) V. Swayambunathan, D. Hayes, K. H. Schmidt, Y. X. Liao and D. Meisel, J. Am. Chem. Soc., 1990, **112**, 3831.

47) A. Chatterjee, A. Priyam, S. K. Das and A. Saha, *J. Coll. Interf. Sci.*, 2006, **294**, 334.

48) M. Green, H. Harwood, C. Barrowman, P. Rahman, A. Eggeman, F. Festry, P. Dobson and T. Ng, *J. Mater. Chem.*, 2007, **17**, 1989.

49) C. H. Fischer, H. Weller, L. Katsikas and A. Henglein, *Langmuir*, 1989, **5**, 429.

50) D. L. Pavia, G. M. Lampman and G. S Kriz , *Introduction to Spectroscopy*, Ed. 3. USA: 2001.

51) A. Santosh, B. K .C. Remant, N. Dharmaraj, N. Bhattarai, C. H. Kim and H. Y. Kim, *Spectrochimica. Acta Part A*, 2006, **63**, 160.

52) X. Hu, W. Cheng, T. Wang, E. Wang and S. Dong, *Nanotechnology*, 2005, **16**, 2164.

53) J. L. Burt, C. Gutierrez-Wing, M. Miki-Yoshida and M. Jose-Yacaman, *Langmuir*, 2004, **20**, 11178.

54) W. Wang, Y. Geng, P. Yan, F. Liu, Y. Xie and Y. Qian, *J. Am .Chem. Soc.*, 1999, **121**, 4062.

55) D. V. Talapin, A. L. Rogach, E. V. Shevchenko, A. Kornowski, M. Haase, and H. Weller, *J. Am .Chem. Soc.*, 2002, **124**, 5782.

56) L. Qu and X. Peng, *J. Am .Chem. Soc.*, 2002, **124**, 2049.

57) X. G. Peng, L. Manna, W. D. Yang, J. Wickham, E. Scher, A. Kadavanich and A. P. Alivisatos, *Nature*, 2000, **404**, 59.

58) B. Cullity, *Handbook of Elements of X-ray Diffraction*, 2nd ed., Addison–Wesley Reading, MA, 1978.

59) J. E. Bowen Katari, V. L. Colvin, A. P. Alivisatos, *J. Phys. Chem.*, 1994, **98**, 4109.

60) M. G. Bawendi, M. L. Steigerwald and L. E. Brus, *Annu. Rev. Phys. Chem.*, 1990, 41, 477.

61) B. O. Dabboussi, J. Rodriguez-Viejo, F. V. Mikulec, J. R. Heine, H. Mattoussi, R. Ober, K. F. Jensen and M. G. Bawendi, *J. Phys. Chem.* B, 1997, **101**, 9463.

62) X. peng, M. C. Schlamp, A. V. Kadavanich and A. P. Alivisatos, *J. Am. Chem. Soc.*, 1997, **119**, 7019.

63) D. V. Talapin, A. L. Rogach, A. Kornowski, M. Haase and H. Weller, *Nano. Lett.*, 2001, **1**, 207.

64) W. C. W. Chan, D. J. Maxwell, X. Gao, R. E. Bailey, M. Han, and S. Nie, *Curr. Opin .Biotech.*, 2002, **13**, 4.

65) W. W. Yu, L. Qu, W. Guo and X. Peng, *Chem. Mater.*, 2003, **15**, 2854.

66) Q. Wang, D. C. Pan, S. C. Jiang, X. L. Ji, L. J. An and B. Z. Jiang, Chem. Eur. J., 2005, **11**, 3843.

67) Q. Wang, D. Pan, S. Jiang, X. Ji, L. An and B. Jiang, *J. Cryst. Growth*, 2006, **286**, 83.

68) J. A. Gaunt, A. E. Knight, S. A. Windsor and V. Chechik, *J. Colloid and Interface Science*, 2005, **290**, 437.

69) G. Guo, W. Lui, J. Liang, Z. He, H. Xu and X. Yang, *Mater. Lett.*, 2007, **16**, 1641.

70) K. Nose, H. Fujita, T. Omata, S. O. Y. Matsuo, H. Nakamura and H. Maeda, *J. Lumin.*, 2007, **126**, 21.

71) L. Manna, E. C. Scher and A. P Alivisatos, *J. Am. Chem. Soc.*, 2000, **122**, 12700.

72) X. Peng, J. Wickham and P. A. Alivisatos, *J. Am. Chem. Soc.*, 1998, **120**, 5343.

73) Z. A. Peng and X. Peng, *J. Am. Chem. Soc.*, 2001, **123**, 1389.

74) Z. A. Peng and X. Peng, *J. Am. Chem. Soc.*, 2002, **124**, 3343.

75) L. Qu, Z. A. Peng and X. Peng, *Nano. Lett.*, 2001, **1**, 333.

76) V. Colvin, M. Schlamp and A. P. Alivisatos, *Nature*, 1994, **370**, 354.

77) B. O. Dabbousi, M. G. Bawendi, O. Onitduka and M. F. Rubner, *Appl. Phys. Lett.*, 1996, 66, 1316.

78) M. N. Rittner and T. Abraham, *Int. J. Powder Metall.*, 1998, **34**, 33.

79) M. S. Selim, R. Seoudi and A. A. Shabaka, *Mater. Lett.*, 2005, **59**, 2650.

# *CHAPTER FIVE*

## SYNTHESIS OF NANOCOMPOSITES AND CORE/SHELL SELENIDE NANOPARTICLES

## 5.1 Introduction.

### 5.1.1 *Nanocomposites and Core/shell Structures*

Surface atoms play an important role in the emission properties of the nanoparticles, as the particle size decreases. For example, as the size of CdSe particles decreases from 10 nm to 1 nm, the percentage of the surface atoms increase from 20 to 100%. For bulk materials, the bulk atoms dominate the properties of the materials whereas, in nanomaterials the surface atoms play a vital role in determining its properties. These surface atoms usually have unsaturated bonds or dangling bonds, extra free energy and are more active than those in the bulk. The phenomenon that nanoparticles can easily transform from one phase to another and have a low transformation temperature can be attributed to this. Furthermore, in a semiconductor, surface atoms usually induce extra electronic states in the band gap. In a large crystal this effect is a small perturbation and can be ignored. However, as the size of the crystal decreases and the percentage of the surface atoms increases, more electronic states are induced in the band gap and this effect cannot be ignored anymore. These states may act as electron and hole trapping centers.

When an electron is promoted from the valence band to the conduction band, the resultant electron-hole pair (or an exciton), may recombine immediately to produce heat or light with energy equal to $E_g$. It is more likely that the trap states within the material caused by defects, such as vacancies, local mismatches, dangling bonds or absorbates at the surface trap either the excited electron or the hole and thus become less available for the radiative recombination of luminescence. Hence, the photoluminescence can be quenched, which is undesirable for some applications such as optical diodes, lasers and biological markers. As a result of this, the surface

modification of nanoparticles has been extensively investigated. Proper surface modification of quantum dots (QDs) can remove the local trap sites from the surface and thus significantly increase the quantum yield (QY) of the near band gap emission. This has been achieved by the capping of the nanocrystallites with organic and inorganic materials.

Coating the surface of the nanocrystals with suitable organic surfactant molecules such as TOPO, HDA and, organic ligands such as thiopyridine, thiolates and 2, 2'bipyrimidine, does not only provide electronic passivation but also prevents agglomeration, controls the growth rate of the nanocrystals, its size, shape and solubility.[1-7] Passivations by means of organic molecule sometimes has a draw-back of incomplete or irreversible passivation, as it is generally very difficult to, simultaneously passivate both anionic and cationic surface sites when using organic ligands. In addition, the organic shell coated on the surface of nanocrystals has poor stability and can be partially removed during post-preparative treatment. Furthermore, the passivation can expose some of the regions of the surface to degradation effects such as photooxidation, over time. In some cases, it can also cause fluorescence quenching when maximum passivation has been attained.[8]

An alternative to the organic passivation is the epitaxial growth of a shell of a second inorganic material (of wider band gap) on a core of another material, to form a heterostructure. When wrapped in a wider band gap material, the electron-hole pair is further confined and the surface states are eliminated. In the colloidal synthesis of these structures the core acts as a seed for the hereterogenous nucleation of the shell. For nanocrystals, inorganic epitaxial growth cannot only eliminate both the anionic

and cationic surface dangling bonds, but also generate new nanocrystal core/shell systems with novel properties and if the interface between the two inorganics is perfect, a near unity quantum yield (QY) material may result.[9] Many core/shell systems have been reported such as CdS/$Cd(OH)_2$, CdSe/ZnS, ZnS/CdS, CdS/HgS, HgS/CdS, CdS/PbS, CdSe/ZnSe and CdSe/CdS with accounts of improved luminescence QYs, decreased fluorescence lifetimes, chemical stability and narrow emission line widths.[8,10-28]

Among the various II-VI semiconductors that have been investigated as shell materials for CdSe QDs, the most intensively studied are CdSe/ZnS and CdSe/CdS whereas, little research has been carried-out on the CdSe/ZnSe core/shell systems. ZnSe should, in principle, be a very good candidate as a shell material. First, its band gap is wider (2.58 eV) than that of CdSe (1.73 eV), and the band alignment is of type I, i.e, both electrons and hole are confined in CdSe.[29] Second, its lattice parameter mismatch relative to the CdSe core (6.3 %), although being larger than that of CdS (3.9 %), is significantly lower than that of the most commonly used shell material, ZnS (10.6%).[18] Third, keeping the same anion at the interface leads to a larger band offset in the conduction band and therefore, to a better compromise in relative confinement of the (light) electrons and (heavy) holes.[30]

These core/shell systems are mostly prepared through the organometallic route and modification thereof, which have been discussed extensively in chapter one, as well as their limitations. Recently CdSe/CdS nanocrystals have been prepared in aqueous solution but their QYs are very low and the bandwidth are quite broad (the full-width at half-maximum, FWHM > 100 nm).[31] As a result of the favourable results

obtained, using our proposed new synthetic route for the synthesis of organically soluble CdSe nanoparticles, with comparable and improved results, in relation to those synthesized by conventional organometallic methods, we decided to extend the methodology to the synthesis of CdSe/ZnSe nanocomposites and core/shell nanoparticles.

This chapter describes the synthesis and characterisation of CdSe/ZnSe core/shell and simple composites of CdSe-ZnSe using our proposed, new, facile and non-organometallic synthetic route. In addition, the systematic study of the growth of the nanoparticles at different reaction times and the effect of temperature on the size, optical and structural properties, were also investigated.

## 5.2 Synthetic methods

### 5.2.1 *Synthesis of core/shell and nanocomposites*

The CdSe/ZnSe core/shell structure was prepared by the injection of CdSe – trioctylphosphine (TOP) solution, prepared as described in Chapter two, into a hot (250 $^{0}$C) hexadecylamine (HDA) solution. The reaction was kept at this temperature for 30 minutes. An aliquot was removed from the reaction at 30 mins for characterisation of the initial CdSe nanoparticles. Then a ZnSe-TOP solution, prepared as described in chapter three, was injected into the red reaction mixture. Aliquots were taken at different reaction times as the reaction proceeded for a further 30 minutes. After completion, toluene was added to the solution; the solution was allowed to cool and methanol was then added to flocculate the nanoparticles. The flocculate was separated by centrifugation and dried. Dispersion of the flocculate in

toluene resulted in an optically transparent solution that could be readily characterised.

The CdSe-ZnSe nanocomposite was prepared by the injection of CdSe-TOP solution, followed by ZnSe-TOP solution, into a hot (160 $^0$C) hexadecylamine (HDA) solution and kept at this temperature for 30 minutes.

## 5.3 Results and discussion

### 5.3.1 *CdSe/ ZnSe Core/shell and Nanocomposites*

#### 5.3.1.1 *CdSe/ ZnSe Core/shell structures*

##### 5.3.1.1.1 *Optical properties*

The UV-absorption spectra of the core CdSe and CdSe/ZnSe nanoparticles at 230 °C and 30 mins reaction time are shown in Figure 5.1. The dosing of the ZnSe is accompanied by an increase in the absorption maxima of the UV/visible spectra. These differences form the evidence for epitaxial growth of the shell. The band-edge of the CdSe/ZnSe (649 nm, 1.91 eV) undergoes a slight red-shift of 15 nm (0.012 eV) as compared to the core CdSe (634 nm, 1.96 eV). This has been attributed to the partial leakage of the exciton into ZnSe. Since the bulk band gap of ZnSe (2.58 eV) is larger than that of CdSe (1.73 eV), the wave function of the excited electron and hole in the core nanocrystals, partly spread into the ZnSe shell easily, leading to an inevitable leakage of the exciton.[18,19,27&32] In addition, the red-shift also indicates that the particle formed is a core/shell nanostructure and not an alloy.[3,8,17,21,22,27&28] In an alloy, a linear blue-shift of absorption and PL spectra will occur.[22,27&33] The overall shape of the CdSe/ZnSe spectrum is similar to that of the CdSe. The excitonic feature at 579 and 584 nm, observed for CdSe and CdSe/ZnSe respectively, is attributed to

the first electronic transition (1s-1s) and the sharp absorption edge suggest particles with narrow size distributions. The broadening of the second absorption band in CdSe/ZnSe is due to the surface passivation by the inorganic shell. Since the second excited state has more electron density close to the particle surface, its energy would be more sensitive to the surface derivatization.[17] The sizes of the particles as calculated from the absorption maxima[34] are 3.79 nm (CdSe) and 3.95 nm (CdSe/ ZnSe). This increase in particle size is also attributed to the epitaxial growth of a ZnSe layer on the CdSe. XRD and TEM confirm this increase in particle size.

The photoluminescence spectra for the core CdSe and CdSe/ZnSe exhibit band-edge luminescence at 400 nm excitation wavelength (Figure 5.2). The emission maxima show a red-shift in relation to the corresponding absorption maxima. The emission maximum of CdSe/ZnSe at 623 nm is slightly red-shifted in relation to the emission maximum of the core CdSe (619 nm). This is consistent with the absorption results. The intensity of the emission maximum increased in the core-shell structure as compared to the parent material (CdSe). This enhanced emission has been reported previously for various core-shell structures and, is attributed to the passivation by the wider band gap material.

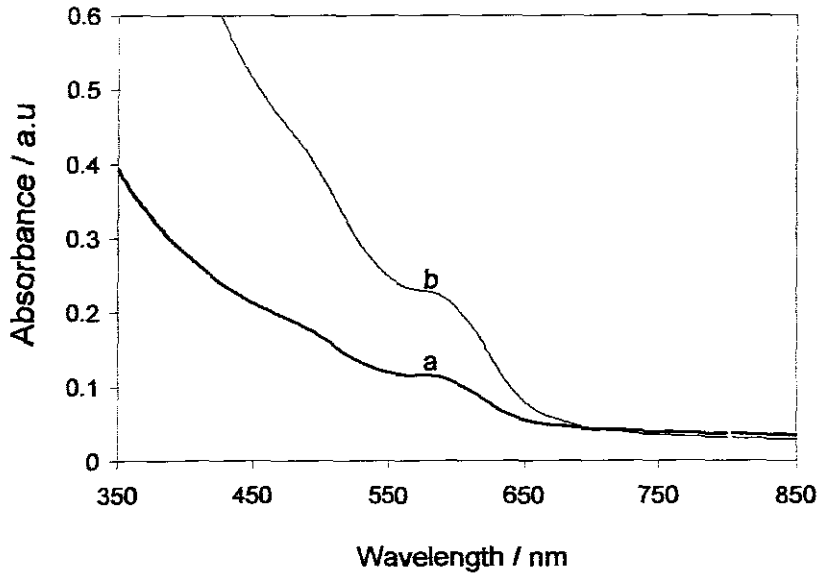


***Figure 5.1*** *Absorption spectra of (a) core CdSe and (b) CdSe/ZnSe at 230 $^0$C for the reaction time of 30 mins.*

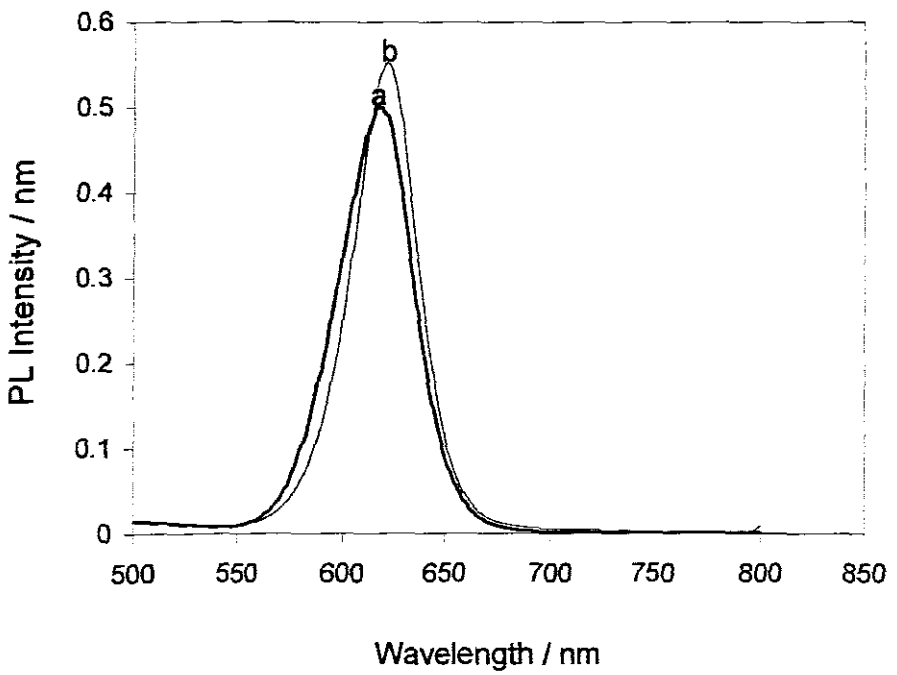


***Figure 5.2*** *Photoluminescence spectra ($\lambda_{400}$ nm) of (a) core CdSe and (b) CdSe/ZnSe at 230 $^0$C for the reaction time of 30 mins.*

The absorption and emission spectra of the core CdSe and CdSe/ZnSe at elevated temperature (250 °C), is shown in Figures 5.3 and 5.4. In general, the particles show similar optical properties with those synthesized at a lower temperature, with a few exceptions. The absorption and emission maxima are red-shifted at elevated temperatures, indicating an increase in particle sizes. The excitonic feature attributed to the first electronic transition (1s-1s) is sharper with a distinct second absorption band (496 nm) in CdSe/ZnSe. However, the emission spectrum of the CdSe/ZnSe shows a small broad tail towards higher energy. This is absent in the CdSe spectrum and will be discussed later.

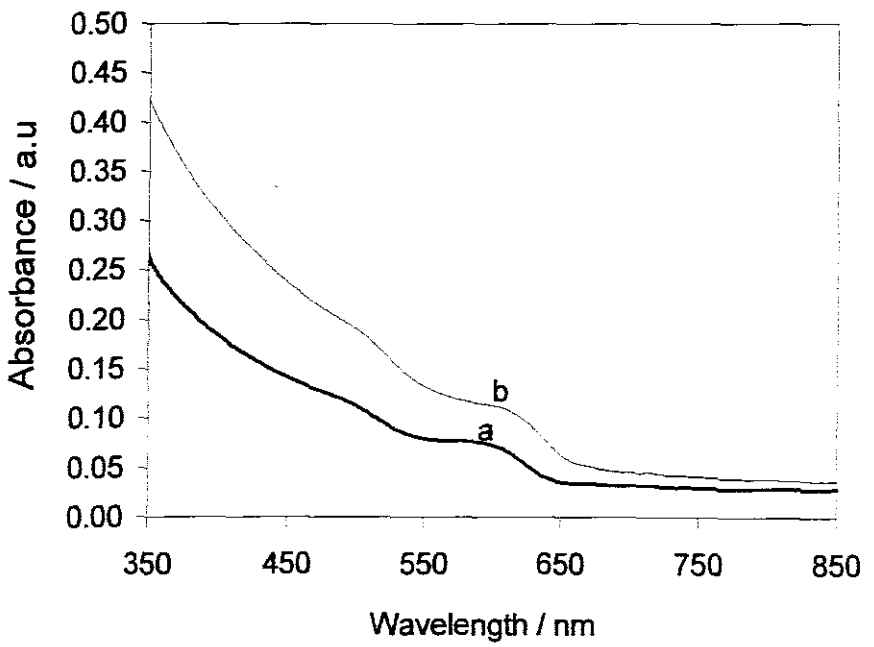


***Figure 5.3*** *Absorption spectra of (a) core CdSe and (b) CdSe/ZnSe at 250 °C for the reaction time of 30 mins.*

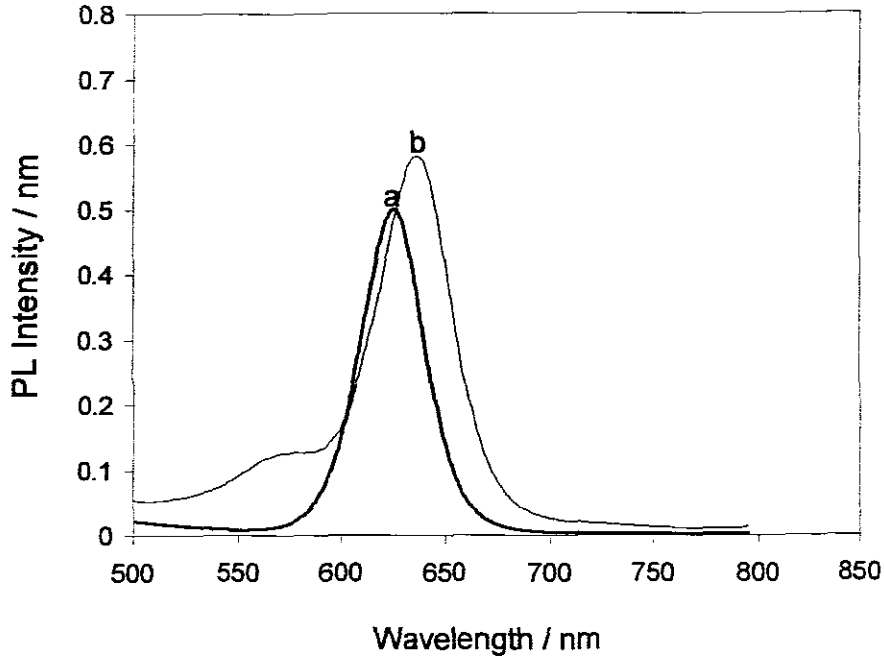


***Figure 5.4*** *Photoluminescence spectra ($\lambda_{400}$ nm) of (a) core CdSe and (b) CdSe/ZnSe at 250 $^{0}$C for the reaction time of 30 mins.*

It's worth mentioning that, compared to the CdSe nanoparticles obtained at lower temperatures (110, 160 and 200 °C) discussed earlier in chapter two, the CdSe nanoparticles prepared at 230 and 250 °C display narrower emission line widths, an increase in particle size and a narrower size distribution, as expected for synthesis at elevated temperatures.

Figure 5.5 shows the UV/visible absorption spectra of the core CdSe and CdSe/ZnSe core/shell nanoparticles at 230 °C and at various capping stages. The absorption maximum of CdSe occurred at 579 nm. After the injection of ZnSe solution, the ZnSe formed on the surface of the CdSe nanoparticles to produce the core/shell structured nanoparticles. The absorption maximum of these core/shell nanoparticles showed a slight red-shift as the reaction times increased, as seen in Table 2. The

absorption changed predominantly in the first 15 mins, from 579 nm to 584 nm and remained unchanged for the rest of the reaction times. This could be attributed to the growth process of the ZnSe on the surface of the CdSe nanoparticles. In the early stages, there is adequate ZnSe source and the shell grows quickly, as the source is depleted the growth of the ZnSe layer slows down.

***Table 2** : Optical properties of the core CdSe and CdSe/ZnSe at 230 $^0$C.*

| Reaction time / mins | 0 | 2 | 5 | 10 | 15 | 20 | 30 |
|---|---|---|---|---|---|---|---|
| Absorption maximum / nm | 579 | 581 | 582 | 583 | 584 | 584 | 584 |
| Emission maximum / nm | 619 | 620 | 620 | 620 | 621 | 621 | 621 |
| FWHM / nm | 42 | 39 | 36 | 36 | 36 | 36 | 36 |

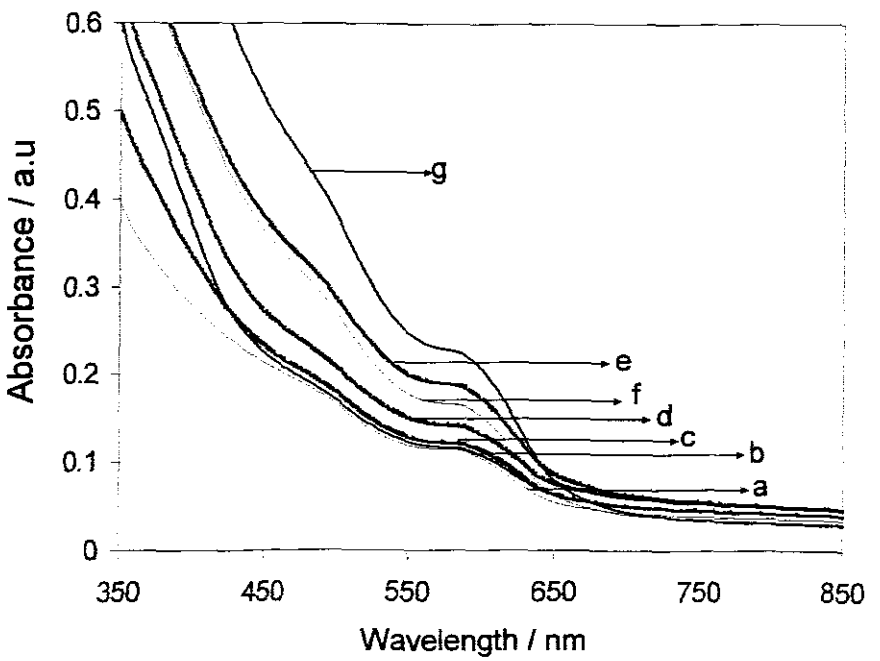


***Figure 5.5** Absorption spectra at 230 $^0$C of (a) core CdSe at 30 mins and CdSe/ ZnSe at (b) 2 mins, (c) 5mins, (d) 10 mins, (e) 15 mins, (f) 20 mins and (g) 30 mins.*

At higher temperature (250 °C), the absorption spectra (Figure 5.6) show a large red-shift of about (11 nm) between the CdSe core (588 nm) and the CdSe/ZnSe (599 nm) at 30 mins, unlike the growth at 230 °C (5 nm). In addition, the absorption maximum becomes stable between 10 and 20 mins after which, it increases gradually as seen in Table 3.

***Table 3** : Absorption and emission maxima of the core CdSe and CdSe/ZnSe at 250 $^0$C*

| Reaction time / mins | 0 | 2 | 5 | 10 | 15 | 20 | 30 |
|---|---|---|---|---|---|---|---|
| Absorption maximum / nm | 588 | 591 | 592 | 594 | 594 | 595 | 599 |
| Emission maximum / nm | 627 | 625 | 517, 626 | 545, 631 | 550, 633 | 561, 633 | 633 |

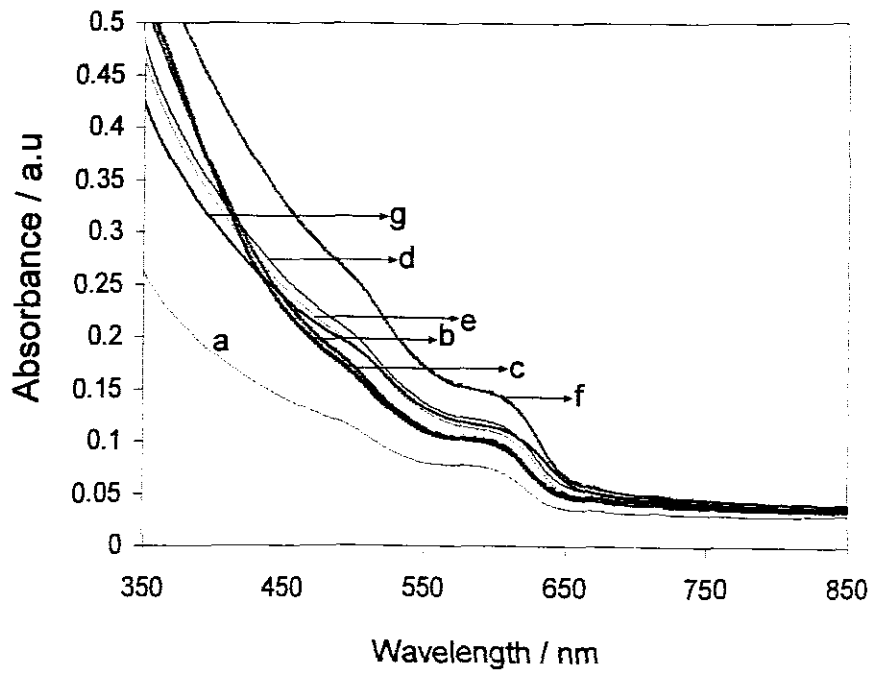


***Figure 5.6** Absorption spectra at 250 $^0$C of (a) core CdSe at 30 mins and CdSe/ ZnSe at (b)2 mins, (c) 5mins, (d) 10 mins, (e) 15 mins, (f)20 mins and (g) 30 mins.*

The photoluminescence spectra at 230 °C and at different growth times are shown in Figure 5.7. The spectra show that there is an absence of emission due ZnSe alone, confirming the growth of ZnSe on the CdSe core. The formation of separate ZnSe nanoparticles is expected to produce ZnSe emission spectra after it is excited above the band gap energy. However, there was no emission observed below 480 nm, when the entire samples were excited with 350 nm light. This can lead us to conclude that no ZnSe nanoparticles were formed in the solution. Similar observations were made by Chen. *et al.* during the growth of CdS on CdSe.[28] The CdSe and CdSe/ZnSe core/shell nanoparticles had good optical qualities and there was no emission from the deep trap states towards the lower energy side. The full width, at half maximum (FWHM) of the emission spectra (36 nm) remains unchanged after 5 mins, suggesting similar size distributions.

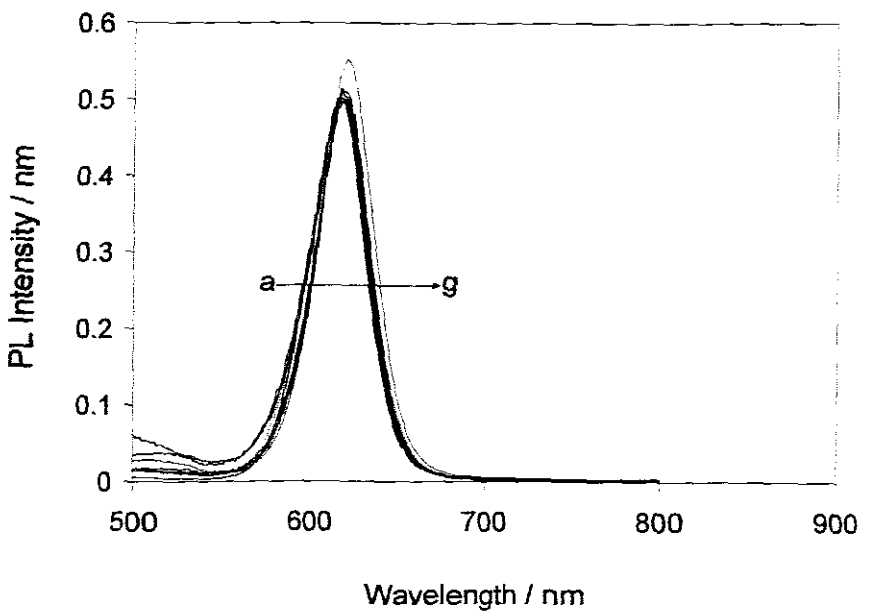


***Figure 5.7*** *Photoluminescence spectra ($\lambda_{350}$ nm) at 230 $^{0}$C of (a) core CdSe and CdSe/ZnSe at reaction time of (b) 2 mins, (c) 5 mins, (d) 10 mins, (e) 15 mins, (f) 20 mins and (g) 30 mins.*

The photoluminescence spectra at 250 °C (Figure 5.8), elucidates further, the growth process at various capping stages. Unlike the spectra at 230 °C, the spectra show two emission maxima, after 2 mins of injecting the ZnSe solution, at lower and higher wavelength to that of the CdSe core. At 5 mins the emission peak, at lower wavelength, was slightly higher in intensity and increased with time compared to the peak at higher wavelength, reaching its maximum after 15 mins. Thereafter it becomes reduced and disappears from the spectrum at 30 mins, reappearing as a small broad tail. Since the emission peak at lower wavelength to that of the CdSe core was observed at higher wavelength (517 nm, 5 mins) than 480 nm ( ZnSe band-edge), it can be concluded that the emission was not due to the presence of ZnSe nanoparticles as discussed earlier. This emission being blue-shifted to the CdSe core and increases with growth time could be assigned to the formation of a CdSe/ZnSe alloy, while the slight red-shifted emission is assigned to the formation of core-shell structure.[17,21,22 & 31]

The presence of the alloy could be attributed to the high temperature used in the synthesis. The initial period, after hot injection, is usually characterised by rapid growth, which results in surface disorder and hence, low emission intensity. This leads to fast nucleation of ZnSe, faster rate of alloy formation compared to the rate of capping on the surface of CdSe core and, low intensity of the CdSe/ZnSe emission peak at the beginning of the capping process. In the early stages, there is enough of ZnSe and so the alloy grows quickly. As the reaction time increases, the ZnSe sources become depleted, the growth rate becomes slower and this reduces surface disorder and facilitates surface ordering and reconstruction during annealing. Thus, the growth of the alloy is suppressed, leading to the formation of a CdSe/ZnSe

core/shell system. This is confirmed by the slight increase in the intensity of the core/shell peak at 20 mins and the disappearance of the alloy peak at 30 mins. In addition, the formation of alloy could also be attributed to the fact, that the lattice of CdSe is larger than that of ZnSe, thus causing lattice mismatch between the CdSe core and ZnSe shell.[17] This lattice mismatch distorts the lattice structure and induces a stress at the interface between the CdSe and ZnSe at the beginning of the reaction. This might also responsible for the slight blue-shift (~ 2 nm) of the CdSe/ZnSe peak at the beginning of the capping process (2 to 5 mins) as seen in Table 3.

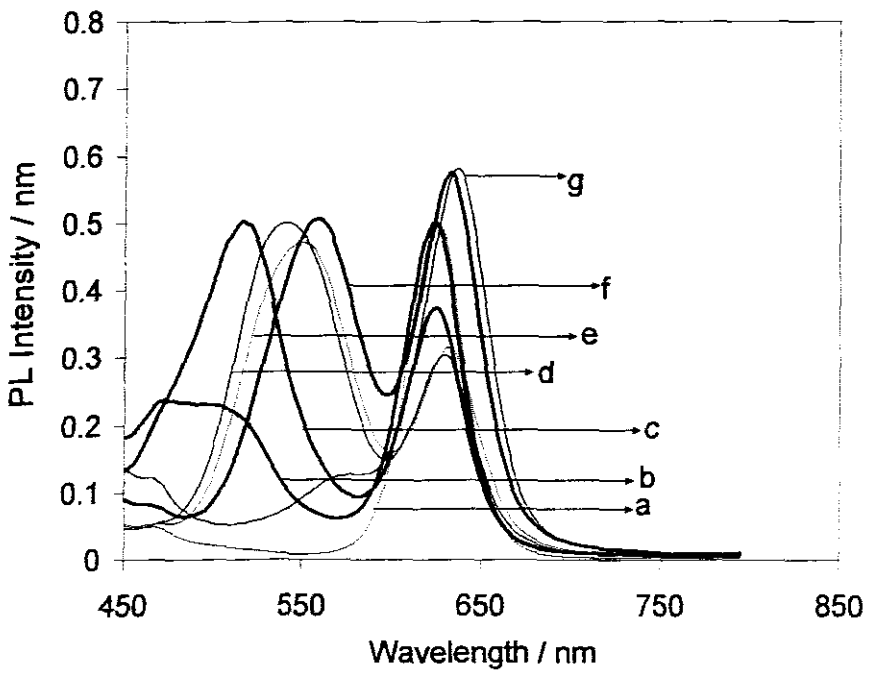


***Figure 5.8*** *Photoluminescence spectra ($\lambda_{350}$ nm) at 250 $^{0}$C of (a) core CdSe and CdSe/ZnSe at reaction time of (b) 2 mins, (c) 5mins, (d) 10 mins, (e) 15 mins, (f)20 mins and (g) 30 mins*

#### 5.3.1.1.2 *Structural properties*

The diffraction patterns of the core CdSe and the CdSe/ZnSe core/shell particles are similar and without any changes in the phase. The diffraction patterns show

broad peaks along the (110), (103) and (112) planes which are assigned to the hexagonal phase of the CdSe, suggesting that the diffraction is predominantly due to the CdSe core. The X-ray data could be consistent with a core/shell or with the formation of a composite, but the formation of composite will result in a blue-shift of absorption and PL spectra because of the larger band gap energy of the composite, compared to pure CdSe.[17,21,22&27] The observed red-shift in the absorption and emission spectra shows that a core/shell structure is present. The X-ray diffraction pattern of the core/shell structures are slightly sharper, an indication of the epitaxial growth of the shell. This also accounts for the slight shift in the peaks to higher 2 theta value in the core/shell structure, since the epitaxy requires that the lattice parameters be the same for both core and shell.[21] Typical representative XRD patterns of the core CdSe and CdSe/ZnSe particles at 230 °C and at different reaction times, are shown in Figures 5.9 to 5.12. The positions of the diffraction peaks at all the various capping stages do not overlap with the diffraction lines of the wurtzite ZnSe. This confirmed that no separate ZnSe is formed but that the diffraction is due to CdSe. The peaks along the (110), (103) and (112) planes at 2 mins (Figure 5.10), are not clearly resolved and are reduced in intensity. As the reaction time increases, the diffraction peaks are more clearly resolved and increase in intensity.

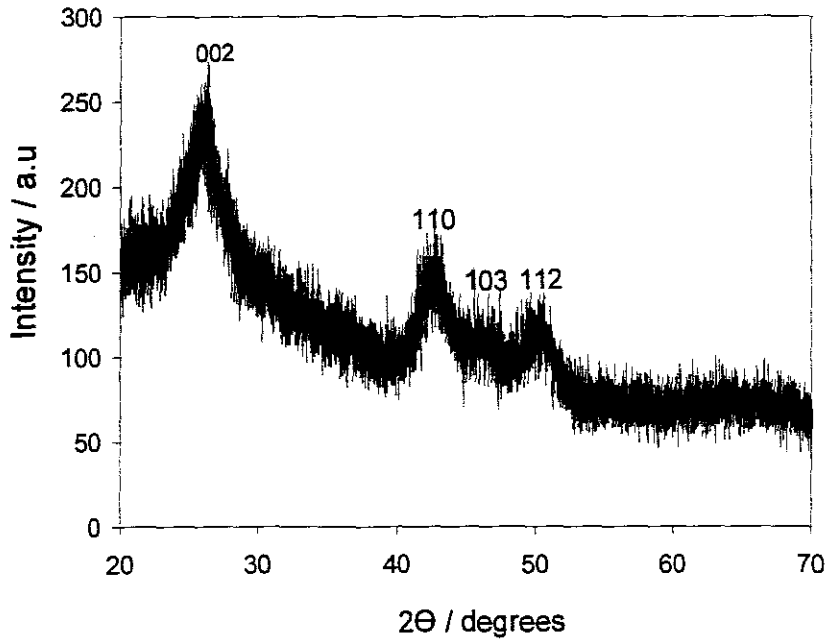


***Figure 5.9*** *XRD pattern of CdSe core at 230 $^0$C at the reaction time of 30 mins.*

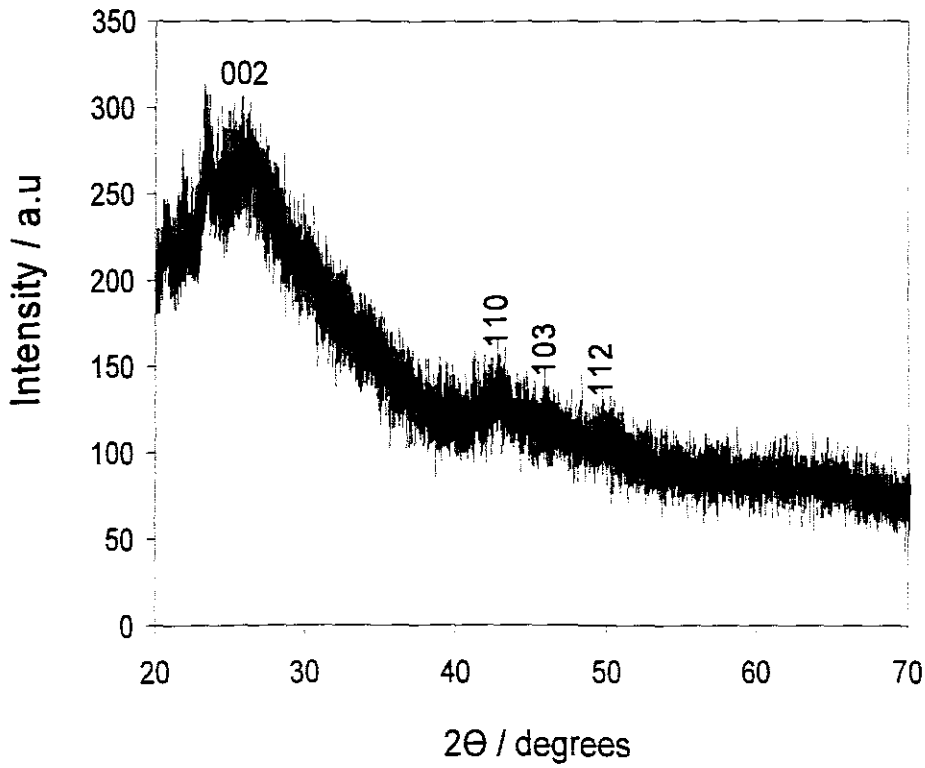


***Figure 5.10*** *XRD pattern of CdSe/ZnSe at 230 $^0$C at the reaction time of 2 mins.*

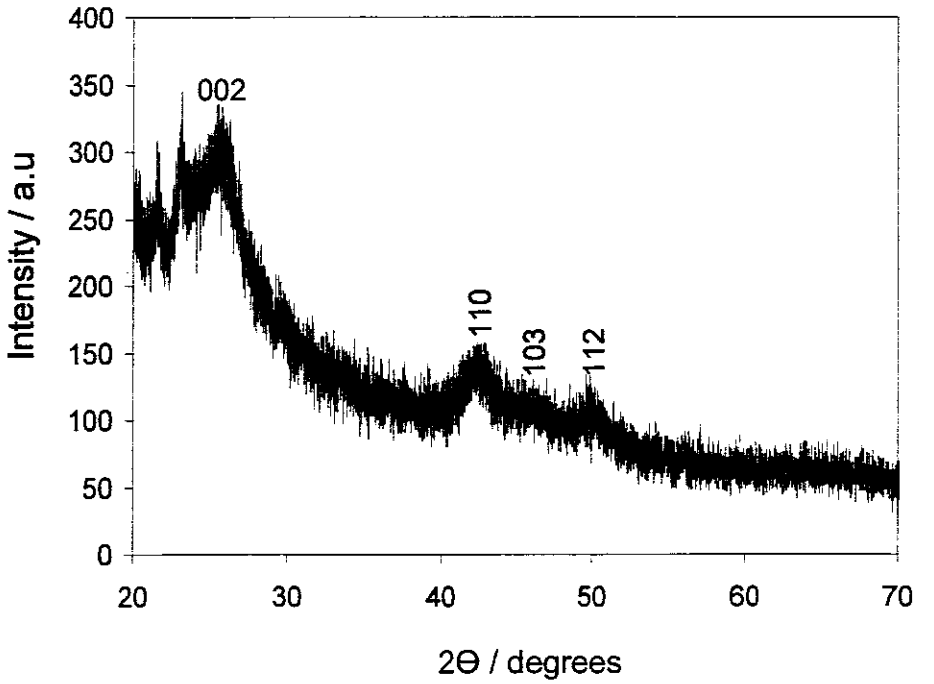


***Figure 5.11*** *XRD pattern of CdSe/ZnSe at 230 $^0$C at the reaction time of 10 mins.*

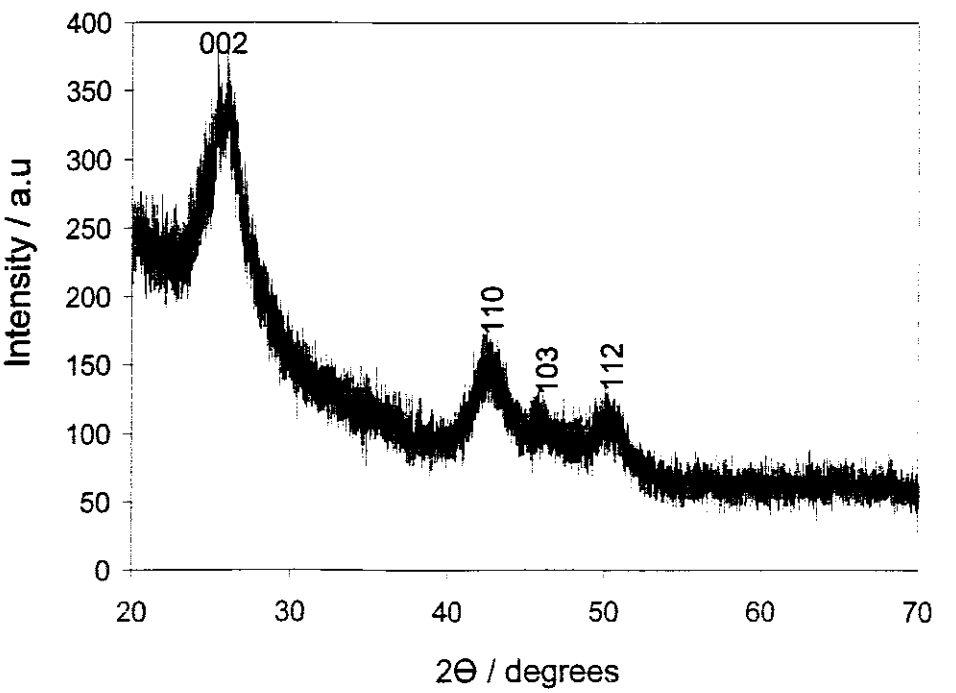


***Figure 5.12*** *XRD pattern of CdSe/ZnSe at 230 $^0$C at the reaction time of 30 mins.*

Typical representative samples of the diffraction patterns of the core CdSe and CdSe/ZnSe nanoparticles synthesised at 250 °C and various capping stages, are shown in Figures 5.13 to 5.16. The diffraction peaks are broad, without any change of phase in relation to the diffraction patterns at 230 °C. The positions of the diffraction peaks at all the various capping stages, do not overlap with the diffraction lines of the wurtzite ZnSe, confirming that the diffraction is due to CdSe. In addition the diffraction peaks are also shifted to higher 2 theta values in relation to the diffraction peaks of the core CdSe, confirming the formation of the CdSe/ZnSe structure. These two observations show that our sample is predominantly of a CdSe/ZnSe core/shell system.

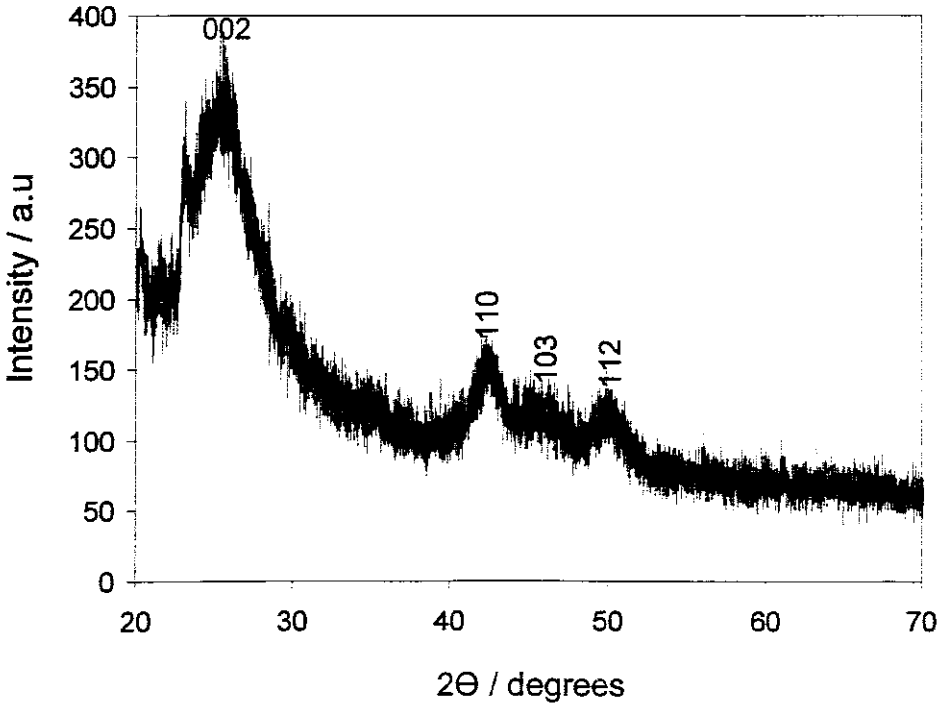


***Figure 5.13*** *XRD pattern of core CdSe at 250 $^{0}$C at the reaction time of 30 mins.*

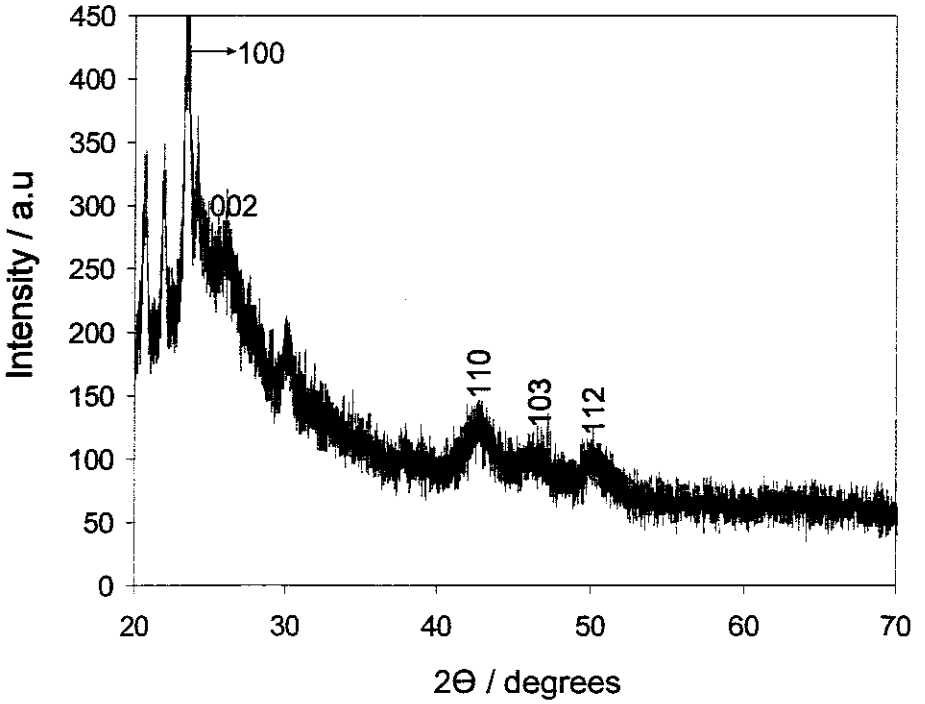


***Figure 5.14*** *XRD pattern of CdSe/ZnSe at 250 $^0$C at the reaction time of 15 mins.*

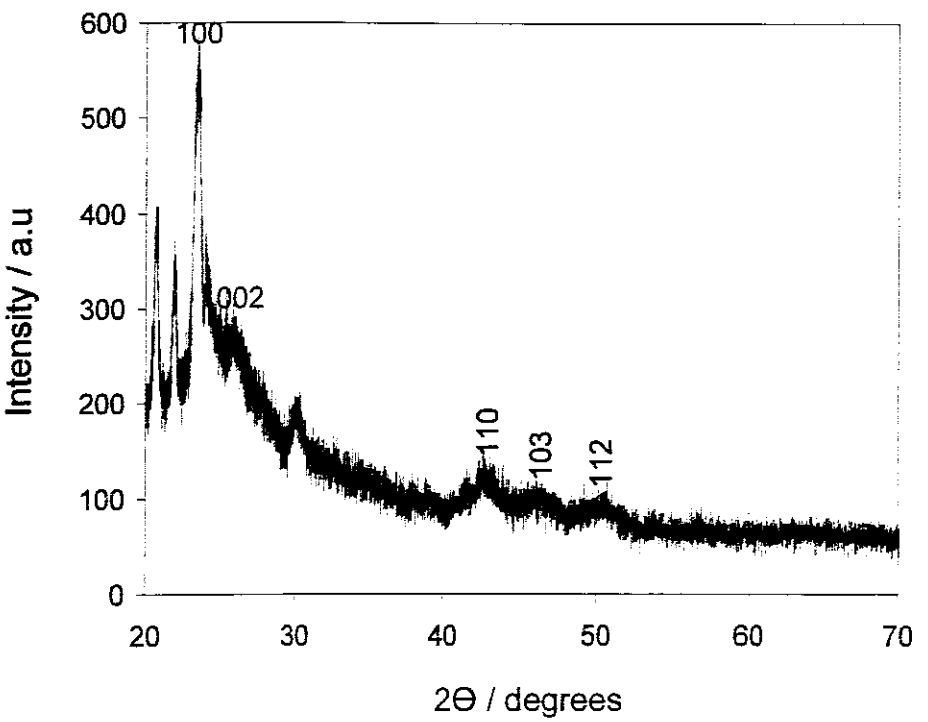


***Figure 5.15*** *XRD pattern of CdSe/ZnSe at 250 $^0$C at the reaction time of 20 mins.*

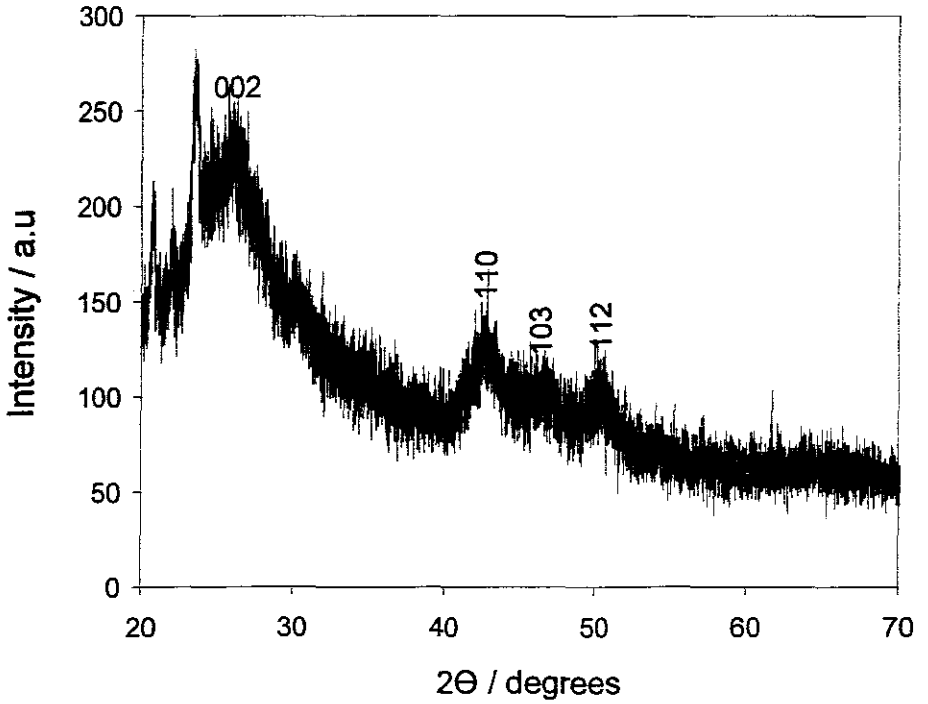


***Figure 5.16*** *XRD pattern of CdSe/ZnSe at 250 $^0$C at the reaction time of 30 mins.*

The TEM image and particle size distribution of CdSe/ZnSe at 230 °C and 250 °C, is shown in Figures 5.17 and 5.18 respectively. The TEM image at 230 °C shows well-defined, monodispersed spherical particles with an increase in diameter compared to the core CdSe. This is consistent with the optical results and has been attributed to the growth of the shell. The average particle diameter of the CdSe/ZnSe at 230 °C, as determined from the TEM image, is 3.99 nm ± 4 %. This correlates with the particle size calculated from the exciton absorption peak. At 250 °C, the TEM image shows well-defined, monodispersed spherical particles with an increase in diameter, compared to the one synthesized at 230 °C. This increase in particle size is in accordance with the fact that higher temperature leads to larger particle sizes. The average particle diameter of the CdSe/ZnSe at 250 °C as determined from the TEM image is 4.51 nm ± 6 %.

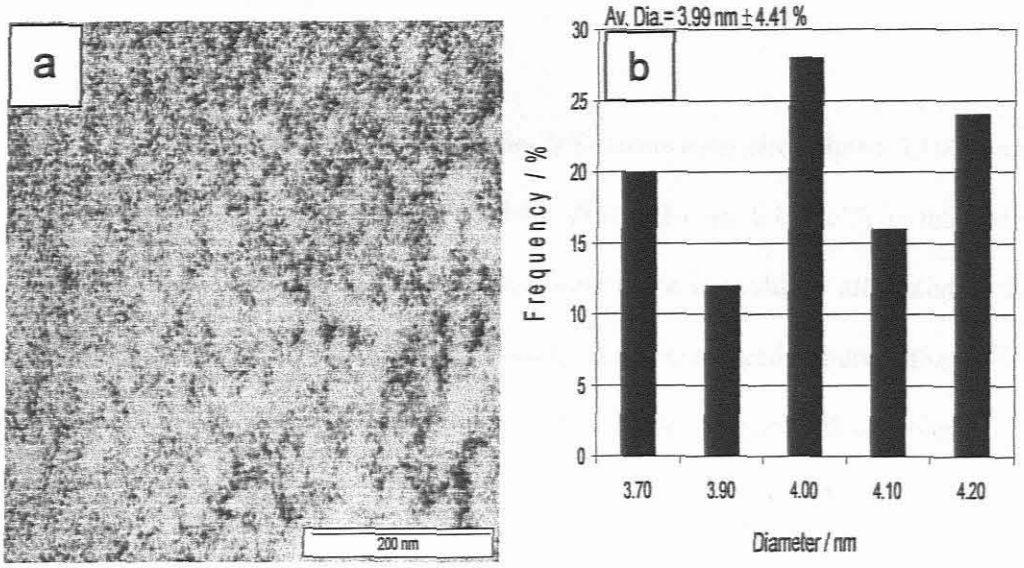


***Figure 5.17*** *The TEM image (a) and Particle size distribution (b) of CdSe/ZnSe at 230 $^0$C at the reaction time of 30 mins.*

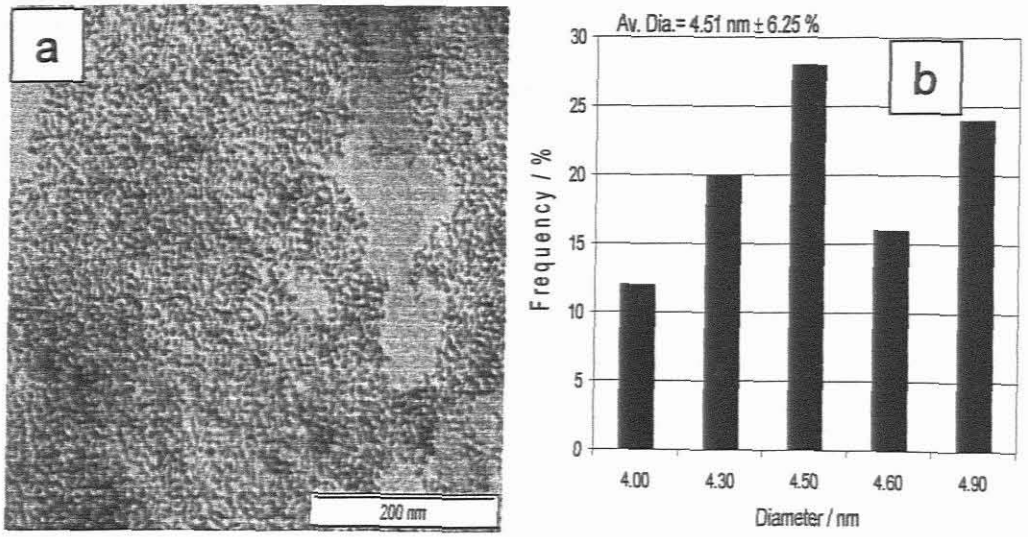


***Figure 5.18*** *The TEM image (a) and Particle size distribution (b) of CdSe/ZnSe at 250 $^0$C at the reaction time of 30 mins.*

### 5.3.1.2 *CdSe/ ZnSe Nanocomposite*

#### 5.3.1.2.1 *Optical Properties*

The absorption spectrum of the CdSe-ZnSe nanocomposite (Figure 5.19) shows an absorption maximum at 531 nm. The blue-shift of 16 nm (0.013 eV), in relation to the pure CdSe is indicative of composite formation and could be attributed to the larger band gap energy of the CdSe-ZnSe composites, compared to pure CdSe.[17, 21, 22 &27] The overall shape of the spectrum is similar to that of pure CdSe however, the excitonic shoulder is broader than that of pure CdSe due to the composite formation. The PL spectrum of the composite ($\lambda_{ex}$ = 400 nm) exhibits band-edge emission (Figure 5.20). The emission maxima show a red-shift in relation to the corresponding absorption maximum. The emission maximum of CdSe-ZnSe nanocomposites at 562 nm is also blue-shifted, in relation to the emission maximum of pure CdSe (588 nm). The intensity of the emission maximum is slightly higher in the composite, as compared to the parent material (CdSe) and, there is no emission towards higher energy side or evidence of deep trap emission.

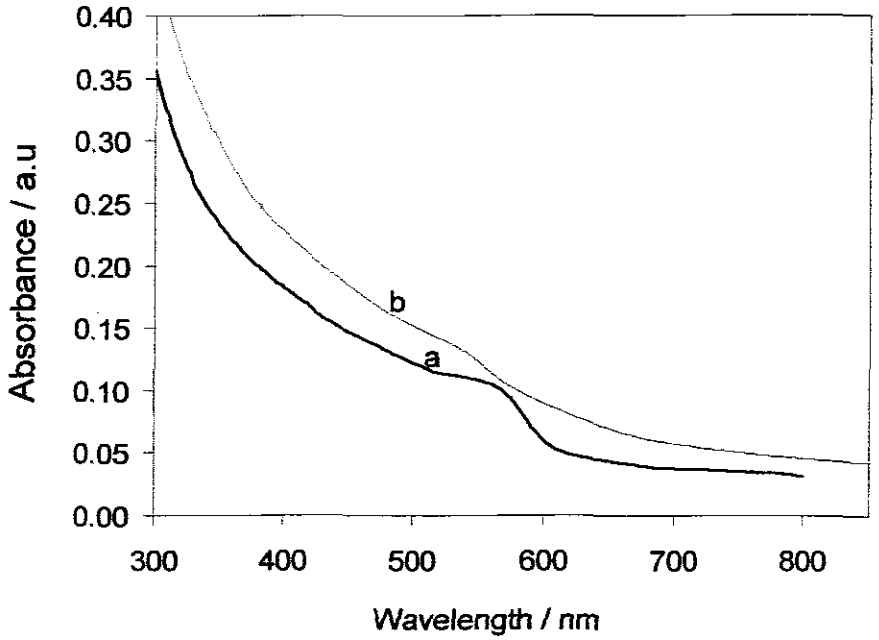


***Figure 5.19*** *Absorption spectra of (a) pure CdSe and (b) CdSe-ZnSe nanocomposite at reaction time of 30 mins.*

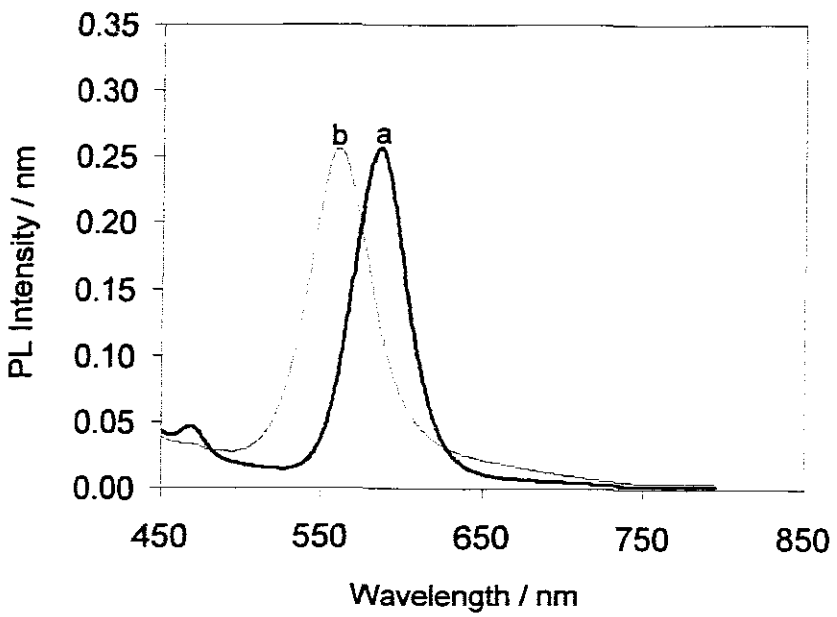


***Figure 5.20*** *Photoluminescence spectra ($\lambda_{400}$ nm) of (a) pure CdSe and (b) CdSe-ZnSe nanocomposite at the reaction time of 30 mins.*

#### 5.3.1.2.2 *Structural Properties*

Figures 5.21 and 5.22, show the XRD diffraction patterns of pure CdSe and the CdSe-ZnSe composites at 160 °C at 30 mins reaction time. The diffraction patterns of the composite consist of broad features that do not overlap with the characteristic diffraction peaks of wurtzite CdSe or wurtzite ZnSe. Such diffraction patterns could be expected from largely alloyed particles. Similar results have been reported by Danek *et al.,* for thin-film CdSe/ZnSe composites.[17] The XRD pattern of the composite shows three diffraction peaks corresponding to the (111), (220) and (311) crystalline planes of cubic CdSe, indicating a phase transition from the hexagonal phase of the pure CdSe. This effect might also be as a result of the smaller size of the CdSe-ZnSe composite, as compared to the pure CdSe.

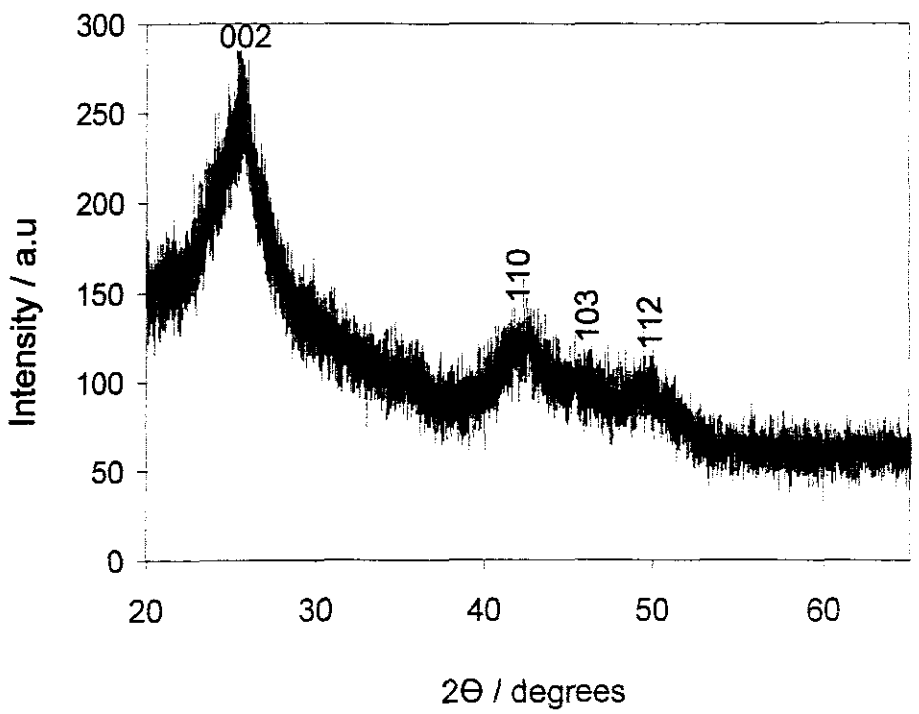


***Figure 5.21*** *XRD pattern of pure CdSe at the reaction time of 30 mins.*

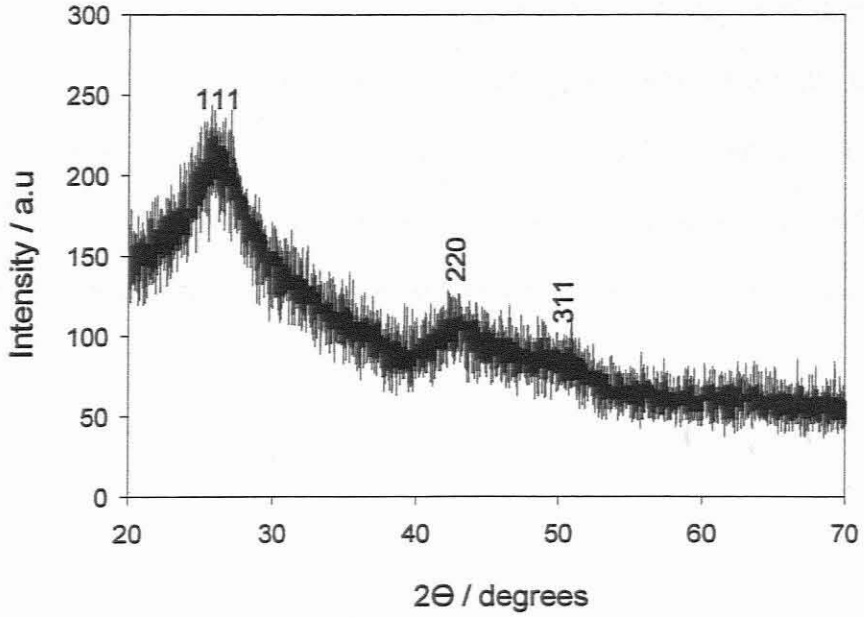


***Figure 5.22*** *XRD pattern of CdSe/ZnSe nanocomposite at the reaction time of 30 mins.*

The TEM image of the CdSe-ZnSe composites (Figure 5.23) shows, well-defined, monodispersed, spherical particles with an average particle size of 2.91 nm (± 7%), which is smaller than that of pure CdSe (3.00 nm, ± 8%). This decrease in particle size is inconsistent with the optical analysis.

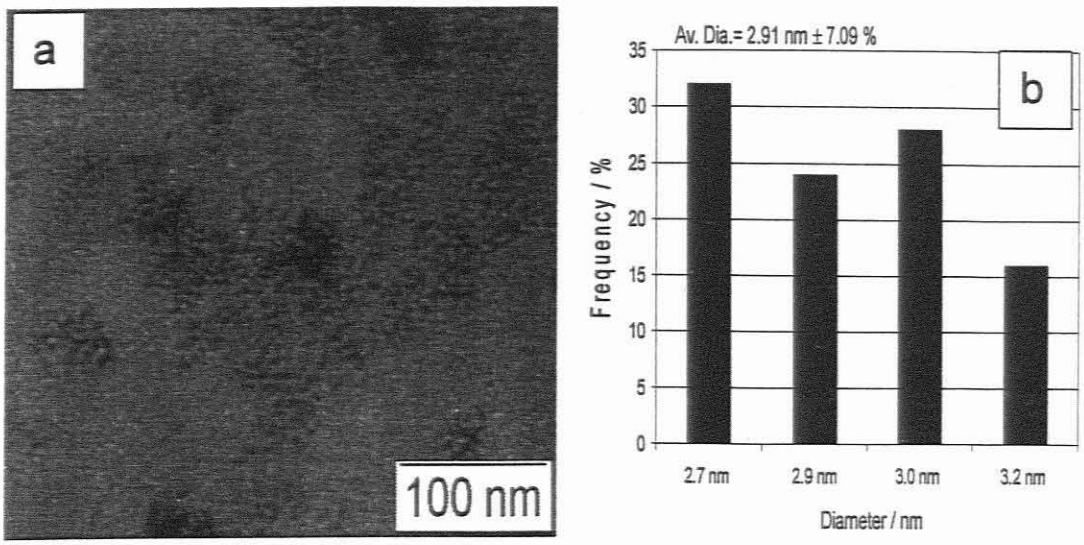


***Figure 5.23*** *The TEM image (a) and particle size distribution (b) of CdSe-ZnSe nanocomposite at the reaction time of 30 min.*

We report the synthesis and characterisation of highly monodispersed HDA-capped CdSe-ZnSe nanocomposites and CdSe/ZnSe core/shell nanoparticles, synthesised via our novel, facile and environmentally-benign non-organometallic synthetic route. The study of the core/shell growth at different reaction times and the effect of temperature on the optical and structural properties, were also investigated.

The absorption and emission maxima of the CdSe/ZnSe at 230 °C and 250 °C are red-shifted in relation to the core CdSe, which indicates an epitaxial growth of the shell and confirmed the formation of a core/shell structure. In addition, there is an increase in the emission intensity as compared to the core material. As expected, the absorption and emission maxima are red-shifted at a higher temperature (250 °C), indicating an increase in particle size and the second absorption band of the CdSe/ZnSe is visible at this temperature.

The emission spectra confirmed that separate ZnSe nanoparticles are not formed in the solution. The emission spectrum at 250 °C shows two emission maxima, after 2 mins of injecting the ZnSe solution, at lower and higher wavelength to that of the CdSe core, attributed to the formation of CdSe/ZnSe alloy and core-shell structure respectively. The presence of the alloy was attributed to the high temperature used in the synthesis and lattice mismatch between the CdSe core and ZnSe shell.

The broad peaks of the X-ray diffraction patterns are assigned to the hexagonal phase of CdSe, indicating that the diffraction is predominantly due to CdSe core. The sharper lines of the diffraction peaks are also an indication of the epitaxial growth of

the shell. In addition the positions of the diffraction peaks, at all the various capping stages, do not overlap with the diffraction lines of the wurtzite ZnSe, confirming that no separate ZnSe is formed. The TEM images of the core/shell structures show well-defined, spherical particles with a narrow size distribution. The average particle diameter of the CdSe/ZnSe are 3.99 ± 0.16 nm (230 °C) and 4.51 ± 0.27 nm at 30 mins reaction time.

The absorption and emission maxima of the CdSe-ZnSe nanocomposite are blue-shifted in relation to pure CdSe, an indication for the formation of a composite 1. The emission spectrum shows no emission towards a higher energy side or, evidence of deep trap emission. The XRD diffraction pattern of the composites shows a phase transition from the hexagonal phase of the pure CdSe to the cubic phase. The TEM image of the composites shows well-defined, monodispersed and spherical particles with smaller diameters than the pure CdSe.

## 5.5 References


1) C. B. Murray, D. J. Norris and M. G. Bawendi, *J. Am. Chem. Soc.*, 1993, **115**, 8706.

2) L. Qu, Z. A. Peng and X. Peng, *Nano. Lett.*, 2001, **1**, 333.

3) I. Mekis, D. V. Talapin, A. Kornowski, M. Hause and H. Weller, *J. Phys. Chem. B*, 2003, **107**, 7454.

4) T. Trindade, P. O'Brien and X. Zhang, *Chem. Mater.*, 1997, **9**, 523.

5) J. E. Bowen Katari, V. L. Colvin and A. P. Alivisatos, *J. Phys. Chem.*, 1994, **98**, 4109.

6) H. Noglik and W. J. Pietro, *Chem. Mater.*, 1994, **6**, 1593.

7) X. G. Peng, L. Manna, W. D. Yang, J. Wickham, E. Scher, A. Kadavanich and A. P. Alivisatos, *Nature*, 2000, **404**, 59.

8) J. A. Gaunt, A. E. Knight, S. A. Windsor and V. Chechik, *J. Colloid and Interface Science*, 2005, **290**, 437.

9) J. McBride, J. Treadway, L. C. Feldman, S. J. Pennycook and S. J. Rosenthal, *Nano Lett.*, 2006, **6**, 1496.

10) L. Spanhel, M. Haase, H. Weller and A. Henglein, *J. Am. Chem. Soc.*, 1987, **109**, 5649.

11) A. R. Koran, R. Hull, R. I. Opila, M. G. Bawendi, M. I. Steigerwald, P. J. Carroll and L. E. Brus, *J. Am. Chem. Soc.*, 1990, **112**, 1327.

12) M. A. Hines and P. J. Guyot-Sionnest, *J. Phys. Chem.*, 1996, **100**, 468.

13) H. Weller, U. Koch, M. Gutierrez, A. Henglein, *Ber. Bunsen- Ges. Phys. Chem* 1987, **91**, 88.

14) A. Hasselbarth, A. Ecychmuller, R. Eichburger, M. Giesi, A. Mews and H. Weller, *J. Phys. Chem.*, 1993, **97**, 5333.

15) A. Hasselbarth, A. Ecychmuller and H. Weller, *J. Lumin.*, 1992, **53**, 112.

16) H. S. Zhou, I. Honma, H. Sasahara, H. Komiyama and J. W. Kraus, *Chem. Mater.*, 1994, **6**, 1534.

17) M. Danek. K. F. Jensen, C. B. Murray, and M. G. Bawendi. *Chem. Mater.*, 1996, **8**, 173.

18) P. Reiss, J. Bleuse and A. Pron, *Nano Lett.*, 2002, **2**, 781.

19) X. Peng, M. C. Schlamp, A. V. Kadavanich and A. P. Alivisatos, *J. Am. Chem. Soc.*, 1997, **119**, 7019.

20) Y. Tian, T. Newton, N. A Kotov, D. M. Guldi and J. H Fendler, *J. Phys.Chem.*, 1996, **100**, 8927.

21) N. Revaprasadu, M. A. Malik, P. O'Brien and G. Wakefield, *Chem. Commun.*, 1999, 1573.

22) D. Yang, Q. Chen and S. Yu, *J. Lumin.*, 2007, **126**, 853.

23) M. Xie, H. H. Liu, P. Chen, Z. Z. Ling, X. H, Wang, Z. X. Lie, Y. M. Du, B. Q. Pan and D. W. Pang, *Chem. Commun.*, 2005, 5518.

24) M. Q. Chu, X. Y. Shen and G. J. Liu, *Nanotechnology*, 2006, **17**, 444.

25 X. J. Ji, J. X. Zheng, J. M. Xu, V. K. Rastogi, T. C. Cheng, J. J. Defrank and R. M. Leblanc, *J. Phys. Chem.* B, 2005, **109**, 3793.

26) B. R. Venugopal, N. Ravishankos, C. R. Perrey, C. Shivakumara and M. Rajamathi, *J. Phys. Chem.* B, 2006, **110**, 772.

27) Q. Wang, D. Pan, S. Jiang, S. Ji, L. An and B. Jiang, *J. Lumin.*, 2006, **118**, 91.

28) X. Chen, Y. Lou and C. Burda, *Int. J. of Nanotechnology*, 2004, **1**, 105.

29) C. Guenaud, E. Deleporte, A. Filoramo, P. Lelong, C. Delalande, C. Morhain, E. Tournie and J. P. Faurie, *J. Appl. Phys.*, 2000, **87**, 1863.

30) S. H. Wei, S. B. Zhang and A. J. Zunger, *J. Appl. Phys.*, 2000, **87**, 1304.

31) F. Teng, A. W. Tang, Y. H. Gao, C. J. Liang, Z. Xu and Y. S. Wang, *Spectrosc. Spect. Anal.*, 2005, **25**, 651.

32) B. O. Dabboussi, J. Rodriguez-Viejo, F. V. Mikulec, J. R. Heine, H. Mattoussi, R. Ober, K. F. Jensen, M. G. Bawendi, *J. Phys. Chem.* B, 1997, **101**, 9463.

33) X. Zhong, Y. Feng, W. Knoll and M. Han, *J. Am. Chem. Soc.*, 2003, **125**, 13559.

34) W. W. Yu, L. Qu, W. Guo and X. Peng, *Chem. Mater.*, 2003, **15**, 2854.

# *CHAPTER SIX*

## EXPERIMENTAL

## 6.1 Chemicals

Cadmium chloride (Aldrich); sodium borohydride ($NaBH_4$, Aldrich); deionised water (HPLC grade, Aldrich); methanol (Aldrich); toluene (Aldrich); hexadecylamine (HDA, Aldrich); tri-n-octylphosphine (TOP 95%, Aldrich); tri-n-octylphosphine oxide (TOPO 90 %, Aldrich); Selenium (Merck); zinc chloride (Aldrich); zinc acetate (Aldrich); ammonia solution (0.1 M); dilute hydrochloric acid (0.1 M); L- cysteine ethyl ester hydrochloride (Aldrich); methionine (Aldrich); ascorbic acid (Aldrich); soluble starch (Aldrich); polyvinyl alcohol (PVA, Aldrich) and poly (vinylpyrrolidone) (PVP, Aldrich).

## 6.2 Synthesis

### 6.2.1 *Synthesis of organically-soluble CdSe Nanoparticles.*

In a typical room temperature reaction, 0.32 mmol of selenium powder was mixed with 20 mL of deionised water in a three-necked flask. 0.81 mmol of $NaBH_4$ was carefully added to this mixture and the flask was immediately purged with nitrogen gas to create an inert atmosphere. After 2 hours, 0.32 mmol of $CdCl_2$ dissolved in 20 mL of deionised water was added to the colourless selenium ion solution. The resultant light-yellow solution was stirred for 30 minutes, followed by the addition of excess methanol. The resultant solution was then centrifuged. The CdSe produced was dispersed in TOP (6.0 mL) and, after continuous stirring, the TOP-CdSe solution was injected into the hot HDA (6.0 g) at 160 °C in an inert atmosphere. A sudden decrease in temperature was observed. The temperature was then gradually raised to 160 °C and the reaction was allowed to continue for 30 mins. As the reaction time increased, the solution in the reaction flask changed from deep yellow to orange in colour. The orange colour solution obtained was allowed to cool

and methanol was added to the solution. Addition of excess anhydrous methanol to the solution resulted in the reversible flocculation of the nanoparticles. The flocculate was separated from the supernatant by centrifugation. Excess methanol was removed, under vacuum, to give HDA-capped CdSe nanoparticles. The resultant particles were dissolved in toluene to give an optically clear orange solution of nanocrystallites for characterization.

#### 6.2.1.1 *Effect of capping group*

##### 6.2.1.1.1 *HDA-capped CdSe nanoparticles*

The reactions were carried-out following the procedure described in section 6.2.1, using 0.64 mmol of selenium powder, 1.59 mmol of $NaBH_4$, 0.64 mmol of $CdCl_2$, 40.0 mL of deionised water, 12.0 mL of TOP and 12.0 g HDA at growth temperature of 180 °C.

##### 6.2.1.1.2 *TOPO-capped CdSe nanoparticles*

The reactions were carried-out following the procedure described in section 6.2.1 using TOPO (15.0 g) as the capping agent, 15.0 mL of TOP, 0.64 mmol of selenium powder, 1.59 mmol of $NaBH_4$, 0.64 mmol of $CdCl_2$ and 40.0 mL of deionised water at growth temperature of 250 °C.

#### 6.2.1.2 *Effects of reduction times*

##### 6.2.1.2.1 *HDA-capped CdSe Nanoparticles*

The reactions were carried-out following the procedure described in section 6.2.1 under reduction times of 2, 4 and 6 hrs. Aliquots were withdrawn, with a needle tip, at 2, 5, 10, 15, 20 and 30 min, to monitor the growth of the particles.

#### 6.2.1.2.2 *TOPO-capped CdSe Nanoparticles*

The reactions were carried-out following the procedure described in section 6.2.1 under reduction times of 2, 4 and 6 hrs using TOPO (7.5 g) as the capping agent and 15.0 mL of TOP at growth temperature of 230 °C.

### 6.2.1.3 *Effects of monomer concentration*

#### 6.2.1.3.1 *HDA-capped CdSe Nanoparticles*

The reactions were carried-out following the procedure described in section 6.2.1 under reduction times of 2, 4 and 6 hrs using 0.64 mmol of selenium powder, 1.59 mmol of $NaBH_4$, 0.64 mmol of $CdCl_2$, 40 mL of deionised water, 12.0 mL of TOP and 12.0 g HDA at growth temperature of 160 °C. Aliquots were withdrawn, with a needle tip, at different times of 5, 10, 15, 20 and 30 mins, to monitor the growth of the particles.

#### 6.2.1.3.2 *TOPO-capped CdSe Nanoparticles*

The reactions were carried-out following the procedure described in section 6.2.1 under reduction times of 2, 4 and 6 hrs using TOPO (15.0 g) as the capping agent, 15.0 mL of TOP, 0.64 mmol of selenium powder, 1.59 mmol of $NaBH_4$, 0.64 mmol of $CdCl_2$ and 40.0 mL of deionised water at growth temperature of 230 °C.

### 6.2.1.4 *Effect of temperature*

#### 6.2.1.4.1 *HDA-capped CdSe Nanoparticles*

The reactions were carried-out following the procedure described in section 6.2.1 at different growth temperatures of 110, 160 and 200 °C. Aliquots were

withdrawn, with a needle tip, at different times of 2, 5, 10, 15, 20, and 30 mins, to monitor the growth of the particles.

#### 6.2.1.4.2 *TOPO-capped CdSe Nanoparticles*

The reactions were carried-out following the procedure described in section 6.2.1 using TOPO (7.5 g) as the capping agent and 15.0 mL of TOP, at different growth temperatures of 170, 230, and 250 °C.

### 6.2.1.5 *Growth Kinetics*

The growth kinetics study was carried-out by using the sample prepared according to the procedure described in section 6.2.1. Aliquots were withdrawn, with a needle tip, at different time of 2, 5, 10, 15, 20 and 30 mins, to monitor the growth of the particles.

## 6.2.2 *Synthesis of organically soluble ZnSe Nanoparticles*

In a typical room temperature reaction, 0.32 mmol of selenium powder was mixed with 20.0 mL of deionised water in a three-necked flask. 0.81 mmol of $NaBH_4$ was carefully added to this mixture and the flask was immediately purged with nitrogen gas to create an inert atmosphere. After 2 hours, 0.32 mmol of $ZnCl_2$ dissolved in 20.0 mL of deionised water was added to the colourless selenium ion solution, resulting in a pale-yellow solution. The solution was stirred for 30 min. after which excess methanol was added. The resultant solution was then centrifuged. The ZnSe produced, was dispersed in TOP (6.0 mL) and after continuous stirring, the TOP-ZnSe solution was injected into the hot HDA (6.0 g) at 160 °C in an inert atmosphere. After an initial drop, the temperature was then gradually raised and

stabilised at 160 °C. The reaction was then allowed to continue for 20 mins. The yellow solution obtained was allowed to cool and methanol was then added. Addition of excess anhydrous methanol to the solution resulted in the reversible flocculation of the nanoparticles. The flocculate was separated from the supernatant by centrifugation. Excess methanol was removed, under vacuum, to give HDA-capped ZnSe nanoparticles. The resultant particles were dissolved in toluene to give an optically yellow solution of ZnSe nanocrystallites for characterization.

#### 6.2.2.1 *Effect of reduction time*

The reactions were carried-out following the procedure described in section 6.2.2 under reduction times of 2, 4 and 6 hrs.

#### 6.2.2.2 *Effect of temperature*

##### 6.2.2.2.1 *HDA-capped ZnSe nanoparticles*

The reactions were carried-out following the procedure described in section 6.2.2 at different growth temperatures of 110, 160 and 200 °C.

##### 6.2.2.2.2 *TOPO-capped ZnSe nanoparticles.*

The reactions were carried-out following the procedure described in section 6.2.2 using TOPO (7.5 g) as the capping agent and 15.0 mL of TOP at different growth temperatures of 160 and 200 °C.

#### 6.2.2.3 *Effect of monomer concentration*

##### 6.2.2.3.1 *HDA-capped ZnSe nanoparticles*

The reactions were carried-out following the procedure described in section 6.2.2 using 0.64 mmol of selenium powder, 1.59 mmol of $NaBH_4$, 0.64 mmol of

$CdCl_2$, 40.0 mL of deionised water, 12.0 mL of TOP and 12.0 g HDA at different growth temperatures of 110, 160 and 200 °C.

#### 6.2.2.3.2 *TOPO-capped ZnSe nanoparticles*

The reactions were carried-out following the procedure described in section 6.2.2 using TOPO (15.0 g) as capping agent, 15.0 mL of TOP, 0.64 mmol of selenium powder, 1.59 mmol of $NaBH_4$, 0.64 mmol of $CdCl_2$ and 40.0 mL of deionised water at different growth temperatures of 160 and 200 °C.

### 6.2.2.4 *Effect of precursor*

The reaction was carried-out following the procedure described in section 6.2.2 using zinc acetate as the zinc source, in place of zinc chloride.

## 6.2.3 *Synthesis of water soluble Nanoparticles*

### 6.2.3.1 *Synthesis at high temperature*

In a typical room temperature reaction, 0.32 mmol of selenium powder was mixed with 20.0 mL of deionised water in a three-necked flask. 0.81 mmol of $NaBH_4$ was carefully added to this mixture and the flask was immediately purged with nitrogen gas to create an inert atmosphere. After 2 hours, 20.0 mL aqueous solution of 0.32 mmol $CdCl_2$ was added to the colourless solution, followed by the addition of 20.0 mL L-cysteine ethyl ester hydrochloride solution with a molar ratio of 1:10 ($Cd^{2+}$:cysteine ester). The pH of the solution was raised to 4 after which the solution was then heated at 90 °C for 18 hrs under nitrogen. Aliquots were withdrawn at 3, 5 and 10 hrs. The cysteine-capped CdSe particles were separated by filtration and concentrated by rotary evaporation. A brownish-red material was precipitated with

acetone and dried under vacuum, to give a material which is readily dispersible in water.

#### 6.2.3.1.1 *Effect of pH*

The reactions were carried-out following the procedure described in section 6.2.3.1 by adjusting the pH of the solution to 7 and 11.

#### 6.2.3.1.2 *Effect of Cadmium: cysteine ratio*

The reactions were carried-out following the procedure described in section 6.2.3.1 by using $Cd^{2+}$ : cysteine ratio of 1:10, 1:20, 1:30, 1:50 and 1:60 at different pHs of 4, 7 and 11.

#### 6.2.3.1.3 *Effect of capping ligand*

The reactions were carried-out following the procedure described in section 6.2.3.1, by replacing the L-cysteine ethyl ester hydrochloride with methionine and starch as the capping agent at different $Cd^{2+}$ : ligand ratio and pHs of 4, 7 and 11.

### 6.2.3.2 *Synthesis of CdSe at room temperature*

In a typical room temperature reaction, 0.32 mmol of selenium powder was mixed with 20.0 mL of deionised water in a three-necked flask. 0.81 mmol of $NaBH_4$ was carefully added to this mixture and the solution was stirred under inert atmosphere for 2 hrs. 3.2 mmol of L-cysteine ethyl ester hydrochloride was added to 20.0 mL of deionised water, in a 100.0 mL flask, to give a colourless solution. $CdCl_2$ solution (0.32 mmol in 20.0 mL of water) was added to the colourless solution under stirring. The pH of the solution was increased to 11 by adding 0.1M ammonia

solution. The selenide ion solution prepared above, was then added under stirring, to give a yellowish solution; stirring was continued at room temperature for 24 hrs. Aliquots were withdrawn at 1, 3, 5 and 24 hrs to monitor the growth of the particles. A similar synthetic procedure was used for the synthesis at pH 4 and 7. The colour of the solution at pH 7 and 4 was pale-orange and orange respectively.

#### 6.2.3.2.1 *Synthesis of methionine and ascorbic acid-capped CdSe at room temperature*

The reactions were carried-out following the procedure described in section 6.2.3.2 by replacing the L-cysteine ethyl ester hydrochloride with methionine and ascorbic acid as capping agent at different pHs of 4, 7 and 11.

#### 6.2.3.2.2 *PVA-capped CdSe at room temperature*

The reactions were carried-out following the procedure described in section 6.2.3.2 by replacing the L-cysteine ethyl ester hydrochloride with 3.0 g PVA as the capping agent. The same process was repeated at a lower monomer concentration of 0.16 mmol of $CdCl_2$.

#### 6.2.3.2.3 *Synthesis of starch-capped CdSe at room temperature*

The reactions were carried-out following the procedure described in section 6.2.3.2 by replacing the L-cysteine ethyl ester hydrochloride with 0.05 wt/% starch and stirring the reaction for 2 hrs after which, it was allowed to age for 24 hrs. The starch-capped CdSe particles were separated from the mixture by filtration and concentrated by rotary evaporation to give a material which is readily dispersible in

water. The same process was repeated at a lower monomer concentration of 0.16 mmol of $CdCl_2$.

#### 6.2.3.3 *Synthesis of ZnSe at room temperature*

The reactions were carried-out following the procedure described in section 6.2.3.2 by using $ZnCl_2$ instead of, $CdCl_2$ and biomolecules such as L-cysteine ethyl ester hydrochloride, ascorbic acid and PVP as the capping agents.

### 6.2.4 *Synthesis of core/shell nanoparticles*

A CdSe-TOP solution (prepared as described in section 6.2.1) was injected into hot (230 °C) HDA (12.0 g) solution and kept at this temperature for 30 mins. An aliquot was removed from the reaction at 30 mins, for characterisation of the initial CdSe nanoparticles. Then a ZnSe-TOP solution (prepared as described in section 6.2.2) was injected into the red reaction mixture. Aliquots were taken at different reaction times as the reaction proceeded for a further 30 mins. After completion, toluene was added and the solution was allowed to cool. Methanol was then added to flocculate the nanoparticles. The flocculate was separated by centrifugation and dried. Dispersion of the flocculate in toluene resulted in an optically transparent solution that could be readily characterised. A similar synthetic procedure was repeated for the synthesis at 250 °C.

### 6.2.5 *Synthesis of CdSe nanocomposite*

CdSe-TOP and ZnSe-TOP solutions, prepared as described in section 6.2.1 and 6.2.2 respectively, were injected into a hot (160 °C) HDA (12.0 g) solution. This temperature was maintained for 30 minutes. After completion, toluene was added to

the solution which was then allowed to cool. Addition of excess anhydrous methanol to the solution resulted in the reversible flocculation of the nanoparticles. The flocculate was separated by centrifugation and dried. Dispersion of the flocculate in toluene resulted in an optically transparent solution that could be readily characterised.

## 6.3 Instrumentation

### 6.3.1 *UV/VIS and IR Spectroscopy*

A Perkin Elmer Lamda 20 UV-vis Spectrophotometer was used to carry-out optical measurements in the 200-1100 nm wavelength range at room temperature. Samples were placed in quartz cuvettes (1 cm path length). Optical measurements on samples from chapters 3 to 5 were performed, using a Perkin Elmer Lamda 25 UV-vis Spectrophotometer in the 200-1000 nm wavelength range at room temperature. Infrared spectroscopy was carried-out using a Perkin Elmer Paragon 1000 FT-IR Spectrometer. Samples were prepared as KBr pellet. A Tenzor 27, Bruker FT-IR spectrophotometer was also used for IR analysis.

### 6.3.2 *Photoluminescence Spectroscopy*

Room temperature photoluminescence (PL) spectra, were recorded on a Perkin Elmer LS 55 luminescence spectrometer with Xenon lamp over 400 - 800 nm range. The samples were placed in quartz cuvettes (1 cm path length). The wavelength of excitation is indicated in the text and was shorter than the onset of absorption of the samples being studied.

### 6.3.3 *X-ray powder diffraction (XRD)*

Powder diffraction patterns were recorded on an Oxford Xcalibur 2 four-circle diffractometer (CCD detector) using Mo Kα radiation (λ = 0.71703 Å). Samples were mounted on glass capillaries in lacquer droplets, roughly 0.8 mm in diameter. The data were collected and averaged over three runs at 2θ = 0°, 90° and 180° with 30 second exposures at an X-ray power of 2.0 kW. The temperature was 100(2) K. XRD pattern on samples from Chapters 2, 3 and 5 were performed using a Bruker aXS D8 advanced diffractometer and using Cu Kα radiation (λ = 1.5406 Å) operated at 40 kV and 40 mA.

### 6.3.4 *Electron microscopy*

A Philips CM120 BIOTWIW transmission electron microscope viewed, at 80 K was used for TEM. Samples for analysis were prepared by placing an aliquot of the sample solution onto an amorphous carbon substrate, supported on a copper grid and then, allowing the solvent to evaporate at room temperature. A JEOL JEM 3010 URP High Resolution Transmission Electron Microscope (HRTEM) operated at 300 kV and coupled with XEDS, was used for the high resolution analysis. Images were recorded using a 1024 x 1024 CCD camera and, SAD patterns were recorded on film.

### 6.3.5 *Energy Dispersive Spectroscopy*

Energy dispersive spectroscopy was performed on a Shimadzu SSX-550 supercan SEM/EDS at 500 kV. Carbon tape was used to suspend the powdered samples before loading onto the machine.

## RECOMMENDATIONS

In order to improve the luminescence and morphology of TOPO-capped CdSe nanoparticles we suggest that an extensive study be carried out on the synthesis using different precursor ratios, sources of cadmium precursors and pH.

Conjugations of semiconductor nanoparticles with biomolecules have extended the area of applications from optoelectronic devices to biological application, such as bio labelling and tags for protein. We recommend that more biomolecules should be used for the synthesis of water soluble nanoparticles and, more work should done on the conjugation of the as-synthesised particles with protein for it biological applications.

## AWARDS

1) **The Best Oral Presentation (PhD),** Faculty of Science and Agriculture, Post-Graduate Symposium, University of Zululand. 02 November 2006

2) **The Frank Nabarro Prize for the Most Outstanding Oral Presentation (PhD),** in the field of Condense Matter Physics and / Material Science, delivered at the Annual SAIP conference by a Doctoral Student at the South African Institution for Tertiary Education, 52nd Annual conferenc of the South African Institute of Physics (SAIP), University of the Witwatersrand, Johannesburg, 3-6 July.

3) **Research Rolls Of Honour.** University of Zululand, 21 Nov. 2007

4) **Certificate of Recognition for Research Service.** University of Zululand, 21 Nov. 2007

## PUBLICATIONS

1) **Oluwatobi S. Oluwafemi** and Neerish Revaprasadu (2007): A Novel Method to Prepare Cysteine Capped Cadmium Selenide Nanoparticles. *Mater. Res. Soc. Symp. Proc.*, ***951***, E03-12.

2) **O. S. Oluwafemi** and N. Revaprasadu (2008): A New Synthetic route to Organically capped Cadmium Selenide Nanoparticles. *New J. Chem.*, 2008, **32**, 1432.

3) **S. O. Oluwafemi**, N. Revaprasadu and A.J Ramirez (2008): A Novel One-Pot route for the Synthesis of Water-Soluble Cadmium Selenide Nanoparticles. *J. Cryst. Growth*, 2008, **310**, 3230.

4) **S. O. Oluwafemi**, N. Revaprasadu and S. H. Swart (2008): Synthesis, Characterization and Evolution of Optical properties of High Quality

Hexadecylamine Capped CdSe nanoparticles via a Facile Non –Organometallic route. *Journal of Luminescence*. (Submitted)

## PRESENTATIONS AT ACADEMIC CONFERENCES

1) **S. O. Oluwafemi** and N. Revaprasadu (2006): New synthetic route to Hexadecylamine Capped Cadmium Selenide Nanoparticles. 37th International Conference on Coordination Chemistry. (ICCC37), Cape Town, 13-18 August.
2) **Oluwatobi. S. Oluwafemi** and N. Revaprasadu (2006): A Novel Method to Prepare Cysteine Capped Cadmium Selenide Nanoparticles. Faculty of Science and Agriculture. Post-Graduate Symposium, University of Zululand. 02 November
3) **S.O. Oluwafemi** and N. Revaprasadu (2006): A Novel Method to Cysteine Passivated Cadmium Selenide Nanoparticle. Material Research Conference Boston MA, 27 Nov.- 1 Dec.
4) **S.O Oluwafemi,** N. Revaprasadu and H.C Swart (2007): A Novel Method to Synthesis Organically capped Cadmium Selenide Nanoparticles. 52nd Annual conference of the South African Institute of Physics (SAIP), University of the Witwatersrand, Johannesburg, 3-6 July.
5) **O. S. Oluwafemi** and Neerish Revaprasadu (2007): One-Pot Synthesis of Water Soluble Cadmium Selenide Nanoparticles. International Centre for Material Research 2007 (ICMR) conference, Richards Bay, SA, 29 Jul.-1 Aug.
6) **S.O Oluwafemi**, N. Revaprasadu and H.C Swart (2008): Synthesis, Characterization and Evolution of Optical properties of High Quality Hexadecylamine Capped CdSe nanoparticles via a Facile Non –Organometallic

route. 53rd Annual conference of the South African Institute of Physics (SAIP), University of Limpopo, 8-11 July.

7) **S.O Oluwafemi** and N. Revaprasadu (2008): The Effect of Reduction Time on the Growth and Photoluminescence of Colloidal CdSe Nanoparticles. 38th International Conference on Coordination Chemistry. (ICCC 38), Jerusalem, Israel, July 20-25.